11-1-2012 12:00 AM

Quantitative Evaluation of Pulmonary Emphysema Using Magnetic Resonance Imaging and x-ray Computed Tomography

Amir M. Owrangi
The University of Western Ontario

Supervisor
Dr. Grace Parraga
The University of Western Ontario

Graduate Program in Biomedical Engineering
A thesis submitted in partial fulfillment of the requirements for the degree in Doctor of Philosophy

Recommended Citation

Owrangi, Amir M., "Quantitative Evaluation of Pulmonary Emphysema Using Magnetic Resonance Imaging and x-ray Computed Tomography" (2012). *Electronic Thesis and Dissertation Repository*. 936.
https://ir.lib.uwo.ca/etd/936

QUANTITATIVE EVALUATION OF PULMONARY EMPHYSEMA USING MAGNETIC RESONANCE IMAGING AND X-RAY COMPUTED TOMOGRAPHY

Spine Title: MRI and CT of Emphysema

(Thesis Format: Integrated Article)

by

Amir M. Owrangi

Graduate Program in Biomedical Engineering

Submitted in partial fulfillment
of the requirements for the degree of
Doctor of Philosophy

The School of Graduate and Postdoctoral Studies
The University of Western Ontario
London, Ontario, Canada

THE UNIVERSITY OF WESTERN ONTARIO
School of Graduate and Postdoctoral Studies

Certificate of Examination

Supervisor

____
Grace Parraga, Ph.D.

Supervisory Committee

____
Aaron Fenster, Ph.D., FCCPM

____
Ian Cunningham, Ph.D., FCCPM

____
David McCormack, M.D. FRCPC

Examiners

____
Steward Gaede, Ph.D.

____
Yves Bureau, Ph.D.

____
Elaine O'Riordan, M.D. FRCPC

____
Narinder Paul, M.D. FRCR.

The thesis by

Amir M. Owrangi

entitled:

Quantitative Evaluation of Pulmonary Emphysema Using Magnetic Resonance Imaging
and
x-ray Computed Tomography

is accepted in partial fulfilment of the
requirements for the degree of
Doctor of Philosophy

Date: __________________________

____
Chair of Thesis Examination Board

Abstract

Chronic obstructive pulmonary disease (COPD) is a leading cause of morbidity and mortality affecting at least 600 million people worldwide. The most widely used clinical measurements of lung function such as spirometry and plethysmography are generally accepted for diagnosis and monitoring of the disease. However, these tests provide only global measures of lung function and they are insensitive to early disease changes. Imaging tools that are currently available have the potential to provide regional information about lung structure and function but at present are mainly used for qualitative assessment of disease and disease progression. In this thesis, we focused on the application of quantitative measurements of lung structure derived from ^{1}H magnetic resonance imaging (MRI) and high resolution computed tomography (CT) in subjects diagnosed with COPD by a physician. Our results showed that significant and moderately strong relationship exists between ^{1}H signal intensity (SI) and ^{3}He apparent diffusion coefficient (ADC), as well as between ^{1}H SI and CT measurements of emphysema. This suggests that these imaging methods may be quantifying the same tissue changes in COPD, and that pulmonary ^{1}H SI may be used effectively to monitor emphysema as a complement to CT and noble gas MRI. Additionally, our results showed that objective multi-threshold analysis of CT images for emphysema scoring that takes into account the frequency distribution of each Hounsfield unit (HU) threshold was effective in correctly classifying the patient into COPD and healthy subgroups. Finally, we found a significant correlation between whole lung average subjective and objective emphysema scores with high inter-observer agreement. It is concluded that ^{1}H MRI and high resolution CT can be used to quantitatively evaluate lung tissue alterations in COPD subjects.

Keywords:

^{1}H Magnetic Resonance Imaging, Computed Tomography, Chronic Obstructive Pulmonary Disease, Pulmonary Emphysema, Hyperpolarized ^{3}He, Apparent Diffusion Coefficient, Principal Component Analysis

Co-Authorship

The following thesis contains three manuscripts. One manuscript was published as a peer-reviewed manuscript in a scientific journal and two manuscripts were submitted for publication. Chapter 2 is an original manuscript entitled "Quantitative ^{1}H and Hyperpolarized ^{3}He Magnetic Resonance Imaging: Comparison in Chronic Obstructive Pulmonary Disease and Healthy Never-Smokers", and was published in the *European Journal of Radiology* in May 2012. The manuscript was coauthored by Amir Owrangi, Jian Wang, Andrew Wheatley, David G. McCormack and Grace Parraga. Amir Owrangi designed and conducted the experiments, analyzed the data, and wrote the manuscript. Dr. Jian Wang and Dr. David G. McCormack, provided technical and clinical expertise and aided in interpretation of the results. Hyperpolarization of ^{3}He was performed by Andrew Wheatley. He also provided assistance with software design and writing. Dr. Grace Parraga, as the principal author's supervisor helped lead the study design, helped to determine the project objectives, provided mentorship, consulted on interpretation of the results, provided editorial assistance and overall guidance.

Chapter 3 is an original manuscript co-authored by Amir Owrangi, Lauren Villemaire, Andrew Wheatley, Roya Etemad-Rezai, Ian Cunningham, David G. McCormack and Grace Parraga. This manuscript, entitled "Quantification of Emphysema using x-ray Computed Tomography Histogram Analysis" is in preparation for submission to the journal of *Investigative Radiology*. Amir Owrangi contributed to study design, study subject visits, performed data analysis and statistical analysis, led interpretation of the results and wrote the manuscript. Lauren Villemaire provided assistance with data and statistical analyses. Dr. Ian Cunningham, Dr. David G. McCormack, Dr. Roya Etemad-Rezai provided technical and clinical expertise and aided in interpretation of the results.

Hyperpolarization of ^{3}He was performed by Andrew Wheatley. He also provided assistance with software design and writing. Dr. Grace Parraga, as the principal author's supervisor helped lead the study design, helped to determine the project objectives, provided mentorship, consulted on interpretation of the results, provided editorial assistance and overall guidance.

Chapter 4 is an original manuscript entitled "Subjective Evaluation of Emphysema: Reproducibility and Comparison with Objective Quantification" and is in preparation for submission to the journal of *Academic Radiology*. The manuscript was co-authored by Amir Owrangi, Lauren Villemaire, Brandon Entwistle, Andrew Lu, Jack Chiu, Nabil Hussain, Roya Etemad-Rezai, David G. McCormack and Grace Parraga. Amir Owrangi contributed to study design, study subject visits, subjective scoring of emphysema, performed data analysis and statistical analysis, led interpretation of the results and wrote the manuscript. Lauren Villemaire provided assistance with subjective scoring of emphysema, data and statistical analyses. Dr. David G. McCormack, Dr. Roya Etemad-Rezai provided technical and clinical expertise and aided in interpretation of the results. Dr. Roya Etemad-Rezai, Dr. Brandon Entwistle, Dr. Andrew Lu, Dr. Jack Chiu and Dr. Nabil Hussain provide assistance in subjective scoring of emphysema. Hyperpolarization of ^{3}He was performed by Andrew Wheatley. He also provided assistance with software design and writing. Dr. Grace Parraga, as the principal author's supervisor helped led the study design, helped to determine the project objectives, provided mentorship, consulted on interpretation of the results, provided editorial assistance and overall guidance.

Appendix A is an original manuscript entitled "Pulmonary Tumour Measurements from X-Ray Computed Tomography in One- Two- and Three-dimensions" and was published in *Academic Radiology* in November 2011. The manuscript was co-authored by Lauren Villemaire, Amir Owrangi, Laura Wilson, Elaine O'Riordan, Roya Etemad-Rezai, Harry Keller, Brandon Driscoll, Glen Bauman, Aaron Fenster and Grace Parraga. Amir Owrangi and Lauren Villemaire contributed equally to study design, tumour measurement, performed data analysis and statistical analysis, led interpretation of the results and wrote the manuscript. Laura Wilson provided assistance with measurement of tumours, data and statistical analyses. Dr. Glen Bauman, Dr. Elaine O'Riordan, Dr. Roya Etemad-Rezai, Dr. Aaron Fenster and Dr. Harald Keller provided technical and clinical expertise and aided in interpretation of the results. Brandon Driscoll performed the phantom tumour measurements and provided assistance with phantom scanning. Dr. Grace Parraga, as the principal author's supervisor helped led the study design, helped to determine the project objectives, provided mentorship, consulted on interpretation of the results, provided editorial assistance and overall guidance.

Appendix B is an original manuscript entitled "Three-dimensional lung tumor segmentation from x-ray computed tomography using sparse field active models" and was published in *Medical Physics* in February 2012. The manuscript was co-authored by, Joseph Awad, Amir Owrangi, Lauren Villemaire, Elaine O'Riordan, Grace Parraga and Aaron Fenster. Joseph Awad contributed to study design, performed data analysis and statistical analysis, led interpretation of the results and wrote the manuscript. Amir Owrangi and Lauren Villemaire provided assistance with measurement of tumours, performed data analysis and statistical analysis. Dr. Grace Parraga provided technical and clinical expertise and aided in interpretation of the results. Dr. Aaron Fenster, as the principal author's supervisor helped led the study design, helped to determine the project objectives, provided mentorship, consulted on interpretation of the results, provided editorial assistance and overall guidance.

Appendix C is an editorial entitled "Chest MRI in children: why bother?" and was published in *Respirology* in January 2012. The manuscript was co-authored Amir Owrangi and Grace Parraga. Amir Owrangi wrote the manuscript. Dr. Grace Parraga, as the principal author's supervisor helped led the helped to determine the manuscript objectives, provided mentorship, provided editorial assistance and overall guidance.

Pulmonary function tests were performed by Sandra Halko and Shayna McKay and MRI data acquisition was performed by Trevor Szekeres.

To my family

Acknowledgements

First, I would like to take a moment and thank my supervisor, Dr. Grace Parraga for giving me the opportunity to be part of her research group, for her guidance, enthusiasm, and everlasting support. She was not only a great supervisor to me, but also a good mentor who inspires and challenges me, and shares her research insight and passion throughout this research project. I owe her many thanks for her constructive criticism during my time in her lab.

I would also like to thank the members of my advisory committee: Dr. Aaron Fenster, Dr. Ian Cunningham and Dr. David McCormack for their invaluable guidance and support. Their insightful suggestions and advice provided me with new thoughts and directions for my project.

I would also like to thank the staff of the Parraga lab: Andrew Wheatley, Trevor Szekeres, Shayna McKay and Sandra Halko. To Andrew Wheatley, who is always helping me with computer related issues and software installation. I really enjoyed sitting near you during my thesis writing period. To Sandra Halko, who answers many of my questions about pulmonary function tests and helps in collecting such a wonderful data set. To Shayna McKay, who collects all the clinical information of all subjects in one Access datasheet. Whenever I asked you a question your thoughtful answers were always helpful. Many thanks to Trevor Szekeres, for performing fast and efficient MRI scans. You've been very helpful in answering all of my questions.

To my lab-mates, for your friendship and support. I am very thankful for the friendships that I have made with all of you and I hope we can keep in touch in the future. I would

like to thank Miranda for helping me with my stats questions and spending time to discuss the physiological aspects of my project. To Lindsay, for being a good friend and shedding some light into some aspects of my project. To Steve for a lot of physics and imaging related discussions that we had. Dan, we had lots of stat related discussion which helped me a lot through the statistical analysis of my projects. Lauren, we started working together during you undergrad fourth year project and I always enjoyed working with you. I wish our collaboration can continue for future projects. Sarah, you have been a great teammate both in the lab and in the soccer field. Nikhil, you have been a good friend to me and I always enjoyed chatting with you. Many thanks to Laura Wilson and Hassan Ahmed for many memorable times that we had together.

A very special thank to my wife, Samaneh, for your true love, patience and support. I would also thank my family for all of their support and encouragement through my PhD.

Finally, I am thankful for the financial support I received during my graduate studies, particularly the Queen Elizabeth II Graduate Scholarship in Science and Technology and the Schulich Graduate Scholarship.

Table of contents

List of Appendices

List of Tables

Chapter 1

Chapter 2

Chapter 3

Chapter 4

List of Figures

Chapter 1

Chapter 2

Chapter 3

Chapter 4

List of Abbreviations

2D	Two-dimensional
3D	Three-dimensional
^{3}He	Helium-3
^{99m}Tc	Technetium-99m
^{129}Xe	Xenon-129
ADC	Apparent diffusion coefficient
ANOVA	Analysis of variance
ATS	American thoracic society
AUC	Area under the curve
BAL	Bronchoalveolar lavage
BMI	Body mass index
BW	Bandwidth
COPD	Chronic obstructive lung disease
CT	Computed tomography
COV	Coefficient of variation
D_HP_CS	Density histogram principal component score (DHPCS)
DL_{CO}	Diffusing capacity of carbon monoxide
DWI	Diffusion-weighted imaging
ERV	Expiratory reserve volume
FDG	Fluorodeoxyglucose
FEV_1	Forced expiratory volume in one second
FENO	Fractional exhaled nitric oxide
FGRE	Fast gradient recalled echo
FOV	Field of view
FRC	Functional residual capacity
FVC	Forced vital capacity
GEHC	General electric health care
GOLD	Global initiative for chronic obstructive lung disease
GUI	Graphical user interface
HIPAA	Health insurance portability and accountability act
HRCT	High resolution computed tomography
HU	Hounsfield units
IC	Inspiratory capacity
ICC	Intraclass correlation coefficient
LAC	Low attenuation cluster analysis
MANOVA	Multivariate analysis of variance
MLD	Mean lung dose
mMRC	Modified medical research council
MRI	Magnetic resonance imaging
PCA	Principal component analysis
PET	Positron emission tomography
PFT	Pulmonary function test
PIPEDA	Personal information protection and electronic documents act
RA	Relative area

RF	Radiofrequency
RV	Residual volume
SGRQ	St. George’s respiratory questionnaire
SNR	Signal-to-noise ratio
SPECT	Single photon emission computed tomography
SpO_2	Oxygen saturation on pulse oximetry
TCV	Thoracic cavity volume
TE	Echo time
TLC	Total lung capacity
TR	Repetition time
TV	Tidal volume
VC	Vital capacity
WHO	World health organization
$\%_{pred}$	Percent of predicted value

CHAPTER 1: Introduction

1.1 Overview and Motivation

Chronic Obstructive Pulmonary Disease (COPD) is currently the fourth leading cause of death worldwide.[1] Its prevalence and mortality rates continue to rise and COPD projected is to be the third leading cause of death by 2020.[2] In Canada, this disease affects at least one million people[3] and is directly responsible for over 10,000 deaths and 100,000 hospitalizations annually, costing over $5 billion per year in estimated direct and indirect costs.[3,4] The worldwide Burden of Obstructive Lung Disease (BOLD) study recently reported that 10% of the world's adults 40 years and older have clinically relevant COPD.[5,6] COPD is characterized by persistent airflow limitation in which small airways disease and parenchymal destruction, or emphysema, are the most important underlying mechanisms.[7] The future morbidity and mortality of COPD patients can be reduced by early detection of the disease and the rate of its progression can be decelerated through smoking cessation.[8,9]

Pulmonary function tests (PFT) widely used in respiratory clinics, such as spirometry, provide established measurements of lung function that are widely accepted for the diagnosis and monitoring of COPD;[10,11] however, these tests are insensitive to early disease changes, progression of the disease and response to treatments.[11,12] Moreover, these tests provide only global measures of lung function and no regional information about the anatomical structure of the lung can be acquired. Imaging tools that are currently available have the potential to provide regional information about lung structure and function and can be utilized as a sensitive tool for detecting and monitoring small structural changes in the lung. High-resolution x-ray computer tomography (CT) provides regional anatomical information and can be used to evaluate COPD abnormalities in the airways,[13-15] regional evaluation of gas trapping[16,17] and quantification of lung tissue structure alterations.[18-24] Conventional proton magnetic resonance imaging (^1H MRI) is also readily available in most clinical care centers and can be used for qualitative[25,26] and quantitative[27-29] evaluations of lung structure.

This thesis focuses on the application of quantitative measurements of lung structure derived from ^1H MRI and high resolution CT in subjects with a smoking history of at least 10 pack-years to differentiate between normal lung and emphysematous lung. In order to test the capability of differentiating between emphysematous and healthy lungs, ^1H MRI were acquired using the short echo time (TE) pulse sequence and novel objective and subjective quantification tools and techniques were developed to evaluate lung CT images. Chapter 1 provides a foundation for understanding the lung structure and function in healthy and COPD subjects. This chapter addresses the literature related to the basics of COPD physiology, diagnosis and treatment options as well as reviewing the subjective and objective methods for quantification of pulmonary emphysema. Finally, an overview of the hypothesis and objective of this thesis related to quantification of pulmonary emphysema using ^1H MRI and CT is described.

1.2 Lung Structure and Function

The respiratory system is responsible for gas exchange and its main task is to allow oxygen to move from air into the blood and allow carbon dioxide to move out from blood into the air. Failure of the respiratory system can cause rapid cell death due to oxygen starvation.[30] The respiratory system is separated into two main divisions: the conducting zone and respiratory zone.

1.2.1 Conducting zone

Airways in the conducting zone start from the trachea and continue down to terminal bronchioles, which are the smallest airways without alveoli (Figure 1.1). The trachea divides into a pair of primary bronchi where each left and right bronchus supplies air to each lung. Within the lung and up to the 11th generation, each bronchus repeatedly divides into smaller bronchi.[31] The smallest bronchi divide into the first bronchioles in the 12th generation and, while they continue to branch, their diameters continue to decrease.[31] Conducting bronchioles start from the 12th generation and continue to the 16th generation.[32] Distal to the 16th generation, conducting bronchioles turn into respiratory bronchioles where alveoli start to appear in the walls of the airways.[32]

The main responsibility of the conducting airways is to carry air to and from the respiratory zones. Since there are no alveoli in the conducting zone, no gas exchange occurs in this region and, therefore, this is called the anatomical dead space. However, anatomical dead space takes up only 150 ml (3% of human lung volume) and the respiratory zone takes up the rest of the lung volume, maximizing the gas exchange area in the lung.[33]

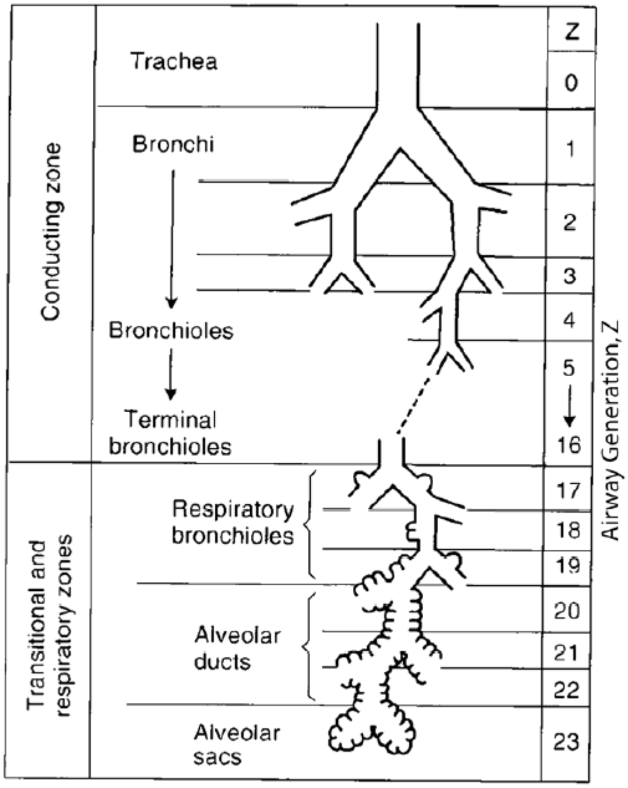

Figure 1.1: Human airway tree by generation
Image adapted from West JB, Respiratory Physiology Eighth Edition[33]. Conducting zone starts from trachea (generation zero) and continue down to terminal bronchioles (16th generation). Respiratory zone starts from respiratory bronchioles (17th generation) and continue down to alveolar sacs (23th generation).

1.2.2 Respiratory zone

The respiratory zone is the region of the lung where gas exchange takes place. This Zone starts at the respiratory bronchioles (17th generation) and continues down to the alveolar sacs (23rd generation). As shown in Figure 1.2, alveoli are the sites for gas exchange in the lung and they start to appear in the respiratory bronchioles wall. Their numbers continue to increase as we move toward to the higher generation airways. On average, the diameter of each alveolus is about 0.2mm, with an average volume of 4.2 x 10^6 μm^3.

It has been shown that there are about 170 alveoli per mm^3 and an average human lung contains 240 – 790 million alveoli.[34]

Proper gas exchange is essential and needs to be performed continuously. Therefore, the blood-gas interface plays an important role in this task. Gas-exchange between lung and blood is carried out by transmembrane diffusion of oxygen and carbon dioxide. Fick's law of diffusion states that the amount of diffusion is proportional to the surface area of the membrane and inversely proportional to the thickness of the surface.[33] The gas exchange surface in the human lung is very thin and an average person has a total surface area of 70 square meters,[35] which makes the lung an ideal place for gas exchange.

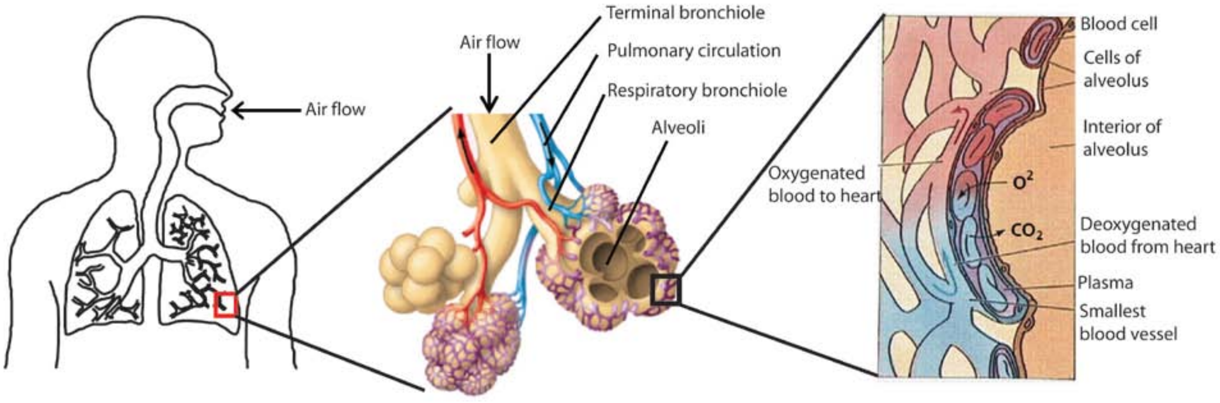

Figure 1.2: Lung function
Air comes from nasal cavity and ultimately goes into alveoli. Alveoli are sites of O_2 and CO_2 exchange with the blood. Diagram of alveoli adapted from an online source[36]. Image of the gas exchange across capillary and alveolus wall adapted from[37].

1.3 Chronic Obstructive Pulmonary Disease (COPD)

Chronic obstructive pulmonary disease (COPD) is characterized as a progressive airflow limitation and is associated with the inflammatory process of the respiratory system related to the introduction of noxious particles and gases.[10,38] COPD is the world's fourth leading cause of death and mortality and morbidity continue to increase.[39,40] In Canada, 1.5 million people have been diagnosed with COPD,[41] which leads to thousands of hospitalizations with a total cost of $1.5 billion a year.[42] However, another 1.6 million Canadians report having symptoms but have not been diagnosed with COPD.[41]

Introduction of noxious gases into the respiratory system can lead to a chain of reactions that ultimately may result in the development of COPD. Noxious gas, in particular, tobacco smoke, is responsible for chronic inflammatory response in the airways and lung tissue, which leads to airflow limitation.[10,43] Chronic inflammation is the main reason for development of COPD that encompasses some pathological changes in different areas of the respiratory system, including central airways, small airways, lung tissue and pulmonary vasculature.[38] However, small airway disease and lung tissue destruction are the two main underlying mechanisms of airflow limitation[7] and will be discussed in more detail in the next two sections. Inflammation in the central airways results in chronic bronchitis, which is accompanied by excessive mucous production.[38] Central airways refer to cartilaginous airways with an internal diameter greater than 2 mm.[38] Small airway obstruction is the consequence of inflammation in noncartilaginous airways with an internal diameter of less than 2 mm.[38] Inflammation in lung parenchyma can result in pulmonary emphysema, which is defined as an abnormal enlargement of the airspaces distal to the terminal bronchioles.[44] Development of COPD, even in the early stages, can lead to some changes in pulmonary vasculature, including vessel wall thickening and endothelial dysfunction.[38,45]

Chronic cough, shortness of breath and sputum production are the common symptoms of COPD;[46] however, the diagnosis can be confirmed by measuring the airflow using spirometry.[47] Forced expiratory volume in one second (FEV_1) and forced vital capacity (FVC) are two main measurements that can be performed using spirometry. To confirm the presence of COPD, the post-bronchodilator $FEV_1/FVC < 70\%$ needs to be achieved.[38] COPD can also be classified into four groups: mild, moderate, severe and very severe (Table 1).

Table 1.1 COPD classification based on spirometry

COPD severity	Post-bronchodilator FEV_1/FVC	FEV_1% predicted
Mild	< 70%	≥ 80%
Moderate	< 70%	50% - 80%
Severe	< 70%	30% - 50%
Very severe	< 70%	< 30%

Table adapted from ATS/ERS Standards for the diagnosis and managements of patients with COPD.[38]

1.3.1 Small Airways Disease

Smoking and inhalation of noxious particles and gases leads to the inflammatory process in the lung,[46] which results in obstruction of small peripheral airways.[48-50] Airways smaller than 2 mm in diameter are the major site of airway obstruction in COPD.[49,51] Moreover, small peripheral airways including bronchioles, lack cartilage[32] and their structure is supported by lung parenchyma and alveolar structure.[38,52] Destruction of alveolar walls that support small airway structures[52] and contribute to elastic recoil of lung parenchyma[53] along with airway narrowing,[54] contribute to an increase in resistance of small airways.

Direct evaluation of the inflammatory changes of the airways using biopsy and indirect evaluation using bronchoalveolar lavage (BAL) have confirmed the inflammatory response of the airways to noxious particles and gases especially cigarette smoke, even in subjects with normal lung function.[46,55]

1.3.2 Parenchymal Destruction

Parenchymal destruction, or emphysema, has been defined as "abnormal permanent enlargement of airspaces distal to terminal bronchioles, accompanied by destruction of their walls without obvious fibrosis."[44] As shown in Figure 1.3, enlargement of the airspaces is mainly due to alveolar wall destruction and ultimately results in the reduction of the gas exchange area in the lung. This will reduce the amount of gas that can diffuse from alveoli to the blood stream and vice versa. Moreover, the chronic inflammation of lung parenchyma can lead to destruction of the attachments between the respiratory bronchioles and the surrounding tissue.[56] Since bronchioles do not have cartilage in their wall and the attachment between their wall and surrounding tissue helps keep them open, any rupture or breakage in the alveolar wall or between these attachments can lead to closure of the airways and can cause air trapping.[56]

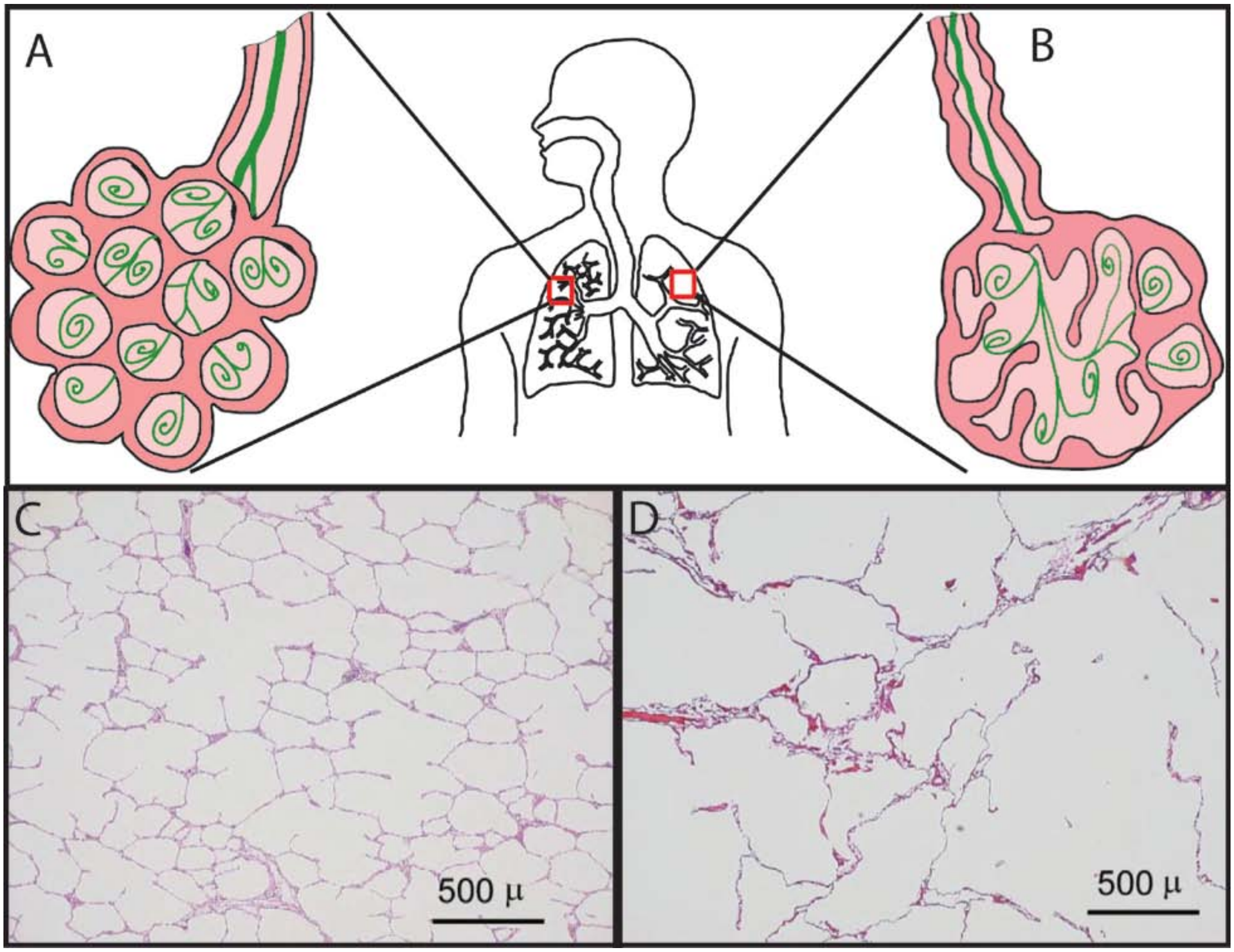

Figure 1.3: Healthy and emphysematous alveoli
Schematic of normal and emphysematous alveoli are shown in A and B. (A): Normal alveoli with healthy walls, (B): Airway with thickened wall and emphysematous alveoli with destructed walls and less gas tissue interface. Histological slice of a (C) healthy lung tissue and (D) emphysematous lung tissue were adapted from Woods et al.[57] Magn Reson Med. 2006; 56(6):1293-300.

Pulmonary emphysema can be classified into two main types: panacinar emphysema and centrilobular emphysema. Panacinar emphysema uniformly affects the entire respiratory acinus and results from α_1-antitrypsin deficiency[58] and it predominantly affects the lower lung regions.[59] On the other hand, centrilobular emphysema refers to airspace wall destruction in the center of the lobul,[56,60] which is primarily associated with smoking[61] and occurs more frequently in the upper lung region when it is in its mild stage[62]. Noxious particles and gases contribute to the inflammatory process in the lung that was mediated by immunological cells such as alveolar macrophages, T lymphocytes and neutrophils.[47,63,64] Proteolytic enzymes that have been released by these immune cells result in destruction of the alveolar walls and enlargement of the airspaces.[62]

1.4 Evaluation of COPD in Clinical Practice

1.4.1 Pulmonary Function Tests

Pulmonary function tests allow us to measure the static and dynamic lung volumes as well as the lung's capacity for transmembrane gas diffusion. Plethysmography can measure and record the static lung volumes at predetermined points during the respiratory maneuver (Figure 1.4). Total lung capacity (TLC) is defined as the volume of gas in the lungs at full inflation and the amount of gas that remains in the lungs after full expiration is called residual volume (RV).[33] Functional residual capacity (FRC) is the gas volume remaining after a normal expiration of the lung. This is a volume where there is a balance between the chest wall and lung elastic recoil.[33] Body plethysmographs measure the FRC by applying Boyle's Law while the subject is in a large airtight box. A shutter present in a mouth piece can measure the pressure of the lung while the subject tries to inhale at the end of a normal expiration. Boyle's Law states that, at a constant temperature, the product of volume and pressure is constant, and since the lung tries to expand while the shutter is closed, by measuring the lung pressure at the shutter we can calculate the lung volume at the end of normal expiration.[33] Tidal volume (V_T) is also defined as the volume of the gas that goes in and out of the lung while the subject breathes normally and no extra effort is applied during the respiratory phases. The total amount of gas that can be inhaled after a normal expiration is called inspiratory capacity (IC) and the total amount of gas that someone can exhale after a full inspiration is called vital capacity (VC).

Dynamic lung volumes can be assessed by measuring the amount of gas that someone can forcefully exhale using spirometry (Figure 1.4). The breathing maneuver for spirometry starts from inhalation of air up to TLC followed by forceful exhalation to RV. The volume of gas that is exhaled in the first second of exhalation is called forced expiratory volume in one second (FEV_1) and the total volume of gas that is exhaled from the lung is called forced vital capacity (FVC). The ratio of FEV_1 over FVC is accepted as a criterion for diagnosis of COPD.[38,47] In a healthy individual, this ratio is above 70% but in obstructive diseases, such as COPD, air trapping and increased residual volume and severe airflow obstruction cause reduction in FEV_1 and FVC. However, FEV_1 reduction is greater than the decrease in FVC, which results in lower FEV_1/FVC. Reductions in the elastic recoil of the lung, along with increase in the airway resistance, are the main causes of FEV_1 reduction in obstructive lung diseases.[33]

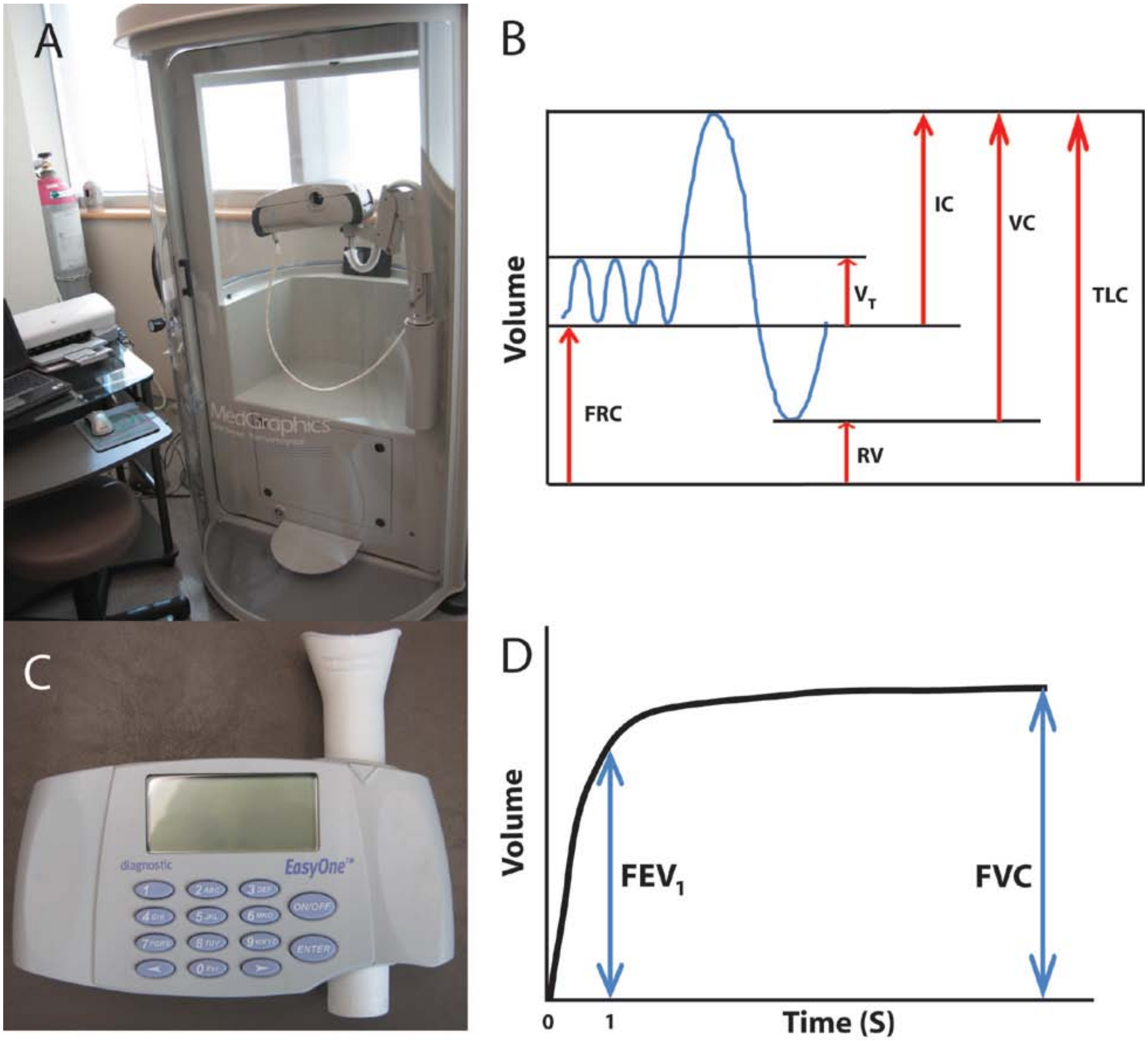

Figure 1.4: Pulmonary function testing

(A) A whole body plethysmograph. Lung volumes shown in (B) were measured using plethysmography. (C) A hand held spirometer. A sample airflow curve measured by spirometry is shown in (D).

Measurements of diffusion capacity of the lung for carbon monoxide (DL_{CO}) enable the evaluation of the lung's capacity for transferring CO from airspaces into the pulmonary capillaries. Many factors can influence the diffusion capacity of CO, including blood volume, surface area of the gas exchange and hemoglobin concentration.[65] In this test, subjects inhale a mixture of gases, including CO, a tracer gas, and a mixture of O_2 and N_2 and hold their breath for about 10 seconds before exhaling into the mouth piece. The concentration of CO is then measured from the exhaled gas after the volume of the gas in the dead space has been discarded.[66] The tracer gas, which is included in the gas mixture, cannot be absorbed by blood and should be chemically and biologically inert.[66] The initial concentration of CO in the alveoli will not be the same as its concentration in the mouth piece during the inhalation. This is because of its dilution with the remaining gases in the alveoli. Since the tracer gas cannot be absorbed by blood, the concentration of CO in the alveoli can be measured by calculating the difference between the concentration of inhaled and exhaled tracer gas.[33]

1.4.2 Measurements of Dyspnea

Dyspnea, or breathlessness, is a subjective experience for individuals who complain of uncomfortable breathing.[67] Different questionnaires have been developed for quantification of dyspnea, and a few of them will be discussed in the next paragraph. The results of these questionnaires depend on how subjects can describe their feelings while performing daily tasks. Another way of assessing dyspnea is through exercise tests where subjects are asked to perform an exercise in a controlled fashion. These tests are accompanied by a scaled questionnaire, such as BORG scale, for rating the dyspnea.[68] The Borg scale is a table with numerical values for evaluation of dyspnea that starts from zero for no dyspnea or shortness of breath to 10 for maximum dyspnea.[69]

The modified medical research council (mMRC) dyspnea scale was designed for evaluating the level of dyspnea or shortness of breath. In this questionnaire that includes five levels of breathlessness, subjects are supposed to choose a section that best describes their shortness of breath.[70] St. George's Respiratory Questionnaire (SGRQ), is a more complete survey which was developed for subjects suffering from airflow limitation. The survey aims to address three areas related to their disease, including symptoms, activities related to breathlessness and daily life disturbances.[71] This is a questionnaire that includes 76 items that need to be filled by the subject, and takes about 10 minutes to complete.[71]

The Six Minute Walk distance (6MWD) refers to an objective test that measures the distance that a subject can walk in 6 min.[72] There is a relationship between the ability of the subjects to perform this test and quality of their life.[73] It has been shown that 6MWD can also predict the risk of hospitalization in subjects with COPD.[74] The rate of dyspnea and overall fatigue should be measured at baseline and after the 6MWD test using the Borg dyspnea scale.[72]

The BODE index is used to help predict the mortality of COPD, with higher scores related to higher risk of death after diagnosis. It includes: body-mass index (BMI), the degree of airflow obstruction and dyspnea, and exercise capacity.[75] The degree of airflow limitation will be determined using FEV$_1$ % predicted, dyspnea will be assessed using mMRC dyspnea scale and exercise capacity will be evaluated using 6MWD. BMI in the BODE index has the score of 0 or 1 and the other three sections have scores ranging from 0 to 3. The sum of all four categories will range from 0 to 10.

1.4.4 Fractional exhaled nitric oxide (FENO)

Nitric oxide (NO) is produced by inflammatory cells in human lungs and presents in the exhale breath. Chronic inflammation of the airways will increase the amount of NO, which has been recognized as a biological mediator.[76] The fractional exhaled nitric oxide (FENO) is a quantitative and non invasive method for evaluation of airway inflammation.[77] In FENO, subjects are asked to exhale their breath into a device where the NO molecules produce light during a chemical reaction. The number of photon emitted during the reaction is proportional to the number of NO molecules present in the exhale breath. However, measurement of exhaled NO may be affected by some factors such as current smoking[78] and needs to be considered in subjects with COPD. It has been shown that there was a correlation between the changes in the amount of NO and the number of neutrophils[76] as well as association between the variability in measurement of FENO and number of exacerbations in COPD subjects.[79] However, the application of FENO in subjects with COPD is not established yet and its exact role needs to be defined.[77]

1.4.5 Bronchial alveolar lavage (BAL)

Inflammation of the respiratory system, especially airways, is one of the biomarkers of COPD. Bronchial alveolar lavage (BAL) enables researchers to measure the inflammatory response of the airways and provide a better understanding of the disease and related treatments.[62] The amount of inflammatory cells and proteins that are contained in the pulmonary secretions can be measured using BAL.[80] While direct visualization of the lumen of the airway is possible using flexible fibre-optic bronchoscopy, it can also be used to collect samples from the airways.[73] For BAL, a small amount of sterile saline is flushed into the desired airways and then drawn back.[73] These samples that contain cells and proteins is sent to a laboratory for further analysis under microscope.[73] Since this is an invasive method, it cannot be used for monitoring the disease in short time intervals and it cannot be tolerated by patients with moderate to severe COPD stages. Therefore, BAL studies are mainly limited to patients with mild to moderate stages of COPD.[62]

Induced sputum is another way of evaluating airway inflammation. This a non-invasive and inexpensive method that can applied on patients repeatedly with moderate to severe COPD.[62] Induction of sputum can be performed by inhalation of hypertonic saline followed by a cough of a sample of sputum for further analysis.[73] However, these tests cannot provide any regional information about the affected areas of the lung.

1.5 Imaging the Lung

1.5.1 Chest x-ray

X-ray radiography is the most common and inexpensive type of imaging for the evaluation of pulmonary structure. Image formation in x-ray radiography depends on the contrast between materials that x-ray photons travel through. Image contrast is dependent on the mass attenuation coefficient of the tissue which varies with photon energy, atomic number and mass density of the absorbing material. Bony tissues in the body absorb much of the x-rays and appear white on the x-ray images; therefore, sufficient effort is needed to avoid their presence in the lung field-of-view (FOV) in chest radiography. For example, one of these bony tissues that may appear in a chest radiograph is the scapula, where subjects are coached to place their hand on the back of their hip and gently move their shoulder forward in order to minimize its presence in the FOV during the anterior-posterior (AP) acquisition.[81] In another example, when it is necessary to acquire a lateral chest radiograph for sagittal evaluation of the lungs, subjects are asked to put their hands on top of their head to minimize the presence the hand's bones in the FOV.[81]

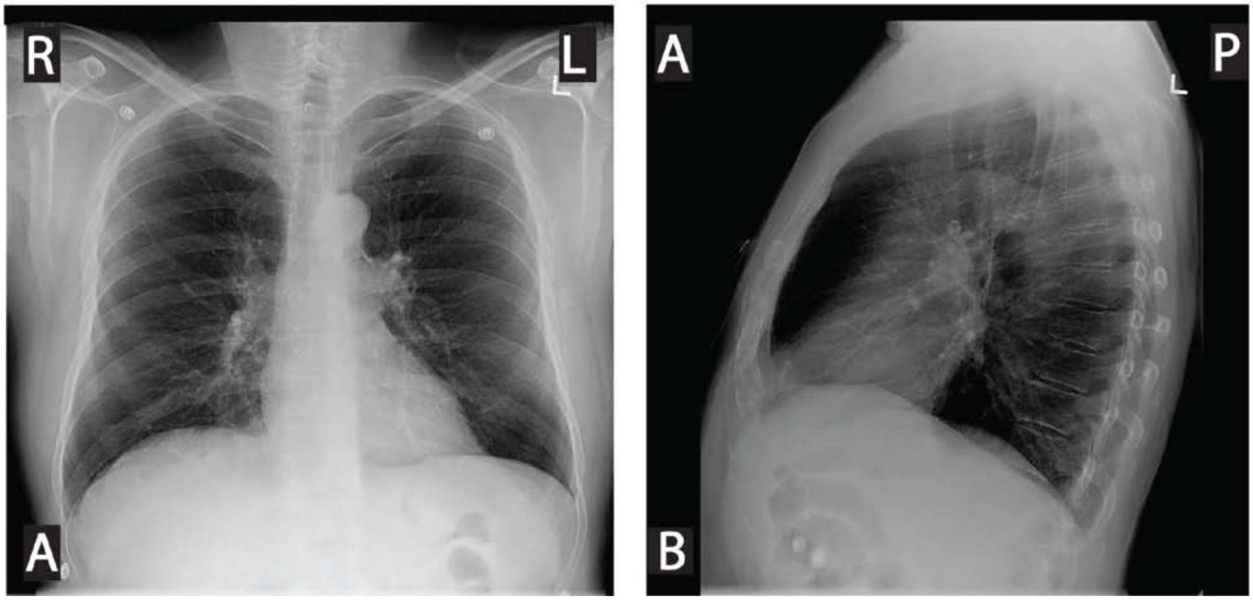

Figure 1.5: Chest x-ray of a COPD subject
X-ray radiograph chest images of 62 year-old male with severe COPD. (A) Coronal view, (B) Sagittal view. Images adapted from Parraga et al.[82] Invest Radiol. 2007; 42(6):384-91.

Lung linear attenuation coefficient is defined as $\mu = (\mu/\rho) \times \rho$, where (μ/ρ) is the mass attenuation coefficient and ρ is the physical density of the absorbing material. Lung linear attenuation is relatively low in comparison to its surrounding tissue, mainly because it is filled with air, which has a very low physical density. The average radiation dose associated with a normal chest x-ray is about 0.02 mSv,[83] which is equivalent to the background radiation dose in 2 days when considering an average background radiation dose of 0.01 mSv/day[84]. This is a relatively small radiation dose, which adds to the other advantages of this imaging modality such as its short acquisition time. However, despite these advantages, diagnostic information of respiratory diseases provided using chest radiographs is restricted due to limited soft tissue contrast and superposition of bones, tissues and air in the path of x-ray. Therefore, its application especially in COPD is more prone toward the assessment of more advanced morphological changes in the lung.[85] Figure 1.5 shows a flattened diaphragm and overall increase in the anterior-posterior diameter of the chest in a patient with severe COPD.

In COPD and especially in emphysema, x-ray radiography can be used to assess some classical features including hyperinflation and detection of bullae. In an AP view of a chest x-ray, it has been shown that an increase in the diameter of the chest and flattening of the diaphragm are correlated with the presence of COPD.[85] Other features including a reduction in pulmonary blood flow associated with emphysema[86] and airway thickening in chronic bronchitis[87] can be detected in x-ray radiography, but presence of hyperinflation in subjects with COPD is the most useful feature for detection of emphysema[88].

1.5.2 X-ray Computed Tomography

The introduction of computed tomography (CT) in the 1970s as a novel imaging technique has revolutionized the field of diagnostic imaging in medicine. Image formation in CT is based on tomographic reconstruction of internal structure from information acquired through multiple projections of an object.[89] In each projection, a fan beam of photons from a x-ray source is transmitted through a desired object and some of those photons that have not been completely attenuated and penetrated through the object can be received by arrays of multiple detectors.[89] Following the acquisition of multiple projections, a 2D cross-sectional image of the object can be displayed in a matrix and subsequently, multiple adjacent 2D slices can be reconstructed into a 3D volumetric image of the object. In CT each pixel is labeled with a value that is determined by the average linear attenuation coefficient of the corresponding region in the object. One of the main advantages of CT over the other imaging modalities, is the ability to provide images with standard pixel values in a unit called the Hounsfield unit (HU), which is named after an inventor of computed tomography, Sir Godfrey Hounsfield.[90] HU is a scale used in CT to convert the linear attenuation coefficient measurements of an object into a universal radio-density scale as shown in equation 1:

$$HU = \frac{\mu_x - \mu_{water}}{\mu_{water}} \times 1000 \qquad (1)$$

where μ_x and μ_{water} are the linear attenuation coefficients of object and water, respectively. Standardized pixel values provide the opportunity for direct comparison of pixel intensities of a same region that were acquired from different scanners with different manufacturers.

The development and improvement of CT over the last four decades provides the capability of volumetric imaging of lungs within a single breath-hold. Rapid image acquisition with high spatial resolution makes this modality an ideal tool for assessment of pulmonary structure, in particular when most pulmonary images are acquired in breath-hold condition.[91] However, development of four-dimensional CT (4DCT) provides the opportunity for acquiring images in free breathing style. 4DCT not only can provide information about lung tissue structure, but also can provide the opportunity to acquire ventilation maps for functional regional evaluation of the respiratory system following the post processing of lung CT images that were acquired in different time-points of the breathing cycle.[92-94] These ventilation maps that have been generated after post processing of dynamic CT images, have been validated against nuclear medicine approaches, which is the standard method for regional evaluation of ventilation maps.[95]

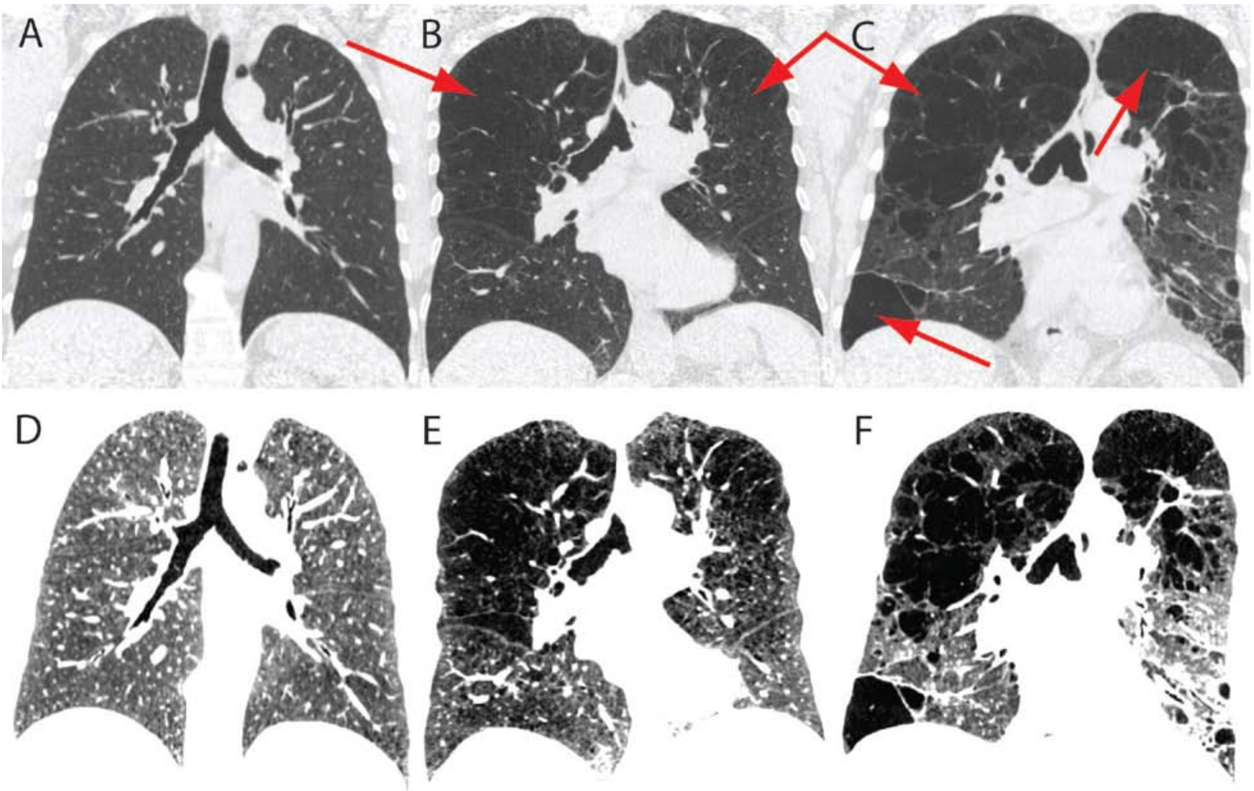

Figure 1.6: X-ray CT of healthy and emphysematous lungs
Lower row displays the same images as upper row in a different window and level. Coronal center slice CT images for a healthy volunteer (left panel), GOLD stage III COPD subject (middle panel) and GOLD stage IV COPD subject (right panel). Emphysematous regions are indicated by arrows. Images A-C are displayed in the standard Lung window (=1500 HU) and level (=-600 HU) and images D-F are the same images displayed in a deferent window (=280) and level (=-850) to highlight the emphysematous regions that are pointed to with arrows in the upper panel.

CT is an established imaging tool for detection and diagnosis of different lung diseases. It can also be used for quantification and follow-up assessment of structural pulmonary abnormalities as well as providing better understanding of pathological and clinical basis of many lung diseases. In COPD studies, CT has a very important role for detecting and quantifying different structural abnormalities that leads to airflow limitation. One of these structural abnormalities is pulmonary emphysema, which CT plays an important role in its quantification. Representative center slice CT images of lung for a healthy volunteer and COPD stage III and IV subjects are shown in Figure 1.6. Such CT images are routinely used to qualitatively detect and evaluate pulmonary emphysema.

1.5.3 Nuclear Medicine Methods

In nuclear medicine, radioactive material(s) administered into body will be absorbed by different organs.[96] Regions with radionuclide uptake will become active sources that emit gamma rays; however, information acquired from these regions depends on the distribution of the radioactive nuclei in the organs. To guide and control the pathway of the administered radionuclide, they are usually attached to molecules that most probably will be absorbed by the organ that needs to be imaged. This will help to increase the concentration of radionuclide in the organ of interest and reduce contamination of other organs in the body.[96] The number of gamma rays emitted from any organ, depends on the concentration of the radioactive materials and the rate of their decay. In nuclear medicine, the challenge is to find the spatial distribution of the radioactive material rather than finding the map of attenuation coefficient like in CT.

All radioactive nuclei that are used in nuclear medicine emit gamma rays and some of those gamma rays that can leave the body, will be captured by gamma cameras.[96] For a projection image to be formed, in addition to the measurements of photon flux density, the direction of the detected photons needs to be determined.[96,97] In planar scintigraphy, 2D projection image acquired based on the radioactivity distribution in the region of interest. However, it is also possible to generate the volumetric image of the radioactivity distribution by acquiring multiple planar projection of the organ at different angles using single photon emission computed tomography (SPECT).[98] These planar projections will be used to reconstruct the tomographic images of the radioactivity distribution.[98]

In lung imaging, nuclear medicine techniques have been developed to study lung perfusion and ventilation. These methods allow for regional evaluation of pulmonary function. Ventilation images in SPECT and planar scintigraphy can be performed using radioactive gases including xenon and krypton (^{133}Xe, ^{127}Xe and ^{81m}Kr) or aerosols that are labeled with radioactive nuclei such as technetium-99m (^{99m}Tc).[99] The distribution of the aerosols in the respiratory system is mainly dependent on their particle sizes.[100] The ideal size range for the aerosols is between 0.1 to 0.5 µm and particles larger than 2 to 3 µm have less chance of passing through large airways.[99] Ventilation imaging can be performed in three phases of wash-in, steady state and wash-out using ^{133}Xe, where regional lung volume and regional gas trapping can be studied.[99] In nuclear medicine, radiation dose exposure to the patient starts from the point the radioactive material administered to the body and continues to decrease until it is completely washed out of the body or physically decays. Effective radiation dose in ventilation imaging ranges between 0.1-0.6 mSv, depending on the protocol and the type of radioactive gas or aerosol that is used.[101]

Perfusion is another parameter for the assessment of lung function, which can be performed by intravenous injection of ^{99m}Tc-labeled macro-aggregates albumin (MAA). The sizes of these particles are between 3 to 150 µm with 95% of them being between 3 to 40 µm.[102] Once these molecules reach pulmonary capillaries, their distribution can demonstrate regional pulmonary perfusion.[99] However, ^{99m}Tc-labeled MAA particles can mainly provide images of the relative pulmonary arterial blood flow because the sizes of many of these molecules are greater than the internal diameter of the arterioles and cannot pass through them to reach the pulmonary veins.[101] In a normal procedure, about 200 000 particles will be injected, which may block less than 0.1% of the total number of arterioles.[101] After a few hours post injection, macrophages will break up the MMA particles and pass them through the arterioles and full perfusion of those blocked regions will be restored.[101] Effective dose in perfusion imaging using ^{99m}Tc-labeled MAA is typically 1.0 mSv.[101]

Planar scintigraphy and SPECT work with radio isotopes (e.g. ^{99m}Tc) that emit single gamma ray photons in each radioactive decay. However, some other isotopes that emit positrons can be used in another nuclear medicine imaging modality, which is called positron emission tomography (PET). Isotopes such as ^{11}C, ^{13}N, ^{15}O, ^{18}F, ^{19}Ne, and ^{68}Ga emit positrons,[103] which after several collisions with surrounding particles, its kinetic energy approaches to zero. During an annihilation interaction of a zero-energy positron with a neighbouring electron, two 511 keV photons are produced and travel 180 degrees apart from each other.[104] Simultaneous production of photons that travel in opposite directions from each other and coincidence detection of them in detector arrays surrounding the patient eliminate the need for collimation because the source of these photons is somewhere along the pathway between two detectors.[104]

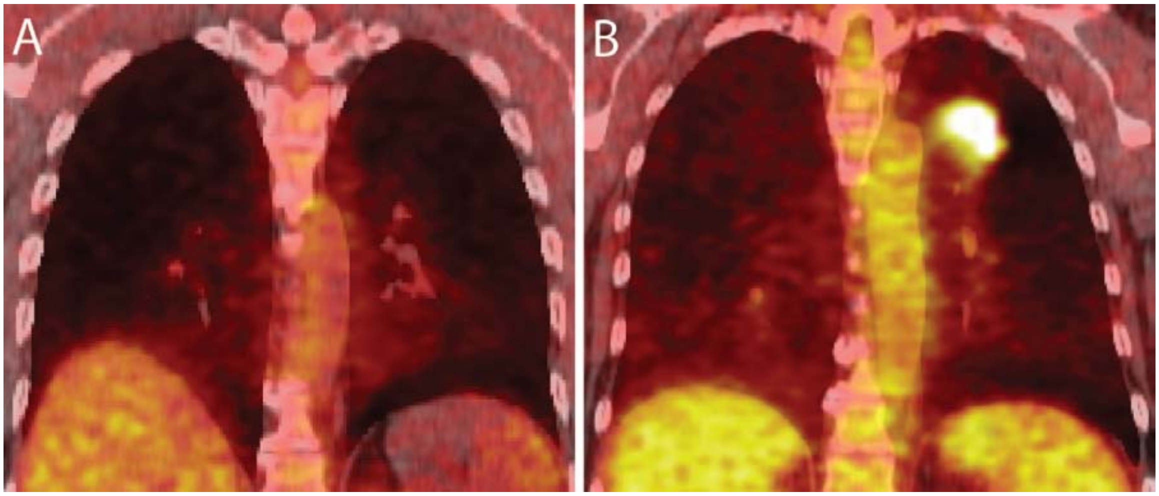

Figure 1.7: PET/CT image of healthy volunteer and subject with lung cancer
Coronal lung PET/CT images (A) healthy volunteer and (B) a subject with lung cancer. Images are courtesy of Harry Marshall.

PET is a great imaging modality for studying lung function, because it can provide volumetric information about the distribution of the inhaled or injected radioisotopes.[103,105] Moreover, most positron emitting radioisotopes have a short half-life, which minimizes the radiation exposure to the subjects. One of the longest half-life among positron emitting radioisotopes belongs to ^{18}F, which is 110 minutes. This radioisotope can also be combined with deoxyglucose, to form ^{18}F-fluodeoxyglucose (FDG), which is one of the most common radioactive tracers for PET imaging. Coronal PET/CT images of a healthy volunteer and a subject with lung tumor are shown in Figure 1.7. Although FDG cannot be metabolized, its uptake is similar to glucose and will be increased in lungs as a result of airway inflammation caused by neutrophilic infiltration.[105]

Nuclear medicine imaging techniques have been used for regional evaluation of lung function in COPD. These methods have been used to find areas of the lungs in COPD subjects with matched ventilation and perfusion defect[99] as well as perfused areas with no ventilation[106]. It has also been shown that there was a significant correlation between radioactive aerosol ventilation imaging and pulmonary function tests.[107] PET imaging can also be used for differentiating emphysematous COPD subjects that have lower tissue density and higher ventilation/perfusion ratio and COPD subjects with airway disease that have lower ventilation and higher pulmonary blood flow.[108]

1.5.4 Magnetic Resonance Imaging

The lung is one of the most difficult organs to image with MRI. Proton (^{1}H) MRI of the lung is challenging mainly because of some conditions of the respiratory system. First, the low tissue density and the proton density of the lung reduce the signal intensity (SI) that can be acquired from lung.[109] Second, the countless number of air-tissue interfaces in the lung causes magnetic field inhomogeneity and high MR susceptibility artifact, which leads to extreme reduction of T2* and rapid decay of the acquired signal from lung tissue.[110] Lastly, the movement of cardiac and respiratory systems causes motion artifacts in the MRI images.[109] However, there are some approaches to mitigate these challenges.

The development of more powerful hardware along with faster pulse sequences enables detailed imaging of pulmonary structure that is comparable with other imaging modalities such as CT.[26,111] For instance, minimizing the rapid signal decay of tissues with very short transverse relaxation time (T2*) currently is feasible using faster pulse sequences with short and ultra short echo time (UTE).[112-114] In some studies, the subtraction between images that have been acquired using UTE and those acquired using higher TE has shown the enhancement of organs with very short T2*.[115,116] In a study by Failo et al. it was shown that lung MRI images with diagnostic quality comparable to CT images can be acquired in subjects with cystic fibrosis (CF) using a short TE pulse sequence.[25] In general, higher signal intensity can be achieved using pulse sequences with shorter TE than conventional pulse sequences that employ longer TE.

To minimize the motion artifact caused by the movement of the respiratory system, lung MRI protocols were designed based on breath-hold techniques[117], even though this method will impose a time limit on the duration of image acquisition. Respiratory motion artifacts in free breathing protocols can be partially eliminated[118] using gated imaging techniques, but standard clinical protocols are mainly based on breath-hold methods.

In MRI imaging, lung diseases can be divided into two groups. Some diseases, such as lung cancer, liquid infiltration or cell accumulation in the airways, will increase the proton density of the lung. The increase of proton density, usually accompanied by a reduction in air-tissue interfaces, will increase the lung signal intensity.[119] Visual assessment of such diseases is often not difficult because they provide a high contrast against the dark background lung tissue.[120] On the other hand, some pathologies such as hyperinflation due to airway obstruction and emphysematous destruction in COPD will cause the loss in lung tissue as well as reduction in blood volume flow, which both contribute to reduction in proton density and MRI signal intensity.[117] It has been shown that airflow obstruction and the level of hyperinflation have a negative relationship with lung tissue MRI signal intensity.[27,29]

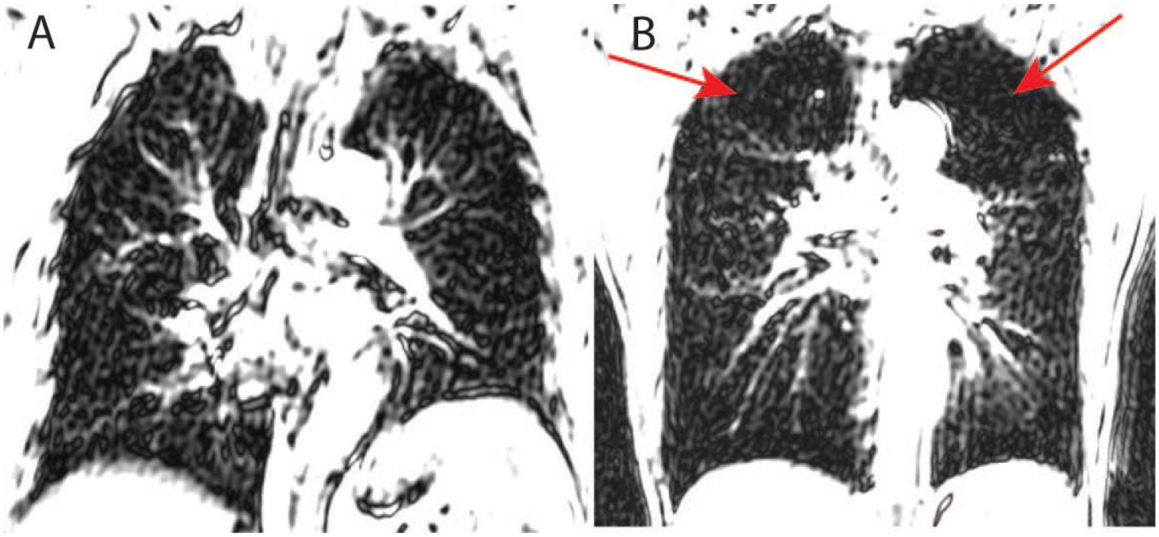

Figure 1.8: Conventional ^{1}H MRI of healthy and emphysematous lungs
Conventional pulmonary ^{1}H MRI of the lung (A) healthy volunteer and (B) COPD subject. Although, lung 1H MRI images are affected by low proton density and high susceptibility artifacts, short TE MRI can provide regional information regarding the emphysematous destruction of the lung tissue as indicated by arrows.

Regional functional assessment of pulmonary ventilation is important for the evaluation of different pathological conditions and pathophysiological analysis of different respiratory diseases. One of the main advantages of MRI is to provide functional information as well as structural information without using any ionizing radiation. The combination of functional and structural information with high spatial and temporal resolution for the entire lung are the main advantages of MRI over the other imaging modalities. This is mainly beneficial for imaging of children and young adults who are more susceptible to ionizing radiation[121-123], as well as follow-up monitoring of subjects who are undergoing medical examinations and clinical trials.[124]

Over the past decade, there were several studies using different MRI techniques for regional evaluation of pulmonary ventilation. Recently, the development of Fourier decomposition techniques allows for direct imaging of pulmonary ventilation.[125] This technique uses a 2D fast steady state pulse sequence for functional assessment of pulmonary ventilation and perfusion without using any contrast agent[125] and has been validated against other imaging techniques including SPECT and CT[126]. Oxygen-enhanced lung MRI[127] along with hyperpolarized noble gas MRI have also played an important role in developing our understanding of lung physiology,[57] lung tissue structure and function in COPD.[82,128] Oxygen-enhanced MRI was first introduced by Edelman et al. as a new method for regional evaluation of pulmonary ventilation using molecular oxygen (O_2) as a contrast agent.[129] O_2 molecules are slightly paramagnetic and their presence will shorten the longitudinal relaxation time (T_1) of protons in lung tissue.[130,131] The amount of oxygen that presents in each lung region not only depends on the ventilation of oxygen in that region of interest, but also depends on the diffusion of oxygen molecules into capillaries and perfusion of blood in the pulmonary system.[131] It has been shown that oxygen-enhanced MRI has a significant correlation with spirometry results (i.e. $\%FEV_1$ and FEV_1/FVC) and $\%DL_{CO}$.[132,133]

Hyperpolarized noble gas MRI has emerged as a robust imaging technique, which gives us valuable information about lung tissue structure and function.[82,134,135] This method was first introduced by Albert et al.[136] in 1994, showing the feasibility of using ^{129}Xe as a contrast agent for MRI imaging in an ex-vivo mouse model. ^{3}He and ^{129}Xe are noble gases with intrinsic spin of ½ and can be polarized using a laser optical pumping method.[136,137] In conventional MRI, the external magnetic field forces the ^{1}H nuclei to be aligned in the direction of the magnetic field, where the number of parallel alignments are slightly higher than the number of anti-parallel alignments. The small ratio of parallel over anti-parallel alignments produces a small polarization, which is however accompanied by a large abundance of ^{1}H nuclei in the body to produce adequate signal. However, in hyperpolarized noble gas MRI the low density of inhaled gas can be compensated by increasing the polarization of the gas prior to inhalation.

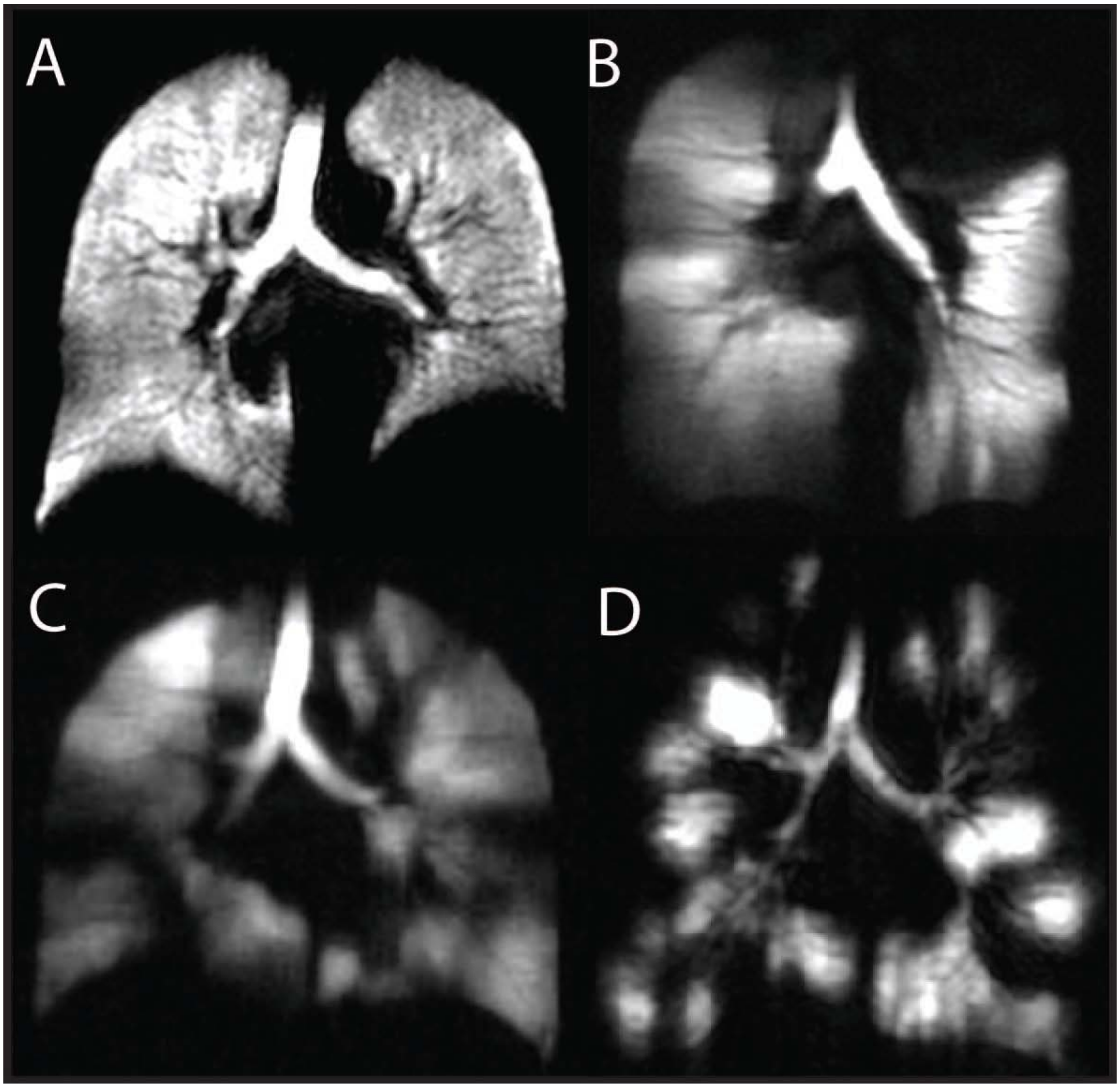

Figure 1.9: Hyperpolarized ^{3}He MRI of a healthy volunteer and subjects with different lung diseases
Pulmonary hyperpolarized ^{3}He MRI of (A) a healthy volunteer and subjects with (B) COPD (C) Asthma and (D) CF.

Nuclear polarization of the noble gases can increase the ratio of parallel over anti-parallel alignments of the nuclei up to 100 000 times compared to conventional MRI polarization.[136] During the polarization process, rubidium (Rb) vapor that is mixed with noble gas atoms in a container will be bombarded by the circularly polarized laser. The absorption of laser light by the Rb atoms polarize them along a small external magnetic field that exists in the polarizer. In duration of 6-8 hours, a polarization of 10-25% can be achieved for the noble gas atoms as a result of the collision with Rb atoms.[138]

Hyperpolarized noble gas MRI can be utilized to acquire both functional and structural information of the pulmonary system using two different imaging techniques. Since the development of these MRI methods, several studies have been performed to measure pulmonary structure and function. For functional information, spin density imaging provides high resolution information about the distribution of gas in the lung. In other words, the signal intensity of each region in the lung represents the abundance of gas molecules in that region. Normal lung function in healthy subjects can be characterized by homogeneous distribution of the gas in the lung; however, in diseases, heterogeneous distribution of the gas can be characterized as presence of regions with no signal or low signal intensity.

The safety of both ^{3}He and ^{129}Xe have been examined and high subject tolerability was shown with the prescribed doses of gas.[139-141] Normal ventilation in healthy volunteers was shown by Kauczor and co-workers with homogenous high signal intensity and inhomogeneous signal intensity was shown for subjects with COPD and bronchogenic carcinoma.[142] Since then, several groups have used this technique to study a variety of lung diseases and complications including lung cancer,[143,144] lung transplantation,[145-147] cystic fibrosis (CF),[148,149] asthma,[150-152] and COPD.[57,153-156] Figure 1.9 shows the centre coronal slice hyperpolarized ^{3}He static ventilation for a healthy volunteer and subjects with COPD, asthma, and CF.

1.6 Imaging of Pulmonary Emphysema

1.6.1 X-ray CT

CT is the imaging modality of choice for evaluation of pulmonary emphysema because of its high spatial resolution, which allows physicians to visually assess the severity of emphysema. Additionally, the digital nature of the CT dataset and the robustness of the pixel values in CT images have fostered considerable interest in developing new tools for the objective quantification of CT images.

Subjective evaluation of lung CT images allows for regional assessment of different lung diseases such as emphysema and can provide information regarding their distribution in the lung. In other words, visual scoring gives radiologists or pulmonologists the opportunity to not only distinguish emphysema from other causes of low attenuation such as hyperinflation or gas trapping related to small airway diseases, but also score it based on its distribution.[157] Moreover, it is shown that visual scoring of emphysema is relatively independent from scanning protocols.[158] However, the main limitations of visual scoring methods in general, are the subjectivity and high variability.[159-161] In a recent study from COPDGene CT workshop,[162] a group of 33 pulmonologists and 25 radiologists scored a large number of subjects including normal non-smokers and subjects with different stages of COPD, where they found a substantial inter-observer variability. However, they recommended that despite the high inter-observer variability, visual scoring may be complementary to quantitative assessment of emphysema.

The relative area of the lung occupied by attenuation values lower than single thresholds and percentiles of the frequency distribution of x-ray attenuation values within the lung have been examined to measure the extent of emphysema quantitatively.[163] These indices with selected thresholds have been shown to correlate well with visual emphysema scores[164,165], PFT[165] and both microscopic and macroscopic measurements of emphysema[19,163,166]. Recently, the relationship between quantitative measurements of CT indices and some other clinical metrics of COPD have been studied. It has been shown that BODE index has a greater relationship with emphysema while SGRQ is more closely related to airway disease.[167] Moreover, Rambod et al demonstrated that the objective quantification of emphysema using CT images correlates with the functional exercise tolerance as measured by 6MWD.[168]

In quantitative scoring of emphysema, different studies suggest different thresholds. The threshold of -910 HU was first proposed by Müller et al.[24] because it had the highest correlation between CT measurements of emphysema in contrast-enhanced 10 mm slice thickness images and emphysema in resected lung tissue. A threshold of -950 HU was reported by Gevenois et al. for the strongest correlation between 1 mm non-contrast-enhanced high-resolution CT assessments of emphysema at total lung capacity (TLC) and macroscopic[19] and microscopic[166] measurement of emphysema. More recently, Madani et al.[163] studied the relationship between the extent of emphysema at TLC quantified by a range of thresholds lower than -900 HU, in 1.25 mm slice thickness images where they found all thresholds lower than -910 HU were significantly correlated with histopathological indices. Thresholds ranging from -960 HU to -980 HU had the highest correlation with microscopic and macroscopic assessment of the extent of emphysema.[163]

Other quantification techniques such as low attenuation cluster analysis (LAC)[169,170] are also susceptible to the HU threshold and their validation against pathologic standards is controversial.[171,172] Madani et al. showed that LAC_{960} does not reflect the extent of emphysema as compared to macroscopic and microscopic measurements[171], but Yuan et al. recently showed that LAC_{856} is significantly correlated with histological measurements.[172] Despite numerous quantitative studies, there is no final consensus regarding an optimal HU threshold.

1.6.2 ^1H and Hyperpolarized ^3He MRI

In emphysema as discussed before, there is loss of tissue, reduced blood volume and significant gas trapping and all of these would be expected to diminish the inherent tissue-specific ^1H MRI signal intensity.[27] Figure 1.8 shows pulmonary ^1H MRI for a healthy volunteer and a patient with pulmonary emphysema acquired using a short TE ^1H MRI methods. It has been shown by Bankier et al. that the gravity-dependent gradient of ^1H MRI signal intensity depends on the lung posture and the magnitude of the gravity-dependent signal intensity gradient is larger than the iso-gravitational signal intensity gradient.[28] It has also been shown that alterations in lung volume resulted in ^1H MRI SI change[27]. These results demonstrate the sensitivity of MRI signal intensity to variations in lung tissue density. In a mouse model, it was shown that there was a relationship between ^1H MRI signal intensity and micro-CT density measurement of lung tissue.[173] It has also been shown that ^1H MRI signal intensity is sensitive to emphysematous destruction of lung tissue[113] as well as different positive end-expiratory pressure levels in mouse models.[174] Nevertheless, the unrealized potential for MRI to provide regional structural and functional measurements for COPD continues to motivate the development of ^{1}H MRI methods in human subjects and animal models.[112,125]

Structural evaluation of the lung is feasible using hyperpolarized noble gas diffusion weighted imaging (DWI). In this method, which is sensitive to gas self-diffusion, measures of the random microscopic movement (Brownian motion) of the gases allow for probing the pulmonary microstructure.[175] After inhalation of hyperpolarized noble gas two interleaved images without and with additional diffusion sensitization are acquired.[82] The first image will be served as a map of ventilation, while the combination of the 2 images can be used to compute the apparent diffusion coefficient (ADC) maps.[82] Figure 1.10 shows the coronal centre slice ^{3}He MRI ADC map of a healthy never-smoker and a COPD subject. ADC imaging allows for direct measurements of pulmonary airspaces. In healthy lungs, ADC has homogeneous distribution and is relatively low; however, in some diseases such as emphysema, destruction of lung tissue leads to enlargement of the airspaces and increasing ADC. The validation of ADC has been examined against histological[57] and CT measurements[176] and its reproducibility has been shown to be high.[177,178]

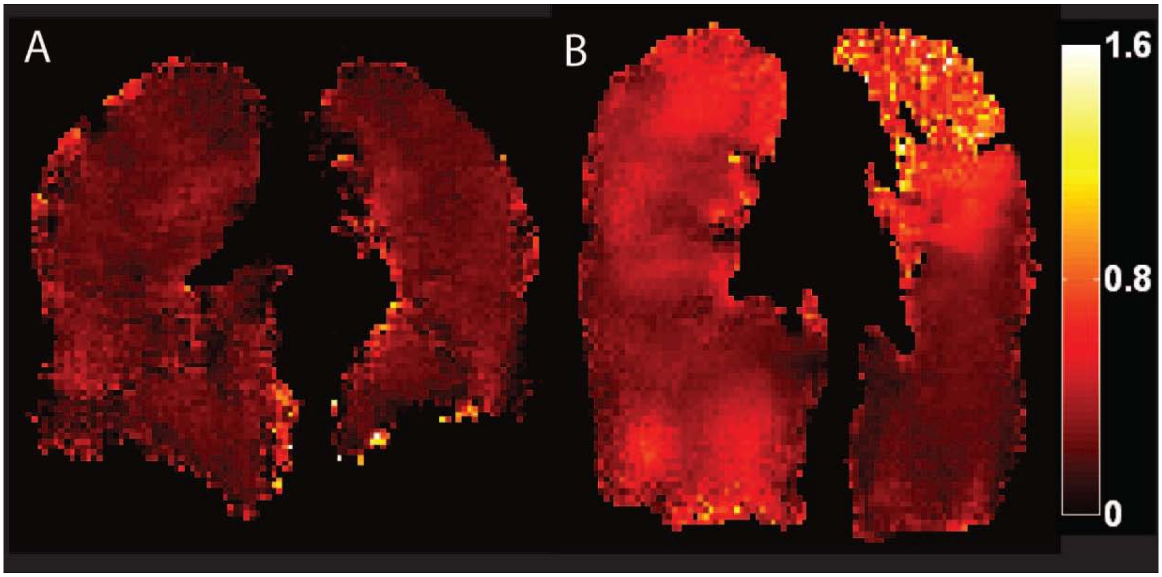

Figure 1.10: Pulmonary hyperpolarized ^{3}He ADC of a healthy volunteer and a subject with COPD.
Pulmonary hyperpolarized ^{3}He ADC of (A) a healthy volunteer and (B) a subject with COPD.

Hyperpolarized noble gas MRI has been used to evaluate lung structure and function in COPD subjects.[82,138,156,178-181] Increases in ventilation defect and ADC have been shown in subjects with COPD in comparison to age matched healthy volunteers.[82,180,182] It has also been shown that the mean ADC value will be increased in animals with elastase induced lung emphysema.[183] Previous COPD studies have shown that the ADC is dependent on the posture and gravity[184,185] and correlates with pulmonary functions tests.[186] It has been shown that ADC in subjects with COPD is dependent on the posture and gravity.[185] ADC can provide the opportunity to assess different features of the lung structure by changing the diffusion time and gradient strength.[187] Small diffusion time is more sensitive to short-range diffusion and can be used in assessment of local microstructure such as alveolar destruction whereas long range diffusion is more sensitive to larger lung structural changes such as airway connectivity.[184,188]

1.7 Thesis Hypothesis and Objectives

The overarching objective of this thesis is to evaluate CT and MRI methods of assessing lung structure in healthy volunteers and subjects with COPD. A short TE pulse sequence was used for ^{1}H MRI and a method for quantifying the extent of emphysema in CT images was developed, and evaluated here, in regards to its sensitivity and specificity for the detection of emphysema. The research objective and hypothesis tested in each chapter of this thesis are described here.

We first evaluated the relationship between short echo time pulmonary ^{1}H MRI signal intensity and ^{3}He ADC, high-resolution CT measurements of emphysema, and pulmonary function measurements, and this is described in Chapter 2. Here we tested the hypothesis that coincident and volume-matched inhalation acquisition of ^{3}He and ^{1}H MRI in COPD would allow for the detection of a relationship between hyperpolarized ^{3}He ADC and ^{1}H MRI signal intensity of the lung parenchyma. Nine healthy never-smokers and 11 COPD subjects underwent same-day plethysmography, spirometry, short echo time ^{1}H and diffusion-weighted hyperpolarized ^{3}He MRI at 3.0T. In addition, for COPD subjects only, CT densitometry was also performed.

We then developed a multi-threshold analysis method in Chapter 3, for objective emphysema scoring that takes into account the frequency distribution of each HU threshold. We hypothesized that this technique would have a high sensitivity and specificity for the detection of emphysema. This method was applied to calculate the whole lung emphysema scores for one hundred and fourteen middle-aged and elderly subjects, including 58 healthy subjects and 56 COPD subjects. These scores were compared with other objective approaches for quantification of emphysema.

In Chapter 4 of this thesis, the inter- and intraobserver reproducibility of the visual scoring was evaluated on a large number of sections for detailed assessment of pulmonary emphysema on whole lung CT. We developed and applied a tool for rapid quantitative evaluation of emphysema in lung CT images. Seven observers with varying degrees of expertise scored extent of emphysema on CT images of 114 middle-aged and elderly subjects, including 58 healthy volunteers and 56 COPD subjects. For comparison, we also evaluated the visual scoring results with whole lung densitometry and low attenuation cluster analysis (LAC) as well as with pulmonary function tests and hyperpolarized ^{3}He ADC.

The hypothesis tested in this thesis is that subjective and objective emphysema scores of high resolution CT, and ^{1}H MRI signal intensity are sensitive measurements for evaluating differences of lung tissue structure and emphysematous destruction between different subject groups. This hypothesis is tested in chapters 2-4 in healthy subjects and subjects with COPD. Chapter 5 of this thesis provides a summary of all chapters and presents the discussion and conclusion of these studies as well as addressing the limitations and directions for future work in the evaluation of pulmonary emphysema with MRI and CT.

1.8 References

Reference List

1. Global strategy for the diagnosis, management, and prevention of chronic obstructive pulmonary disease. NHLBI/WHO, 2701. 1-1-2003.
   Ref Type: Report

2. Murray CJ, Lopez AD. Alternative projections of mortality and disability by cause 1990-2020: Global Burden of Disease Study. *Lancet* 1997; **349**: 1498-504.

3. Chapman KR, Bourbeau J, Rance L. The burden of COPD in Canada: results from the Confronting COPD survey. *Respir. Med.* 2003; **97 Suppl C**: S23-S31.

4. Chapman KR, Mannino DM, Soriano JB *et al*. Epidemiology and costs of chronic obstructive pulmonary disease. *Eur. Respir. J.* 2006; **27**: 188-207.

5. Buist AS, McBurnie MA, Vollmer WM *et al*. International variation in the prevalence of COPD (the BOLD Study): a population-based prevalence study. *Lancet* 2007; **370**: 741-50.

6. Menezes AM, Perez-Padilla R, Jardim JR *et al*. Chronic obstructive pulmonary disease in five Latin American cities (the PLATINO study): a prevalence study. *Lancet* 2005; **366**: 1875-81.

7. Global strategy for the diagnosis, management, and prevention of chronic obstructive pulmonary disease (Revised 2011). 2011. Global Initiative for Chronic Obstructive Lung Disease.
   Ref Type: Report

8. Soriano JB, Zielinski J, Price D. Screening for and early detection of chronic obstructive pulmonary disease. *Lancet* 2009; **374**: 721-32.

9. Ulrik CS, Lokke A, Dahl R *et al*. Early detection of COPD in general practice. *Int. J. Chron. Obstruct. Pulmon. Dis.* 2011; **6**: 123-7.

10. Rabe KF, Hurd S, Anzueto A *et al*. Global strategy for the diagnosis, management, and prevention of chronic obstructive pulmonary disease: GOLD executive summary. *Am. J. Respir. Crit Care Med.* 2007; **176**: 532-55.

11. Vestbo J, Anderson W, Coxson HO *et al*. Evaluation of COPD Longitudinally to Identify Predictive Surrogate End-points (ECLIPSE). *Eur. Respir. J.* 2008; **31**: 869-73.

12. Franciosi LG, Page CP, Celli BR *et al*. Markers of disease severity in chronic obstructive pulmonary disease. *Pulm. Pharmacol. Ther.* 2006; **19**: 189-99.

13. Hasegawa M, Nasuhara Y, Onodera Y *et al*. Airflow limitation and airway dimensions in chronic obstructive pulmonary disease. *Am. J. Respir. Crit Care Med.* 2006; **173**: 1309-15.

14. King GG, Muller NL, Pare PD. Evaluation of airways in obstructive pulmonary disease using high-resolution computed tomography. *Am. J. Respir. Crit Care Med.* 1999; **159**: 992-1004.

15. Ohara T, Hirai T, Sato S *et al*. Longitudinal study of airway dimensions in chronic obstructive pulmonary disease using computed tomography. *Respirology.* 2008; **13**: 372-8.

16. Akira M, Toyokawa K, Inoue Y *et al*. Quantitative CT in chronic obstructive pulmonary disease: inspiratory and expiratory assessment. *AJR Am. J. Roentgenol.* 2009; **192**: 267-72.

17. Coxson HO, Rogers RM. Quantitative computed tomography of chronic obstructive pulmonary disease. *Acad. Radiol.* 2005; **12**: 1457-63.

18. Fujimoto K, Kitaguchi Y, Kubo K *et al*. Clinical analysis of chronic obstructive pulmonary disease phenotypes classified using high-resolution computed tomography. *Respirology.* 2006; **11**: 731-40.

19. Gevenois PA, De M, V, De VP *et al*. Comparison of computed density and macroscopic morphometry in pulmonary emphysema. *Am. J. Respir. Crit Care Med.* 1995; **152**: 653-7.

20. Hansell DM. High-resolution computed tomography in the evaluation of fibrosing alveolitis. *Clin. Chest Med.* 1999; **20**: 739-60, viii.

21. Hayhurst MD, MacNee W, Flenley DC *et al*. Diagnosis of pulmonary emphysema by computerised tomography. *Lancet* 1984; **2**: 320-2.

22. Hoffman EA, Reinhardt JM, Sonka M *et al*. Characterization of the interstitial lung diseases via density-based and texture-based analysis of computed tomography images of lung structure and function. *Acad. Radiol.* 2003; **10**: 1104-18.

23. Kazerooni EA. Radiologic evaluation of emphysema for lung volume reduction surgery. *Clin. Chest Med.* 1999; **20**: 845-61.

24. Muller NL, Staples CA, Miller RR *et al*. "Density mask". An objective method to quantitate emphysema using computed tomography. *Chest* 1988; **94**: 782-7.

25. Failo R, Wielopolski PA, Tiddens HA *et al*. Lung morphology assessment using MRI: a robust ultra-short TR/TE 2D steady state free precession sequence used in cystic fibrosis patients. *Magn Reson. Med.* 2009; **61**: 299-306.

26. Ley-Zaporozhan J, Ley S, Eberhardt R *et al*. Visualization of morphological parenchymal changes in emphysema: comparison of different MRI sequences to 3D-HRCT. *Eur. J. Radiol.* 2010; **73**: 43-9.

27. Bankier AA, O'Donnell CR, Mai VM *et al*. Impact of lung volume on MR signal intensity changes of the lung parenchyma. *J. Magn Reson. Imaging* 2004; **20**: 961-6.

28. Bankier AA, Storey P, Mai VM *et al*. Gravity-dependent signal gradients on MR images of the lung in supine and prone positions: a comparison with isogravitational signal variability. *J. Magn Reson. Imaging* 2006; **23**: 115-22.

29. Iwasawa T, Takahashi H, Ogura T *et al*. Correlation of lung parenchymal MR signal intensity with pulmonary function tests and quantitative computed tomography (CT) evaluation: a pilot study. *J. Magn Reson. Imaging* 2007; **26**: 1530-6.

30. Tortora G. *Principles of Human Anatomy*.Hoboken, NJ : John Wiley & Sons, 2012.

31. Silverthorn DU. *Human Physiology: An Integrated Approach*.Benjamin Cummings, 2010.

32. Khurana I. *Textbook Of Medical Physiology*.Elsevier, 2006.

33. West JB. *Respiratory Physiology: The Essentials*.Lippincott Williams & Wilkins, 2008.

34. Ochs M, Nyengaard JR, Jung A *et al*. The number of alveoli in the human lung. *Am. J. Respir. Crit Care Med.* 2004; **169**: 120-4.

35. Notter RH. *Lung surfactants: basic science and clinical applications*.Marcel Dekker., New York, N.Y, 2008.

36. Respiratory System Diagram. http://www.hyperbaric-oxygen-info.com/respiratory-system-diagram.html . 2011.
Ref Type: Electronic Citation

37. Purves WK, Orians GH, Heller HCR, and Heller HC. Life: The Science of Biology. (4th). 1994. Sinauer Associates Inc.
Ref Type: Conference Proceeding

38. Standards for the Diagnosis and Management of Patients with COPD. 2004. American Thoracic Society and European Respiratory Society.
Ref Type: Report

39. Bethesda M. *Chronic obstructive pulmonary disease. Morbidity and mortality*.National Heart Lung and Blood Institute, Department of Health and Human Services, 2002.

40. World Health Organization. Global surveillance, prevention and control of chronic respiratory diseases: a comprehensive approach. 2007. Geneva, Switzerland, World Health Organization.
Ref Type: Report

41. Facts about COPD. 2009. Canadian Thoracic Society.
Ref Type: Report

42. The Human and Economic Burden of COPD: A Leading Cause of Hospital Admission in Canada. 2010. Canadian Thoracic Society.
Ref Type: Report

43. Celli BR, Snider GL, Heffner J *et al*. Standards for the diagnosis and care of patients with chronic obstructive pulmonary disease. *Am J Respir Crit Care Med* 1995; **152**: S77-S121.

44. Snider GL, Kleinerman J, Thurlbeck WM *et al*. The definition of emphysema. Report of a National Heart, Lung and Blood Institute, Division of Lung Diseases Workshop. *Am. Rev. Respir. Dis.* 1985; **132**: 182-5.

45. Wright JL, Lawson L, Pare PD *et al*. The structure and function of the pulmonary vasculature in mild chronic obstructive pulmonary disease. The effect of oxygen and exercise. *Am. Rev. Respir. Dis.* 1983; **128**: 702-7.

46. Barnes PJ, Drazen JM, Rennard SI, and Thomson NC. Asthma and COPD: Basic Mechanisms and Clinical Management. 2002. Academic Press.
Ref Type: Report

47. Pauwels RA, Buist AS, Calverley PM *et al*. Global strategy for the diagnosis, management, and prevention of chronic obstructive pulmonary disease. NHLBI/WHO Global Initiative for Chronic Obstructive Lung Disease (GOLD) Workshop summary. *Am. J. Respir. Crit Care Med.* 2001; **163**: 1256-76.

48. Cosio M, Ghezzo H, Hogg JC *et al*. The relations between structural changes in small airways and pulmonary-function tests. *N. Engl. J. Med.* 1978; **298**: 1277-81.

49. Hogg JC, Chu F, Utokaparch S *et al*. The nature of small-airway obstruction in chronic obstructive pulmonary disease. *N. Engl. J Med* 2004; **350**: 2645-53.

50. Janoff A. Biochemical links between cigarette smoking and pulmonary emphysema. *J. Appl. Physiol* 1983; **55**: 285-93.

51. Hogg JC, McDonough JE, Sanchez PG *et al*. Micro-computed tomography measurements of peripheral lung pathology in chronic obstructive pulmonary disease. *Proc. Am. Thorac. Soc.* 2009; **6**: 546-9.

52. Lamb D, McLean A, Gillooly M *et al*. Relation between distal airspace size, bronchiolar attachments, and lung function. *Thorax* 1993; **48**: 1012-7.

53. Turato G, Zuin R, Saetta M. Pathogenesis and pathology of COPD. *Respiration* 2001; **68**: 117-28.

54. Hogg JC, McDonough JE, Gosselink JV *et al*. What drives the peripheral lung-remodeling process in chronic obstructive pulmonary disease? *Proc. Am. Thorac. Soc.* 2009; **6**: 668-72.

55. Barnes PJ, Chowdhury B, Kharitonov SA *et al*. Pulmonary biomarkers in chronic obstructive pulmonary disease. *Am. J. Respir. Crit Care Med.* 2006; **174**: 6-14.

56. Gough J. THE PATHOLOGY OF EMPHYSEMA. *Postgrad. Med. J.* 1965; **41**: 392-400.

57. Woods JC, Choong CK, Yablonskiy DA *et al*. Hyperpolarized 3He diffusion MRI and histology in pulmonary emphysema. *Magn Reson. Med.* 2006; **56**: 1293-300.

58. Stoller JK. Clinical features and natural history of severe alpha 1-antitrypsin deficiency. Roger S. Mitchell Lecture. *Chest* 1997; **111**: 123S-8S.

59. Lee P, Gildea TR, Stoller JK. Emphysema in nonsmokers: alpha 1-antitrypsin deficiency and other causes. *Cleve. Clin. J. Med.* 2002; **69**: 928-9, 933, 936.

60. LEOPOLD JG, Gough J. The centrilobular form of hypertrophic emphysema and its relation to chronic bronchitis. *Thorax* 1957; **12**: 219-35.

61. Anderson AE, Jr., Foraker AG. Centrilobular emphysema and panlobular emphysema: two different diseases. *Thorax* 1973; **28**: 547-50.

62. Hansel TT, Barnes PJ. *Recent Advances in the Pathophysiology of Copd*.Birkhäuser Basel, 2004.

63. Cosio MG, Majo J, Cosio MG. Inflammation of the airways and lung parenchyma in COPD: role of T cells. *Chest* 2002; **121**: 160S-5S.

64. Cosio MG, Saetta M, Agusti A. Immunologic aspects of chronic obstructive pulmonary disease. *N. Engl. J Med* 2009; **360**: 2445-54.

65. American Thoracic Society. Single-breath carbon monoxide diffusing capacity (transfer factor). Recommendations for a standard technique--1995 update. *Am. J. Respir. Crit Care Med.* 1995; **152**: 2185-98.

66. Macintyre N, Crapo RO, Viegi G *et al*. Standardisation of the single-breath determination of carbon monoxide uptake in the lung. *Eur. Respir. J.* 2005; **26**: 720-35.

67. Dyspnea. Mechanisms, assessment, and management: a consensus statement. American Thoracic Society. *Am. J Respir. Crit Care Med.* 1999; **159**: 321-40.

68. Mahler DA. Mechanisms and measurement of dyspnea in chronic obstructive pulmonary disease. *Proc. Am. Thorac. Soc.* 2006; **3**: 234-8.

69. Borg GA. Psychophysical bases of perceived exertion. *Med. Sci. Sports Exerc.* 1982; **14**: 377-81.

70. Doherty DE, Belfer MH, Brunton SA *et al*. Chronic Obstructive Pulmonary Disease: Consensus Recommendations for Early Diagnosis and Treatment. *Supplement to J Fam Pract* 2006.

71. Cotes JE, Chinn DJ, Miller MR. Respiratory Surveys. *Lung Function: physiology, measurement and application in medicine*. Wiley-Blackwell, 2006; 82-96.

72. ATS statement: guidelines for the six-minute walk test. *Am. J. Respir. Crit Care Med.* 2002; **166**: 111-7.

73. Wilken LA, Joo MJ. Pulmonary Function and Related Tests. In:Lee M (ed.) *Basic Skills in Interpreting Laboratory Data*. American Society of Health-System Pharmacists, Inc., 2009; 191-206.

74. Kessler R, Faller M, Fourgaut G *et al*. Predictive factors of hospitalization for acute exacerbation in a series of 64 patients with chronic obstructive pulmonary disease. *Am. J. Respir. Crit Care Med.* 1999; **159**: 158-64.

75. Celli BR, Cote CG, Marin JM *et al*. The body-mass index, airflow obstruction, dyspnea, and exercise capacity index in chronic obstructive pulmonary disease. *N. Engl. J Med.* 2004; **350**: 1005-12.

76. Silkoff PE, Martin D, Pak J *et al*. Exhaled nitric oxide correlated with induced sputum findings in COPD. *Chest* 2001; **119**: 1049-55.

77. Dweik RA, Boggs PB, Erzurum SC *et al*. An official ATS clinical practice guideline: interpretation of exhaled nitric oxide levels (FENO) for clinical applications. *Am. J. Respir. Crit Care Med.* 2011; **184**: 602-15.

78. ATS/ERS recommendations for standardized procedures for the online and offline measurement of exhaled lower respiratory nitric oxide and nasal nitric oxide, 2005. *Am. J. Respir. Crit Care Med.* 2005; **171**: 912-30.

79. de LG, Maniscalco M, Cianciulli F *et al*. Exhaled nitric oxide monitoring in COPD using a portable analyzer. *Pulm. Pharmacol. Ther.* 2008; **21**: 689-93.

80. Linden M, Rasmussen JB, Piitulainen E *et al*. Inflammatory indices for chronic bronchitis and chronic obstructive airway disease. Cell populations in bronchial and bronchoalveolar lavage. *Agents Actions Suppl* 1990; **30**: 183-97.

81. Joarder R, Crundwell N. The Normal Chest X-ray: An approach to interpretation. *Chest X-Ray in Clinical Practice*. Springer, 2009; 15-30.

82. Parraga G, Ouriadov A, Evans A *et al*. Hyperpolarized 3He ventilation defects and apparent diffusion coefficients in chronic obstructive pulmonary disease: preliminary results at 3.0 Tesla. *Invest Radiol.* 2007; **42**: 384-91.

83. Joarder R, CrundwellN. Computed Tomography: Technical information. *Chest X-Ray in Clinical Practice*. Springer, 2009; 167-184.

84. Bonner WM. Low-dose radiation: thresholds, bystander effects, and adaptive responses. *Proc. Natl. Acad. Sci. U. S. A* 2003; **100**: 4973-5.

85. Reich SB, Weinshelbaum A, Yee J. Correlation of radiographic measurements and pulmonary function tests in chronic obstructive pulmonary disease. *AJR Am. J. Roentgenol.* 1985; **144**: 695-9.

86. Kalra S, Levin DL. Chronic Obstructive Pulmonary Disease. In:Desai SR, Franquet T, Hartman TE (eds.) *Pulmonary Imaging: Contributions to Key Clinical Questions*. Informa Healthcare, 2007; 135-144.

87. Friedman PJ. Radiology of the airways with emphasis on the small airways. *J. Thorac. Imaging* 1986; **1**: 7-22.

88. Pratt PC. Role of conventional chest radiography in diagnosis and exclusion of emphysema. *Am. J. Med.* 1987; **82**: 998-1006.

89. Computed Tomography. In:Bushberg JT, Seibert JA, Leidholdt EM (eds.) *The Essential Physics of Medical Imaging*. Lippincott Williams & Wilkins, 2002; 327-372.

90. Buzug TM. Practical Aspects of Computed Tomography. *Computed Tomography: From Photon Statistics to Modern Cone-Beam CT*. Springer, 2008; 471-484.

91. Hartman TE. Basic Principles of Thoracic Imaging. In:Desai SR, Franquet T, Hartman TE, Wells AU (eds.) *Pulmonary Imaging: Contributions to Key Clinical Questions*. Informa Healthcare, 2007; 9-14.

92. Castillo R, Castillo E, Martinez J *et al*. Ventilation from four-dimensional computed tomography: density versus Jacobian methods. *Phys. Med. Biol.* 2010; **55**: 4661-85.

93. Guerrero T, Sanders K, Noyola-Martinez J *et al*. Quantification of regional ventilation from treatment planning CT. *Int. J. Radiat. Oncol. Biol. Phys.* 2005; **62**: 630-4.

94. Guerrero T, Sanders K, Castillo E *et al*. Dynamic ventilation imaging from four-dimensional computed tomography. *Phys. Med. Biol.* 2006; **51**: 777-91.

95. Castillo R, Castillo E, McCurdy M *et al*. Spatial correspondence of 4D CT ventilation and SPECT pulmonary perfusion defects in patients with malignant airway stenosis. *Phys. Med. Biol.* 2012; **57**: 1855-71.

96. Sharp PF, Goatman KA. Nuclear Medicine Imaging. In:Sharp PF, Gemmell HG, Murray AD (eds.) *Practical Nuclear Medicine*. Springer, 2005; 1-19.

97. Bushberg JT, Seibert JA, Leidholdt Jr.EM, Boone JM. Nuclear Imaging - The Scintillation Camera. *The Essential Physics of Medical Imaging*. Lippincott Williams & Wilkins, 2012; 669-702.

98. Gemmell HG, Staff RT. Single Photon Emission Computed Tomography (SPECT). In:Sharp PF, Gemmell HG, Murray AD (eds.) *Practical Nuclear Medicine*. Springer, 2005; 21-33.

99. Bajc M, Jonson B, Steinert HC. Lung. In:Biersack H-J, Freeman LM (eds.) *Clinical Nuclear Medicine*. Springer, 2007; 118-146.

100. Strong JC, Agnew JE. The particle size distribution of technegas and its influence on regional lung deposition. *Nucl. Med. Commun.* 1989; **10**: 425-30.

101. Gray HW. The Lung. In:Sharp PF, Gemmell HG, Murray AD (eds.) *Practical Nuclear Medicine*. Springer, 2005; 179-204.

102. Maus S, Buchholz HG, Ament S *et al*. Labelling of commercially available human serum albumin kits with 68Ga as surrogates for 99mTc-MAA microspheres. *Appl. Radiat. Isot.* 2011; **69**: 171-5.

103. Rhodes CG, Hughes JM. Pulmonary studies using positron emission tomography. *Eur. Respir. J.* 1995; **8**: 1001-17.

104. Sharp PF, Welch A. Positron Emission Tomography. In:Sharp PF, Gemmell HG, Murray AD (eds.) *Practical Nuclear Medicine*. Springer, 2005; 35-48.

105. Harris RS, Schuster DP. Visualizing lung function with positron emission tomography. *J. Appl. Physiol* 2007; **102**: 448-58.

106. Chapman CN, Sziklas JJ, Spencer RP *et al*. Pulmonary perfusion "without ventilation". *J. Nucl. Med.* 1983; **24**: 1149-50.

107. Garg A, Gopinath PG, Pande JN *et al*. Role of radio-aerosol and perfusion lung imaging in early detection of chronic obstructive lung disease. *Eur. J. Nucl. Med.* 1983; **8**: 167-71.

108. Brudin LH, Rhodes CG, Valind SO *et al*. Regional structure-function correlations in chronic obstructive lung disease measured with positron emission tomography. *Thorax* 1992; **47**: 914-21.

109. Kauczor HU, Kreitner KF. MRI of the pulmonary parenchyma. *Eur. Radiol.* 1999; **9**: 1755-64.

110. Su S, Saunders JK, Smith IC. Resolving anatomical details in lung parenchyma: theory and experiment for a structurally and magnetically inhomogeneous lung imaging model. *Magn Reson. Med.* 1995; **33**: 760-5.

111. Ley-Zaporozhan J, Ley S, Kauczor HU. Morphological and functional imaging in COPD with CT and MRI: present and future. *Eur. Radiol.* 2008; **18**: 510-21.

112. Mayo JR, MacKay A, Muller NL. MR imaging of the lungs: value of short TE spin-echo pulse sequences. *AJR Am. J. Roentgenol.* 1992; **159**: 951-6.

113. Takahashi M, Togao O, Obara M *et al*. Ultra-short echo time (UTE) MR imaging of the lung: comparison between normal and emphysematous lungs in mutant mice. *J. Magn Reson. Imaging* 2010; **32**: 326-33.

114. Togao O, Tsuji R, Ohno Y *et al*. Ultrashort echo time (UTE) MRI of the lung: assessment of tissue density in the lung parenchyma. *Magn Reson. Med.* 2010; **64**: 1491-8.

115. Helmes JE, Bydder GM. MR imaging with ultrashort TE (UTE) pulse sequences: basic principles. *Radiography* 2005; **11**: 163-74.

116. Reichert IL, Benjamin M, Gatehouse PD *et al*. Magnetic resonance imaging of periosteum with ultrashort TE pulse sequences. *J. Magn Reson. Imaging* 2004; **19**: 99-107.

117. Ley-Zaporozhan J, Ley S, Kauczor HU. Proton MRI in COPD. *COPD.* 2007; **4**: 55-65.

118. Biederer J, Reuter M, Both M *et al*. Analysis of artefacts and detail resolution of lung MRI with breath-hold T1-weighted gradient-echo and T2-weighted fast spin-echo sequences with respiratory triggering. *Eur. Radiol.* 2002; **12**: 378-84.

119. Wielputz M, Kauczor HU. MRI of the lung: state of the art. *Diagn. Interv. Radiol.* 2012.

120. Biederer J, Mirsadraee S, Beer M *et al*. MRI of the lung (3/3)-current applications and future perspectives. *Insights. Imaging* 2012.

121. Montella S, Santamaria F, Salvatore M *et al*. Assessment of chest high-field magnetic resonance imaging in children and young adults with noncystic fibrosis chronic lung disease: comparison to high-resolution computed tomography and correlation with pulmonary function. *Invest Radiol.* 2009; **44**: 532-8.

122. Montella S, Maglione M, Bruzzese D *et al*. Magnetic resonance imaging is an accurate and reliable method to evaluate non-cystic fibrosis paediatric lung disease. *Respirology*. 2011.

123. Owrangi AM, Parraga G. Chest MRI in children: Why bother? *Respirology*. 2012; **17**: 3-4.

124. Biederer J. General Requirements of MRI of the Lung and Suggested Standard Protocol. In:Kauczor HU (ed.) *MRI of the Lung*. 2009; 3-16.

125. Bauman G, Puderbach M, Deimling M *et al*. Non-contrast-enhanced perfusion and ventilation assessment of the human lung by means of fourier decomposition in proton MRI. *Magn Reson. Med.* 2009; **62**: 656-64.

126. Bauman G, Lutzen U, Ullrich M *et al*. Pulmonary functional imaging: qualitative comparison of Fourier decomposition MR imaging with SPECT/CT in porcine lung. *Radiology* 2011; **260**: 551-9.

127. Ohno Y, Sugimura K, Hatabu H. Clinical oxygen-enhanced magnetic resonance imaging of the lung. *Top. Magn Reson. Imaging* 2003; **14**: 237-43.

128. Woodhouse N, Wild JM, Paley MN *et al*. Combined helium-3/proton magnetic resonance imaging measurement of ventilated lung volumes in smokers compared to never-smokers. *J. Magn Reson. Imaging* 2005; **21**: 365-9.

129. Edelman RR, Hatabu H, Tadamura E *et al*. Noninvasive assessment of regional ventilation in the human lung using oxygen-enhanced magnetic resonance imaging. *Nat. Med.* 1996; **2**: 1236-9.

130. Chen Q, Jakob PM, Griswold MA *et al*. Oxygen enhanced MR ventilation imaging of the lung. *MAGMA.* 1998; **7**: 153-61.

131. Ohno Y, Hatabu H. Basics concepts and clinical applications of oxygen-enhanced MR imaging. *Eur. J. Radiol.* 2007; **64**: 320-8.

132. Ohno Y, Koyama H, Nogami M *et al*. Dynamic oxygen-enhanced MRI versus quantitative CT: pulmonary functional loss assessment and clinical stage classification of smoking-related COPD. *AJR Am. J. Roentgenol.* 2008; **190**: W93-W99.

133. Ohno Y, Iwasawa T, Seo JB *et al*. Oxygen-enhanced magnetic resonance imaging versus computed tomography: multicenter study for clinical stage classification of smoking-related chronic obstructive pulmonary disease. *Am. J. Respir. Crit Care Med.* 2008; **177**: 1095-102.

134. Fain SB, Korosec FR, Holmes JH *et al*. Functional lung imaging using hyperpolarized gas MRI. *J. Magn Reson. Imaging* 2007; **25**: 910-23.

135. Moller HE, Chen XJ, Saam B *et al*. MRI of the lungs using hyperpolarized noble gases. *Magn Reson. Med.* 2002; **47**: 1029-51.

136. Albert MS, Cates GD, Driehuys B *et al*. Biological magnetic resonance imaging using laser-polarized 129Xe. *Nature* 1994; **370**: 199-201.

137. Bouchiat MA, Carver TR, Varnum CM. Nuclear Polarization in He3 Gas Induced by Optical Pumping and Dipolar Exchange. *Phys. Rev. Lett.* 1960; **5**: 373-5.

138. de Lange EE, Mugler JP, III, Brookeman JR *et al*. Lung air spaces: MR imaging evaluation with hyperpolarized 3He gas. *Radiology* 1999; **210**: 851-7.

139. Driehuys B, Martinez-Jimenez S, Cleveland ZI *et al*. Chronic obstructive pulmonary disease: safety and tolerability of hyperpolarized 129Xe MR imaging in healthy volunteers and patients. *Radiology* 2012; **262**: 279-89.

140. Lutey BA, Lefrak SS, Woods JC *et al*. Hyperpolarized 3He MR imaging: physiologic monitoring observations and safety considerations in 100 consecutive subjects. *Radiology* 2008; **248**: 655-61.

141. Shukla Y, Wheatley A, Kirby M *et al*. Hyperpolarized (129)Xe Magnetic Resonance Imaging: Tolerability in Healthy Volunteers and Subjects with Pulmonary Disease. *Acad. Radiol.* 2012.

142. Kauczor HU, Hofmann D, Kreitner KF *et al*. Normal and abnormal pulmonary ventilation: visualization at hyperpolarized He-3 MR imaging. *Radiology* 1996; **201**: 564-8.

143. Mathew L, Gaede S, Wheatley A *et al*. Detection of longitudinal lung structural and functional changes after diagnosis of radiation-induced lung injury using hyperpolarized 3He magnetic resonance imaging. *Med. Phys.* 2010; **37**: 22-31.

144. Ward ER, Hedlund LW, Kurylo WC *et al*. Proton and hyperpolarized helium magnetic resonance imaging of radiation-induced lung injury in rats. *Int. J. Radiat. Oncol. Biol. Phys.* 2004; **58**: 1562-9.

145. Bink A, Hanisch G, Karg A *et al*. Clinical aspects of the apparent diffusion coefficient in 3He MRI: results in healthy volunteers and patients after lung transplantation. *J. Magn Reson. Imaging* 2007; **25**: 1152-8.

146. Gast KK, Zaporozhan J, Ley S *et al*. (3)He-MRI in follow-up of lung transplant recipients. *Eur. Radiol.* 2004; **14**: 78-85.

147. Zaporozhan J, Ley S, Gast KK *et al*. Functional analysis in single-lung transplant recipients: a comparative study of high-resolution CT, 3He-MRI, and pulmonary function tests. *Chest* 2004; **125**: 173-81.

148. Kirby M, Svenningsen S, Ahmed H *et al*. Quantitative evaluation of hyperpolarized helium-3 magnetic resonance imaging of lung function variability in cystic fibrosis. *Acad. Radiol.* 2011; **18**: 1006-13.

149. Woodhouse N, Wild JM, van Beek EJ *et al*. Assessment of hyperpolarized 3He lung MRI for regional evaluation of interventional therapy: a pilot study in pediatric cystic fibrosis. *J. Magn Reson. Imaging* 2009; **30**: 981-8.

150. de Lange EE, Altes TA, Patrie JT *et al*. Evaluation of asthma with hyperpolarized helium-3 MRI: correlation with clinical severity and spirometry. *Chest* 2006; **130**: 1055-62.

151. Fain SB, Gonzalez-Fernandez G, Peterson ET *et al*. Evaluation of structure-function relationships in asthma using multidetector CT and hyperpolarized He-3 MRI. *Acad. Radiol.* 2008; **15**: 753-62.

152. Tzeng YS, Lutchen K, Albert M. The difference in ventilation heterogeneity between asthmatic and healthy subjects quantified using hyperpolarized 3He MRI. *J. Appl. Physiol* 2009; **106**: 813-22.

153. Kirby M, Mathew L, Wheatley A *et al*. Chronic obstructive pulmonary disease: longitudinal hyperpolarized (3)He MR imaging. *Radiology* 2010; **256**: 280-9.

154. Kirby M, Mathew L, Heydarian M *et al*. Chronic obstructive pulmonary disease: quantification of bronchodilator effects by using hyperpolarized (3)He MR imaging. *Radiology* 2011; **261**: 283-92.

155. Mathew L, Kirby M, Etemad-Rezai R *et al*. Hyperpolarized (3)He magnetic resonance imaging: Preliminary evaluation of phenotyping potential in chronic obstructive pulmonary disease. *Eur. J. Radiol.* 2009.

156. van Beek EJ, Dahmen AM, Stavngaard T *et al*. Hyperpolarised 3He MRI versus HRCT in COPD and normal volunteers: PHIL trial. *Eur. Respir. J.* 2009; **34**: 1311-21.

157. Gietema HA, Muller NL, Fauerbach PV *et al*. Quantifying the extent of emphysema: factors associated with radiologists' estimations and quantitative indices of emphysema severity using the ECLIPSE cohort. *Acad. Radiol.* 2011; **18**: 661-71.

158. Koyama H, Ohno Y, Yamazaki Y *et al*. Quantitative and qualitative assessments of lung destruction and pulmonary functional loss from reduced-dose thin-section CT in pulmonary emphysema patients. *Acad. Radiol.* 2010; **17**: 163-8.

159. Cavigli E, Camiciottoli G, Diciotti S *et al*. Whole-lung densitometry versus visual assessment of emphysema. *Eur. Radiol.* 2009; **19**: 1686-92.

160. Hochhegger B, Marchiori E, Irion K *et al*. Visual vs automated assessment of emphysema. *Chest* 2011; **140**: 1384.

161. Mascalchi M, Diciotti S, Sverzellati N *et al*. Low agreement of visual rating for detailed quantification of pulmonary emphysema in whole-lung CT. *Acta Radiol.* 2012; **53**: 53-60.

162. Barr RG, Berkowitz EA, Bigazzi F *et al*. A combined pulmonary-radiology workshop for visual evaluation of COPD: study design, chest CT findings and concordance with quantitative evaluation. *COPD.* 2012; **9**: 151-9.

163. Madani A, Zanen J, De M, V *et al*. Pulmonary emphysema: objective quantification at multi-detector row CT--comparison with macroscopic and microscopic morphometry. *Radiology* 2006; **238**: 1036-43.

164. Bankier AA, De M, V, Keyzer C *et al*. Pulmonary emphysema: subjective visual grading versus objective quantification with macroscopic morphometry and thin-section CT densitometry. *Radiology* 1999; **211**: 851-8.

165. Park KJ, Bergin CJ, Clausen JL. Quantitation of emphysema with three-dimensional CT densitometry: comparison with two-dimensional analysis, visual emphysema scores, and pulmonary function test results. *Radiology* 1999; **211**: 541-7.

166. Gevenois PA, De VP, De M, V *et al*. Comparison of computed density and microscopic morphometry in pulmonary emphysema. *Am. J. Respir. Crit Care Med.* 1996; **154**: 187-92.

167. Martinez CH, Chen YH, Westgate PM *et al*. Relationship between quantitative CT metrics and health status and BODE in chronic obstructive pulmonary disease. *Thorax* 2012; **67**: 399-406.

168. Rambod M, Porszasz J, Make BJ *et al*. Six-minute walk distance predictors, including CT scan measures, in the COPDGene cohort. *Chest* 2012; **141**: 867-75.

169. Coxson HO, Whittall KP, Nakano Y *et al*. Selection of patients for lung volume reduction surgery using a power law analysis of the computed tomographic scan. *Thorax* 2003; **58**: 510-4.

170. Mishima M, Hirai T, Itoh H *et al*. Complexity of terminal airspace geometry assessed by lung computed tomography in normal subjects and patients with

chronic obstructive pulmonary disease. *Proc. Natl. Acad. Sci. U. S. A* 1999; **96**: 8829-34.

171. Madani A, Van MA, De M, V *et al*. Pulmonary emphysema: size distribution of emphysematous spaces on multidetector CT images--comparison with macroscopic and microscopic morphometry. *Radiology* 2008; **248**: 1036-41.

172. Yuan R, Nagao T, Pare PD *et al*. Quantification of lung surface area using computed tomography. *Respir. Res.* 2010; **11**: 153.

173. Olsson LE, Lindahl M, Onnervik PO *et al*. Measurement of MR signal and T2* in lung to characterize a tight skin mouse model of emphysema using single-point imaging. *J. Magn Reson. Imaging* 2007; **25**: 488-94.

174. Togao O, Tsuji R, Ohno Y *et al*. Ultrashort echo time (UTE) MRI of the lung: Assessment of tissue density in the lung parenchyma. *Magn Reson. Med.* 2010.

175. Kauczor HU. Hyperpolarized helium-3 gas magnetic resonance imaging of the lung. *Top. Magn Reson. Imaging* 2003; **14**: 223-30.

176. Tanoli TS, Woods JC, Conradi MS *et al*. In vivo lung morphometry with hyperpolarized 3He diffusion MRI in canines with induced emphysema: disease progression and comparison with computed tomography. *J. Appl. Physiol* 2007; **102**: 477-84.

177. Diaz S, Casselbrant I, Piitulainen E *et al*. Hyperpolarized 3He apparent diffusion coefficient MRI of the lung: reproducibility and volume dependency in healthy volunteers and patients with emphysema. *J. Magn Reson. Imaging* 2008; **27**: 763-70.

178. Morbach AE, Gast KK, Schmiedeskamp J *et al*. Diffusion-weighted MRI of the lung with hyperpolarized helium-3: a study of reproducibility. *J. Magn Reson. Imaging* 2005; **21**: 765-74.

179. Saam BT, Yablonskiy DA, Kodibagkar VD *et al*. MR imaging of diffusion of (3)He gas in healthy and diseased lungs. *Magn Reson. Med.* 2000; **44**: 174-9.

180. Salerno M, de Lange EE, Altes TA *et al*. Emphysema: hyperpolarized helium 3 diffusion MR imaging of the lungs compared with spirometric indexes--initial experience. *Radiology* 2002; **222**: 252-60.

181. Stavngaard T, Sogaard LV, Mortensen J *et al*. Hyperpolarized 3He MRI and 81mKr SPECT in chronic obstructive pulmonary disease. *Eur. J. Nucl. Med. Mol. Imaging* 2005; **32**: 448-57.

182. Mathew L, Evans A, Ouriadov A *et al*. Hyperpolarized 3He magnetic resonance imaging of chronic obstructive pulmonary disease: reproducibility at 3.0 tesla. *Acad. Radiol.* 2008; **15**: 1298-311.

183. Chen XJ, Hedlund LW, Moller HE *et al*. Detection of emphysema in rat lungs by using magnetic resonance measurements of 3He diffusion. *Proc. Natl. Acad. Sci. U. S. A* 2000; **97**: 11478-81.

184. Evans A, McCormack D, Ouriadov A *et al*. Anatomical distribution of 3He apparent diffusion coefficients in severe chronic obstructive pulmonary disease. *J. Magn Reson. Imaging* 2007; **26**: 1537-47.

185. Fichele S, Woodhouse N, Swift AJ *et al*. MRI of helium-3 gas in healthy lungs: posture related variations of alveolar size. *J. Magn Reson. Imaging* 2004; **20**: 331-5.

186. Ley S, Zaporozhan J, Morbach A *et al*. Functional evaluation of emphysema using diffusion-weighted 3Helium-magnetic resonance imaging, high-resolution computed tomography, and lung function tests. *Invest Radiol.* 2004; **39**: 427-34.

187. Coxson HO, Mayo J, Lam S *et al*. New and current clinical imaging techniques to study chronic obstructive pulmonary disease. *Am. J. Respir. Crit Care Med.* 2009; **180**: 588-97.

188. Choong CK, Macklem PT, Pierce JA *et al*. Transpleural ventilation of explanted human lungs. *Thorax* 2007; **62**: 623-30.

CHAPTER 2: Quantitative ^{1}H and Hyperpolarized ^{3}He Magnetic Resonance Imaging: Comparison in Chronic Obstructive Pulmonary Disease and Healthy Never-smokers

The work presented in this chapter has been previously published in *European Journal of Radiology* as indicated below, and is reproduced here with permission.

Amir M. Owrangi, Jian X. Wang, Andrew Wheatley, David G. McCormack, Grace Parraga.

"Quantitative ^{1}H and Hyperpolarized ^{3}He Magnetic Resonance Imaging: Comparison in Chronic Obstructive Pulmonary Disease and Healthy Never-smokers" Eur J Radiol. 2012 May 7. [Epub ahead of print]

2.1 Introduction

Chronic obstructive pulmonary disease (COPD) is a leading cause of morbidity and mortality affecting at least 600 million people worldwide.[1] It is the world's fourth leading cause of death and unlike other major chronic diseases, COPD continues to increase in prevalence and in worldwide mortality statistics.[2,3] While pulmonary function tests provide established measurements of global lung function that are widely accepted for the diagnosis and monitoring of COPD,[4,5] high-resolution x-ray computer tomography (CT) imaging is often used to provide regional anatomical information. CT is used to evaluate COPD abnormalities of the airways,[6-8] regional evaluation of gas trapping[9,10] and quantitative information about lung tissue structure alterations.[11-17] Conventional proton magnetic resonance imaging (^{1}H MRI) is also readily available in most clinical care centers but has historically posed a number of major challenges for the evaluation of the respiratory system and in particular for COPD. Low tissue and ^{1}H density in the lung results in relatively low ^{1}H MRI signal intensity (SI); in addition, the countless air-tissue interfaces in the lung also result in substantial susceptibility artifacts.[18] Moreover, in emphysematous COPD, there are no facilitating disease-related effects. In fact, typically in emphysema, there is loss of tissue, reduced blood volume and significant gas trapping and all of these would be expected to diminish the inherent tissue-specific ^{1}H MR signal.[19] In addition, unlike CT, different calibration scales are employed across MRI scanners and therefore MR SI cannot be easily compared from site to site or between different scanners.[19-24]

Nevertheless, the yet unrealized potential for MRI to provide regional and quantitative measurements for COPD continues to drive the development of ^{1}H MRI methods in human subjects and animal models based on ultra-short echo times[25] for structural information and more recently based on Fourier-decomposition methods, for functional information.[26] For example, ^{1}H MRI showed that alterations in lung volume resulted in SI[19] changes and in addition, gravity-dependent ^{1}H SI gradients were shown to be dependent upon subject positioning, suggesting that ^{1}H SI is proportional to lung tissue density.[27] In mice, ^{1}H SI correlates with pulmonary micro-CT density and histology[28] and is sensitive to lung parenchyma changes in mouse models of emphysema[29] as well as lung changes in normal mice introduced by different positive end-expiratory pressure levels.[30]

We recently evaluated a group of healthy never-smokers and subjects with COPD using fast gradient echo (echo time=1.2ms) ^{1}H MRI that we typically acquire for registration purposes and hyperpolarized ^{3}He MRI. The high sensitivity of ^{3}He MRI apparent diffusion coefficients (ADC) and ventilation abnormalities in healthy elderly and COPD subjects is well established[31,32] as is the relationship between pulmonary function measurements and ^{3}He MRI measurements.[33,34] We hypothesized that coincident and volume-matched inhalation acquisition of ^{3}He and ^{1}H MRI in COPD would allow for the detection of a relationship between hyperpolarized ^{3}He ADC and ^{1}H SI of the lung parenchyma, lending more weight to the idea that gas trapping and tissue destruction may be quantified using short echo time MR methods. To test this hypothesis, we quantified ^{1}H MRI SI and ^{3}He MRI ADC measurements acquired within 1 minute and using the same volume breath-hold in COPD ex-smokers and healthy never-smokers and compared these to pulmonary function and CT measurements acquired within 30 minutes of MRI.

2.2 Materials and Methods

2.2.1 Study Subjects

Nine healthy never-smokers and 11 COPD ex-smokers were enrolled from the general population and a local tertiary health care center, as previously described.[33,34] All subjects provided written informed consent to the study protocol approved by the local research ethics board and Health Canada, and the study was compliant with the Personal Information Protection and Electronic Documents Act (PIPEDA). COPD subjects between 55 and 80 years of age were included with a disease diagnosis of at least 1 year, having had a smoking history of at least 10 pack-years. COPD subjects were categorized according to Global Initiative for Chronic Obstructive Lung Disease (GOLD) criteria.[4,35] Healthy subjects between 55 and 80 years of age were included if they had no history of chronic respiratory disease (including asthma), less than one pack-year smoking history, forced expiratory volume in 1 second (FEV_1) greater than 80% predicted, FEV_1 divided by the forced vital capacity (FVC) (FEV_1/FVC) greater than 70%, and no current diagnosis or history of cardiovascular disease. Throughout the duration of the study, a hypoxic adverse event was defined as any decrease < 88% arterial oxygen saturation (SAO_2); subjects were to be withdrawn if they experienced a decrease in SAO_2 to 80% for 15 continuous seconds during any procedure.

2.2.2 Spirometry and Plethysmography

A medical history and vital signs were recorded and then subjects completed plethysmography, spirometry and measurements of the diffusing capacity of carbon monoxide (DL_{CO}) according to American Thoracic Society guidelines.[36] Briefly, spirometry was performed using an *ndd EasyOne spirometer* (ndd Medizintchnik AG, Zurich, CH) reporting FEV_1 and FVC and a minimum of three acceptable spirometry maneuvers was performed. Whole body plethysmography (MedGraphics Corporation, 350 Oak Grove Parkway, St. Paul, MN, USA) was also performed for the measurement of total lung capacity (TLC), inspiratory capacity (IC), residual volume (RV), and functional residual capacity (FRC).

Table 2.1 Subject Demographics

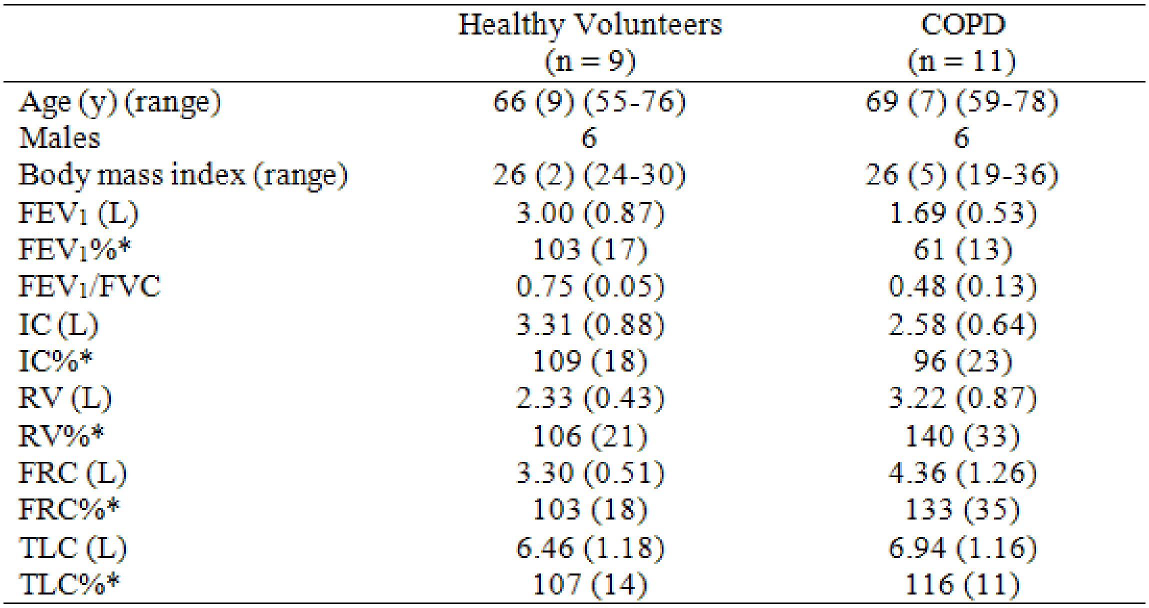

	Healthy Volunteers (n = 9)	COPD (n = 11)
Age (y) (range)	66 (9) (55-76)	69 (7) (59-78)
Males	6	6
Body mass index (range)	26 (2) (24-30)	26 (5) (19-36)
FEV_1 (L)	3.00 (0.87)	1.69 (0.53)
FEV_1%*	103 (17)	61 (13)
FEV_1/FVC	0.75 (0.05)	0.48 (0.13)
IC (L)	3.31 (0.88)	2.58 (0.64)
IC%*	109 (18)	96 (23)
RV (L)	2.33 (0.43)	3.22 (0.87)
RV%*	106 (21)	140 (33)
FRC (L)	3.30 (0.51)	4.36 (1.26)
FRC%*	103 (18)	133 (35)
TLC (L)	6.46 (1.18)	6.94 (1.16)
TLC%*	107 (14)	116 (11)

FEV1: forced expiratory volume in 1 second; FVC: forced vital capacity; FRC: functional residual capacity; IC: inspiratory capacity; TLC: total lung capacity. Data are presented as mean (± standard deviation).*Percent predicted.

2.2.3 Image Acquisition

Subjects were screened for MRI and coil compatibility (inner diameter of elliptical coil = 50 cm) prior to imaging, and digital pulse oximetry was used to monitor SAO_2 during MRI. A spin-exchange polarizer system (HeliSpin; General Electric Healthcare (GEHC), Durham, NC) was used to polarize ^{3}He gas to 30%–40%, as previously described.[37] Doses of hyperpolarized ^{3}He gas (5 mL per kilogram of body weight) were administered in 1-L plastic bags (Tedlar; Jensen Inert Products, Coral Springs, Fla) and were diluted with ultrahigh purity, medical grade nitrogen (Spectra Gases, Alpha, NJ). Polarization of the diluted dose was quantified at a polarimetry station (GEHC, Durham, NC) immediately prior to ^{3}He gas administration to subject.

MRI was performed on a whole-body 3T system (Discovery MR750 GEHC, Milwaukee, WI USA) with broadband imaging capability, as previously described.[31] Coronal two-dimensional ^{1}H MRI was acquired prior to ^{3}He MRI, with subjects imaged during a 1-L breath-hold of a ^{4}He-N_2 mixture from FRC using a whole-body radiofrequency (RF) coil and a proton fast spoiled-gradient-echo sequence ((FGRE) 16-second total data acquisition; repetition time (TR)/echo time (TE) 4.7ms/1.2ms; flip angle=30°; field of view (FOV)=40×40 cm; matrix, 128 × 128; 15-mm section thickness. An FGRE pulse sequence was used in order to take advantage of a lower TE with the understanding that signal decay is influenced by transverse relaxation and intra-voxel signal dephasing caused by microscopic magnetic field inhomogeneities[38] and that minimizing TE, typically results in higher lung parenchyma SI.

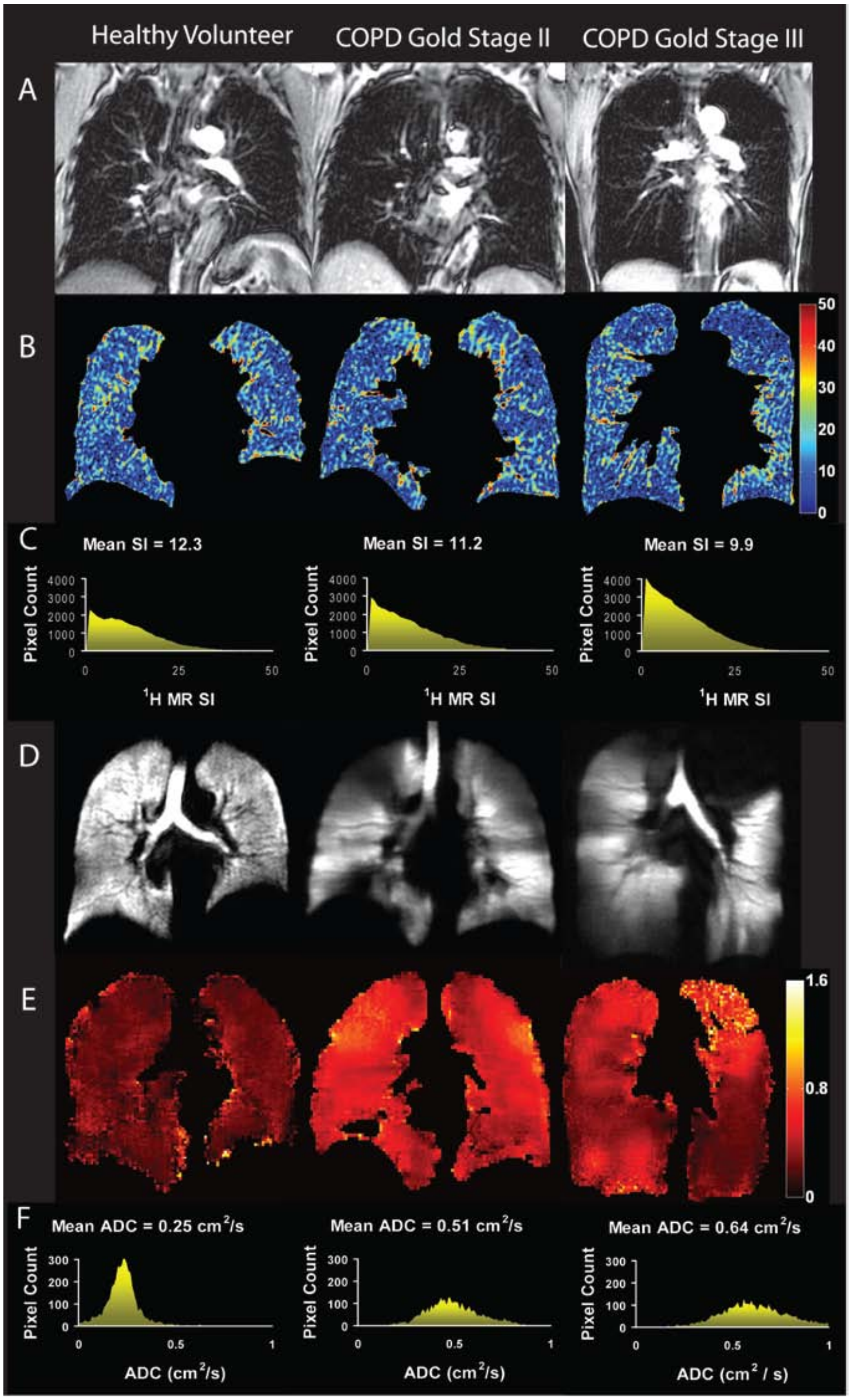

Figure 2.1: ^{1}H and ^{3}He MRI for a healthy never-smoker and GOLD stage II and III COPD.

Coronal center slice (A) ^{1}H MRI, (B) ^{1}H SI map, (C) ^{1}H SI map histogram, (D) hyperpolarized ^{3}He ventilation MRI, (E) ^{3}He ADC map, and (F) ^{3}He ADC histograms for of healthy never-smoker (left panels), Gold stage II COPD (centre panels) and Gold stage III COPD (right panels).

^{3}He MRI was immediately performed with a whole-body gradient set with a maximum gradient amplitude of 1.94 G/cm and a single-channel, rigid elliptical transmit-receive chest coil (RAPID Biomedical, Würzburg, Germany). The basis frequency of the coil was 97.3 MHz, and excitation power was 3.2 kW using an RF power amplifier (AMT 3T90; GEHC Milwaukee, WI USA). For diffusion-weighted imaging, coronal multi-slice images were obtained using a fast gradient echo method with centric k-space sampling as previously described.[32] Two interleaved images (14-second total data acquisition; TR/TE 7.6ms/3.7ms; flip angle= 8°; FOV=40×40 cm; matrix=128 × 128; 30-mm slice thickness), with and without additional diffusion sensitization (maximum gradient amplitude = 1.94 G/cm, rise and fall time = 0.5 ms, gradient duration = 0.46 ms, diffusion time = 1.46 ms, b value = 1.6 s/cm^2), were acquired. All imaging was completed within approximately 7–10 minutes of subjects first lying in the scanner. CT scans were also performed for COPD subjects within 30 minutes after MRI on a 64-slice Lightspeed VCT scanner (GEHC, Milwaukee, WI USA) using a detector configuration of 64×0.625 mm, 120 kVp, 100 effective mA, tube rotation time of 500 ms and a pitch of 1.0. A single spiral acquisition of the entire lung was acquired from the apex to the base with subjects in the supine position and in breath-hold after inhalation of a 1L ^{4}He-N$_2$ mixture from FRC with image acquisition time of 15s. Reconstruction of the data was performed using a slice thickness of 1.25-mm with a standard convolution kernel. To match the lung volume and tissue distention in ^{1}H MRI, CT and ^{3}He MRI, all images were acquired in breath-hold after inspiration of a 1-L He-N$_2$ mixture from FRC.

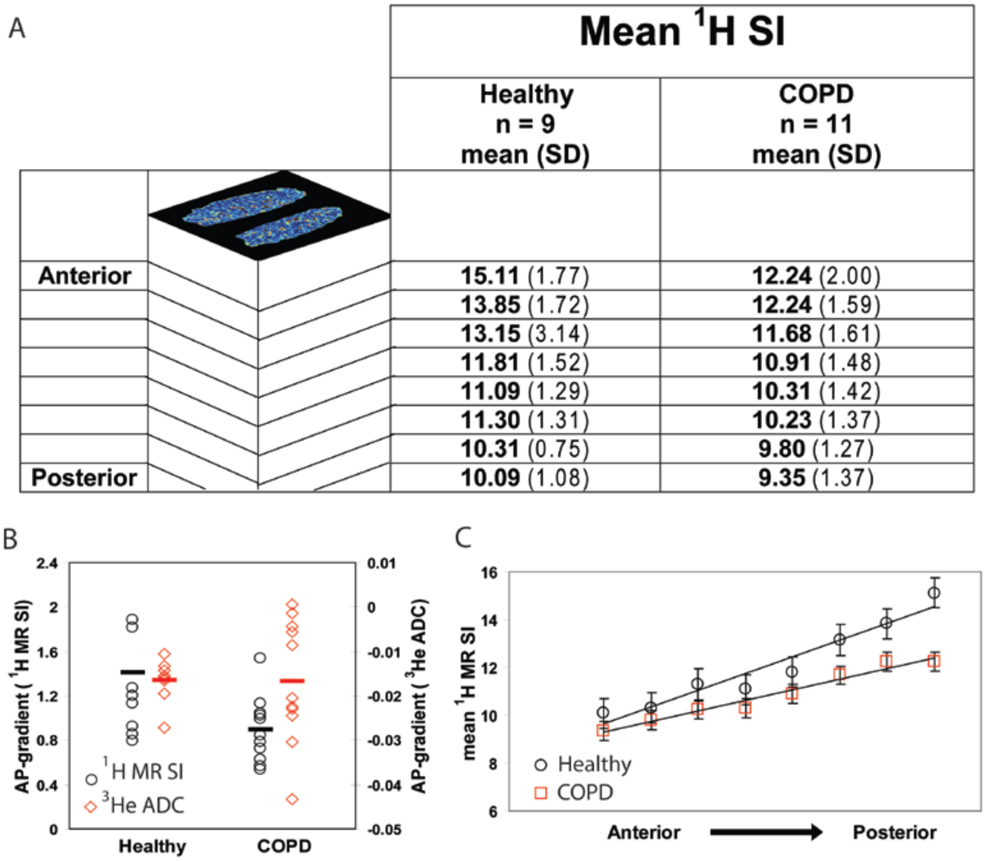

Mean ^{1}H SI	Healthy n = 9 mean (SD)	COPD n = 11 mean (SD)
Anterior	**15.11** (1.77)	**12.24** (2.00)
	13.85 (1.72)	**12.24** (1.59)
	13.15 (3.14)	**11.68** (1.61)
	11.81 (1.52)	**10.91** (1.48)
	11.09 (1.29)	**10.31** (1.42)
	11.30 (1.31)	**10.23** (1.37)
	10.31 (0.75)	**9.80** (1.27)
Posterior	**10.09** (1.08)	**9.35** (1.37)

Figure 2.2: Mean ^{1}H SI anatomical differences in the anterior-to-posterior (AP) ROI.

(A) Mean ^{1}H SI for each of the eight centermost coronal slices. Round bracketed values are SDs of mean ^{1}H SI for each subgroup. (B) AP-gradients for ^{1}H SI (triangles) and ^{3}He ADC (diamonds) for healthy and COPD subjects. Stars indicate subgroup mean, and error bars are SD of the mean. (C) Mean ^{1}H SI for each of eight centermost coronal slices for healthy volunteers and COPD subjects from anterior to-posterior. Error bars indicate standard error of the mean.

2.2.4 Image Analysis

All images were transferred to a remote workstation for post-processing and image analysis. For ^{1}H MRI, image processing was performed using MATLAB (MATLAB version R2008b; The MathWork Inc., Cambridge, MA, USA). The lung parenchyma was segmented automatically from the heart, mediastinum, central pulmonary vessels, diaphragm, and chest wall using a seeded region growing algorithm.[39] Mean ^{1}H SI and corresponding standard deviation (SD) for each slice was calculated using the arithmetic mean. ^{3}He MRI ADC was calculated as previously described.[31] For CT image analysis, the Pulmonary Workstation 2.0 (VIDA Diagnostics Inc., Iowa City, IA) was used to quantify tissue attenuation in Hounsfield units (HU) on a voxel by voxel basis and for ROI. The software automatically determined the boundaries of each lung and calculated the relative area (RA) with attenuation values below -950 HU (RA_{950}), and the 15th percentile of the frequency distribution histogram in HU (HU_{15}). These two parameters were previously shown to be related to the macroscopic and microscopic extent of pulmonary emphysema[40,41] and emphysema progression.[42]

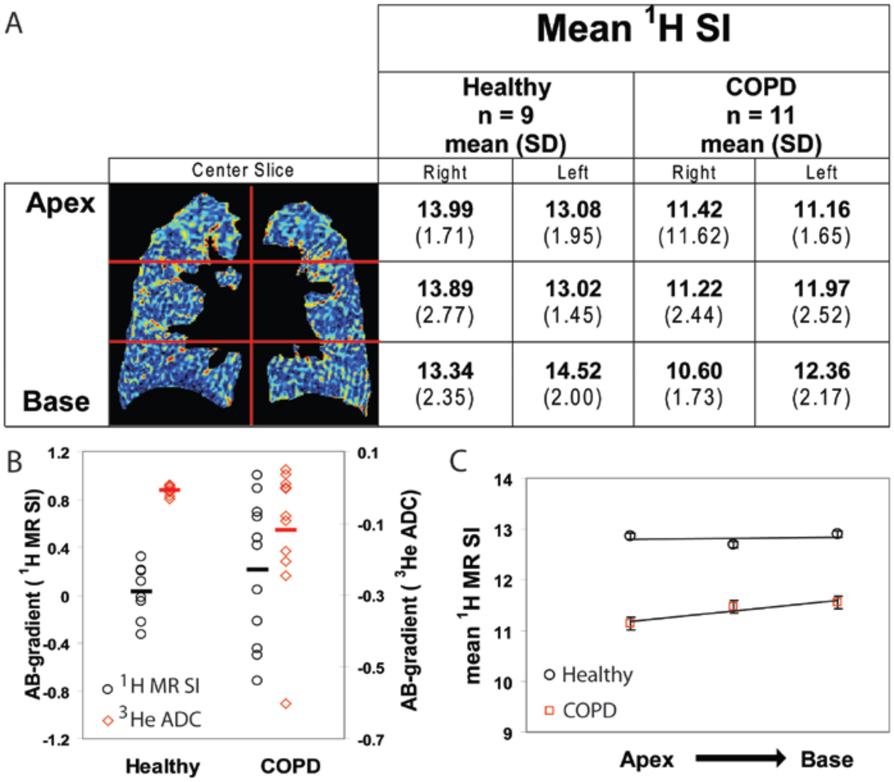

	Center Slice	Mean ^{1}H SI Healthy n = 9 mean (SD) Right	 Left	 COPD n = 11 mean (SD) Right	 Left
Apex		**13.99** (1.71)	**13.08** (1.95)	**11.42** (11.62)	**11.16** (1.65)
		13.89 (2.77)	**13.02** (1.45)	**11.22** (2.44)	**11.97** (2.52)
Base		**13.34** (2.35)	**14.52** (2.00)	**10.60** (1.73)	**12.36** (2.17)

Figure 2.3: Mean ^{1}H SI anatomical differences in the apex-to-base (AB) ROI. (A) Mean ^{1}H SI for ROI in the center coronal slice. Round bracketed values are SDs of the mean for each subgroup. (B) AB-gradients for ^{1}H SI (triangles) and ^{3}He ADC (diamonds) for healthy and COPD subjects. Stars indicate mean of subgroups, and error bars are SD of the mean. (C) Mean ^{1}H SI for healthy volunteers and COPD subjects from the apex-to-base in center coronal slice. Error bars indicate standard error of the mean.

Anatomical differences in ^{1}H MR SI, ^{3}He MRI ADC, CT RA_{950} and HU_{15} were quantified by evaluating anterior-to-posterior (AP) and apex-to-base (AB) differences and gradients. The absolute difference between the most anterior and posterior coronal slices (ΔAP) was evaluated for ^{1}H MRI SI, (eight of the most central 15mm slices) and for ^{3}He MRI ADC, (4 diffusion-weighted 30 mm ADC maps). The absolute difference between the most apical and most basal ROI (ΔAB) was also evaluated for ^{1}H MRI SI and ^{3}He MRI ADC whereby each coronal slice was divided into six ROI in which the carina was used as an anatomical reference point as previously described.[43] ΔAB was calculated as the mean of both the right and left lung. We also calculated AP- and AB-gradients where gradient was defined as the slope of the lines that described the AP (8 slices or 120mm) and AB (3 ROI, mean of L and R lung, 240mm) changes respectively over the ROI evaluated. For comparison, CT volumes were reconstructed in the coronal plane and 180 x 0.7mm slices (126mm) were evaluated to approximate the same volume to facilitate direct comparison with ^{1}H SI.

2.2.5 Statistical Analysis

One-way analysis of variance (ANOVA) was performed to evaluate the significant interactions between ^{1}H SI, ^{3}He ADC measurements between subject subgroups using SPSS (SPSS version 19, SPSS An IBM Company, Somers, NY USA). Comparisons between healthy never-smokers and COPD subjects for whole lung mean ^{1}H SI, ^{3}He ADC, and ΔAP, ΔAB, AP-gradient and AB-gradient for ^{1}H SI and ^{3}He ADC were then performed using one-way (ANOVA) in SPSS. The relationships between ^{1}H SI and ^{3}He ADC, pulmonary function and CT measurements were determined using linear regression and Pearson correlation coefficients using Prism Graphpad (Prism, version 4.00; GraphPad Software, San Diego, CA).

2.3 Results

Demographic characteristics are provided in Table 2.1 for all 20 subjects enrolled (12 males) with very similar mean ages and age ranges for COPD and healthy never-smokers. Spirometry and plethysmography measurements acquired a few minutes before imaging are also shown and reflect the inclusion criteria for healthy never-smokers and subjects with COPD. For COPD subjects, nine were classified according to GOLD[4] as stage II COPD and two subjects were GOLD stage III COPD.

Figure 2.1 shows the centre coronal slice ^{1}H MR image, ^{1}H SI map and frequency distribution histogram as well as hyperpolarized ^{3}He ventilation image, ^{3}He MRI ADC map, and ADC histogram for a healthy never-smoker and a single stage II and stage III COPD subject each.

Table 2.2 shows mean whole lung (WL) ^{1}H SI and ^{3}He ADC for both subject subgroups as well as mean CT measurements for COPD subjects. Mean ^{1}H SI for healthy volunteers (HV) and COPD was significantly different (p=.04). In addition, ^{1}H SI ΔAP (p=.01), and the AP-gradient (p=.05) was significantly different for healthy and COPD subjects. We evaluated mean ^{3}He MRI ADC for the same subject subgroups and this was significantly different (p=.0001) but anatomical AB and AP differences were not different between subgroups, except for AB-gradient (p=.049).

Figure 2.2 shows in more detail the ^{1}H SI and ^{3}He ADC anterior-to-posterior (AP) differences and gradients. Figure 2.2A shows mean ^{1}H SI for each of the eight most central coronal slices by subgroup, and Figure 2.2B shows the ^{1}H SI and ^{3}He ADC AP-gradients by subgroup. Figure 2.2C shows mean ^{1}H SI for anterior and posterior slices by subgroup with slope (AP gradient).

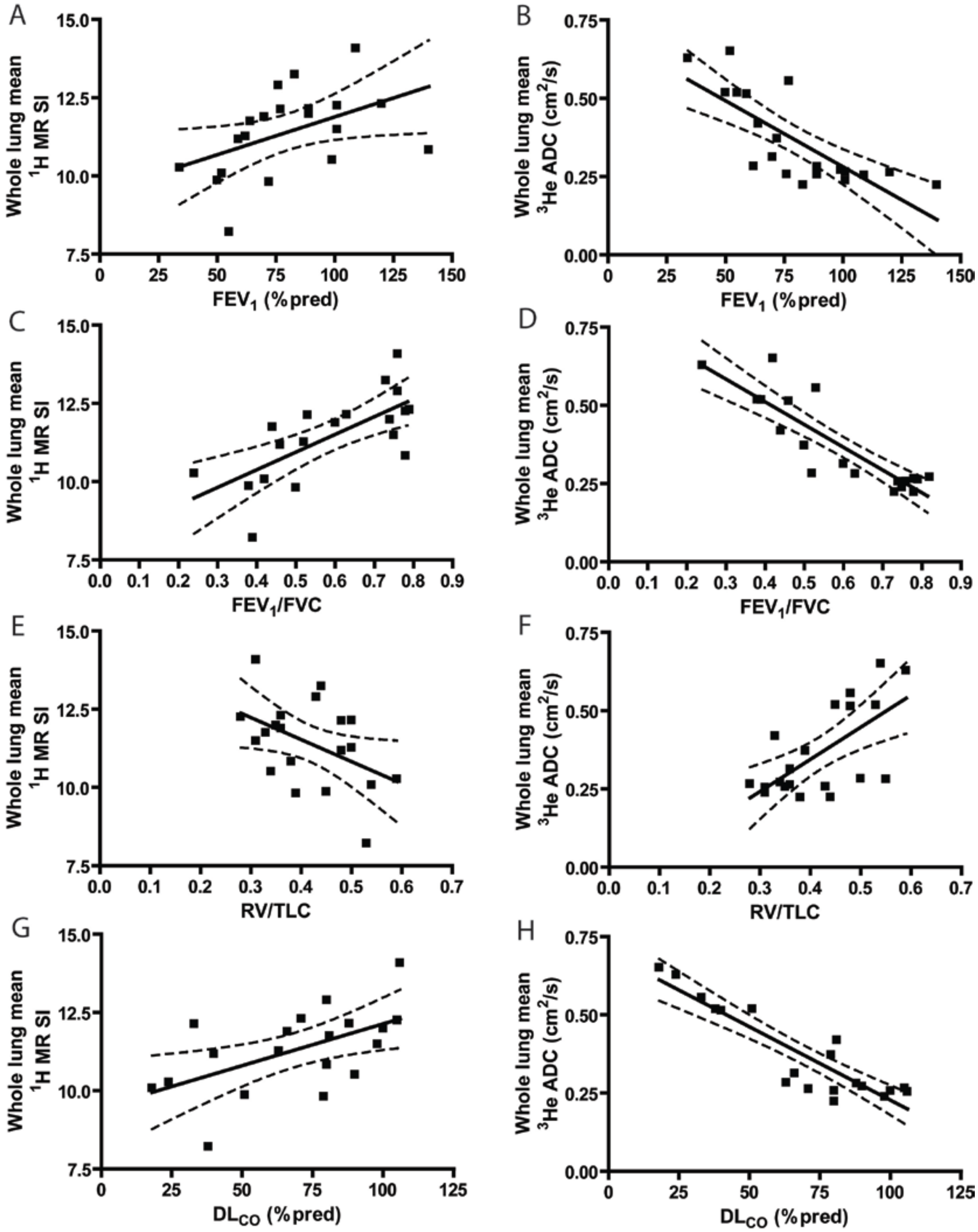

Figure 2.4: Relationship between ^{1}H SI, ^{3}He ADC and pulmonary function measurements.
The 95% confidence intervals for the regressions are shown as dotted lines. Association between whole lung mean ^{1}H SI and (A) FEV_1 (%pred) (r = 0.46, $p = 0.0392$), (C) FEV/FVC (r = 0.70, $p = 0.0008$), (E) RV/TLC (r =- 0.46, $p = 0.0423$) and (G) DL_{CO} (r = 0.56, $p = 0.0132$,). Association between whole lung mean ^{3}He ADC and (B) FEV_1 (%pred) (r = -0.77, $p < 0.0001$), (D) FEV/FVC (r = -0.87, $p < 0.0001$), (F) RV/TLC (r = 0.65, $p = 0.0018$,) and (H) DL_{CO} (r = -0.90, $p < 0.0001$,).

Figure 2.3 shows the ^{1}H SI and ^{3}He ADC apex-to-base (AB) differences and gradients in more detail. Figure 2.3A shows mean ^{1}H SI for each ROI by subgroup and Figure 2.3B shows the ^{1}H SI and ^{3}He ADC AB-gradients for all subjects by subgroup. In Figure 2.3C, the mean ^{1}H SI values for apical and basal slices by subgroup are shown with mean AB gradient.

Figure 2.4 shows the relationship between ^{1}H SI and ^{3}He ADC with pulmonary function measurements for all subjects. There was a significant correlation between whole lung ^{1}H SI and $FEV_{1\%pred}$ (r = 0.46, $p = 0.04$), FEV_1/FVC (r = 0.70, $p = 0.0008$), $DL_{CO\%pred}$ (r = 0.56, $p = 0.01$) and RV/TLC (r =- 0.46, $p = 0.04$). There were also significant relationships detected between ^{3}He ADC and $FEV_{1\%pred}$ (r = -0.77, $p < 0.0001$), FEV_1/FVC (r = -0.87, $p < 0.0001$), $DL_{CO\%pred}$ (r = -0.90, $p < 0.0001$) and RV/TLC (r = 0.65, $p = 0.0018$). Figure 2.5 shows the significant relationship between ^{1}H SI and ^{3}He ADC (r = -0.58, $p = 0.008$) and Figure 2.6 shows the significant relationships of CT measurements RA_{950}, and HU_{15} with ^{1}H SI (RA_{950}; r = -0.69, $p = 0.02$) and $HU_{15;}$ r = 0.66, $p = 0.03$) and with ^{3}He ADC (RA_{950}; r = 0.87, $p = 0.0005$ and HU_{15}; r = -0.88, $p = 0.0003$) for COPD subjects only.

2.4 Discussion

In this pilot study we evaluated 20 middle-aged and elderly subjects, including nine subjects with stage II COPD, two subjects with stage III COPD and nine never-smokers to compare short echo-time ^{1}H MRI, ^{3}He MRI and well-established pulmonary function measurements. We made a number of observations including: 1) a significant difference was detected between ^{1}H SI in healthy never-smokers and subjects with COPD, 2) a significant difference in ^{1}H SI AP-gradient and ΔAP was detected between healthy and COPD subjects, 3) a significant and moderately strong relationship was observed between ^{1}H SI and ^{3}He ADC, 4) significant and moderately strong relationships were detected between ^{1}H SI and CT measurements of emphysema, and, 5) significant correlations were detected between both ^{1}H SI and ^{3}He ADC with FEV_1, FEV_1/FVC, RV/TLC and DL_{CO}.

Table 2.2 MRI and CT Measurements

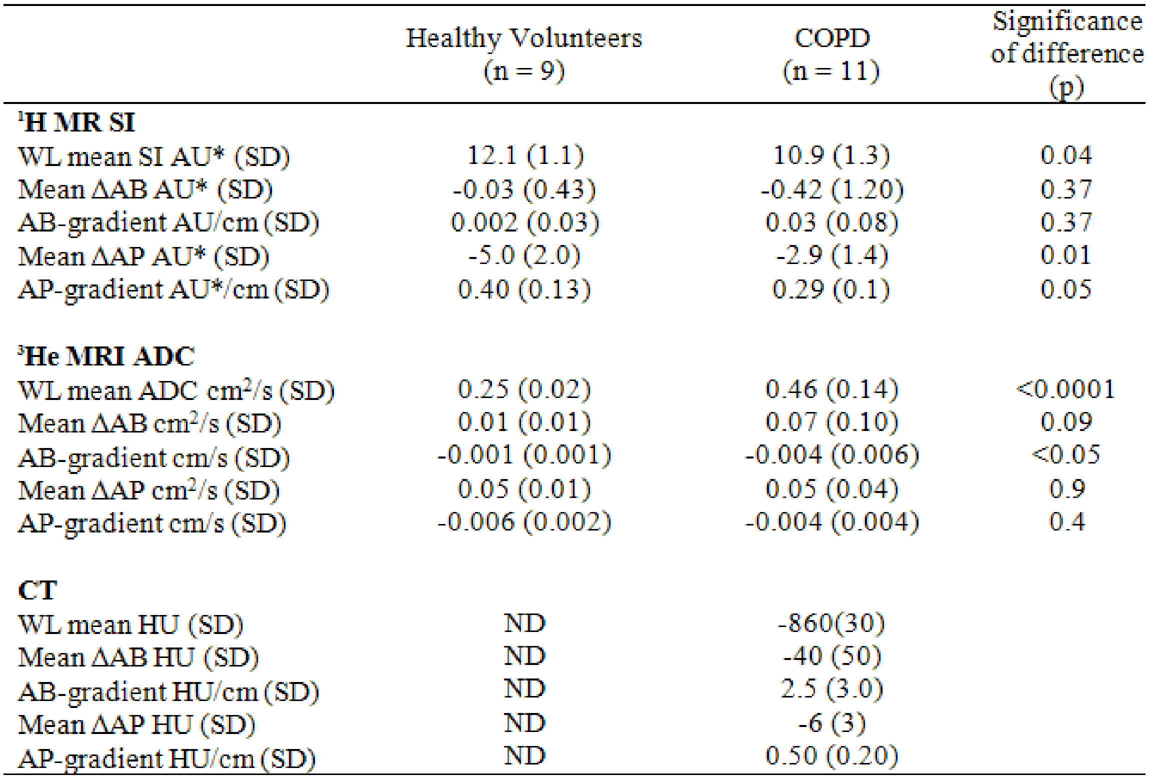

	Healthy Volunteers (n = 9)	COPD (n = 11)	Significance of difference (p)
^{1}H MR SI			
WL mean SI AU* (SD)	12.1 (1.1)	10.9 (1.3)	0.04
Mean ΔAB AU* (SD)	-0.03 (0.43)	-0.42 (1.20)	0.37
AB-gradient AU/cm (SD)	0.002 (0.03)	0.03 (0.08)	0.37
Mean ΔAP AU* (SD)	-5.0 (2.0)	-2.9 (1.4)	0.01
AP-gradient AU*/cm (SD)	0.40 (0.13)	0.29 (0.1)	0.05
^{3}He MRI ADC			
WL mean ADC cm^2/s (SD)	0.25 (0.02)	0.46 (0.14)	<0.0001
Mean ΔAB cm^2/s (SD)	0.01 (0.01)	0.07 (0.10)	0.09
AB-gradient cm/s (SD)	-0.001 (0.001)	-0.004 (0.006)	<0.05
Mean ΔAP cm^2/s (SD)	0.05 (0.01)	0.05 (0.04)	0.9
AP-gradient cm/s (SD)	-0.006 (0.002)	-0.004 (0.004)	0.4
CT			
WL mean HU (SD)	ND	-860(30)	
Mean ΔAB HU (SD)	ND	-40 (50)	
AB-gradient HU/cm (SD)	ND	2.5 (3.0)	
Mean ΔAP HU (SD)	ND	-6 (3)	
AP-gradient HU/cm (SD)	ND	0.50 (0.20)	

^{1}H SI is in arbitrary units, (AU).

In addition to observing a significant difference between ^{1}H SI in healthy never-smokers and subjects with COPD, we also observed differences in anterior-to-posterior SI gradients and the absolute difference in SI between the most anterior and most posterior slice (ΔAP). This AP-gradient has been attributed to a gravity dependence in the supine and other positions,[27] which influences ^{1}H MR SI because of lung tissue compression in the dependent (posterior) regions. The lower AP-gradient in COPD subjects may be due to gas trapping and similar differences between normal and severe (GOLD stage III/IV) COPD subjects have been shown previously using hyperpolarized ^{3}He ADC[43] but not significantly different in this ^{3}He MRI results in much milder COPD subjects evaluated here. We also did not observe a significantly different AB-gradient for mean ^{1}H SI between subgroups which might be expected, however heterogeneity in the COPD subgroup may have resulted in the large variance in the mean ΔAB and AB gradient that precludes detection of differences between subgroups.

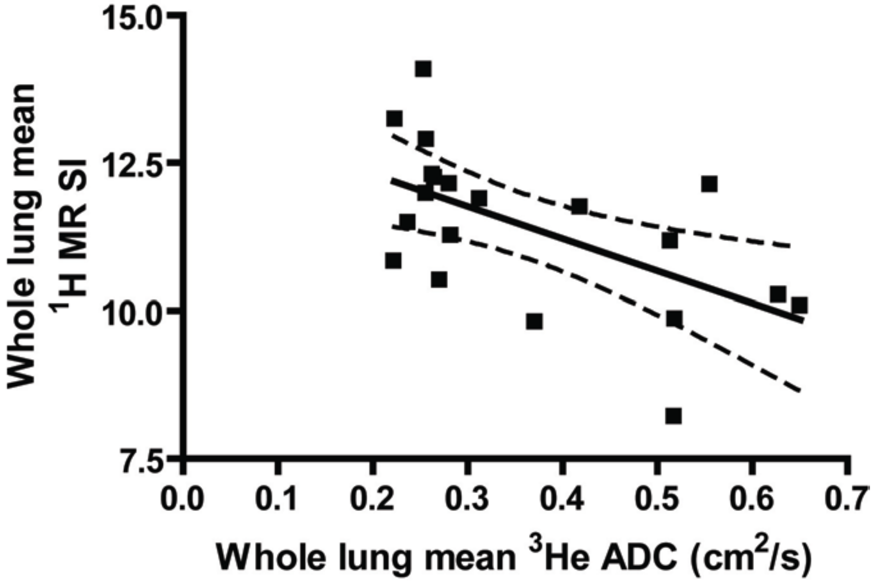

Figure 2.5: Relationship between ^{1}H SI and ^{3}He ADC.

The 95% confidence intervals for the regressions are shown as dotted lines. Association between whole lung mean ^{1}H SI and whole lung mean ^{3}He ADC (r = -0.58, *p* = 0.008).

We were surprised to observe a significant and moderately strong relationship between ^{1}H SI and ^{3}He ADC, as well as significant and moderately strong relationships between ^{1}H SI and CT measurements of emphysema. The significant correlation between ^{1}H SI with CT and ^{3}He MRI measurements of emphysema suggests that these methods and measurements may be quantifying similar tissue changes and also that lung ^{1}H SI can be used to monitor emphysema as a complement to CT and noble gas MRI.

Finally, we also observed significant and moderate correlations between both ^{1}H SI and ^{3}He ADC with FEV_1, FEV_1/FVC, DLCO and RV/TLC. ^{3}He ADC,[44] can be considered a surrogate measurement of airspace size,[45-48] and has been previously histologically validated[37] and correlated with CT measurements of emphysema.[49] Previous work with short echo time ^{1}H MRI also suggested a relationship between parenchymal tissue changes or gas trapping abnormalities and ^{1}H SI.[29,50,51] We note in Figure 2.1 for the representative stage III COPD subject, in the L upper lobe the correspondence of low ^{1}H SI and very high ^{3}He ADC and as well very poor ^{3}He ventilation. These preliminary regional findings and the significant relationships between established pulmonary function measurements and both ^{1}H SI and ^{3}He are somewhat expected, but to our knowledge this is the first report of relationships between ^{1}H SI and ^{3}He ADC in the same patients. We think these findings support the further development of improved ^{1}H methods providing enhanced signal-to-noise of the parenchyma. Short echo time MR methods together with previously reported Fourier-decomposition MR methods that provide lung functional information have the potential to provide clinically relevant information that can be undertaken in intensive serial studies of COPD without regard to radiation burden.

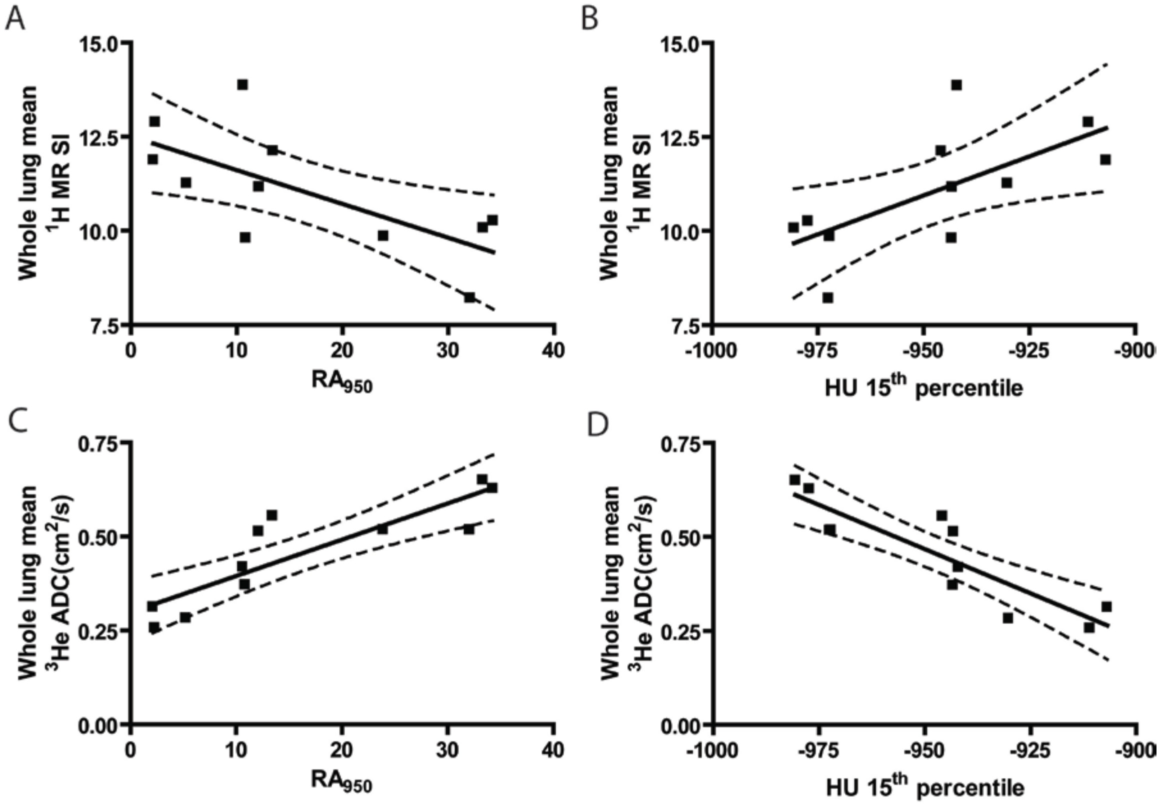

Figure 2.6: Relationship between ^{1}H SI and ^{3}He ADC with CT tissue attenuation measurements.

The 95% confidence intervals for the regressions are shown as dotted lines. Association between whole lung mean ^{1}H MR SI and (A) RA_{950} (r = -0.69, p = 0.0186) and (B) HU_{15} (r = 0.66, p = 0.0263). Association between whole lung mean ^{3}He ADC and (C) RA_{950} (r = 0.87, p = 0.0005) and (D) HU_{15} (r = -0.88, p = 0.0003).

We recognize that this small pilot study -the first to evaluate short echo time ^{1}H MRI SI quantification and ^{3}He ADC in the same subjects should be viewed as hypothesis generating. First, the small number of subjects studied necessitates cautious interpretation and extrapolation to the general COPD population, and underscores the requirement for larger studies to test the relationships identified here. We also acknowledge that improvements in the technique are required, such as conducting three dimensional image acquisition methods using shorter echo time and respiratory gated pulse sequences. Nevertheless, regardless of the specific underlying pathology, lung tissue destruction and/or gas trapping/hyperinflation is a likely prerequisite for the decreased SI we observed in COPD using ^{1}H MRI. We also must underscore that all the measurements in this study were performed at 3T, where magnetic susceptibility issues further degrade ^{1}H MRI SI estimations. For this study, mean signal-to-noise ratio (SNR) for the ^{1}H image slices was 1.6 and for ^{3}He images (diffusion-weighted slices) it was 56 with no significant difference in SNR detected between subgroups. It is also important to note that the relationship between ^{1}H SI and SNR was not significant nor was the relationship between SNR and FEV$_1$. The significant results and correlations reported here however, must be viewed as conservative approximations of results that could be achieved with much short echo times and lower field strengths.

Short echo-time ^{1}H pulmonary MRI was first developed for thoracic imaging[23] almost 2 decades ago and the fundamental limitations were well understood, as was the pathway towards the improvements required to enable clinical utility in respiratory medicine. Inhaled gas contrast MR methods that can be achieved using hyperpolarized noble gas[52,53] and oxygen-enhancement[54] certainly have played an important role in developing our understanding of lung physiology,[37] lung tissue structure and function in COPD[31,55] and changes over time[33] in the COPD lung. However, it is likely that ^{1}H methods will remain along with CT as the main thoracic imaging tools available at most clinical centres and any improvements in SNR, feasibility and our understanding of the physiological and clinical relevance of the ^{1}H lung tissue measurements are justifiable on this basis.

In conclusion, our study confirms the hypothesis that short echo time ^{1}H MRI can be used to quantitatively evaluate lung tissue alterations in COPD based on differences in ^{1}H density due to tissue destruction and/or gas trapping. In the case where intensive or serial thoracic imaging is required for research or clinical purposes, we think ^{1}H MR methods can be further improved to better detect changes in lung tissue and gas trapping, both hallmarks of COPD.

2.5 References

Reference List

1. Mannino DM, Buist AS. Global burden of COPD: risk factors, prevalence, and future trends. *Lancet* 2007; **370**: 765-73.

2. Bethesda M. *Chronic obstructive pulmonary disease. Morbidity and mortality*.National Heart Lung and Blood Institute, Department of Health and Human Services, 2002.

3. World Health Organization. Global surveillance, prevention and control of chronic respiratory diseases: a comprehensive approach. 2007. Geneva, Switzerland, World Health Organization.
   Ref Type: Report

4. Rabe KF, Hurd S, Anzueto A *et al*. Global strategy for the diagnosis, management, and prevention of chronic obstructive pulmonary disease: GOLD executive summary. *Am. J. Respir. Crit Care Med.* 2007; **176**: 532-55.

5. Vestbo J, Anderson W, Coxson HO *et al*. Evaluation of COPD Longitudinally to Identify Predictive Surrogate End-points (ECLIPSE). *Eur. Respir. J.* 2008; **31**: 869-73.

6. Hasegawa M, Nasuhara Y, Onodera Y *et al*. Airflow limitation and airway dimensions in chronic obstructive pulmonary disease. *Am. J. Respir. Crit Care Med.* 2006; **173**: 1309-15.

7. King GG, Muller NL, Pare PD. Evaluation of airways in obstructive pulmonary disease using high-resolution computed tomography. *Am. J. Respir. Crit Care Med.* 1999; **159**: 992-1004.

8. Ohara T, Hirai T, Sato S *et al*. Longitudinal study of airway dimensions in chronic obstructive pulmonary disease using computed tomography. *Respirology.* 2008; **13**: 372-8.

9. Akira M, Toyokawa K, Inoue Y *et al*. Quantitative CT in chronic obstructive pulmonary disease: inspiratory and expiratory assessment. *AJR Am. J. Roentgenol.* 2009; **192**: 267-72.

10. Coxson HO, Rogers RM. Quantitative computed tomography of chronic obstructive pulmonary disease. *Acad. Radiol.* 2005; **12**: 1457-63.

11. Fujimoto K, Kitaguchi Y, Kubo K *et al*. Clinical analysis of chronic obstructive pulmonary disease phenotypes classified using high-resolution computed tomography. *Respirology*. 2006; **11**: 731-40.

12. Gevenois PA, De M, V, De VP *et al*. Comparison of computed density and macroscopic morphometry in pulmonary emphysema. *Am. J. Respir. Crit Care Med.* 1995; **152**: 653-7.

13. Hansell DM. High-resolution computed tomography in the evaluation of fibrosing alveolitis. *Clin. Chest Med.* 1999; **20**: 739-60, viii.

14. Hayhurst MD, MacNee W, Flenley DC *et al*. Diagnosis of pulmonary emphysema by computerised tomography. *Lancet* 1984; **2**: 320-2.

15. Hoffman EA, Reinhardt JM, Sonka M *et al*. Characterization of the interstitial lung diseases via density-based and texture-based analysis of computed tomography images of lung structure and function. *Acad. Radiol.* 2003; **10**: 1104-18.

16. Kazerooni EA. Radiologic evaluation of emphysema for lung volume reduction surgery. *Clin. Chest Med.* 1999; **20**: 845-61.

17. Muller NL, Staples CA, Miller RR *et al*. "Density mask". An objective method to quantitate emphysema using computed tomography. *Chest* 1988; **94**: 782-7.

18. Kauczor HU, Kreitner KF. MRI of the pulmonary parenchyma. *Eur. Radiol.* 1999; **9**: 1755-64.

19. Bankier AA, O'Donnell CR, Mai VM *et al*. Impact of lung volume on MR signal intensity changes of the lung parenchyma. *J. Magn Reson. Imaging* 2004; **20**: 961-6.

20. Hatabu H, Tadamura E, Prasad PV *et al*. Noninvasive pulmonary perfusion imaging by STAR-HASTE sequence. *Magn Reson. Med.* 2000; **44**: 808-12.

21. Hatabu H, Stock KW, Sher S *et al*. Magnetic resonance imaging of the thorax. Past, present, and future. *Radiol. Clin. North Am.* 2000; **38**: 593-620, x.

22. Mai VM, Chen Q, Li W *et al*. Effect of respiratory phases on MR lung signal intensity and lung conspicuity using segmented multiple inversion recovery turbo spin echo (MIR-TSE). *Magn Reson. Med.* 2000; **43**: 760-3.

23. Mayo JR. Thoracic magnetic resonance imaging: physics and pulse sequences. *J. Thorac. Imaging* 1993; **8**: 1-11.

24. Mayo JR. MR imaging of pulmonary parenchyma. *Magn Reson. Imaging Clin. N. Am.* 2000; **8**: 105-23.

25. Mayo JR, MacKay A, Muller NL. MR imaging of the lungs: value of short TE spin-echo pulse sequences. *AJR Am. J. Roentgenol.* 1992; **159**: 951-6.

26. Bauman G, Puderbach M, Deimling M *et al*. Non-contrast-enhanced perfusion and ventilation assessment of the human lung by means of fourier decomposition in proton MRI. *Magn Reson. Med.* 2009; **62**: 656-64.

27. Bankier AA, Storey P, Mai VM *et al*. Gravity-dependent signal gradients on MR images of the lung in supine and prone positions: a comparison with isogravitational signal variability. *J. Magn Reson. Imaging* 2006; **23**: 115-22.

28. Olsson LE, Lindahl M, Onnervik PO *et al*. Measurement of MR signal and T2* in lung to characterize a tight skin mouse model of emphysema using single-point imaging. *J. Magn Reson. Imaging* 2007; **25**: 488-94.

29. Takahashi M, Togao O, Obara M *et al*. Ultra-short echo time (UTE) MR imaging of the lung: comparison between normal and emphysematous lungs in mutant mice. *J. Magn Reson. Imaging* 2010; **32**: 326-33.

30. Togao O, Tsuji R, Ohno Y *et al*. Ultrashort echo time (UTE) MRI of the lung: Assessment of tissue density in the lung parenchyma. *Magn Reson. Med.* 2010.

31. Parraga G, Ouriadov A, Evans A *et al*. Hyperpolarized 3He ventilation defects and apparent diffusion coefficients in chronic obstructive pulmonary disease: preliminary results at 3.0 Tesla. *Invest Radiol.* 2007; **42**: 384-91.

32. Parraga G, Mathew L, Etemad-Rezai R *et al*. Hyperpolarized 3He magnetic resonance imaging of ventilation defects in healthy elderly volunteers: initial findings at 3.0 Tesla. *Acad. Radiol.* 2008; **15**: 776-85.

33. Kirby M, Mathew L, Wheatley A *et al*. Chronic obstructive pulmonary disease: longitudinal hyperpolarized (3)He MR imaging. *Radiology* 2010; **256**: 280-9.

34. Mathew L, Evans A, Ouriadov A *et al*. Hyperpolarized 3He magnetic resonance imaging of chronic obstructive pulmonary disease: reproducibility at 3.0 tesla. *Acad. Radiol.* 2008; **15**: 1298-311.

35. Global strategy for the diagnosis, management, and prevention of chronic obstructive pulmonary disease. NHLBI/WHO, 2701. 1-1-2003.
Ref Type: Report

36. Standardization of Spirometry, 1994 Update. American Thoracic Society. Am J Respir Crit Care Med 152(3), 1107-1136. 1-9-1995.
Ref Type: Magazine Article

37. Woods JC, Choong CK, Yablonskiy DA *et al*. Hyperpolarized 3He diffusion MRI and histology in pulmonary emphysema. *Magn Reson. Med.* 2006; **56**: 1293-300.

38. Boss A, Schaefer S, Martirosian P *et al*. Magnetic resonance imaging of lung tissue: influence of body positioning, breathing and oxygen inhalation on signal decay using multi-echo gradient-echo sequences. *Invest Radiol.* 2008; **43**: 433-8.

39. Adams R, Bischof L. Seeded Region Growing. *Ieee Transactions on Pattern Analysis and Machine Intelligence* 1994; **16**: 641-7.

40. Madani A, Zanen J, De M, V *et al*. Pulmonary emphysema: objective quantification at multi-detector row CT--comparison with macroscopic and microscopic morphometry. *Radiology* 2006; **238**: 1036-43.

41. Madani A, Van MA, De M, V *et al*. Pulmonary emphysema: size distribution of emphysematous spaces on multidetector CT images--comparison with macroscopic and microscopic morphometry. *Radiology* 2008; **248**: 1036-41.

42. Dirksen A, Friis M, Olesen KP *et al*. Progress of emphysema in severe alpha 1-antitrypsin deficiency as assessed by annual CT. *Acta Radiol.* 1997; **38**: 826-32.

43. Evans A, McCormack D, Ouriadov A *et al*. Anatomical distribution of 3He apparent diffusion coefficients in severe chronic obstructive pulmonary disease. *J. Magn Reson. Imaging* 2007; **26**: 1537-47.

44. Yablonskiy DA, Sukstanskii AL, Leawoods JC *et al*. Quantitative in vivo assessment of lung microstructure at the alveolar level with hyperpolarized 3He diffusion MRI. *Proc. Natl. Acad. Sci. U. S. A* 2002; **99**: 3111-6.

45. de Lange EE, Mugler JP, III, Brookeman JR *et al*. Lung air spaces: MR imaging evaluation with hyperpolarized 3He gas. *Radiology* 1999; **210**: 851-7.

46. Kauczor HU, Hofmann D, Kreitner KF *et al*. Normal and abnormal pulmonary ventilation: visualization at hyperpolarized He-3 MR imaging. *Radiology* 1996; **201**: 564-8.

47. Kauczor HU, Ebert M, Kreitner KF *et al*. Imaging of the lungs using 3He MRI: preliminary clinical experience in 18 patients with and without lung disease. *J. Magn Reson. Imaging* 1997; **7**: 538-43.

48. MacFall JR, Charles HC, Black RD *et al*. Human lung air spaces: potential for MR imaging with hyperpolarized He-3. *Radiology* 1996; **200**: 553-8.

49. Diaz S, Casselbrant I, Piitulainen E *et al*. Validity of apparent diffusion coefficient hyperpolarized 3He-MRI using MSCT and pulmonary function tests as references. *Eur. J. Radiol.* 2009; **71**: 257-63.

50. Iwasawa T, Takahashi H, Ogura T *et al*. Correlation of lung parenchymal MR signal intensity with pulmonary function tests and quantitative computed tomography (CT) evaluation: a pilot study. *J. Magn Reson. Imaging* 2007; **26**: 1530-6.

51. Togao O, Tsuji R, Ohno Y *et al*. Ultrashort echo time (UTE) MRI of the lung: Assessment of tissue density in the lung parenchyma. *Magn Reson. Med.* 2010.

52. Ebert M, Grossmann T, Heil W *et al*. Nuclear magnetic resonance imaging with hyperpolarised helium-3. *Lancet* 1996; **347**: 1297-9.

53. Mugler JP, III, Driehuys B, Brookeman JR *et al*. MR imaging and spectroscopy using hyperpolarized 129Xe gas: preliminary human results. *Magn Reson. Med.* 1997; **37**: 809-15.

54. Ohno Y, Sugimura K, Hatabu H. Clinical oxygen-enhanced magnetic resonance imaging of the lung. *Top. Magn Reson. Imaging* 2003; **14**: 237-43.

55. Woodhouse N, Wild JM, Paley MN *et al*. Combined helium-3/proton magnetic resonance imaging measurement of ventilated lung volumes in smokers compared to never-smokers. *J. Magn Reson. Imaging* 2005; **21**: 365-9.

CHAPTER 3: Computed Tomography Density Histogram Analysis to Evaluate Pulmonary Emphysema in Ex-smokers

The work presented in this chapter has been submitted to *Academic Radiology*.

Amir M. Owrangi, Roya Etemad-Rezai, David G. McCormack, Ian A. Cunningham and Grace Parraga PhD

3.1 INTRODUCTION

Pulmonary emphysema is defined as a "progressive condition of the lung characterized by abnormal and permanent enlargement of the airspaces distal to the terminal bronchioles, accompanied by the destruction of their walls, and without obvious fibrosis".[1,2] Currently, thoracic x-ray computed tomography (CT) is typically used to diagnose and evaluate the presence and extent of emphysema by exploiting the difference in x-ray attenuation of air and the lung parenchyma in Hounsfield units (HU). To facilitate computerized and automated analysis, the CT density histogram of all HU values is evaluated using a number of HU thresholds to generate the relative area of the lung occupied by attenuation values lower than specific thresholds and percentiles.[3] Although such automated threshold-based measurements correlate well with manual radiologist' emphysema scores,[4,5] pulmonary function tests (PFT)[5] and both microscopic and macroscopic measurements of emphysema,[3,6,7] there is no definitive consensus regarding an optimal HU threshold for emphysema. Other quantification techniques such as low attenuation cluster analysis (LAC) also employ HU thresholds and the validation of LAC with pathologic standards is still not completely understood.[8,9] Indeed, although single HU threshold-based techniques are the most common methods to generate automated CT measurements of emphysema, lower HU thresholds differentiate more severe emphysematous regions,[10] disregarding regions with mild tissue destruction. Conversely, higher HU thresholds identify mild emphysematous regions[11] but underestimate severe tissue destruction. Another approach involves texture feature analysis that takes into account the spatial or regional relationships between image voxels and their densities; this has been used to characterize emphysema[12-16] and centrilobular emphysema in combination with centrilobular nodularity[17] from thoracic CT images.

Thoracic CT images acquired in lung cancer screening studies[18,19] have also been used to study the relationship between emphysema and lung cancer. Lung cancer and emphysema share smoking as a risk factor with lung cancer risk models[20] having identified emphysema as a strong cancer predictor. Thus, thoracic CT acquired in lung cancer screening trials[21-23] may provide important information relevant to the study of the relationship between emphysema and airways disease with lung cancer.[24-29] Recently, the direct relationship between emphysema and lung cancer was reported using manual expert radiologist scores[24,28] but this relationship was not significant when computer-generated single threshold methods were used.[25,26,29] Although it is difficult to directly pinpoint the reason for these differences, it is possible that single threshold measurements might not take into account all the factors that a radiologist considers when scoring emphysema in thoracic CT.

The limitation of single threshold methods has motivated the current proof-of-concept study. Our objective was to explore the potential for automated evaluation of the CT density histogram using principal component analysis (PCA) to generate a principal component score based on each frequency-HU pair. We hypothesized that such a density histogram principal component score (D_HP_CS) would provide a robust, automated measurement of emphysema that takes into account all frequency-HU pairs and would yield strong correlations with an expert radiologist emphysema score.

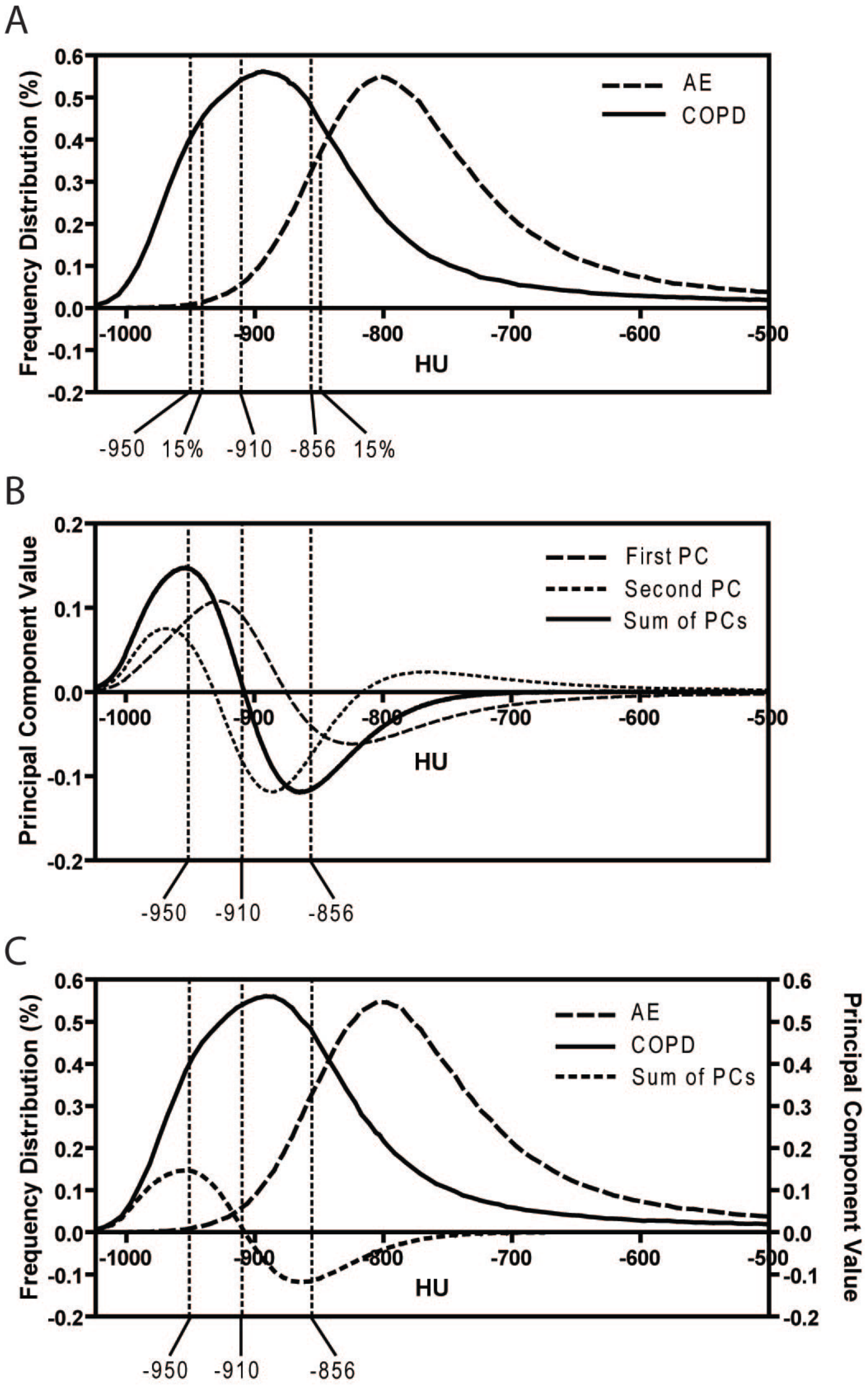

Figure 3.1: Schematic Representation of Method
A) Representative density histograms for AE (solid line) and COPD subjects (dashed lines) with thresholds (dotted lines) of -950 HU, -910 HU, -856 HU and percentile (15th) of the distribution of attenuation coefficients. B) Principal components generated by PCA with first principal component (dashed line), second principal component (dotted line) and the sum of both principal components (solid line). (C) Representative density histograms for AE (solid line) and COPD subjects (dashed lines) and the sum of both principal components (dotted line)

3.2 MATERIALS AND METHODS

3.2.1 Study Subjects

Ex-smokers were enrolled from the general population and a local tertiary health care center, as previously described[30,31] with a smoking history of at least 10 pack-years. COPD subjects were categorized according to the Global Initiative for Chronic Obstructive Lung Disease (GOLD) criteria.[32,33] All subjects provided written informed consent to the study protocol approved by the local research ethics board and Health Canada, and the study was compliant with the Personal Information Protection and Electronic Documents Act (PIPEDA).

3.2.2 Spirometry and Plethysmography

Prior to imaging, plethysmography, spirometry and measurements of the diffusing capacity of carbon monoxide (DL_{CO}) were performed according to American Thoracic Society guidelines.[34] An *ndd EasyOne spirometer* (ndd Medizintchnik AG, Zurich, CH) was used to measure the FEV_1 and FVC where the minimum of three acceptable spirometry maneuvers was accepted. Whole body plethysmography (MedGraphics Corporation, 350 Oak Grove Parkway, St. Paul, MN, USA) was also performed for the measurement of total lung capacity (TLC), inspiratory capacity (IC), residual volume (RV), and functional residual capacity (FRC). Prior to these measurements a medical history and vital signs were recorded.

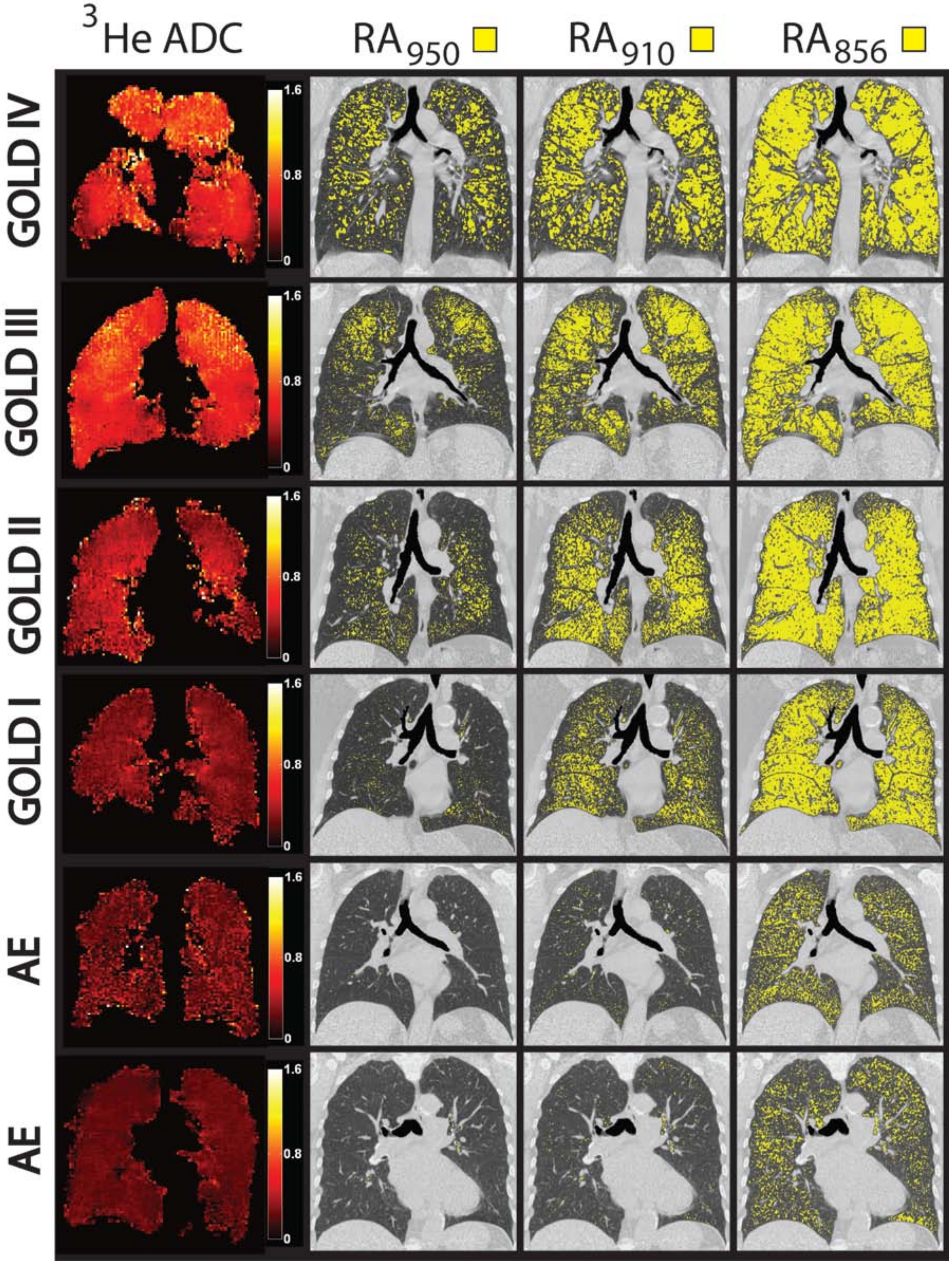

Figure 3.2: Coronal center slice ^{3}He ADC maps, CT images and Relative area (RA) Masks for HU thresholds.

Emphysema masks for -950 HU, -910 HU and -856 HU for representative AE subjects and subjects with COPD GOLD stages I, II, III and IV.

3.2.3 Image Acquisition

Thoracic CT was acquired within 30 minutes of MRI using a single spiral acquisition of the entire lung from the apex to the base with subjects in the supine position in a 64-slice Lightspeed VCT scanner (General Electric Health Care GEHC, Milwaukee, WI USA) using a detector configuration of 64×0.625 mm, 120 kVp, 100 effective mA, tube rotation time of 500 ms and a pitch of 1.0. Images were reconstructed in a slice thickness of 1.25-mm with a standard convolution kernel. To match the lung volume and tissue distention with hyperpolarized ^{3}He MRI, all images were acquired in breath-hold after inspiration of a 1L N_2 gas mixture from FRC.

Hyperpolarized ^{3}He MRI was performed using a single channel rigid elliptical transmit-receive chest coil (RAPID Biomedical, Wuerzburg, Germany) on a whole-body 3.0T system (Discovery MR750 GEHC, Milwaukee, WI USA) with broadband imaging capability, as previously described.[35] The basis frequency of the coil was 97.3 MHz, and excitation power was 3.2 kW using an RF power amplifier (AMT 3T90; GEHC Milwaukee, WI USA). Doses of hyperpolarized ^{3}He gas (5 mL per kilogram of body weight) were diluted with ultrahigh purity, medical grade nitrogen (Spectra Gases, Alpha, NJ) before administering in 1L Tedlar® bags (Tedlar; Jensen Inert Products, Coral Springs, Fla). Coronal multi-slice images were obtained for diffusion-weighted imaging using a fast gradient echo method with centric k-space sampling as previously described.[36] Two interleaved images (14-second total data acquisition; TR/TE 7.6ms/3.7ms; flip angle= 8°; FOV=40×40 cm; matrix=128 × 128; 30-mm slice thickness), with and without additional diffusion sensitization (maximum gradient amplitude = 1.94 G/cm, rise and fall time = 0.5 ms, gradient duration = 0.46 ms, diffusion time = 1.46 ms, *b* value = 1.6 s/cm^2), were acquired.

Table 3.1: Subject Demographics and Emphysema measurements

	Asymptomatic ex-smokers (AE) (n = 44)	COPD (n = 53)	Significance of difference (*p*-value)
Age y (range)	70 (8) (50-85)	71 (9) (48-87)	0.825
Males	28	37	
Pack years yr	26 (19)	48 (31)*	<0.0001
$FEV_{1\%pred}$	103 (14)	61 (23)	<0.0001
FEV_1/FVC	0.81 (0.06)	0.49 (0.13)	<0.0001
$IC_{\%pred}$	109 (21)	87 (25)	<0.0001
$RV_{\%pred}$	101 (26)	154 (41)	<0.0001
$FRC_{\%pred}$	95 (19)	138 (31)	<0.0001
$TLC_{\%pred}$	99 (19)	116 (15)	<0.0001
$DL_{CO\%pred}$**	76 (18)	51 (18)	<0.0001
D_HP_CS	-4.32 (0.75)	-0.61 (2.68)	<0.0001
Emphysema score***	0.08 (0.15)	1.13 (0.79)	<0.0001
RA_{950} (%)	1.45 (1.09)	12.56 (10.26)	<0.0001
RA_{910} (%)	9.80 (6.26)	34.19 (15.37)	<0.0001
RA_{856} (%)	39.00 (14.60)	64.24 (13.47)	<0.0001
$HU_{15\%}$	-893 (19)	939 (26)	<0.0001
^{3}He ADC#	0.27 (0.03)	0.43 (0.12)	<0.0001

FEV_1: forced expiratory volume in 1 second; FVC: forced vital capacity; IC: inspiratory capacity; RV: residual volume; FRC: functional residual capacity; TLC: total lung capacity; DL_{CO}: Diffusing capacity of lung for carbon monoxide; D_HP_CS: density histogram principal component score; Emphysema score: Subjective scoring of emphysema by an expert chest radiologist; RA_{950}(%): relative area of the lung with attenuation values below −950 HU; RA_{910}(%): relative area of the lung with attenuation values below −910 HU; RA_{856}(%): relative area of the lung with attenuation values below −856 HU; HU_{15}: 15th percentile of the frequency distribution histogram in HU. 3He ADC: 3He apparent diffusion coefficient. Data are presented as mean (± standard deviation). *n = 47 COPD; **n = 43 AE, n = 52 COPD; *** n = 43 AE, n= 50 COPD; # n = 41 AE, n = 52 COPD

3.2.4 Density Histogram Principal Component Analysis Score (D_HP_CS)

All images were transferred to a remote workstation for post-processing and image analysis. For CT image analysis, the Pulmonary Workstation 2.0 (VIDA Diagnostics Inc., Iowa City, IA) was used to quantify tissue attenuation in HU on a voxel by voxel basis. The software automatically determined the boundaries of each lung and generated a histogram of HU values. All histograms were imported into MATLAB (MATLAB version R2010b; The MathWorks Inc., Cambridge, MA, USA). A cutoff threshold of -500 HU was applied and voxel values ranging from−1024 HU to −500 HU were used to generate the emphysema score for each subject. Principal component analysis (PCA) was performed on the relative area (RA) under the histogram curve for each HU value resulting in 525 RA input variables for each subject. PCA generated new variables, called ‘principal components’ based on the variation between input variables.[37] The first two principal components (PC) that have the highest eigenvalues were selected. As previously described[38] the ‘component scores’ can be calculated by the summation of the principal components, where in this case we summed the first two principal components. Each input variable (RA_i) was associated with new principal components, and the final score for each subject was then calculated by the sum of the products of all input variable (RA_i), and their principal component or component scores, PC_i, as:

$$D_H P_C S = \sum_{i=-1024}^{-500} RA_i PC_i \tag{1}$$

where RA is relative area under the histogram curve for each HU value and PC is principal component calculated from PCA analysis. The leave-one-out method[16] was performed and all histograms except one were used as the training data for the calculation of principal components with the excluded histogram used as the test data; the process was repeated for all subject histograms.

Figure 3.1B shows the first (PC_1), second (PC_2) and the sum ($D_H P_C$) of the first two principal components calculated for 525 bins of RA_i ranging from -1024 HU to -500 HU.

The value of each principal component on this curve shows the size and direction of variation between histograms for all subjects at each HU value; the higher the variation, the larger the principal component value. Whole lung D_HP_C score was calculated as the sum (D_HP_C) of the first two principal components. We note in Figure 3.1C, D_HP_C is shown relative to the density histograms of all AE and COPD subjects in this study. The points of inflection for D_HP_C were -953HU for the maximum principal component value and -865HU for the minimum principal component value, crossing the x-axis at -908HU. In addition to determining the whole lung D_HP_C score, the lung was divided into three regions of interest (ROI, superior, medial, inferior) by dividing the centre coronal slice into three ROI from superior to inferior and applying these boundaries to all slices.

3.2.5 CT Density Histogram Thresh-hold Measurements

All images were transferred to a remote workstation for post-processing and image analysis. The Pulmonary Workstation 2.0 (VIDA Diagnostics Inc., Iowa City, IA) was used to quantify tissue attenuation in HU on a voxel by voxel basis. The software automatically determined the boundaries of each lung and generated a histogram of HU values. As shown in Figure 3.1A, four different thresholds were applied to each density histogram and the relative area (RA) of the lung was calculated for attenuation values below −950 HU (RA_{950}), −910 HU (RA_{910}), −856 HU (RA_{856})[6,7,9-11] as was the 15th percentile of the frequency distribution histogram in HU ($HU_{15\%}$).[39]

3.2.6 Expert Observer Emphysema Quantification

A standard window width of 1500 and level of -600 HU was used by a single expert observer (RER) -a thoracic CT radiologist who was blinded to subject identity, disease status as well as all other subject measurements. The emphysema score that the expert employed was semi-automated and adapted from Bankier et al.[4] with assessments performed from superior to inferior axial views, starting with the first slice containing both left and right lungs and continuing to the slice above the diaphragm. Each CT slice was viewed and scored individually, and left and right lungs were scored separately. The emphysema score was based on the relative area displaying low attenuation and tissue destruction. A score of 0 was assigned if there was no emphysema present. The presence of emphysema for each CT slice was scored according to Bankier[4] as follows: 1 = 1–25%, 2 = 26–50%, 3 = 51–75%, and 4 = >75%. The maximum possible score for each lung was 4 and a final score was calculated as percentage of the maximum possible score as:

$$Emphysema\ Score = 4 \times \frac{\sum_{i=1}^{n}(ES_L + ES_R)}{n \times 8} \tag{2}$$

where ES_L and ES_R are the left and right lung emphysema scores in each of n slices.

3.2.7 Statistical Analysis

Mean measurements and standard deviations of the emphysema scores were generated for both subgroups. Multivariate analysis of variance (MANOVA) and one-way analysis of variance (ANOVA) were performed using PASW Statistics version 20 (PASW Inc., Chicago, IL, 2009). GraphPad Prism 4.01 (GraphPad Software Inc., La Jolla, CA, 2004) was used to perform linear regressions and for the generation of Pearson correlation coefficients. A Holm-Bonferroni correction[40] was used for all correlations. Receiver operating characteristic (ROC) analyses were used to characterize the performance of D_HP_CS, expert emphysema score, RA_{950} and ^{3}He ADC as predictors of COPD using $FEV_1/FVC<70\%$ as the diagnostic threshold. Correlation coefficients were compared[41] by calculating the Fisher *z'* transformation for each *r* value. In all statistical analyses, results were considered significant when the probability of making a type I error was less than 5% ($p < 0.05$).

3.3 RESULTS

Demographic characteristics are provided in Table 3.1 for 97 ex-smokers including 44 AE subjects (n = 28 males, mean age = 70 [±8], range = 50–85) and 53 subjects with COPD (n = 37 males, mean age = 71 [±9], range = 48–87). Spirometry and plethysmography measurements acquired a few minutes before imaging are also shown and reflect the inclusion criteria for COPD and AE subjects. COPD ex-smokers included 11 subjects with Global initiative for chronic Obstructive Lung Disease (GOLD) stage I COPD, 25 subjects with stage II COPD, 13 subjects with stage III COPD and 4 subjects with stage IV COPD.

Table 3.2: Pearson correlation coefficients

	D_HP_CS	PC_1	PC_2
Emphysema Score	0.87	0.69	0.51
RA_{950}	0.93	0.74	0.63
RA_{910}	0.96	0.95	0.35
RA_{856}	0.76	0.98	NS
$HU_{15\%}$	-0.87	-0.92	-0.22
^{3}He ADC	0.85	0.68	0.54
FEV_1/FVC	-0.85	-0.82	-0.33
$DL_{CO\%pred}$	-0.67	-0.59	-0.34

* All correlations $p<0.05$; PC_1: D_HP_C emphysema scores using the first principal component, PC_2: D_HP_C emphysema scores using the second principal component, D_HP_CS: D_HP_C emphysema scores based on the summation of both first and second principal components; NS: Not significant.

In Figure 3.2, center coronal slice ^{3}He ADC maps and CT images with a colour mask (in yellow) showing the relative area of lung with HU values below -950 HU, -910 HU and -856 HU are demonstrated for two representative AE subjects and four representative

COPD ex-smokers. Generally, from top to bottom, as the stage of the disease declined, the yellow threshold mask was also diminished. For the higher threshold, (i.e. -856 HU), COPD coronal CT was nearly completed saturated with the yellow threshold mask and for AE subjects there was partial saturation of the yellow mask. For the lower thresholds (i.e. -910 and -950 HU), lung CT images of COPD subjects were less saturated than at the higher threshold, and for AE subjects even less saturated by the yellow mask, allowing for differences between subjects to be more visibly obvious.

In Figure 3.3 box-and-whisker plots for mean D_HP_CS and ROC curves are provided. As shown there was a significant difference ($p < 0.0001$) for whole lung D_HP_CS (Figure 3.3A) and regional D_HP_CS (Figure 3.3B) between COPD and AE subjects. For both COPD and AE subjects, D_HP_CS for the superior lung region was significantly greater than for the inferior ($p < 0.0001$) and medial lung ($p < 0.0001$). ROC curves for whole lung D_HP_CS, expert emphysema score, RA_{950} and ^{3}He ADC as predictors of COPD ($FEV_1/FVC<70\%$) are shown in Figure 3.3C. The areas under the curve (AUC) were 0.91 (D_HP_CS), 0.94 (expert observer emphysema score), 0.91 (RA_{950}) and 0.93 (^{3}He ADC).

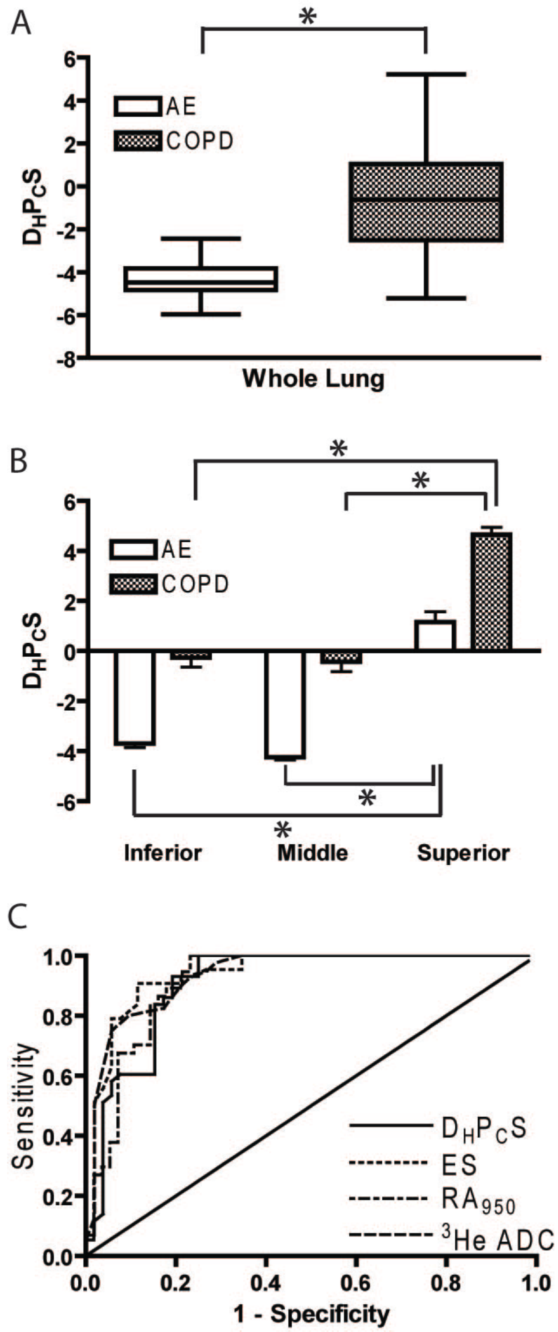

Figure 3.3: Whole lung and regional D_HP_CS for AE and COPD subjects

A) Whole lung box-and-whisker plot of D_HP_CS for AE and COPD subjects showing the 25th to 75th percentile range in the boxes, bars show the range and median value represented by the solid line.

B) Box-and-whisker plots for D_HP_CS for superior, medial and inferior lung regions of interest.

C) ROC curve for D_HP_CS, expert emphysema score (ES), RA_{950}(%) and ^{3}He ADC as predictors of COPD. The areas under the curve were 0.91 (D_HP_CS), 0.94 (expert emphysema score), 0.91 (RA_{950}(%)) and 0.93 (^{3}He ADC).

Figure 3.4 and Table 3.2 shows the significant relationships between D_HP_CS and FEV_1/FVC, $DL_{CO(\%pred)}$, ^3He ADC, expert emphysema score, RA_{950}, RA_{910}, RA_{856} and $HU_{15\%}$. There were significant correlations between whole lung D_HP_CS with emphysema score ($r = 0.87$, $p < 0.0001$), RA_{950} ($r = 0.93$, $p < 0.0001$), RA_{910}, ($r = 0.96$, $p < 0.0001$), RA_{856}, ($r = 0.76$, $p < 0.0001$), $HU_{15\%}$, ($r = -0.87$, $p < 0.0001$), ^3He ADC ($r = 0.85$, $p < 0.0001$), FEV_1/FVC ($r = -0.85$, $p < 0.0001$) and $DL_{CO(\%pred)}$ ($r = -0.67$, $p < 0.0001$).

Table 3.3 shows the comparison of Pearson correlation coefficients between D_HP_CS and all significant correlates using Fisher's z transformation; the relationship between D_HP_CS and RA_{950} and RA_{910} was significantly stronger than the relationship between D_HP_CS and other emphysema measures.

3.4 DISCUSSION

Until very recently, automated methods for the quantification of emphysema have been based on single HU thresholds of the CT density histogram. To address some of the limitations of this robust and straightforward approach, more complex and texture-based methods have been devised and applied to a number of pulmonary conditions.[12-17] This important previous work has broadened our understanding of the information content within thoracic CT, but there is still no consensus about the type of classifier or approach that is optimal for lung parenchyma characterization. Other studies have used PCA to determine the correlation between the regional (superior-inferior) distribution of emphysema and pulmonary function tests[42] and as well to classify COPD subjects based on non-imaging measurements including spirometry, demographic data, degree of dyspnea and frequency of exacerbation.[43] This important previous work provides a framework for the PCA method developed and applied here to 97 ex-smokers. In this proof-of concept study we explored the potential for PCA evaluation of the CT density histogram and made a number of observations in ex-smokers with and without spirometry evidence of COPD as follows: 1) a significant difference was observed between AE and COPD subjects for whole lung D_HP_CS, with superior-inferior regional differences in D_HP_CS typical of smoking-related emphysema, 2) ROC analysis for D_HP_CS showed an AUC classification rate of 91% , which was similar to the expert observer, and, 3) significant and strong correlations were observed for D_HP_CS, an expert observer emphysema score, ^{3}He ADC, FEV_1/FVC, $DL_{CO\%pred}$, RA_{910}, RA_{950}, and RA_{856}.

As might be expected, there was a significant difference between AE and COPD subjects for whole lung D_HP_CS and superior-inferior regional differences in D_HP_CS that were typical of emphysema gradients observed in ex-smokers with significant smoking history. All subjects recruited for this study had a smoking history of > 10 pack years -a risk factor for centrilobular emphysema, which dominates in the superior lung zones.[44] Not surprisingly, in both subject groups, the superior lung regions had a significantly greater D_HP_CS. ROC analysis estimated a classification rate of 91% for D_HP_CS, which was similar to the expert observer's classification rate and also for RA_{950} and hyperpolarized ^{3}He ADC – a sensitive measurement of early emphysema.[45] It is important to note that the mean emphysema scores for this study were low, which is in agreement with the fact that nearly half of the subjects evaluated did not meet the GOLD criteria for COPD. In view of this fact, the rather high classification rate must be considered a conservative estimate of results in more severe disease. In this regard, we think it's important to test new approaches in early/asymptomatic disease as well as more severe disease that has already progressed to later stages.

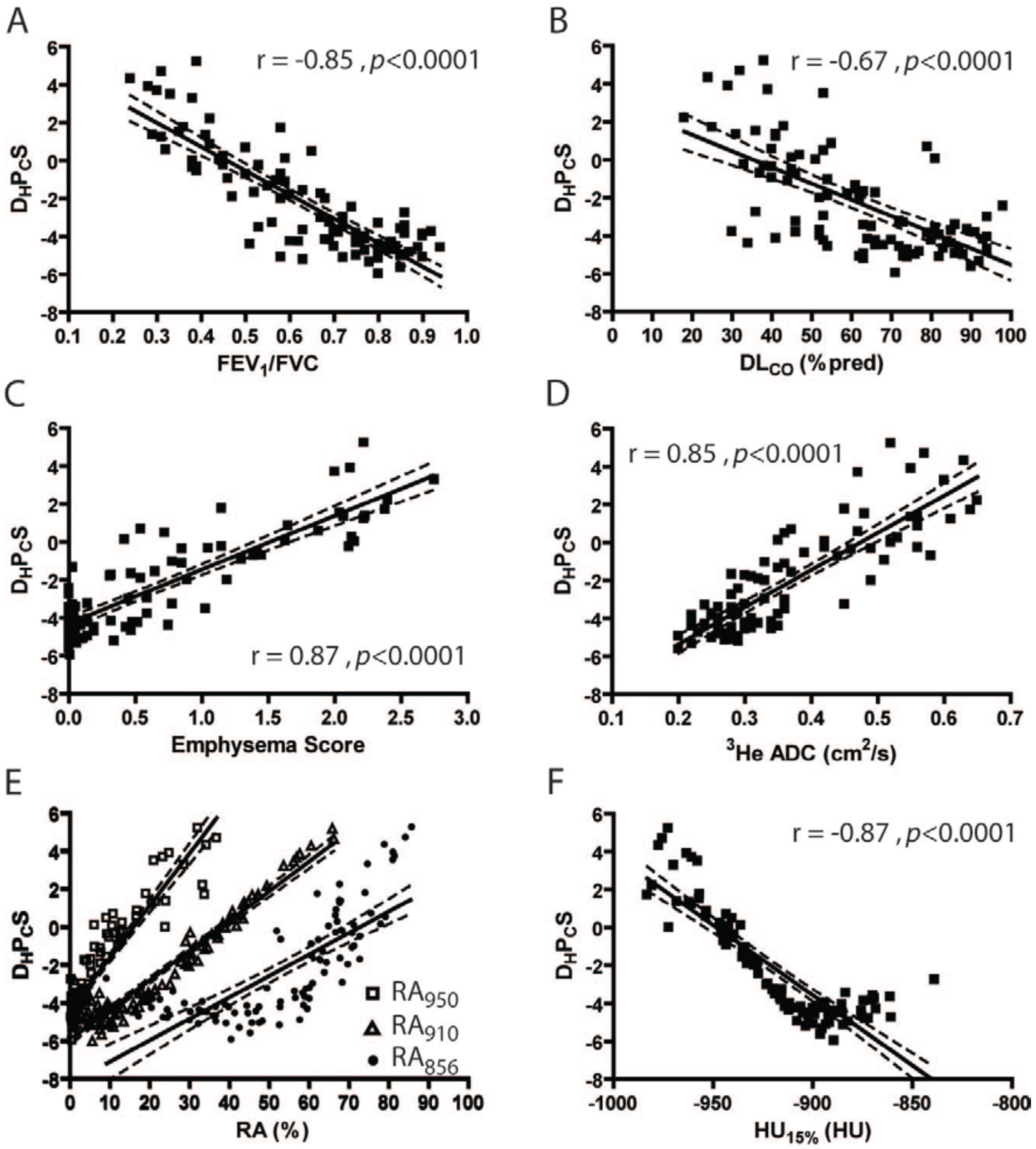

Figure 3.4: Significant Correlations for whole lung D_HP_CS and emphysema measurements

Linear Regressions for A) FEV_1/FVC (r = -0.85, p < 0.0001), B) DL_{CO}% (r = -0.67, p < 0.0001), C) emphysema score (r = 0.87, p < 0.0001), D) ^{3}He ADC (r = 0.85, p < 0.0001), E) RA_{950} (r = 0.93, p < 0.0001), RA_{910} (r = 0.96, p < 0.0001), RA_{856} (r = 0.76, p < 0.0001), F) $HU_{15\%}$ (r = -0.87, p < 0.0001). The 95% confidence intervals are shown as dotted lines.

Finally, significant and strong correlations were observed for D_HP_CS, with the expert observer emphysema score, ^{3}He ADC, FEV_1/FVC, $DL_{CO\%pred}$, RA_{910}, RA_{950}, and RA_{856}. D_HP_CS showed stronger correlations with RA_{950} and RA_{910} as compared to RA_{856}, and this is in agreement with previous findings.[3,6,7] As shown in Figure 3.1, when the histograms for all subjects are evaluated, the major inflection points for the sum of the first and second principal components (D_HP_C) were very close to the emphysema estimates previously determined and evaluated.[6,7,9-11] This intriguing result certainly raises the question as to why these inflection points at -953HU, -908HU, and, -865HU are so close to emphysema thresholds (-950HU, -910HU, -856HU) that were empirically determined.

Table 3.3: Significant differences between Pearson correlation (PC) coefficients for DHPCS and other emphysema measurements

D_HP_CS PC	**RA_{950}**	**RA_{910}**	**RA_{856}**	**$HU_{15\%}$**	**^{3}He ADC**	**FEV_1/FVC**	**$DL_{CO\%pred}$**
Emphysema Score	0.31	0.0005	0.27	1	1	1	0.006
RA_{950}		0.54	0.0001	0.33	0.09	0.09	<0.0001
RA_{910}			<0.0001	0.0006	<0.0001	<0.0001	<0.0001
RA_{856}				0.29	0.75	0.67	1
$HU_{15\%}$					1	1	0.006
^{3}He ADC						1	0.04
FEV_1/FVC							0.04

Pearson correlation (PC) coefficients for the relationship between D_HP_CS and other emphysema measures were compared using Fisher's z transformation; *p*-values after Holm Bonferoni correction

We must acknowledge a number of study shortcomings that limit application of our approach to other CT studies of emphysema. First, and foremost, the majority of subjects in this study showed mild or very modest emphysema and a significant fraction did not fulfil the GOLD criteria for COPD. Thus, our findings may not be generalized to subjects with more severe disease. However, we also think that this work provides an important first step in expanding our repertoire of automated tools for the evaluation of emphysema. It is also important to note that although there is considerable evidence to support the use of quantitative CT to emphysema,[3,46,47] we did not compare D_HP_CS with the gold standard – pulmonary histology and this would have provided a clear and definitive comparison. We also must point out that in order provide a way to compare our results to MRI, we acquired CT and MRI at the same inhalation volume (ie. FRC + 1 litre of inhaled gas) and not full inspiration; unlike most CT studies of emphysema, in the current evaluation we acquired CT relative to FRC and not TLC. For example, for AE subjects, mean FRC was 3.14 ±0.70L and for COPD subjects mean FRC was 4.55 ±1.04L. Although these are non-standard CT acquisition volumes, this certainly allowed us to directly compare MRI and CT measurements of emphysema. Finally, this study was performed at a single centre, on a single 64-slice scanner which likely helped to diminish scanner issues as compared to recent evaluations in larger multi-centre studies such as the COPDgene study.[17,48] It is yet to be determined how the new approach and measurements described here can be used in larger studies across different scanners and reconstruction protocols. However, we expect that compared to single threshold measurements that are certainly sensitive to variations in scanner calibrations and scanner manufacturer settings, D_HP_CS is likely more robust because it is derived across a wide range of the frequency distribution of HU.

In conclusion, in this proof-of-concept study, we explored the utility of a new automated estimate of pulmonary emphysema that was generated by applying PCA to the CT density histogram. The strength of this approach relates to the fact that a broad frequency distribution of pixel intensities across wide range of HU values was evaluated to generate a single score. The D_HP_CS measurement showed strong and significant correlations with pulmonary function tests, ^{3}He ADC and expert radiologist emphysema scores as well as a 91% classification rate with the all the inherent advantages of an automated measurement.

3.5 References

Reference List

1. Snider GL, Kleinerman J, Thurlbeck WM *et al*. The definition of emphysema. Report of a National Heart, Lung and Blood Institute, Division of Lung Diseases Workshop. *Am. Rev. Respir. Dis.* 1985; **132**: 182-5.

2. Thurlbeck WM, Muller NL. Emphysema: definition, imaging, and quantification. *AJR Am. J. Roentgenol.* 1994; **163**: 1017-25.

3. Madani A, Zanen J, De M, V *et al*. Pulmonary emphysema: objective quantification at multi-detector row CT--comparison with macroscopic and microscopic morphometry. *Radiology* 2006; **238**: 1036-43.

4. Bankier AA, De M, V, Keyzer C *et al*. Pulmonary emphysema: subjective visual grading versus objective quantification with macroscopic morphometry and thin-section CT densitometry. *Radiology* 1999; **211**: 851-8.

5. Park KJ, Bergin CJ, Clausen JL. Quantitation of emphysema with three-dimensional CT densitometry: comparison with two-dimensional analysis, visual emphysema scores, and pulmonary function test results. *Radiology* 1999; **211**: 541-7.

6. Gevenois PA, De M, V, De VP *et al*. Comparison of computed density and macroscopic morphometry in pulmonary emphysema. *Am. J. Respir. Crit Care Med.* 1995; **152**: 653-7.

7. Gevenois PA, De VP, De M, V *et al*. Comparison of computed density and microscopic morphometry in pulmonary emphysema. *Am. J. Respir. Crit Care Med.* 1996; **154**: 187-92.

8. Madani A, Van MA, De M, V *et al*. Pulmonary emphysema: size distribution of emphysematous spaces on multidetector CT images--comparison with macroscopic and microscopic morphometry. *Radiology* 2008; **248**: 1036-41.

9. Yuan R, Nagao T, Pare PD *et al*. Quantification of lung surface area using computed tomography. *Respir. Res.* 2010; **11**: 153.

10. Muller NL, Staples CA, Miller RR *et al*. "Density mask". An objective method to quantitate emphysema using computed tomography. *Chest* 1988; **94**: 782-7.

11. Coxson HO, Rogers RM, Whittall KP *et al*. A quantification of the lung surface area in emphysema using computed tomography. *Am. J. Respir. Crit Care Med.* 1999; **159**: 851-6.

12. Park YS, Seo JB, Kim N *et al*. Texture-based quantification of pulmonary emphysema on high-resolution computed tomography: comparison with density-based quantification and correlation with pulmonary function test. *Invest Radiol.* 2008; **43**: 395-402.

13. Prasad M, Sowmya A. Multi-level classification of emphysema in HRCT lung images using delegated classifiers. *Med. Image Comput. Comput. Assist. Interv.* 2008; **11**: 59-66.

14. Sorensen L, Shaker SB, de BM. Quantitative analysis of pulmonary emphysema using local binary patterns. *IEEE Trans. Med. Imaging* 2010; **29**: 559-69.

15. Uppaluri R, Mitsa T, Sonka M *et al*. Quantification of pulmonary emphysema from lung computed tomography images. *Am. J. Respir. Crit Care Med.* 1997; **156**: 248-54.

16. Xu Y, Sonka M, McLennan G *et al*. MDCT-based 3-D texture classification of emphysema and early smoking related lung pathologies. *IEEE Trans. Med. Imaging* 2006; **25**: 464-75.

17. Ginsburg SB, Lynch DA, Bowler RP *et al*. Automated Texture-based Quantification of Centrilobular Nodularity and Centrilobular Emphysema in Chest CT Images. *Acad. Radiol.* 2012; **19**: 1241-51.

18. Swensen SJ, Jett JR, Hartman TE *et al*. CT screening for lung cancer: five-year prospective experience. *Radiology* 2005; **235**: 259-65.

19. Wilson DO, Weissfeld JL, Fuhrman CR *et al*. The Pittsburgh Lung Screening Study (PLuSS): outcomes within 3 years of a first computed tomography scan. *Am. J. Respir. Crit Care Med.* 2008; **178**: 956-61.

20. Spitz MR, Hong WK, Amos CI *et al*. A risk model for prediction of lung cancer. *J. Natl. Cancer Inst.* 2007; **99**: 715-26.

21. Church TR. Chest radiography as the comparison for spiral CT in the National Lung Screening Trial. *Acad. Radiol.* 2003; **10**: 713-5.

22. Henschke CI, McCauley DI, Yankelevitz DF *et al*. Early Lung Cancer Action Project: overall design and findings from baseline screening. *Lancet* 1999; **354**: 99-105.

23. Sone S, Takashima S, Li F *et al*. Mass screening for lung cancer with mobile spiral computed tomography scanner. *Lancet* 1998; **351**: 1242-5.

24. de Torres JP, Bastarrika G, Wisnivesky JP *et al*. Assessing the relationship between lung cancer risk and emphysema detected on low-dose CT of the chest. *Chest* 2007; **132**: 1932-8.

25. Kishi K, Gurney JW, Schroeder DR *et al*. The correlation of emphysema or airway obstruction with the risk of lung cancer: a matched case-controlled study. *Eur. Respir. J.* 2002; **19**: 1093-8.

26. Maldonado F, Bartholmai BJ, Swensen SJ *et al*. Are airflow obstruction and radiographic evidence of emphysema risk factors for lung cancer? A nested case-control study using quantitative emphysema analysis. *Chest* 2010; **138**: 1295-302.

27. Smith BM. Quantitative computed tomography analysis of emphysema and lung cancer risk. *J. Thorac. Oncol.* 2011; **6**: 1965-6.

28. Wilson DO, Weissfeld JL, Balkan A *et al*. Association of radiographic emphysema and airflow obstruction with lung cancer. *Am. J. Respir. Crit Care Med.* 2008; **178**: 738-44.

29. Wilson DO, Leader JK, Fuhrman CR *et al*. Quantitative computed tomography analysis, airflow obstruction, and lung cancer in the pittsburgh lung screening study. *J. Thorac. Oncol.* 2011; **6**: 1200-5.

30. Kirby M, Mathew L, Wheatley A *et al*. Chronic obstructive pulmonary disease: longitudinal hyperpolarized (3)He MR imaging. *Radiology* 2010; **256**: 280-9.

31. Mathew L, Evans A, Ouriadov A *et al*. Hyperpolarized 3He magnetic resonance imaging of chronic obstructive pulmonary disease: reproducibility at 3.0 tesla. *Acad. Radiol.* 2008; **15**: 1298-311.

32. Global strategy for the diagnosis, management, and prevention of chronic obstructive pulmonary disease. NHLBI/WHO, 2701. 1-1-2003.
Ref Type: Report

33. Redelmeier DA, Bayoumi AM, Goldstein RS *et al*. Interpreting small differences in functional status: the Six Minute Walk test in chronic lung disease patients. *Am. J. Respir. Crit Care Med.* 1997; **155**: 1278-82.

34. Standardization of Spirometry, 1994 Update. American Thoracic Society. *Am J Respir Crit Care Med* 1995; **152**: 1107-36.

35. Parraga G, Ouriadov A, Evans A *et al*. Hyperpolarized 3He ventilation defects and apparent diffusion coefficients in chronic obstructive pulmonary disease: preliminary results at 3.0 Tesla. *Invest Radiol.* 2007; **42**: 384-91.

36. Parraga G, Mathew L, Etemad-Rezai R *et al*. Hyperpolarized 3He magnetic resonance imaging of ventilation defects in healthy elderly volunteers: initial findings at 3.0 Tesla. *Acad. Radiol.* 2008; **15**: 776-85.

37. Quinn GP, Keough MJ. Principal Components and Correspondence Analysis. *Experimental Design and Data Analysis for Biologists*. Cambridge University Press, 2002; 541-572.

38. DiStefano C, Zhu M, Mindrila D. Understanding and Using Factor Scores: Considerations for the Applied Researcher. *Practical Assessment Research & Evaluation* 2009; **14**: 1-11.

39. Dirksen A, Dijkman JH, Madsen F *et al*. A randomized clinical trial of alpha(1)-antitrypsin augmentation therapy. *Am. J. Respir. Crit Care Med.* 1999; **160**: 1468-72.

40. Van Bell G, Fisher L, Heagerty P, Lumley T. *Multiple comparisons in biostatistics: a methodology for the health sciences*.Wiley-Interscience, Seattle, Wash, 2004.

41. Comrey AL, Lee HB. Confidence intervals for means and tests on correlations. *Elementary Statistics: A Problem Solving Approach*. Lulu, Morrisville, NC, 2009; 103-112.

42. Mohamed Hoesein FA, van RE, van GB *et al*. Computed tomography-quantified emphysema distribution is associated with lung function decline. *Eur. Respir. J.* 2012; **40**: 844-50.

43. Burgel PR, Paillasseur JL, Caillaud D *et al*. Clinical COPD phenotypes: a novel approach using principal component and cluster analyses. *Eur. Respir. J.* 2010; **36**: 531-9.

44. Anderson AE, Jr., Foraker AG. Centrilobular emphysema and panlobular emphysema: two different diseases. *Thorax* 1973; **28**: 547-50.

45. Fain SB, Panth SR, Evans MD *et al*. Early emphysematous changes in asymptomatic smokers: detection with 3He MR imaging. *Radiology* 2006; **239**: 875-83.

46. Cavigli E, Camiciottoli G, Diciotti S *et al*. Whole-lung densitometry versus visual assessment of emphysema. *Eur. Radiol.* 2009; **19**: 1686-92.

47. Gietema HA, Muller NL, Fauerbach PV *et al*. Quantifying the extent of emphysema: factors associated with radiologists' estimations and quantitative indices of emphysema severity using the ECLIPSE cohort. *Acad. Radiol.* 2011; **18**: 661-71.

48. Regan EA, Hokanson JE, Murphy JR *et al*. Genetic epidemiology of COPD (COPDGene) study design. *COPD.* 2010; **7**: 32-43.

CHAPTER 4: Semi-automated Scoring of Pulmonary Emphysema from x-ray CT: Trainee Reproducibility and Accuracy

The work presented in this chapter is in preparation for submission to *Academic Radiology.*

Amir M. Owrangi, Brandon Entwistle, Andrew Lu, Jack Chiu, Nabil Hussain, Roya Etemad-Rezai and Grace Parraga

4.1 INTRODUCTION

Concomitant with airway abnormalities and other morphological consequences of chronic pulmonary inflammation, the lungs of smokers and many ex-smokers also typically show evidence of emphysema, defined as lung tissue destruction resulting in reduced gas exchange in the respiratory system[1,2] -a major component of chronic obstructive pulmonary disease (COPD).[3] Early detection of pulmonary emphysema in at-risk patients, even in the absence of symptoms, remains a diagnostic challenge but may help prevent obstructive ventilatory impairment later in life.[4]

Although magnetic resonance imaging (MRI) and nuclear medicine methods can be used to quantify the extent of pulmonary emphysema,[5-8] thoracic x-ray computed tomography (CT) is the imaging modality of choice for clinical detection and for research studies that aim to monitor emphysema longitudinally,[9,10] mainly because of short acquisition times, high spatial resolution and the rich tissue information content based on the differential attenuation of x-ray in the lung tissue and airspaces. In this regard, pulmonary emphysema is characterized by low x-ray attenuation related to tissue destruction in emphysematous regions, although these findings are usually not evaluated in asymptomatic subjects and often remain un-diagnosed until symptoms arise and disease is already well-advanced.[11] Visual evaluation of emphysema is routinely used in daily practice, alone or in combination with more quantitative evaluation of the CT density histogram[12-19] and allows emphysema to be distinguished from image noise and hyper-inflated regions related to “gas-trapping” caused by small airways disease.[20] Automated methods for the evaluation of CT evidence of emphysema are mainly related to straightforward single thresholds of the CT density histogram such as the relative area of the density histogram at -950 Hounsfield units (HU), -910HU, -856HU, and the 15th percentile ($HU_{15\%}$).[21-26] More complex textural approaches including the evaluation of low attenuation clusters[20,27,28] and texture classifiers[29-34] have also been employed as a way to better mimic visual scoring approaches.

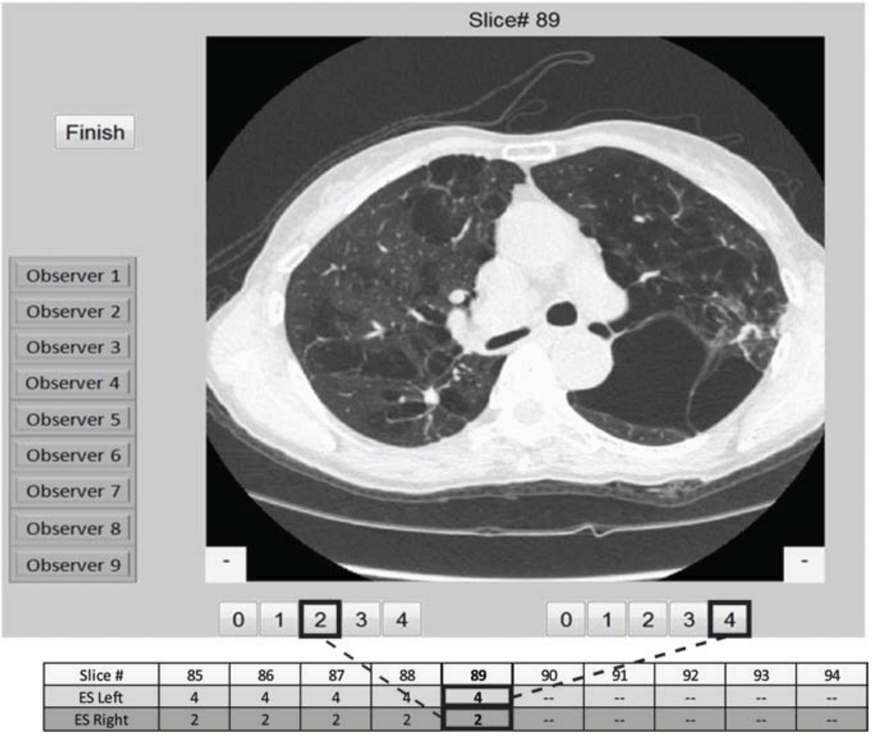

Slice #	85	86	87	88	89	90	91	92	93	94
ES Left	4	4	4	4	4	--	--	--	--	--
ES Right	2	2	2	2	2	--	--	--	--	--

Figure 4.1. CT emphysema scoring Graphic User Interface.
Selected axial slice of the thorax with scoring system located below the image. Each observer provided a score from 0 to 4 for each lung on each slice and as each observer clicked the selected score, a score matrix was automatically generated.

The main limitations of visual scoring methods are the high subjectivity and variability that result in low inter-observer reproducibility.[14,18,35] These shortcomings have recently been underscored in the COPDGene study with the analysis of thoracic CT by 58 expert observers (33 respirologists and 25 chest radiologists).[36] Poor kappa values in COPDGene[36] suggested that both the detection and quantification of centrilobular emphysema were significantly limited by the subjectivity of the expert readers that resulted in low inter-observer reproducibility. We think that user-friendly, interactive scoring methods can be developed to simplify and accelerate emphysema scoring training; there is the potential as well to use such a tool to evaluate the inter-observer reproducibility of experts thereby reducing inter-observer variability in clinical practice and in multi-center clinical trial evaluations. Towards this goal, we describe the use of a radiological viewing interface dedicated to emphysema scoring of thoracic CT. This graphic user interface (GUI) provides a way for multiple readers to evaluate the same randomized CT scans on multiple occasions to facilitate comparisons and measurements of inter- and intra-observer reproducibility and comparisons to an expert chest radiologist. Here we describe this visualization and scoring tool and its use in six trainees with little or no experience and compare their emphysema scores with a single experienced thoracic radiologist and with well-established measurements of pulmonary emphysema.

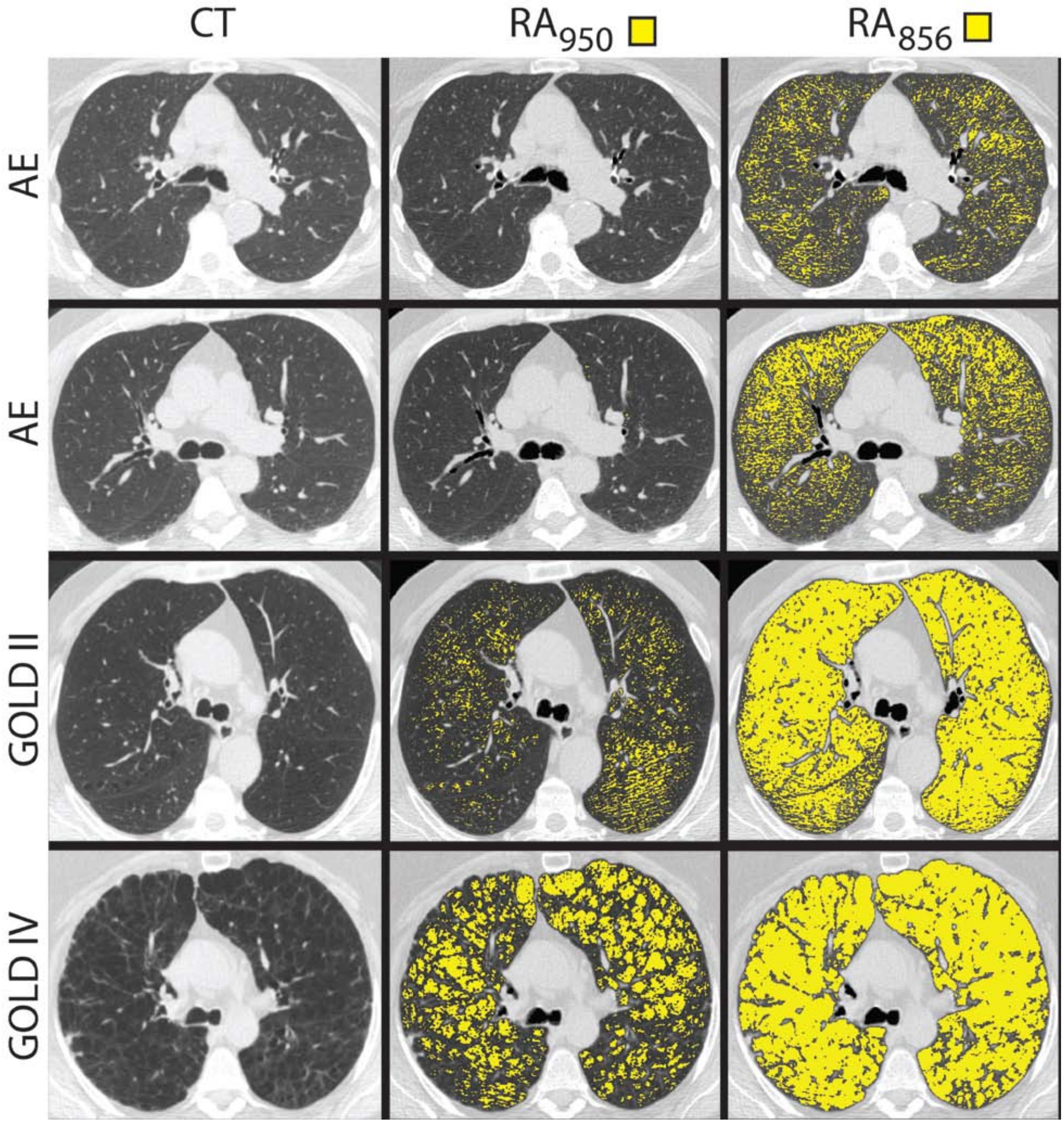

Figure 4.2. Axial center slice CT images for Representative AE and GOLD stage II and IV COPD subjects.

Center slice CT images of lung in axial view are shown in left panel and emphysema masks for -950 HU and -856 HU are shown in yellow in middle panel and right panel respectively.

4.2 METHODS

4.2.1 Study Subjects

Ex-smokers were enrolled from the general population and a local tertiary health care center, as previously described[37,38] with a smoking history of at least 10 pack years. COPD subjects were categorized according to Global Initiative for Chronic Obstructive Lung Disease (GOLD) criteria.[3] All subjects provided written informed consent to the study protocol approved by the local research ethics board and Health Canada, and the study was compliant with the Personal Information Protection and Electronic Documents Act (PIPEDA).

4.2.2 Spirometry and Plethysmography

A medical history and vital signs were recorded and then subjects completed plethysmography, spirometry and measurements of the diffusing capacity of carbon monoxide (DL_{CO}) according to American Thoracic Society guidelines.[39] Briefly, spirometry was performed using an *ndd EasyOne spirometer* (ndd Medizintchnik AG, Zurich, CH) reporting FEV_1 and FVC and a minimum of three acceptable spirometry maneuvers were performed. Whole body plethysmography (MedGraphics Corporation, 350 Oak Grove Parkway, St. Paul, MN, USA) was also performed for the measurement of total lung capacity (TLC), inspiratory capacity (IC), residual volume (RV), and functional residual capacity (FRC).

4.2.3 Image Acquisition

Thoracic CT was acquired within 1 hour of spirometry and plethysmography on a 64-slice Lightspeed VCT scanner (GEHC, Milwaukee, WI USA) using a detector configuration of 64×0.625 mm, 120 kVp, 100 effective mA, tube rotation time of 500 ms and a pitch of 1.0. A single spiral acquisition of the entire lung was acquired from the apex to the base with subjects in the supine position and in breath-hold after inhalation of a 1L ^{4}He-N_2 gas mixture from functional residual capacity (FRC). In this way, all inhalation breath-hold volumes were controlled to FRC+1L. Reconstruction of the data was performed using a slice thickness of 1.25-mm with a standard convolution kernel (FOV=36×36 cm; matrix=512 × 512). The total number of CT image slices per volume ranged from 300-450 slices.

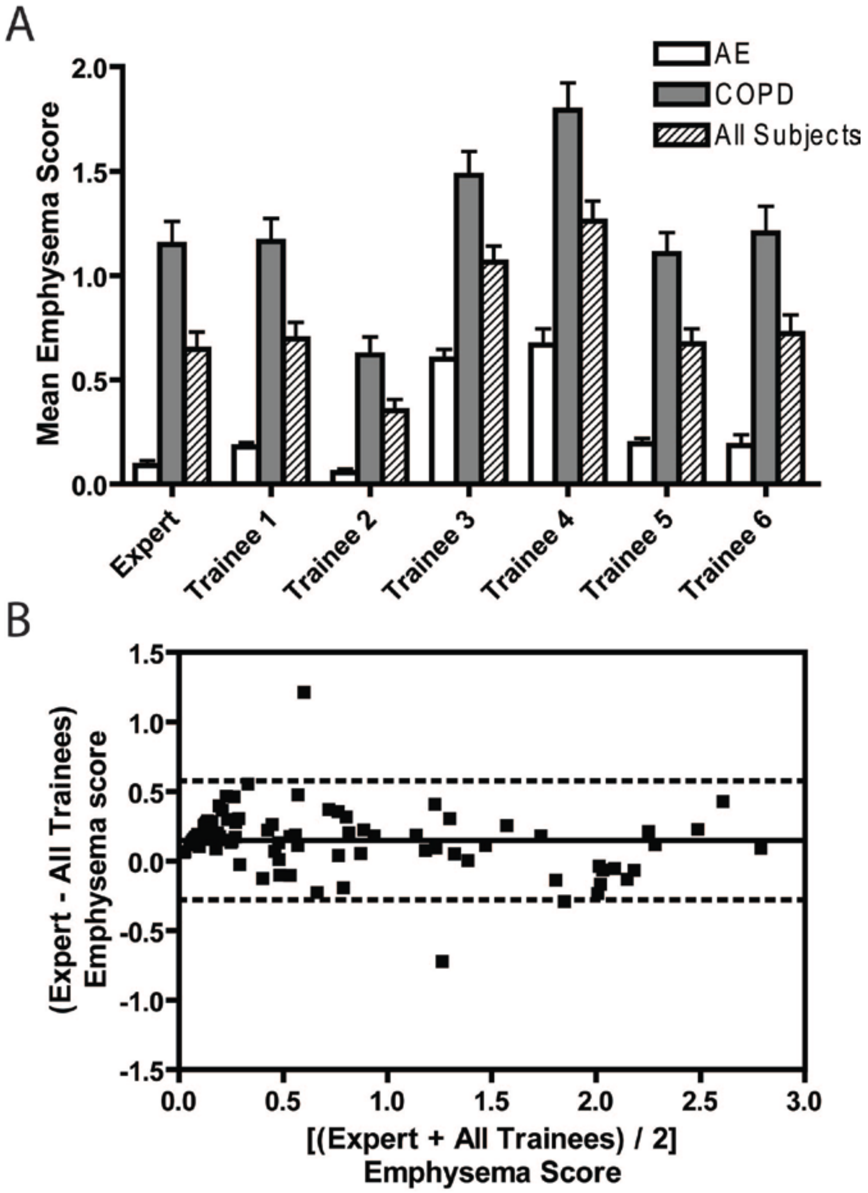

Figure 4.3. Mean emphysema scores and Bland-Altman analysis for all observers. A) Bar graphs with mean and standard error of mean for the Expert and all Trainees. For all observers there was a significant difference between AE and COPD emphysema scores

B) Bland-Altman plot shows the difference between the expert and all trainee mean emphysema scores versus the mean emphysema score. The solid line is the mean difference (0.15 ±022; lower limit = -0.28, upper limit = 0.58) and dotted lines are the 95% confidence interval.

4.2.4 Emphysema Quantification

All images were transferred to a remote workstation for post-processing and image analysis. For CT image analysis, the Pulmonary Workstation 2.0 (VIDA Diagnostics Inc., Iowa City, IA) was used to quantify tissue attenuation in Hounsfield units (HU) on a voxel by voxel basis. The software automatically determined the boundaries of each lung and calculated the histogram of the frequency distribution of HU. All histograms were imported into MATLAB (MATLAB version R2010b; The MathWorks Inc., Cambridge, MA, USA) and the relative area (RA) of the lung with attenuation values below −950 HU (RA_{950}), and the 15th percentile of the frequency distribution histogram in HU (HU_{15}) was calculated. These two parameters were previously shown to be related to the macroscopic and microscopic extent of pulmonary emphysema[40] and emphysema progression.[41] The size of the emphysematous lesions was estimated using low attenuation cluster (LAC) analysis.[20,27,28] In LAC analysis the cumulative size of the lesion (the number of connected low attenuation voxels) is plotted against the cumulative number of lesions (clusters of a given size) on a log-log scale. The slope of this relationship is an indication of average lesion size with steeper slopes identifying smaller lesions.[20]

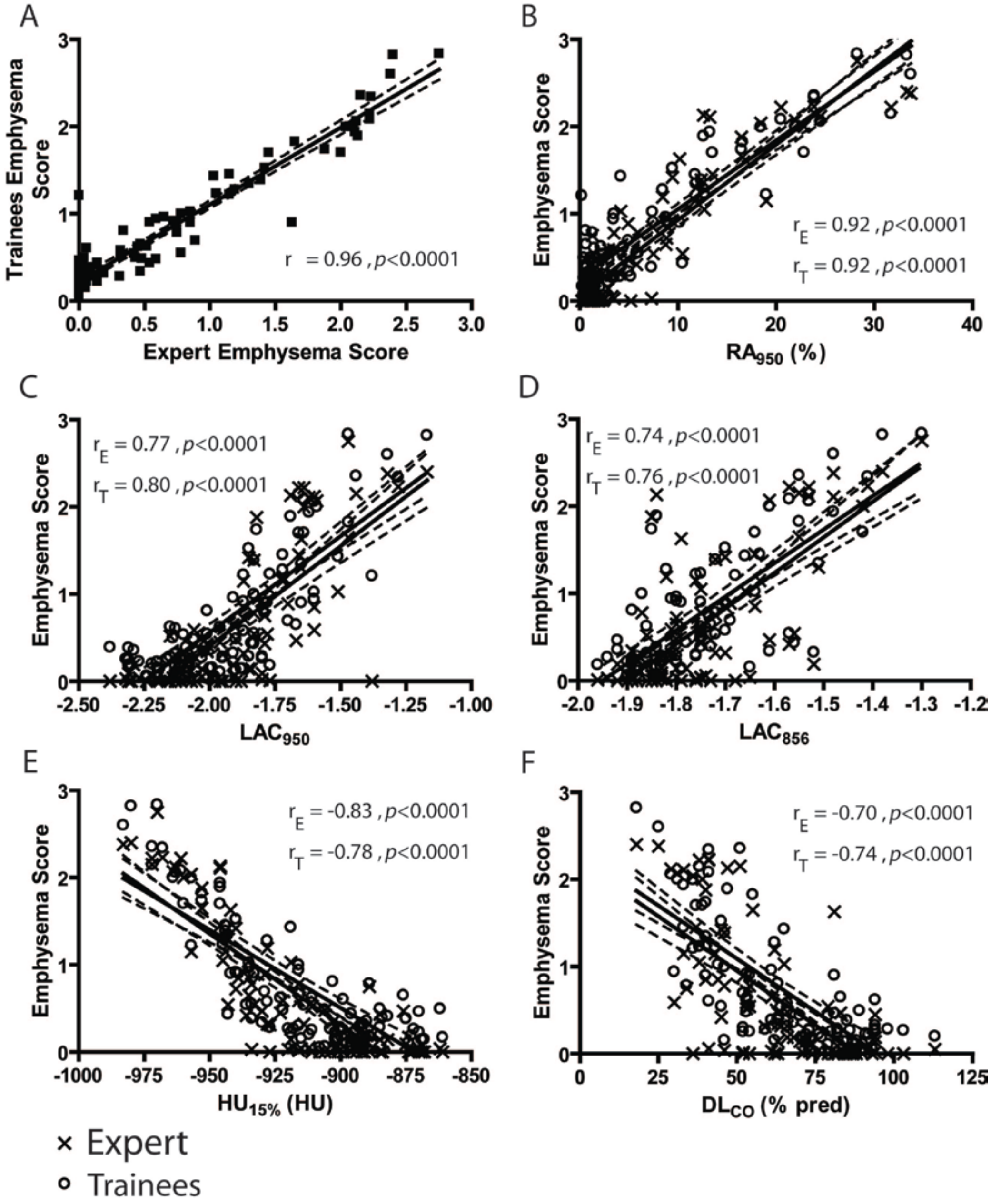

Figure 4.4. Relationship between Emphysema scores of Trainees with Expert, CT densitometry and DL$_{CO}$.

A) Linear regression for Expert and all Trainee mean emphysema score (r = 0.94, *p* < 0.0001)

B) Expert-RA$_{950}$ (r = 0.92, *p* < 0.0001), Trainee-RA$_{950}$ (r = 0.92, *p* < 0.0001)

C) Expert-LAC$_{950}$ (r = 0.77, *p* < 0.0001), Trainee-LAC$_{950}$ (r = 0.80, *p* < 0.0001)

D) Expert-LAC$_{856}$ (r = 0.74, *p* < 0.0001), Trainee-LAC$_{856}$ (r = 0.76, *p* < 0.0001)

E) Expert-HU$_{15}$ (r = -0.83, *p* < 0.0001), Trainee-HU$_{15}$ (r = -0.78, *p* < 0.0001)

F) Expert-DL_{CO}(%) ($r = -0.70$, $p < 0.0001$), Trainee-DL_{CO} ($r = -0.74$, $p < 0.0001$)

The 95% confidence intervals for the regressions are shown as dotted lines.

4.2.5 Semi-automated Emphysema Scoring

Images were reviewed such that all CT images were visible on a digital workstation monitor system (consisting of identical 19-inch flat panel monitors). Qualitative analysis was performed using a fixed standard window width of 1500 and a window level of -600 HU. As shown in Figure 4.1, we developed a graphical user interface (GUI) that enables observers to scroll through CT images in the axial view. In order to reduce scoring time, the scores for the each slice were ported to next slice and remained unchanged unless the observer elected to change the score for that specific slice. The GUI automatically recorded and archived all scores to generate an overall score for each CT volume (subject). All observers except for the expert chest radiologist completed two full rounds of measurements. All observers were blinded to subject identity, disease status as well as the other observer's measurements. The approach we used to semi-automate scoring was adapted directly from the previous work by Bankier et al.[12] Evaluations were performed from superior to inferior in the axial view and scoring commenced from the slice that both left and right lungs were visible and continued to the slice just above the diaphragm. Each CT slice was scored individually, with left and right lungs scored independently. The emphysema score was based on the percentage area of low attenuation, tissue destruction and vascular disruption whereby a score of 0 was assigned if there was no abnormality and the presence of emphysema in the lungs was scored as follows: 1 = 1–25%, 2 = 26–50%, 3 = 51–75%, and 4 = >75%. As previously described by Bankier and colleagues[12] the maximum possible score for each lung was 4 and a final score was calculated as percentage of the maximum possible score as:

$$Emphysema\ Score = 4 \times \frac{\sum_{i=1}^{n}(ES_L + ES_R)}{n \times 8} \tag{1}$$

where ES_L and ES_R are the left and right lung emphysema scores in each of n slices. For each slice, the score was automatically saved and the final score for each subject was automatically computed.

4.2.6 Statistical Analysis

Mean measurements and standard deviations were calculated for two repeated measurements by all observers for all subjects. All statistical analyses was performed using PASW Statistics version 20 (PASW Inc., Chicago, IL, 2009) and results were considered significant when the probability of making a type I error was less than 5% ($p<.05$). A two-sided paired t-test was performed to compare the mean measurements of each observer between round 1 and round 2 as well as to compare subjective emphysema scores in AE subjects and subjects with COPD. A one-way analysis of variance (ANOVA) followed by a Tukey's multiple comparison test was used to compare the measurements between observers.

Table 4.1. Subject Demographics

	Asymptomatic ex-smokers (AE) (n = 43)	COPD (n = 50)
Age (y) (range)	70 (8) (55-85)	71 (9) (48-87)
Males	27	34
FEV_1%	103 (13)	63 (22)
FEV_1/FVC	0.81 (0.06)	0.51 (0.12)
IC%	109 (21)	88 (25)
RV%	102 (26)	151 (40)
FRC%	94 (19)	135 (29)
TLC%	99 (20)	115 (15)
$DL_{CO\%pred}$*	75 (18)	52 (18)

FEV_1: forced expiratory volume in 1 second; FVC: forced vital capacity; IC: inspiratory capacity; RV: residual volume; FRC: functional residual capacity; TLC: total lung capacity; DL_{CO}: Diffusing capacity of lung for carbon monoxide; Data are presented as mean (± standard deviation). **n = 42 AE, n = 49 COPD;

Inter- and intra-observer reproducibility were evaluated using the coefficient of variation (COV, standard deviation divided by the mean), the intra-class correlation coefficient (ICC) for absolute agreement [ICC(A)] and Pearson correlations. GraphPad Prism version 4.01 (GraphPad Software Inc., La Jolla, CA; 2004) was used to perform linear regressions and for the calculation of Pearson correlation coefficients and for Bland-Altman plots to evaluate inter-observer agreement.

4.3 RESULTS

4.3.1 Subject Demographics

Demographic characteristics are provided in Table 4.2 for all 93 subjects enrolled including 43 AE subjects (n=27 males) and 50 subjects with COPD (n=34 males). Spirometry and plethysmography measurements acquired a few minutes before imaging are also shown and reflect the inclusion criteria for COPD and AE subjects. Figure 4.2 shows center axial slice CT images and the relative area of lung below -950HU and -856HU for representative AE, and COPD stage III and IV subjects. In summary, six trainee observers scored 93 CT volumes consisting of 300-450 slices each, in randomized order and on two occasions and a single expert scored the same CT slices in randomized order on a single occasion.

4.3.2 Trainee Accuracy

To evaluate trainee accuracy, we compared the trainee and expert observer scores (Figure 4.3, Figure 4.4A and Table 4.2) and we also compared trainee scores with well-established measurements of emphysema (Figure 4.4B-F). Figure 4.3A shows a bar chart for all trainee and expert mean emphysema scores for all subjects, and for the COPD and AE subject subgroups. For all observers, a one-way analysis of variance (ANOVA) showed a significant difference (*p* < 0.0001) between the visual emphysema score for all, and the COPD and AE subject subgroups. In Figure 4.3B, a Bland-Altman plot shows the agreement between all trainees and the expert observer. There was a significant mean bias (0.15 ±0.22) observed for the trainees and individual trainee bias is shown in Table 4.2 and ranged from 0.03 to 0.62. In Table 4.2 the relationship between the mean emphysema scores for all trainees and the expert radiologist are also provided. Pearson correlations ranged from 0.85 to 0.97 and in Figure 4.4A, the mean score for all Trainees and expert are shown (r=0.96). For two trainees, emphysema scores were significantly different from the expert and Bland Altman bias was also highest for these two trainees, and ICC was low.

Table 4.2. Trainee-Expert Observer Comparisons

Reader-Reader	**Difference *p*-value**	**COV (%)**	**Pearson (r)***	**Bland-Altman Bias (SD)**	**ICC (95% CI)**
Expert - Trainee 1	0.999	5	0.97	0.05 (0.21)	0.96 (0.94-0.98)
Expert - Trainee 2	0.122	42	0.91	-0.29 (0.38)	0.77 (0.39-0.89)
Expert - Trainee 3	0.004	34	0.90	0.42 (0.34)	0.79 (0.08-0.093)
Expert - Trainee 4	<0.0001	45	0.85	0.62 (0.50)	0.67 (0.01-0.87)
Expert - Trainee 5	1.000	3	0.97	0.03 (0.19)	0.97 (0.95-0.98)
Expert - Trainee 6	0.994	8	0.93	0.08 (0.29)	0.94 (0.90-0.96)

Trainee 1: Graduate student; Trainee 2: Medical student; Trainee 3: Medical resident post graduate year 2; Trainee 4: Medical resident post graduate year 2; Trainee 5: Medical resident post graduate year 3; Trainee 6: Medical resident post graduate year 4; Expert: Chest radiologist with more than 10 years of experience. * All Pearson correlations were statistically significant (*p*<0.0001). ICC= Intra-class correlation coefficient

Figure 4.4A shows the relationship between trainee emphysema score (mean of both scoring rounds was used) and the expert observer. Figure 4.4B-F shows the same comparison but with CT densitometry results, LAC analysis and $DL_{CO\%pred}$. There were significant and strong correlations between emphysema score and RA_{950} ($r = 0.92$, $p < 0.0001$), HU_{15} ($r = -0.78$, $p < 0.0001$), LAC_{950} ($r = 0.80$, $p < 0.0001$) and LAC_{856} ($r = 0.76$, $p = 0.0001$). There was also a significant correlation between emphysema score and $DL_{CO\%pred}$ ($r = -0.74$, $p < 0.0001$).

4.3.3 Trainee Reproducibility

To evaluate trainee precision/reproducibility, we evaluated intra- and inter-observer variability in Table 4.3 and Figure 4.5. For all trainees, mean emphysema score (round 1 and 2) is shown in Table 4.3 as well as the comparison of the mean emphysema scores between rounds. For all trainees but one, a paired sample repeated measures t-test showed that the measurements made in round 2 were significantly higher than those in round 1. Intra-observer ICC and COV for both rounds of scoring are also provided in Table 4.3. Intra-observer COV ranged from 4% to 27% and ICC (Absolute) ranged from 0.75 to 0.94. Figure 4.5 shows the relationship between intra-observer (Figure 4.5A) and inter-observer (Figure 4.5B) COV and trainee emphysema score. A negative non-linear correlation was observed between emphysema score and intra- and inter-observer (trainee) COV.

Finally in Table 4.4, we show the rank of each trainee with respect to accuracy in terms of ICC (ranked highest-lowest), Bland-Altman bias (ranked lowest-highest) and COV (ranked lowest-highest) and with respect to precision in terms of ICC (ranked highest-lowest), Bland-Altman bias (ranked lowest-highest) and COV (ranked lowest-highest).

Common to accuracy and precision ranking schemes are Trainees 1, 5 and 6, with Trainees 5 and 6 representing the longest experience in radiology training (Postgraduate training years 3 and 4 respectively) and Trainee 1 representing a medical physics graduate student with 10 years CT background and training – but no experience reading diagnostic CT scans clinically.

4.4 DISCUSSION

In this study we developed a semi-automated method for scoring emphysema from multi-slice, high resolution CT that allows for multiple observers to score the same CT image slices using the same visualization environment and scoring template. We evaluated six novice trainees with very little or no previous thoracic CT emphysema scoring experience and compared these to a single expert chest radiologist with 15 years of experience reading COPD chest CT. The trainees and expert evaluated multi-slice thoracic CT for 93 middle-aged and elderly ex-smokers, including 43 subjects without symptoms, pulmonary function tests consistent with, or a diagnosis of COPD and 50 subjects with COPD -38 of these with stage I or II COPD, the mildest form of the disease. We compared the trainee measurements with the expert's emphysema score and with CT densitometry and well-established pulmonary function measurements and made a number of observations related to trainee accuracy and reproducibility both of which were facilitated by the use of the GUI we designed and developed.

Table 4.3. Inter- and Intra-observer Reproducibility for Trainees

Observer*	Emphysema Score (SD)		(R1-R2) *p*-value	COV (%)	Pearson (r)*	Bland-Altman Bias (SD)	ICC (95% CI)
	R1	R2					
Trainee 1	0.62 (0.73)	0.78 (0.80)	<0.0001	16	0.95	0.16 (0.25)	0.93 (0.82-0.97)
Trainee 2	0.34 (0.51)	0.36 (0.58)	0.473	4	0.87	0.02 (0.29)	0.86 (0.80-0.91)
Trainee 3	0.86 (0.79)	1.26 (0.79)	<0.0001	27	0.84	0.40 (0.44)	0.75 (0.26-0.89)
Trainee 4	1.15 (1.00)	1.37 (0.98)	0.001	12	0.80	0.22 (0.63)	0.78 (0.67-0.86)
Trainee 5	0.64 (0.68)	0.71 (0.74)	0.021	7	0.92	0.07 (0.28)	0.92 (0.88-0.95)
Trainee 6	0.68 (0.81)	0.77 (0.93)	0.012	9	0.93	0.09 (0.34)	0.92 (0.88-0.95)
All Trainees	0.72 (0.69)	0.87 (0.76)	<0.0001	12	0.97	0.16 (0.20)	0.94 (0.77-0.98)

R1 = round 1, R2=round 2 * Trainee 1: Graduate student; Trainee 2: Medical student; Trainee 3: Medical resident post graduate year 2; Trainee 4: Medical resident post graduate year 2; Trainee 5: Medical resident post graduate year 3; Trainee 6: Medical resident post graduate year 4; Expert: Chest radiologist with more than 10 years of experience. ** All Pearson correlations were statistically significant (*p*<0.0001). ICC= Intra-class correlation coefficient

First, we used the tool as a way to directly and relatively rapidly compare trainees to the expert observer and other clinical and radiological measurements that are well-established measurements of pulmonary emphysema. It is important to note that nearly half of all subjects included in the analysis did not have a diagnosis or self-reported symptoms of COPD, but were ex-smokers, in whom we expected to see some evidence of mild-moderate emphysema. Because many of these subjects had very low emphysema scores, we think our estimates of accuracy can be considered conservative because scoring of emphysema tends to be less straightforward and more difficult for novice readers in less severe disease.[42] Although for all trainee observers there was as expected, a difference between the emphysema score for COPD and AE subgroups and strong Pearson correlations for all trainee-expert comparisons, for two trainees, emphysema scores were significantly greater than the expert. We think that this is an important finding for the study which highlights the utility of using standardized tools for training purposes and for quantitative multi-reader studies. In other words, using a semi-automated tool such as we described, provides a way to standardize the visualization and scoring environment without any manual recording required so that the differences between trainees and an expert can be readily identified and remedial activities can be planned and undertaken. We also note that the mean emphysema score for all trainees was significantly greater than the expert's score – and this is common in naïve, or newly trained observers.[43] The relationship between trainee emphysema score was also evaluated with other well-established measurements of emphysema derived from CT densitometry and using $DL_{CO\%pred}$ as a way to determine how trainee subjective scores differ from other objective measurements. In general there was good agreement for all trainees with objective CT measurements and DL_{CO} which was not expected given the mild-moderate disease in most subjects in this study.

Table 4.4. Trainee Rank for Accuracy and Precision

	Trainee # Rank (highest to lowest)					
Accuracy						
ICC	5	1	6	3	2	4
Bias	5	1	6	2	3	4
COV	5	1	6	3	2	4
Precision						
ICC	1	5	6	2	4	3
Bias	2	5	6	4	1	3
COV	2	5	6	1	4	3

ICC: Intra-class correlation coefficient, Bias: Bland-Altman bias, COV: Coefficient of variation

We also used the results of the use of the GUI to evaluate trainee precision and inter-observer reproducibility – likely an important factor to take into account before enlisting readers to multi-reader studies. Intra-observer COV and ICC ranged from modest to very good (COV=4%-27%; ICC=0.75-0.94). It is important to note that there was good agreement between all measurements of precision so that in general the trainee with the highest reproducibility measured using COV also had a high ICC and low bias. What is also important to recognize is the relationship between intra- and inter-observer reproducibility and emphysema severity. As shown in Figure 4.5 the relationship between COV and emphysema score was negative so that the higher the score or more severe the disease – the lower the variability. This relationship was also non-linear and likely exponential. This makes intuitive sense even in a relatively small group of subjects with less severe disease as evaluated here, where this relationship holds.

This study can be considered a proof-of-concept demonstration of how a dedicated GUI can be used to help train and evaluate the inter- and intra-observer reproducibility of observers for research studies. It also provides a way to rank trainees and experts in terms of precision and accuracy. Our results showed that when trainees are ranked in terms of three different metrics of precision and accuracy, there are some trends that we think are important to point out. For example, common to all ranking schemes are three trainees each with the greatest experience either in radiology training or CT physics. In other words, experience with CT and anatomy and physics are important considerations when evaluating trainees and a standardized training environment allowed such differences to be detected. In general, high agreement with the expert also resulted in high intra- and inter-observer variability which is also an important finding in our study of the use of this semi-automated tool and for all training paradigms.

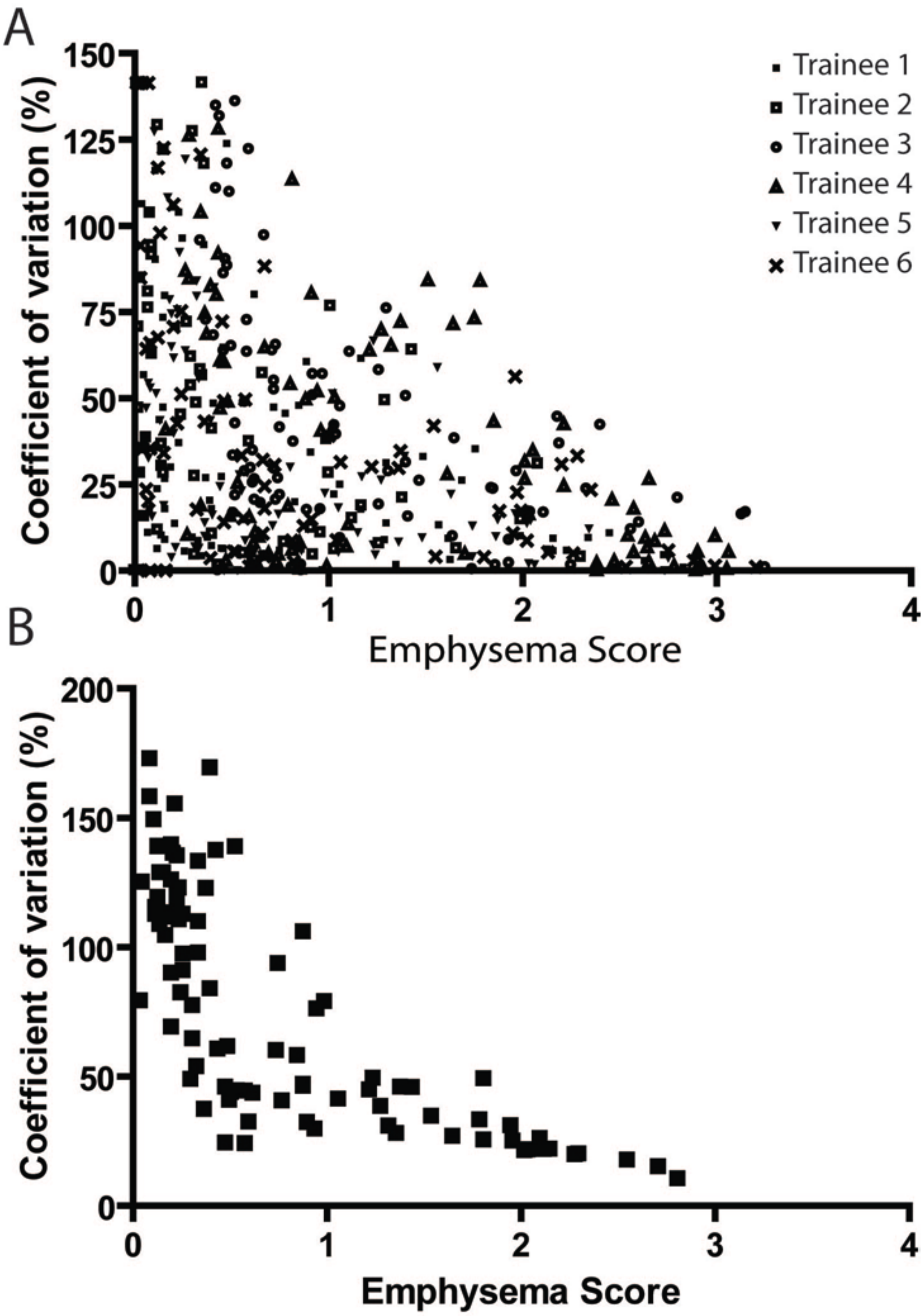

Figure 4.5. Relationship of Emphysema Score and Intra- and Inter-observer Coefficients of Variation (COV)

A) Intra-observer COV for Trainees as a function of emphysema score

B) Inter-observer COV for Trainees as a function of emphysema score

In summary, we developed and used a radiological viewing interface dedicated to emphysema scoring that provided a standardized environment for multiple readers to evaluate the same randomized CT scans on multiple occasions. Our results in six novice trainees allows for the comparison of multiple observer precision and accuracy after scoring emphysema on thoracic CT for 93 ex-smokers.

4.5 References

Reference List

1. Snider GL, Kleinerman J, Thurlbeck WM *et al*. The definition of emphysema. Report of a National Heart, Lung and Blood Institute, Division of Lung Diseases Workshop. *Am. Rev. Respir. Dis.* 1985; **132**: 182-5.

2. Thurlbeck WM, Muller NL. Emphysema: definition, imaging, and quantification. *AJR Am. J. Roentgenol.* 1994; **163**: 1017-25.

3. Rabe KF, Hurd S, Anzueto A *et al*. Global strategy for the diagnosis, management, and prevention of chronic obstructive pulmonary disease: GOLD executive summary. *Am. J. Respir. Crit Care Med.* 2007; **176**: 532-55.

4. Morgan MD. Detection and quantification of pulmonary emphysema by computed tomography: a window of opportunity. *Thorax* 1992; **47**: 1001-4.

5. Diaz S, Casselbrant I, Piitulainen E *et al*. Validity of apparent diffusion coefficient hyperpolarized 3He-MRI using MSCT and pulmonary function tests as references. *Eur. J. Radiol.* 2009; **71**: 257-63.

6. Gierada DS, Woods JC, Jacob RE *et al*. Emphysema quantification in inflation-fixed lungs using low-dose computed tomography and 3He magnetic resonance imaging. *J. Comput. Assist. Tomogr.* 2010; **34**: 773-9.

7. van Beek EJ, Dahmen AM, Stavngaard T *et al*. Hyperpolarised 3He MRI versus HRCT in COPD and normal volunteers: PHIL trial. *Eur. Respir. J.* 2009; **34**: 1311-21.

8. Woods JC, Choong CK, Yablonskiy DA *et al*. Hyperpolarized 3He diffusion MRI and histology in pulmonary emphysema. *Magn Reson. Med.* 2006; **56**: 1293-300.

9. Regan EA, Hokanson JE, Murphy JR *et al*. Genetic epidemiology of COPD (COPDGene) study design. *COPD.* 2010; **7**: 32-43.

10. Vestbo J, Anderson W, Coxson HO *et al*. Evaluation of COPD Longitudinally to Identify Predictive Surrogate End-points (ECLIPSE). *Eur. Respir. J.* 2008; **31**: 869-73.

11. Gelb AF, Hogg JC, Muller NL *et al*. Contribution of emphysema and small airways in COPD. *Chest* 1996; **109**: 353-9.

12. Bankier AA, De M, V, Keyzer C *et al*. Pulmonary emphysema: subjective visual grading versus objective quantification with macroscopic morphometry and thin-section CT densitometry. *Radiology* 1999; **211**: 851-8.

13. Bastarrika G, Wisnivesky JP, Pueyo JC *et al*. Low-dose volumetric computed tomography for quantification of emphysema in asymptomatic smokers participating in an early lung cancer detection trial. *J. Thorac. Imaging* 2009; **24**: 206-11.

14. Cavigli E, Camiciottoli G, Diciotti S *et al*. Whole-lung densitometry versus visual assessment of emphysema. *Eur. Radiol.* 2009; **19**: 1686-92.

15. Desai SR, Hansell DM, Walker A *et al*. Quantification of emphysema: a composite physiologic index derived from CT estimation of disease extent. *Eur. Radiol.* 2007; **17**: 911-8.

16. Hersh CP, Washko GR, Jacobson FL *et al*. Interobserver variability in the determination of upper lobe-predominant emphysema. *Chest* 2007; **131**: 424-31.

17. Koyama H, Ohno Y, Yamazaki Y *et al*. Quantitative and qualitative assessments of lung destruction and pulmonary functional loss from reduced-dose thin-section CT in pulmonary emphysema patients. *Acad. Radiol.* 2010; **17**: 163-8.

18. Mascalchi M, Diciotti S, Sverzellati N *et al*. Low agreement of visual rating for detailed quantification of pulmonary emphysema in whole-lung CT. *Acta Radiol.* 2012; **53**: 53-60.

19. Remy-Jardin M, Edme JL, Boulenguez C *et al*. Longitudinal follow-up study of smoker's lung with thin-section CT in correlation with pulmonary function tests. *Radiology* 2002; **222**: 261-70.

20. Gietema HA, Muller NL, Fauerbach PV *et al*. Quantifying the extent of emphysema: factors associated with radiologists' estimations and quantitative indices of emphysema severity using the ECLIPSE cohort. *Acad. Radiol.* 2011; **18**: 661-71.

21. Coxson HO, Rogers RM, Whittall KP *et al*. A quantification of the lung surface area in emphysema using computed tomography. *Am. J. Respir. Crit Care Med.* 1999; **159**: 851-6.

22. Dirksen A, Dijkman JH, Madsen F *et al*. A randomized clinical trial of alpha(1)-antitrypsin augmentation therapy. *Am. J. Respir. Crit Care Med.* 1999; **160**: 1468-72.

23. Gevenois PA, De M, V, De VP *et al*. Comparison of computed density and macroscopic morphometry in pulmonary emphysema. *Am. J. Respir. Crit Care Med.* 1995; **152**: 653-7.

24. Gevenois PA, De VP, De M, V *et al*. Comparison of computed density and microscopic morphometry in pulmonary emphysema. *Am. J. Respir. Crit Care Med.* 1996; **154**: 187-92.

25. Muller NL, Staples CA, Miller RR *et al*. "Density mask". An objective method to quantitate emphysema using computed tomography. *Chest* 1988; **94**: 782-7.

26. Yuan R, Nagao T, Pare PD *et al*. Quantification of lung surface area using computed tomography. *Respir. Res.* 2010; **11**: 153.

27. Coxson HO, Whittall KP, Nakano Y *et al*. Selection of patients for lung volume reduction surgery using a power law analysis of the computed tomographic scan. *Thorax* 2003; **58**: 510-4.

28. Mishima M, Hirai T, Itoh H *et al*. Complexity of terminal airspace geometry assessed by lung computed tomography in normal subjects and patients with chronic obstructive pulmonary disease. *Proc. Natl. Acad. Sci. U. S. A* 1999; **96**: 8829-34.

29. Ginsburg SB, Lynch DA, Bowler RP *et al*. Automated Texture-based Quantification of Centrilobular Nodularity and Centrilobular Emphysema in Chest CT Images. *Acad. Radiol.* 2012; **19**: 1241-51.

30. Park YS, Seo JB, Kim N *et al*. Texture-based quantification of pulmonary emphysema on high-resolution computed tomography: comparison with density-based quantification and correlation with pulmonary function test. *Invest Radiol.* 2008; **43**: 395-402.

31. Prasad M, Sowmya A. Multi-level classification of emphysema in HRCT lung images using delegated classifiers. *Med. Image Comput. Comput. Assist. Interv.* 2008; **11**: 59-66.

32. Sorensen L, Shaker SB, de BM. Quantitative analysis of pulmonary emphysema using local binary patterns. *IEEE Trans. Med. Imaging* 2010; **29**: 559-69.

33. Uppaluri R, Mitsa T, Sonka M *et al*. Quantification of pulmonary emphysema from lung computed tomography images. *Am. J. Respir. Crit Care Med.* 1997; **156**: 248-54.

34. Xu Y, Sonka M, McLennan G *et al*. MDCT-based 3-D texture classification of emphysema and early smoking related lung pathologies. *IEEE Trans. Med. Imaging* 2006; **25**: 464-75.

35. Hochhegger B, Marchiori E, Irion K *et al*. Visual vs automated assessment of emphysema. *Chest* 2011; **140**: 1384.

36. Barr RG, Berkowitz EA, Bigazzi F *et al*. A combined pulmonary-radiology workshop for visual evaluation of COPD: study design, chest CT findings and concordance with quantitative evaluation. *COPD.* 2012; **9**: 151-9.

37. Kirby M, Mathew L, Wheatley A *et al*. Chronic obstructive pulmonary disease: longitudinal hyperpolarized (3)He MR imaging. *Radiology* 2010; **256**: 280-9.

38. Mathew L, Evans A, Ouriadov A *et al*. Hyperpolarized 3He magnetic resonance imaging of chronic obstructive pulmonary disease: reproducibility at 3.0 tesla. *Acad. Radiol.* 2008; **15**: 1298-311.

39. Standardization of Spirometry, 1994 Update. American Thoracic Society. *Am J Respir Crit Care Med* 1995; **152**: 1107-36.

40. Madani A, Zanen J, De M, V *et al*. Pulmonary emphysema: objective quantification at multi-detector row CT--comparison with macroscopic and microscopic morphometry. *Radiology* 2006; **238**: 1036-43.

41. Dirksen A, Friis M, Olesen KP *et al*. Progress of emphysema in severe alpha 1-antitrypsin deficiency as assessed by annual CT. *Acta Radiol.* 1997; **38**: 826-32.

42. Moulopoulos SD, Stamatelopoulos S, Nanas S *et al*. Medical education and experience affecting intra-observer variability. *Med. Educ.* 1986; **20**: 133-5.

43. Charlson ME, Karnik J, Wong M *et al*. Does experience matter? A comparison of the practice of attendings and residents. *J. Gen. Intern. Med.* 2005; **20**: 497-503.

CHAPTER 5: CONCLUSIONS AND FUTURE DIRECTIONS

5.1 Overview and Summary

The limitations of current tools for diagnosis and monitoring of lung disease drives the motivation for developing more sensitive techniques for early detection of pulmonary disorders as well as monitoring their progression and their response to treatments. Pulmonary function tests (PFT) provide established measurements for diagnosis and evaluation of treatment responses. However, PFT and other established measurements of lung function can only provide global information of the regional anatomical, morphological and functional contribution of the underlying component of the disease. Moreover, the lung is not a homogeneous organ and obstructive lung diseases such as chronic obstructive pulmonary disease (COPD) have heterogeneous distribution and progression within the lung. COPD is characterized by two major pathologies (i.e. small airway disease and parenchymal destruction) and although both disease phenotypes are related to each other, the overall response of COPD to treatments might be improved if therapeutic interventions were designed based on the underlying mechanisms of each component of the disease. Therefore, new measurement methods need to be developed to improve the understanding of the underlying regional functional and structural impairment of the pulmonary system in COPD. These methods mainly include imaging techniques such as nuclear medicine, x-ray radiography and x-ray CT and MRI which can regionally assess the structural and functional impairments and have the potential to stratify the pathologic phenotypes of COPD.

X-ray radiography is the most common imaging tool for the assessment of pulmonary structure; however, its quantitative information is limited and it does not provide any information regarding lung function. Over the last few years, CT has been the imaging modality of choice for evaluation of pulmonary diseases[1] mainly because of its high spatial resolution, short acquisition time, as well as its ability to remove overlapping structures in projection views and provide tomographic images.[2] In COPD, CT can be used for quantitative and qualitative evaluation of lung tissue structure. Measurements of lung tissue attenuation can be used for the evaluation of pulmonary emphysema[2-5] and lung airways can be studied through the measurements of airway wall thickness[6-8]. Recently, CT has been used for evaluation of lung function.[9] The development of four-dimensional CT (4DCT) provides the opportunity for functional regional evaluation of the respiratory system.[9-11] Nuclear medicine techniques can also provide regional information about lung function by mapping the distribution of inhaled and intravenously administered radioactive nuclei in the pulmonary system; however, nuclear medicine imaging suffers from poor spatial resolution and deposition of the radioactive particles in the central airways.[12,13] MRI can be used to acquire quantitative and qualitative information about lung tissue structure and function. Although ^{1}H MRI of the lung is challenging, the development of more powerful hardware along with faster pulse sequences enables detailed imaging of pulmonary structure that is comparable with other imaging modalities such as CT.[14,15] Hyperpolarized noble gas MRI can also provide valuable information about lung tissue structure and function.[16-18] For functional information, spin density imaging provides high resolution information about the distribution of gas in the lung. Structural evaluation of the lung is feasible using diffusion-weighted imaging (DWI). However, the high costs, particularly for ^{3}He and the complicated physics behind hyperpolarization of noble gas at the imaging site have limited the clinical application of this technology.

Based in this framework of imaging modalities for evaluation of pulmonary structure and function, we embarked on developing techniques to extract quantitative information about the extent of emphysema derived from lung ^{1}H MRI and CT images. In this thesis we quantitatively evaluated the extent emphysema in healthy volunteers and subjects with COPD using ^{1}H MRI and CT images. Based on these measurements the following hypotheses were tested: 1) coincident and volume-matched inhalation acquisition of ^{3}He and ^{1}H MRI in COPD would allow for the detection of a relationship between hyperpolarized ^{3}He ADC and ^{1}H SI of the lung parenchyma 2) histogram analysis of lung CT images in COPD subjects and healthy volunteers would have a high sensitivity and specificity for the detection of emphysema 3) The direct quantitative measure of pulmonary emphysema that can be made through visual scoring has high reproducibility.

The objective of Chapter 2 was to quantitatively evaluate the relationship between short echo time pulmonary ^{1}H magnetic resonance imaging (MRI) signal intensity (SI) and ^{3}He MRI apparent diffusion coefficients (ADC), high-resolution computed tomography (CT) measurements of emphysema, and pulmonary function measurements. In this study nine healthy never-smokers and 11 COPD subjects underwent same-day plethysmography, spirometry, short echo time ((TE) =1.2ms) ^{1}H and diffusion-weighted hyperpolarized ^{3}He MRI (b=1.6 s/cm^2) at 3.0T. In addition, for COPD subjects only, CT densitometry was also performed. Mean ^{1}H SI was significantly greater for never-smokers (12.1 ± 1.1 arbitrary units (AU)) compared to COPD subjects (10.9 ± 1.3 AU, *p*=.04). The ^{1}H SI AP-gradient was also significantly greater for never-smokers (0.40 AU/cm, $R^2 = 0.94$)

compared to COPD subjects (0.29 AU/cm, R^2 = 0.968, p = 0.05). There was a significant correlation between ^{1}H SI and ^{3}He ADC (r = -0.58, p = 0.008) and significant correlations between ^{1}H MR SI and CT measurements of emphysema (RA_{950} r = -0.69, p = 0.02 and $HU_{15\%}$, r = 0.66, p = 0.03). Overall in Chapter 2 the significant and moderately strong relationship between ^{1}H SI and ^{3}He ADC, as well as between ^{1}H SI and CT measurements of emphysema suggests that these imaging methods and measurements may be quantifying similar tissue changes in COPD and that pulmonary ^{1}H SI may be used to monitor emphysema as a complement to CT and noble gas MRI.

In Chapter 3, a principal component analysis (PCA) method to score the severity of emphysema that takes into account the frequency distribution of each Hounsfield unit (HU) threshold was developed. For this study, ninety-seven ex-smokers including 53 subjects with chronic obstructive pulmonary disease (COPD) and 44 asymptomatic subjects (AE) provided written informed consent to imaging as well as plethysmography and spirometry. We applied PCA to the CT density histogram to generate whole lung and regional density histogram principal components (D_HP_C) including the first (PC_1), second (PC_2) and sum of both principal components (D_HP_CS). Significant relationships for D_HP_CS with single HU thresholds, pulmonary function measurements, an expert's emphysema score and hyperpolarized ^{3}He magnetic resonance imaging (MRI) apparent diffusion coefficients (ADC) were determined using linear regression and Pearson coefficients. Receiver Operator Characteristics (ROC) analysis was performed using FEV_1/FVC as the independent diagnostic. There was a significant difference (p<0.0001) between AE and COPD subjects for D_HP_CS, FEV_1/FVC, $DL_{CO\%pred}$, RA_{950}, RA_{856}, RA_{910} and ^{3}He ADC. There were significant correlations for D_HP_CS with FEV_1/FVC (r=-0.85,

$p<0.0001$), $DL_{CO\%pred}$ (r=-0.67, $p<0.0001$), $RA_{950/}$ RA_{910}/RA_{856} (r=0.93/0.96/0.76, $p<0.0001$) and ^{3}He ADC (r=0.85, $p<0.0001$). ROC analysis showed a 91% classification rate for D_HP_CS. In conclusion, we generated an automated emphysema score using PCA of the CT density histogram with a 91% COPD classification rate that showed strong and significant correlations with pulmonary function tests, single HU thresholds and ^{3}He MRI ADC.

In Chapter 4, we developed a semi-automated tool to quantify emphysema from thoracic x-ray multi-detector (64-slice) computed tomography (CT) for training purposes and multi-reader studies. Thoracic x-ray CT was acquired in 93 ex-smokers, who were evaluated by six trainees with little or no expertise (trainees) and a single experienced thoracic radiologist (expert). A graphic user interface (GUI) was developed for emphysema quantification based on the percentile of lung where a score of 0= no abnormalities, 1=1-25%, 2=26-50%, 3=51-75% and 4= 76-100% for each lung side/slice. Trainees blinded to subject characteristics scored randomized images twice; accuracy was determined by comparison to expert scores, density histogram 15th percentile ($HU_{15)}$, relative area at -950HU (RA_{950}), low attenuation clusters at -950HU (LAC_{950}), -856HU (LAC_{856}) and the diffusing capacity for carbon monoxide ($DL_{CO\%pred}$). Intra- and inter-observer reproducibility was evaluated using coefficients-of-variation (COV), intra-class (ICC) and Pearson correlations. Trainee-expert correlations were significant (r=0.85-0.97, $p < 0.0001$) and a significant trainee bias (0.15 ±0.22) was observed. Emphysema score was correlated with RA_{950} ($r = 0.88$, $p < 0.0001$), HU_{15} ($r = -.77$, $p < 0.0001$), LAC_{950} ($r = .76$, $p < 0.0001$), LAC_{856} ($r = .74$, $p = 0.0001$) and $DL_{CO\%pred}$ ($r = -.71$, $p < 0.0001$). Intra-observer reproducibility (COV=4%-27%; ICC=.75-.94) was moderate to high for trainees; intra- and inter-observer COV were negatively and non-linearly correlated with emphysema score. In conclusion, we developed a GUI for rapid and interactive emphysema scoring that allows for comparison of multiple readers with clinical and radiological standards.

Here in Chapter 5, the conclusions of the studies that were performed in this thesis are discussed. In this chapter, the limitation of these studies as well as possible directions for future work will be discussed. In Section 5.2, the summary of conclusions of this thesis will be presented and the limitations of these studies and the possible solutions will be discussed in section 5.3. Finally in section 5.4, we will discuss the possible future direction for this thesis.

5.2 Summary of Conclusions

Overall, in this thesis we presented quantitative measurements of pulmonary emphysema derived from ^{1}H MRI and high resolution CT in subjects with smoking history of 10 pack-years and subjects that were diagnosed with COPD by a physician. Measurement of ^{1}H MRI signal intensity showed a significant difference between healthy volunteers and subjects with COPD. We found a significant and moderately strong relationship between ^{1}H SI and ^{3}He ADC. Significant and moderately strong relationships were also detected between ^{1}H SI and CT measurements of emphysema, and significant correlations were detected between both ^{1}H SI and ^{3}He ADC with FEV_1, FEV_1/FVC, RV/TLC and DL_{CO}. Additionally our results showed that objective histogram analysis of CT images for emphysema scoring that takes into account the frequency distribution of each HU has a very high rate of correctly classifying the patient into COPD and healthy subgroups along with a high sensitivity and specificity. With this method, a significant difference was detected between the whole lung emphysema score in healthy subjects and subjects with COPD. Significant and strong correlations were also detected between whole lung emphysema score and subjective scoring, as well as objective measures including ^{3}He ADC, FEV_1/FVC, DL_{CO}(%). We also found that emphysema scores for upper, middle and lower lung correspond with the expected distribution of the lung damage in smoking related emphysema. Finally, we found a significant difference between whole lung visual emphysema score in healthy subjects and subjects with COPD. A significant and very strong relationship was found between all observers for whole lung emphysema severity scores and significant and strong relationships were detected between round 1 and round 2 measurements of emphysema severity scores. However, there is less variability between observers as the severity of the emphysema increases. We also found that there were significant and strong correlations between subjective emphysema scores and RA_{950}, HU_{15}, LAC_{950}, LAC_{856}, ^{3}He ADC and DL_{CO}(%pred).

In summary we have shown that 1) Pulmonary ^{1}H MRI has the potential to detect lung tissue loss and gas trapping and it can be used to monitor emphysema as a complement to CT and noble gas MRI, 2) with a new technique that takes into account the frequency distribution of each HU threshold, emphysema can be scored with less concern that there is underestimation or overestimation of its extent based on the chosen threshold and 3) visual scoring is time efficient and has a strong agreement with measurements obtained by objective scoring, further confirming its utility in clinical practice.

5.2 Limitation of Current Tools and Solutions

We first acknowledge the small number of subjects that have been studied in Chapter 2. In this pilot study we evaluated 20 middle-aged and elderly subjects, including nine subjects with stage II COPD, two subjects with stage III COPD and nine never-smokers to compare short echo-time ^{1}H MRI, ^{3}He MRI and well-established pulmonary function measurements. Small sample size was a major limitation of the work presented in this chapter and a cautious interpretation and extrapolation of the results is necessary. This also highlights the necessity for larger sample sizes, when testing the relationships between different metrics of the disease.

We also acknowledge that improvements in some of the techniques that we have used in this study are required. For example, the countless number of air-tissue interfaces in the lung causes magnetic field inhomogeneity and high MR susceptibility artifact, which leads to extreme reduction of T2* and rapid decay of the acquired signal from lung tissue.[19] In this study we used a pulse sequence with a short TE (~1.2ms); however, pulse sequences with ultra short TE (UTE) can improve the signal acquisition of tissues with very short T2*.[20-22] Moreover, to acquire MRI images with higher SNR, longer acquisition time is required but, to minimize the motion artifact caused by the movement of the respiratory system, lung MRI protocols were designed based on breath-hold conditions[23], even though this method will impose a time limit on the duration of image acquisition. Respiratory motion artifacts in free breathing protocols can be partially eliminated[24] using gated imaging techniques, but standard clinical protocols are mainly based on breath-hold methods.

In Chapter 3, there are a few limitations that we acknowledged. CT is generally accepted to be the imaging modality of choice for the evaluation of lung tissue. High resolution CT can provide a detailed morphological assessment of the lung and therefore, it is generally accepted as the gold standard imaging technique for structural assessment of the lung.[25] However, considering histology as the gold standard diagnosis for a wide range of diseases, there is no gold standard in our study to compare the CT based emphysema scores against. Nevertheless, there is a considerable amount of literature supporting the use of quantitative CT scanning to measure emphysema.[26-28]

The second limitation of this chapter, concerns the extent of emphysema for the majority of subjects in this study. Most subjects have mild or no emphysema and therefore, our findings may not be accurately generalized to all patients suffering from emphysema, particularly those with more severe disease. However, the high rate of correctly classifying the patients into COPD and healthy subgroups given objective emphysema scores along with a high sensitivity and specificity using the database with majority of subjects have mild or no emphysema, suggests this method’s capability of for detecting early changes of the disease.

Another related limitation of all objective emphysema quantification methods, is their dependence on technical features including scanner type, tube current and voltage as well as post processing algorithms and filters.[29-32] In fact, although there is a considerable amount of effort to evaluate emphysema using quantitative densitometry, the above technical diversities along with the lack of standardization of the scoring systems[33], limit the translation of quantitative densitometry into daily clinical practice.

Often it is favorable to look towards an objective method of quantification. However, in the case of assessing emphysema, current objective measurements have several limitations that cannot be ignored.[27] These limitations mainly stem from the fact that the scoring is done in a very indirect fashion. The lack capability to stratify gas-trapping from pulmonary emphysema, is one of the limitations of the objective methods. In general, visual scoring of emphysema provides the opportunity for the observer to distinguish between lung tissue destruction and other causes of lowered attenuation such as gas-trapping that may be caused by small airway diseases. In other words, observers such as radiologists, not only can assess and classify the extent, type and the distribution of emphysema, but also can differentiate it from other lung abnormalities.

The focus of Chapter 4 was on studying the inter- and intraobserver reproducibility of the visual scoring of a large number of CT slices and a large number of subjects. Moreover in this chapter, the visual scoring results were compared against the whole lung densitometry and low attenuation cluster analysis as well as compared against pulmonary function tests and hyperpolarized ^{3}He ADC, which can be considered a surrogate measurement of airspace size.[34-37] However, there are a few limitations to this study that we have to acknowledge.

Firstly, as we discussed before, there is no histology measurement to compare the CT emphysema scores against. Secondly, our chest radiologist performed one round, and other observers performed two rounds of measurements. It would have been favorable for all observers to have completed more than two rounds of measurements to make our assessment of intraobserver reproducibility more reliable. However, the large number of observers and extensive amount of images that were scored does ensure that interobserver reproducibility can be reliably assessed.

Thirdly, as we discussed before, the majority of subjects in this study have mild or no emphysema. This may lead to unbiased interpretation of the results and cannot be accurately generalized and extrapolated to all subject groups; however, it is less of a concern mainly because it was shown that the variability between observers reduces as the severity of the emphysema increases. Finally, observers may have benefitted from more extensive prior training for emphysema scoring with reference images. This may have improved interobserver concordance, especially for those without previous experience in emphysema scoring.

5.3 Future Directions

Developing better *in vivo* pulmonary MRI techniques may be associated with an increase in complexity; however, they improve our understanding of the underlying mechanisms of diseases. They might also provide the opportunity for early detection of the disease as well as longitudinal monitoring of its progression and its responses to treatments. MRI has the potential to non-invasively provide structural and functional information about pathologies related to pulmonary system. However, significant effort needs to be made to increase the quality and reproducibility of the lung MRI images. One way that needs to be considered in future studies is through increasing the image acquisition time, although it is limited to the ability of the patients to hold their breath. Novel and advanced imaging techniques that can correct the breathing motion in the respiratory gated techniques need to be developed to allow for longer image acquisition time.

Development of free breathing imaging protocols also provides the opportunity to acquire functional information about the pulmonary system. Non-contrast enhanced imaging of pulmonary ventilation and perfusion is feasible using a Fourier decomposition MRI technique.[38] This method uses a fast and short TE pulse sequence to acquire a series of images of the lung in a free breathing condition. A non-rigid registration algorithm will be applied on the stack of images to compensate the motion of the respiratory system.[38] Once all images were registered to a reference image, a spectral analysis will be performed on the signal intensity variations of lung tissue and pulmonary vasculature using Fourier decomposition. This technique allows for identification of the peaks related to pulmonary ventilation and perfusion. The peak related to pulmonary ventilation can be found close to the breathing frequency and the peak related to pulmonary perfusion can be found close to the heart beat frequency. Regional changes of proton density in the pulmonary blood flow and lung parenchyma determine the amplitude of these peaks. Ventilation and perfusion weighted images can be reconstructed based on regional changes of the peaks amplitude and can be used for functional evaluation of pulmonary disorders.[38,39]

The availability of conventional ^{1}H MRI in most clinical centers provides the opportunity for structural evaluation of the pulmonary system. However, one of the inherent problems with lung ^{1}H MRI, besides the low proton density of lung tissue, is the high-field MRI susceptibility artifacts, which result in very short transverse relaxation times (T2*). Developing ultra short TE (UTE) pulse sequences might be a possible pathway towards the improvements required to enable utilizing structural ^{1}H MRI in clinical utility in respiratory medicine. In other words, pulse sequences must be optimized for faster echo times (on the order of 10–100 ms). Taken together, low proton density and susceptibility artifacts mean that lung MRI must incorporate both short echo time/acquisition and long acquisition times for signal averaging and improved signal-to-noise ratios.

The role of CT in quantification of pulmonary emphysema is established; however, important problems remain to be investigated despite all the accomplishments that have been made in this field. For example, expiratory CT images can also reveal quantitative information about the emphysematous destruction of lung tissue; however, they are not as adequate as measurements from inspiratory images.[29] Expiratory CT images have the potential to provide information about the lung's airways and diseases related to them such as small airway disease in COPD. The role of CT can be further highlighted in stratifying different phenotypes of COPD because CT has the potential to distinguish between irreversible lung tissue destruction and partially reversible airway disease in COPD.

5.4 Conclusion

Overall in this thesis we have developed new methods for quantification of pulmonary emphysema using ^{1}H MRI and high resolution CT. ^{1}H MRI signal intensity is sensitive to emphysematous destruction of pulmonary emphysema and can be used in regional evaluation of lung tissue destruction in COPD subjects. Furthermore in this thesis, it has been shown that quantitative histogram analysis of lung tissue CT images can be performed using PCA. This method can correctly classify the patients into COPD and healthy subgroups given objective emphysema scores along with a high sensitivity and specificity. It has also been shown that the measurement of whole lung visual emphysema scores is a valuable tool for quantifying the extent of emphysema in the lungs. It was suggested that visual scoring is time efficient and has a strong agreement with measurements obtained by objective scoring, further confirming its utility in clinical practice. Our results show that CT derived emphysema scores using PCA histogram analysis and ^{1}H MRI signal intensity are sensitive tools for structural evaluation of lung tissue destruction both globally and regionally.

5.5 References

Reference List

1. Turner MO, Mayo JR, Muller NL *et al*. The value of thoracic computed tomography scans in clinical diagnosis: a prospective study. *Can. Respir. J.* 2006; **13**: 311-6.

2. Coxson HO, Mayo J, Lam S *et al*. New and current clinical imaging techniques to study chronic obstructive pulmonary disease. *Am. J. Respir. Crit Care Med.* 2009; **180**: 588-97.

3. Bankier AA, De M, V, Keyzer C *et al*. Pulmonary emphysema: subjective visual grading versus objective quantification with macroscopic morphometry and thin-section CT densitometry. *Radiology* 1999; **211**: 851-8.

4. Coxson HO, Rogers RM. Quantitative computed tomography of chronic obstructive pulmonary disease. *Acad. Radiol.* 2005; **12**: 1457-63.

5. Madani A, Keyzer C, Gevenois PA. Quantitative computed tomography assessment of lung structure and function in pulmonary emphysema. *Eur. Respir. J.* 2001; **18**: 720-30.

6. Nakano Y, Muller NL, King GG *et al*. Quantitative assessment of airway remodeling using high-resolution CT. *Chest* 2002; **122**: 271S-5S.

7. Nakano Y, Wong JC, de Jong PA *et al*. The prediction of small airway dimensions using computed tomography. *Am. J. Respir. Crit Care Med.* 2005; **171**: 142-6.

8. Orlandi I, Moroni C, Camiciottoli G *et al*. Chronic obstructive pulmonary disease: thin-section CT measurement of airway wall thickness and lung attenuation. *Radiology* 2005; **234**: 604-10.

9. Castillo R, Castillo E, Martinez J *et al*. Ventilation from four-dimensional computed tomography: density versus Jacobian methods. *Phys. Med. Biol.* 2010; **55**: 4661-85.

10. Guerrero T, Sanders K, Noyola-Martinez J *et al*. Quantification of regional ventilation from treatment planning CT. *Int. J. Radiat. Oncol. Biol. Phys.* 2005; **62**: 630-4.

11. Guerrero T, Sanders K, Castillo E *et al*. Dynamic ventilation imaging from four-dimensional computed tomography. *Phys. Med. Biol.* 2006; **51**: 777-91.

12. Jogi J, Jonson B, Ekberg M *et al*. Ventilation-perfusion SPECT with 99mTc-DTPA versus Technegas: a head-to-head study in obstructive and nonobstructive disease. *J. Nucl. Med.* 2010; **51**: 735-41.

13. Petersson J, Sanchez-Crespo A, Larsson SA *et al*. Physiological imaging of the lung: single-photon-emission computed tomography (SPECT). *J. Appl. Physiol* 2007; **102**: 468-76.

14. Ley-Zaporozhan J, Ley S, Kauczor HU. Morphological and functional imaging in COPD with CT and MRI: present and future. *Eur. Radiol.* 2008; **18**: 510-21.

15. Ley-Zaporozhan J, Ley S, Eberhardt R *et al*. Visualization of morphological parenchymal changes in emphysema: comparison of different MRI sequences to 3D-HRCT. *Eur. J. Radiol.* 2010; **73**: 43-9.

16. Fain SB, Korosec FR, Holmes JH *et al*. Functional lung imaging using hyperpolarized gas MRI. *J. Magn Reson. Imaging* 2007; **25**: 910-23.

17. Moller HE, Chen XJ, Saam B *et al*. MRI of the lungs using hyperpolarized noble gases. *Magn Reson. Med.* 2002; **47**: 1029-51.

18. Parraga G, Ouriadov A, Evans A *et al*. Hyperpolarized 3He ventilation defects and apparent diffusion coefficients in chronic obstructive pulmonary disease: preliminary results at 3.0 Tesla. *Invest Radiol.* 2007; **42**: 384-91.

19. Su S, Saunders JK, Smith IC. Resolving anatomical details in lung parenchyma: theory and experiment for a structurally and magnetically inhomogeneous lung imaging model. *Magn Reson. Med.* 1995; **33**: 760-5.

20. Mayo JR, MacKay A, Muller NL. MR imaging of the lungs: value of short TE spin-echo pulse sequences. *AJR Am. J. Roentgenol.* 1992; **159**: 951-6.

21. Takahashi M, Togao O, Obara M *et al*. Ultra-short echo time (UTE) MR imaging of the lung: comparison between normal and emphysematous lungs in mutant mice. *J. Magn Reson. Imaging* 2010; **32**: 326-33.

22. Togao O, Tsuji R, Ohno Y *et al*. Ultrashort echo time (UTE) MRI of the lung: assessment of tissue density in the lung parenchyma. *Magn Reson. Med.* 2010; **64**: 1491-8.

23. Ley-Zaporozhan J, Ley S, Kauczor HU. Proton MRI in COPD. *COPD.* 2007; **4**: 55-65.

24. Biederer J, Reuter M, Both M *et al*. Analysis of artefacts and detail resolution of lung MRI with breath-hold T1-weighted gradient-echo and T2-weighted fast spin-echo sequences with respiratory triggering. *Eur. Radiol.* 2002; **12**: 378-84.

25. Verschakelen JA, DeWeaver W. *Computed Tomography of the Lung: A Pattern Approach.*Springer, 2007.

26. Cavigli E, Camiciottoli G, Diciotti S *et al*. Whole-lung densitometry versus visual assessment of emphysema. *Eur. Radiol.* 2009; **19**: 1686-92.

27. Gietema HA, Muller NL, Fauerbach PV *et al*. Quantifying the extent of emphysema: factors associated with radiologists' estimations and quantitative indices of emphysema severity using the ECLIPSE cohort. *Acad. Radiol.* 2011; **18**: 661-71.

28. Madani A, Zanen J, De M, V *et al*. Pulmonary emphysema: objective quantification at multi-detector row CT--comparison with macroscopic and microscopic morphometry. *Radiology* 2006; **238**: 1036-43.

29. Litmanovich D, Boiselle PM, Bankier AA. CT of pulmonary emphysema--current status, challenges, and future directions. *Eur. Radiol.* 2009; **19**: 537-51.

30. Lynch DA, Newell JD. Quantitative imaging of COPD. *J. Thorac. Imaging* 2009; **24**: 189-94.

31. Newell JD, Jr., Hogg JC, Snider GL. Report of a workshop: quantitative computed tomography scanning in longitudinal studies of emphysema. *Eur. Respir. J.* 2004; **23**: 769-75.

32. Stoel BC, Stolk J. Optimization and standardization of lung densitometry in the assessment of pulmonary emphysema. *Invest Radiol.* 2004; **39**: 681-8.

33. Hersh CP, Washko GR, Jacobson FL *et al*. Interobserver variability in the determination of upper lobe-predominant emphysema. *Chest* 2007; **131**: 424-31.

34. de Lange EE, Mugler JP, III, Brookeman JR *et al*. Lung air spaces: MR imaging evaluation with hyperpolarized 3He gas. *Radiology* 1999; **210**: 851-7.

35. Kauczor HU, Hofmann D, Kreitner KF *et al*. Normal and abnormal pulmonary ventilation: visualization at hyperpolarized He-3 MR imaging. *Radiology* 1996; **201**: 564-8.

36. Kauczor HU, Ebert M, Kreitner KF *et al*. Imaging of the lungs using 3He MRI: preliminary clinical experience in 18 patients with and without lung disease. *J. Magn Reson. Imaging* 1997; **7**: 538-43.

37. MacFall JR, Charles HC, Black RD *et al*. Human lung air spaces: potential for MR imaging with hyperpolarized He-3. *Radiology* 1996; **200**: 553-8.

38. Bauman G, Puderbach M, Deimling M *et al*. Non-contrast-enhanced perfusion and ventilation assessment of the human lung by means of fourier decomposition in proton MRI. *Magn Reson. Med.* 2009; **62**: 656-64.

39. Bauman G, Lutzen U, Ullrich M *et al*. Pulmonary functional imaging: qualitative comparison of Fourier decomposition MR imaging with SPECT/CT in porcine lung. *Radiology* 2011; **260**: 551-9.

Appendices

Appendix – A: Pulmonary Tumour Measurements from X-Ray Computed Tomography in One- Two- and Three-dimensions

The work presented in this chapter has been previously published in *Academic Radiology* as indicated below, and is reproduced here with permission (Appendix C).

Lauren Villemaire, Amir M. Owrangi, Laura Wilson, Elaine O'Riordan, Roya Etemad-Rezai, Harry Keller, Brandon Driscoll, Glen Bauman, Aaron Fenster and Grace Parraga."Pulmonary Tumour Measurements from X-Ray Computed Tomography in One- Two- and Three-dimensions" Acad Radiol. 2011 Nov;18(11):1391-402.

Pulmonary Tumor Measurements from X-Ray Computed Tomography in One, Two, and Three Dimensions

Lauren Villemaire, BSc, Amir M. Owrangi, MSc, Roya Etemad-Rezai, MD, FRCPC,
Laura Wilson, MSc, Elaine O'Riordan, MD, FRCPC, Harry Keller, PhD, Brandon Driscoll, MSc,
Glenn Bauman, MD, FRCPC, Aaron Fenster, PhD, FCCPM, Grace Parraga, PhD

Rationale and Objectives: We evaluated the accuracy and reproducibility of three-dimensional (3D) measurements of lung phantoms and patient tumors from x-ray computed tomography (CT) and compared these to one-dimensional (1D) and two-dimensional (2D) measurements.

Materials and Methods: CT images of three spherical and three irregularly shaped tumor phantoms were evaluated by three observers who performed five repeated measurements. Additionally, three observers manually segmented 29 patient lung tumors five times each. Follow-up imaging was performed for 23 tumors and response criteria were compared. For a single subject, imaging was performed on nine occasions over 2 years to evaluate multidimensional tumor response. To evaluate measurement accuracy, we compared imaging measurements to ground truth using analysis of variance. For estimates of precision, intraobserver and interobserver coefficients of variation and intraclass correlations (ICC) were used. Linear regression and Pearson correlations were used to evaluate agreement and tumor response was descriptively compared.

Results: For spherical shaped phantoms, all measurements were highly accurate, but for irregularly shaped phantoms, only 3D measurements were in high agreement with ground truth measurements. All phantom and patient measurements showed high intra- and interobserver reproducibility (ICC >0.900). Over a 2-year period for a single patient, there was disagreement between tumor response classifications based on 3D measurements and those generated using 1D and 2D measurements.

Conclusion: Tumor volume measurements were highly reproducible and accurate for irregular, spherical phantoms and patient tumors with nonuniform dimensions. Response classifications obtained from multidimensional measurements suggest that 3D measurements provide higher sensitivity to tumor response.

Key Words: Response evaluation criteria in solid tumors; World Health Organization; pulmonary metastases; three-dimensional tumor measurements; x-ray computed tomography.

Quantitative radiological evaluation of tumor response to therapy using one-dimensional (1D) measurements is still the mainstay of clinical practice, but it is well-understood that in some cases, the responses derived from 1D measurements may not adequately reflect the clinical situation (1,2). The two-dimensional (2D) measurement pioneered by the World Health Organization (WHO) is generated as the cross-product of the longest axis of the tumor and its longest perpendicular bisector (3,4), whereas the 1D measurement or Response Evaluation Criteria in Solid Tumors method (RECIST) is the length of the longest tumor axis (5). Both 1D and 2D measurements require the radiologist to first evaluate all image slices and typically, manual measurements are performed. These and other limitations (6–11) have led to the development of three-dimensional (3D) or volumetric measurements (12–14), which in some cases may be considered more representative estimates of the clinical situation (8,15–18).

The effect of tumor shape on measurement accuracy is important, because lesions are seldom perfectly spherical and often have irregular or difficult-to-define margins in which a change in diameter may not accurately reflect overall changes in tumor size (19). Tumor measurements that incorporate multiple dimensions provide a way to evaluate irregular masses (13,20) and there is consensus that with the increased dimensions, the precision of the measurements is not compromised (20,21). Moreover, it has been suggested that the sensitivity of 3D measurements to therapy response is

---

Acad Radiol 2011; 18:1391–1402

From the Imaging Research Laboratories, Robarts Research Institute, 100 Perth Drive, London, Canada N6A 5K8 (L.V., A.M.O., L.W., A.F., G.P.); Departments of Medical Biophysics (L.V., A.F., G.P.) and Medical Imaging (R.E.-R., E.O'R., A.F., G.P.), Graduate Program in Biomedical Engineering (A.M.O., A.F., G.P.), Princess Margaret Hospital (H.K., B.D.), University Health Network, Toronto, Canada; Department of Oncology, The University of Western Ontario, London, Canada (G.B.). Received April 9, 2011; accepted July 27, 2011. Supported by the Ontario Institute for Cancer Research and Canadian Institutes of Health Research New Investigator

doi:10.1016/j.acra.2011.07.010

TABLE 1. Overview of Analysis Plan

			Observers (*n*)			Measurements per Observer (*n*)		
Tumor Phantoms	Tumors (*n*)	Slice Thicknesses (*n*)	1D	2D	3D	1D	2D	3D
Spheres	3	4	3	3	3	60	60	60
Irregular shapes	3	4	3	3	3	60	60	60
Subject Tumors		Subjects						
Cross-sectional analysis	29	7	3	3	3	145	145	145
Longitudinal analysis: 2 time points	23	5	3	3	3	230	230	230
Longitudinal analysis: 9 time points	2	1	3	3	3	90	90	90

1D, one-dimensional; 2D, two-dimensional; 3D, three-dimensional.

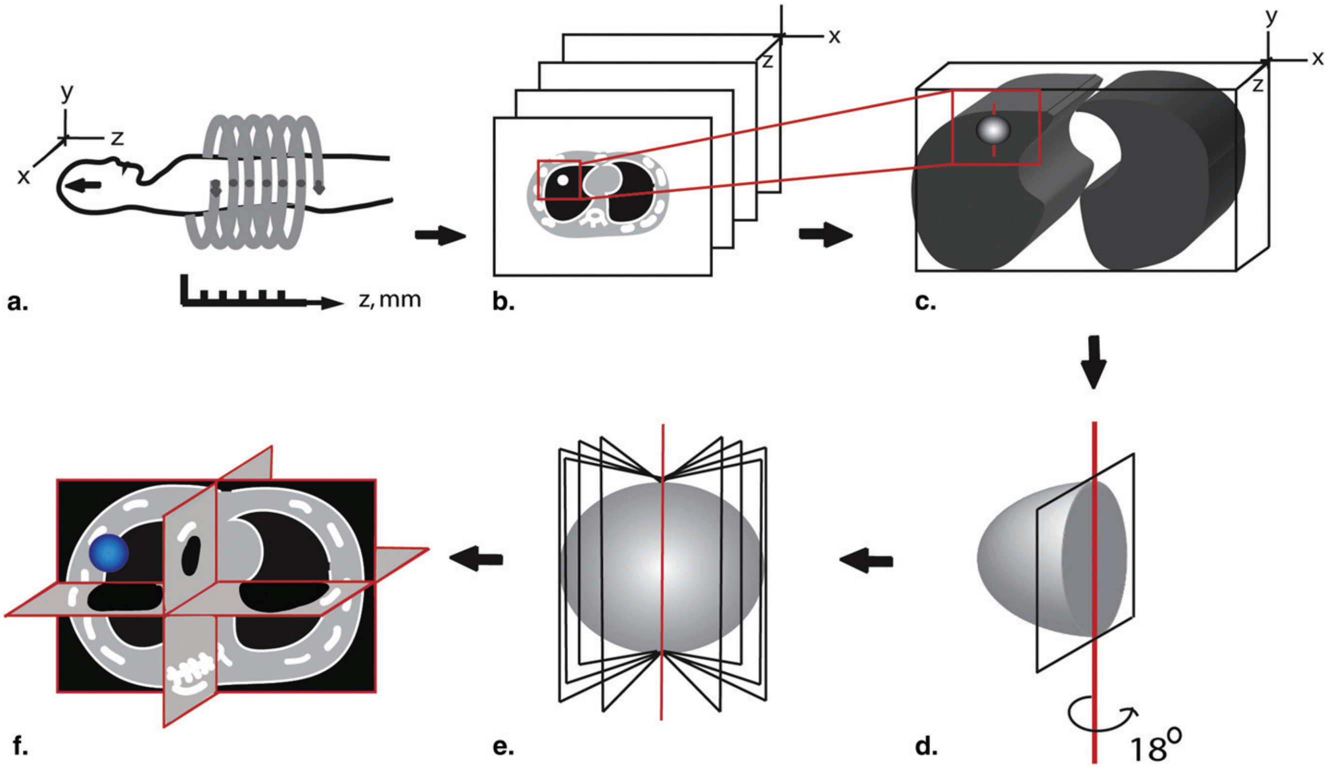

Figure 1. Three-dimensional (3D) segmentation method. **(a)** Phantom/patient is scanned in the craniocaudal direction; **(b)** image slices are displayed on computer monitors using ClearCanvas; **(c)** slices are reconstructed into a volume in 3D Quantify; **(d)** a user-defined rotational axis rotates the tumor volume by 18° and the tumor boundary is delineated; **(e)** after contouring at all 10 rotations, the 3D volume is rendered; **(f)** surface area of segmented tumor is shown in blue as viewed in 3D Quantify.

significantly greater than 1D and 2D measurements (8,14). Unfortunately, there is not yet sufficient evidence to qualify lung tumor volume as a biomarker of solid tumor response (8) and to incorporate this into mainstream radiology workflow. In this regard, it is important to consider tumor response over more than two or three individual time points and currently the majority of previous studies have been limited to at most three independent imaging sessions.

Therefore, the objectives of this study were to: evaluate the accuracy and precision of 1D, 2D, and 3D measurements of pulmonary tumor phantoms of spherical and irregular geometries and compare pulmonary tumor measurements and response according to 1D, 2D, and 3D quantification of pulmonary metastases at multiple time points in subjects with lung cancer. To our knowledge, this is the first direct comparison of a volumetric manual segmentation approach with established 1D and 2D methods in tumor phantoms and patient lung tumors across multiple time points and provides a first step toward semiautomated multidimensional segmentation of lung tumors from computed tomography (CT).

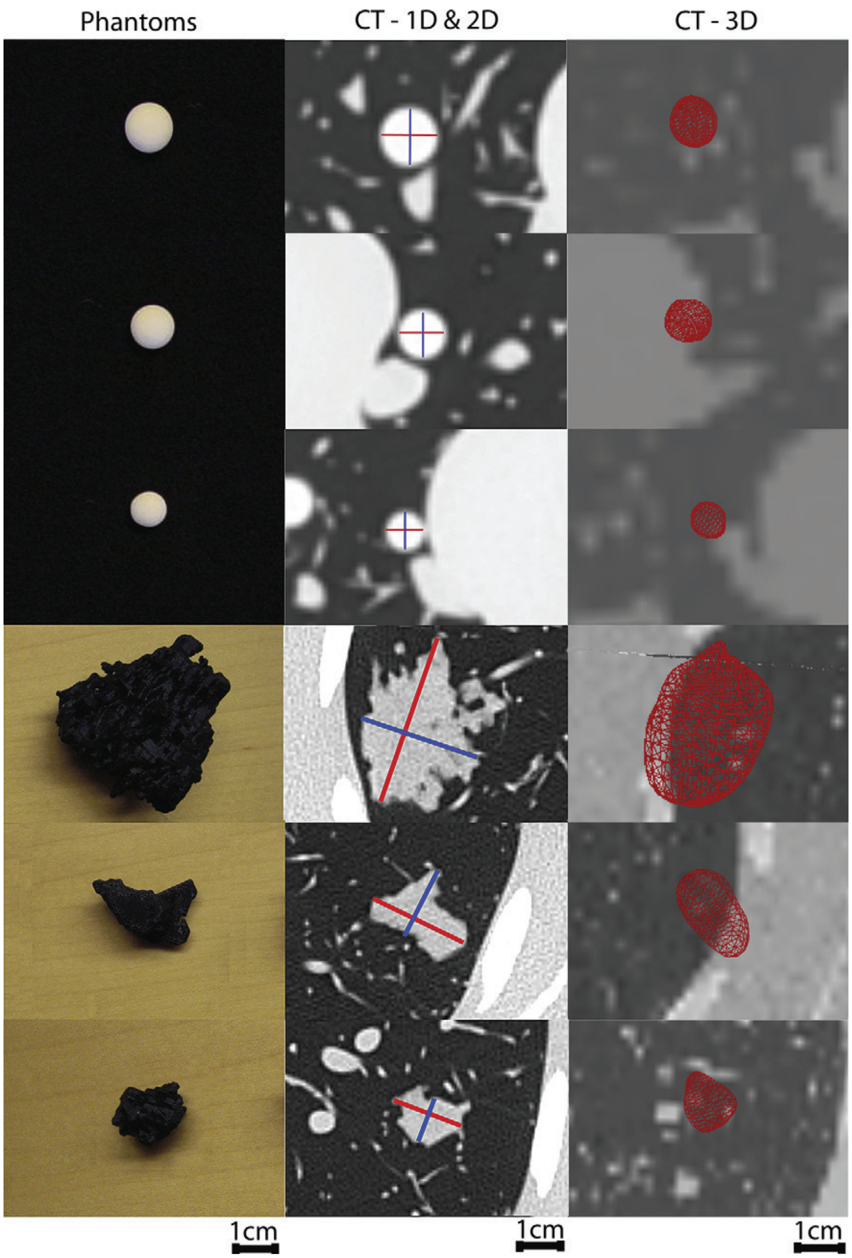

Figure 2. Scaled photographs (*left panel*) of the three spherical (*top panels*) and three irregular-shaped tumor phantoms (*bottom panels*) and computed tomography images with one-dimensional (1D), two-dimensional (2D; *middle panels*), and three-dimensional measurements (*right panel*). In the middle panels, red denotes the longest axis of the tumor for the 1D measurement and blue represents the longest perpendicular axis of the tumor used to calculate the cross-product for 2D measurements.

MATERIALS AND METHODS

Lung Tumor Phantom Imaging

A commercially available chest phantom (Kyoto Kagaku Co. Ltd., Kyoto, Japan) constructed with the relative proportions of a Japanese human adult thorax simulating soft tissue, bone, mediastinum (including the heart and trachea), and the pulmonary arterial tree was used. Three spherical tumor phantoms included with the chest phantom were used for imaging as well as three irregularly shaped tumor phantoms custom-built for this study using a plastic, acrylonitrile butadiene styrene. The irregularly shaped phantoms were constructed using 3D lithography based on 3D renderings of patient lung tumors from a database of lung tumors generated in house. Ground truth 1D and 2D measurements were estimated based on calliper measurements of the spherical tumors, and volumes were calculated based on the diameter (D) obtained from the calliper measurements using:

$$V = \frac{1}{6}\pi D^3 \qquad (1)$$

For the irregular phantoms, ground truth 1D and 2D measurements were based on caliper measurements, and volume estimates were made based on measurements using volumetric displacement measurement. All phantom CT imaging was performed using a Toshiba Aquilion One 320-slice system (Toshiba America Medical Systems, Tustin, CA). Images were acquired in helical mode at 120 kV,

TABLE 2. Mean of Measurements at 2.0-mm Slice Thickness of Solid Spherical Tumors and Irregular-shaped Tumors and Ground Truth Measurements

Mean (SD) [COV]			
Observers	1D (cm)	2D (cm^2)	3D (cm^3)
Spherical phantoms		Tumor 1	
1	1.20 (0.00) [0]	1.44 (0.00) [0]	0.82 (0.08) [9.4]
2	1.20 (0.00) [0]	1.44 (0.00) [0]	1.00 (0.13) [12.8]
3	1.20 (0.00) [0]	1.42 (0.05) [3.8]	0.89 (0.05) [6.1]
Ground truth	1.19 (0.00) [0.4]	1.40 (0.00) [0.6]	0.87 (0.01) [1.2]
Interobserver COV	0	0.8	10
		Tumor 2	
1	1.00 (0.00) [0]	1.00 (0.00) [0]	0.50 (0.06) [9.7]
2	1.00 (0.00) [0]	1.00 (0.00) [0]	0.58 (0.08) [13.6]
3	1.00 (0.00) [0]	1.00 (0.00) [0]	0.53 (0.03) [5.5]
Ground truth	0.99 (0.00) [0.2]	0.99 (0.00) [0.4]	0.51 (0.00) [0.5]
Interobserver COV	0	0	7.5
		Tumor 3	
1	0.80 (0.00) [0]	0.64 (0.00) [0]	0.23 (0.02) [10.9]
2	0.80 (0.00) [5.7]	0.61 (0.07) [11]	0.30 (0.05) [16.5]
3	0.80 (0.00) [5.7]	0.55 (0.03) [5.7]	0.27 (0.02) [6.1]
Ground truth	0.78 (0.00) [0.5]	0.62 (0.00) [1]	0.25 (0.00) [1.5]
Interobserver COV	0	7.6	13.2
Irregular shapes		Tumor 4	
1	4.20 (0.00) [1.3]	11.54 (0.32) [3.7]	14.69 (0.54) [3]
2	4.01 (0.2) [5.1]	11.87 (0.60) [5]	15.24 (1.34) [8.8]
3	4.16 (0.05) [1.3]	11.57 (0.42) [3.7]	13.71 (0.41) [3]
Ground truth	5.16 (0.00) [0]	23.33 (0.03) [0.1]	16.83 (0.02) [0.1]
Interobserver COV	1.7	9.4	18.6
		Tumor 5	
1	2.60 (0.00) [1.7]	4.00 (0.00) [4.5]	2.61 (0.06) [6.3]
2	2.53 (0.02) [0.9]	4.25 (0.18) [4.1]	2.99 (0.25) [8.4]
3	2.58 (0.04) [1.7]	3.97 (0.18) [4.5]	2.48 (0.16) [6.3]
Ground truth	3.26 (0.00) [0]	7.38 (0.00) [0.1]	2.66 (0.04) [1.4]
Interobserver COV	3.4	5.5	10.3
		Tumor 6	
1	1.30 (0.00) [0]	1.66 (0.06) [3.5]	1.08 (0.05) [1.8]
2	1.87 (0.03) [1.6]	2.19 (0.08) [3.6]	1.46 (0.15) [10.3]
3	1.30 (0.00) [0]	1.66 (0.06) [3.5]	1.17 (0.14) [12.3]
Ground truth	2.11 (0.00) [0]	3.42 (0.00) [0.1]	1.21 (0.03) [2.4]
Interobserver COV	16.9	18.6	29.9

1D, one-dimensional; 2D, two-dimensional; 3D, three-dimensional; COV, coefficient of variance; SD, standard deviation.
Intra- and interobserver COV is expressed in %.

200 mA (512 × 512 matrix, field of view 35 × 35cm), and were reconstructed with 0.5-, 1.0-, 2.0-, and 5.0-mm slice thicknesses.

Study Subject Imaging

The study protocol was approved by The University of Western Ontario Research Ethics Board and written informed consent was not required from the study subjects because image data were deidentified, anonymized, and retrospectively collected from clinical cases in which CT images were acquired between January 2005 and December 2007. Seven study subjects with 29 tumors were evaluated at a single time point: six of these subjects had a clinical diagnosis of renal cell carcinoma with lung metastases, and one subject had an unknown primary cancer diagnosis with lung metastases. Five subjects with 23 tumors returned for a follow-up imaging, whereas a single subject with 2 tumors returned for a total of 9 follow-up visits over 2 years. All subjects scans were performed using a helical General Electric LightSpeed Series CT scanner (VCT or Ultra; GE HealthCare, Waukesha, WI) with the following parameters: 120 kV, exposure time = 600 ms, field of view = 36 × 36 cm, and pixel matrix = 512 × 512. For three subjects, CT data were reconstructed with a 2.5-mm slice thickness, and the remaining scans were reconstructed with a 5.0-mm slice thickness.

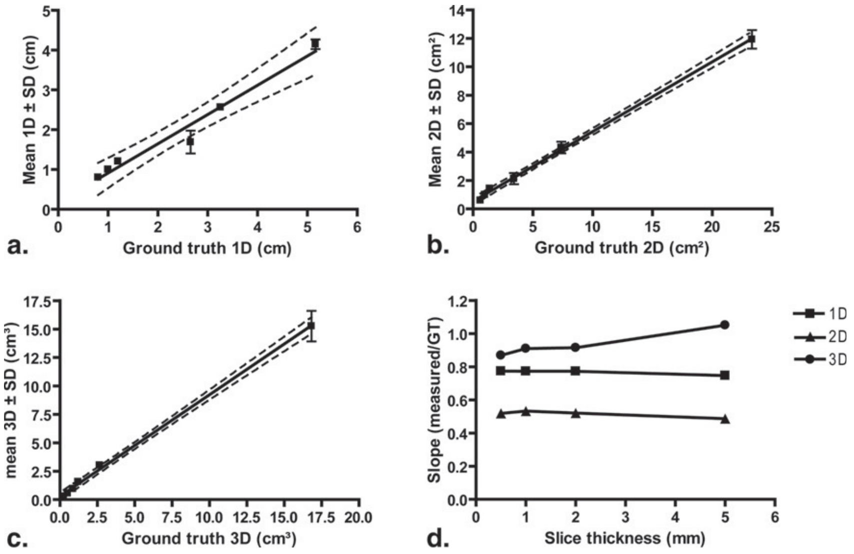

Figure 3. Relationship between ground truth and multidimensional measurements for all phantom tumors at 2.0-mm slice thickness. The 95% confidence intervals for the regressions are shown as dotted lines. Association between measurements and ground truth **(a)** one-dimensional (1D; r^2 = 0.97, r = 0.98, P < .001), **(b)** two-dimensional (2D; r^2 = 0.99, r = 0.99, P < .001), and **(c)** three-dimensional (3D; r^2 = 0.99, r = 0.99, P < .001). **(d)** Accuracy as a function of slice thickness and measurement dimensionality for irregular-shaped phantoms. Mean tumor phantom measurements were plotted versus ground truth measurements and the slope of the line of best fit was calculated. The mean linear slope for 3D volume was 0.94, 2D = 0.52, and 1D = 0.77. GT, ground truth.

Image Analysis

Table 1 provides an overview of the image analyses performed by multiple observers for all phantom and patient tumors. For the phantoms, three observers measured three tumors at four slice thicknesses and repeated the measurements five times generating a total of 60 measurements per observer. Each observer was blinded to the ground truth dimensions and repeated measurement trials were performed with at least 1 day between trials. In addition, to try to minimize the potential for memory bias, we provided each observer with randomized and blinded datasets for each repeated measurement trial and the observers performed other radiological evaluations in the downtime between repetition rounds to diminish potential tumor segmentation memory.

For subject tumor images, one medical oncologist first retrospectively reviewed all CT images; the tumor locations were confirmed by two experienced radiologists. For the single time-point analysis, three observers performed five repeated measurements of 29 tumors generating 145 measurements per observer. For the time-points analysis, 23 tumors were measured at two time points and repeated five times for 230 measurements per observer. Finally, for the nine time-points analysis, two tumors were measured at nine time points and repeated five times each, generating 90 measurements per observer. Observers were blinded to subject identity, clinical status, and time point. CT images were displayed on LCD screens using conventional parameters for lung (window width: 1600 HU, window center: -550) (22). Each observer was enabled to magnify and manipulate window and level settings to optimize the display of each tumor deposit. All observers were medical physicists trained by an experienced chest radiologist (R.E.R.) over three 1-hour training sessions and this radiologist also identified all tumor locations prior to segmentation. To evaluate the relationship between trained observer measurements with expert measurements, linear regression was performed. Once strong (r^2 ≥ 0.9) and significant correlations were observed for any individual trainee, they were deemed appropriately trained to perform measurements.

TABLE 3. Intraclass Correlation Coefficients for 1D, 2D, and 3D Measurements of Spherical and Irregular-shaped Tumor Phantoms and Patient Tumors

	1D		2D		3D	
Observer	ICC (A)	ICC (C)	ICC (A)	ICC (C)	ICC (A)	ICC (C)
Spherical phantoms						
1	1.000	1.000	1.000	1.000	0.967	0.963
2	0.985	0.985	0.991	0.991	0.937	0.986
3	0.985	0.985	0.993	0.996	0.986	0.990
All observers	0.999	0.999	0.995	0.996	0.965	0.990
Irregular shapes						
1	0.988	0.988	0.995	0.995	0.989	0.991
2	1.000	1.000	0.991	0.995	0.996	0.996
3	0.999	0.999	0.997	0.998	0.999	0.999
All observers	0.973	0.971	0.994	1.000	0.982	0.993
Patient tumors						
1	0.992	0.994	0.994	0.994	0.966	0.969
2	0.978	0.982	0.989	0.991	0.992	0.993
3	0.970	0.973	0.938	0.953	0.970	0.974
All observers	0.949	0.949	0.976	0.975	0.985	0.987

1D, one-dimensional; 2D, two-dimensional; 3D, three-dimensional; ICC, intraclass correlation coefficients.

Image analysis for 1D and 2D measurements was performed using electronic calipers using an open-source picture archiving and communication system (ClearCanvas, Inc., Toronto, Canada). Volumetric analysis was performed using a customized visualization and segmentation software developed in-house, 3D Quantify (Robarts Research Institute, London, ON), as previously described (23). Lung tumor volumes were estimated from the manual segmentation of tumor boundaries using VTK (Visualization Toolkit; Kitware, Inc, Clifton Park, NY). The method used to quantify tumor volume is illustrated in the schematic in Figure 1 whereby axial CT images of the subject/phantom were reconstructed into a volume in 3D Quantify. The observer first defined a rotational axis by generating a line segment across the observer estimated geometric center of the tumor. After segmenting the tumor boundary in this central plane, the plane was rotated about this axis at an angle of 18° and the tumor boundary was segmented again in the new plane. In this manner, 10 unique boundaries were segmented for each tumor to generate a surface, and each contour set was converted to a 3D mesh, in which the radial distance from the center of mass was calculated at each angle to generate the total volume of the tumor. Ten surface segmented boundaries per tumor was selected as a consensus based on the tumor sizes and slice thickness of the dataset, but it is important to note that any number of tumor boundaries could be selected to estimate volume.

Statistical Analysis

Mean 1D, 2D, and 3D measurements and standard deviations were calculated from five repeated measurements for all phantom tumors as well as individual subject tumors. All statistical analyses was performed using PASW Statistics version 18 (PASW Inc., Chicago, IL, 2009) and results were considered significant when the probability of making a type I error was less than 5% ($P < .05$). Measurement accuracy for tumor phantoms was estimated whereby the observer measurements obtained at different reconstructed slice thicknesses and ground truth measurements were evaluated using a one-way analysis of variance (ANOVA).

To evaluate precision for phantoms and patient tumors, inter- and intra-observer reproducibility was evaluated using the coefficient of variation (COV, standard deviation divided by the mean), the Intraclass Correlation Coefficient (ICC) for absolute agreement [ICC(A)] and consistency [ICC(C)]. The difference between baseline and follow-up tumor measurements was evaluated using the new RECIST 1.1 and WHO criteria and a mean difference was reported. GraphPad Prism version 4.01 for Windows (GraphPad Software Inc., La Jolla, CA, 2004) was used to perform linear regressions and for the generation of Pearson correlation coefficients.

The accuracy of each measurement was estimated as a function of slice thickness by plotting ground truth measurements versus CT-derived measurements for 1D, 2D, and 3D measurements at each slice thickness with the slope of the line of best fit through the data and origin used to describe accuracy (21).

RESULTS

Phantom Measurements

Scaled photographs and CT images of the three spherical and three irregularly shaped tumor phantoms with 1D, 2D, and 3D measurements are provided in Figure 2.

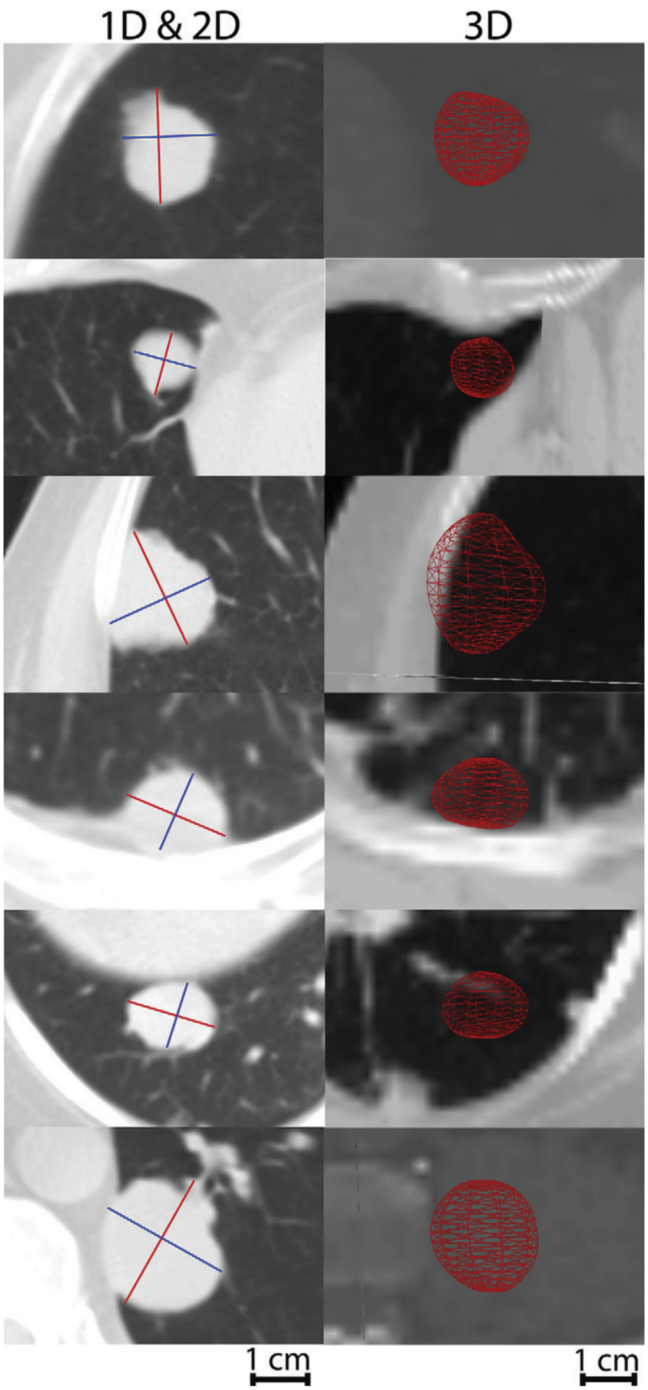

Figure 4. Computed tomography images of six representative patient lung tumors with one-dimensional, two-dimensional (*left panel*), and three-dimensional measurements (*right panel*).

As summarized in Table 1, all tumor phantoms were measured using four different slice thicknesses (0.5 mm, 1.0 mm, 2.0 mm, 5.0 mm). Here we focus on 2.0-mm reconstruction image measurement accuracy because this is most applicable to the clinical standard. Mean, standard deviation, and COV of all measurements for spherical tumor phantoms 1–3 and irregularly shaped phantoms 4–6 at 2.0-mm slice thickness and the corresponding ground truth measurements

TABLE 4. Mean of 1D, 2D, and 3D Measurements Total Tumor Burden For Each Subject

Mean (SD) [COV]			
Observers	1D (cm)	2D (cm^2)	3D (cm^3)
Subject 1			
1	1.70 (0.20) [10.9)	2.54 (0.50) [19.65]	3.49 (0.46) [13.1]
2	1.70 (0.10) [7.7]	2.72 (0.30) [11]	3.84 (0.66) [17.2]
3	1.60 (0.00) [0.0]	2.18 (0.09) [4]	3.27 (0.14) [4.4]
Interobserver COV	6.3	11.9	11.9
Subject 2			
1	6.80 (0.20) [2.8]	20.14 (0.71) [3.6]	38.69 (4.47) [11.6]
2	6.70 (0.40) [5.4)	20.42 (1.69) [8.3]	38.30 (2.35) [6.1]
3	6.50 (0.20) [2.6]	20.50 (0.84) [4.1]	37.60 (4.22) [11.2]
Interobserver COV	3.6	5.3	9.6
Subject 3			
1	14.70 (0.20) [1.4]	42.12 (1.18) [2.8]	96.70 (7.56) [7.8]
2	14.50 (0.30) [1.9]	41.90 (1.28) [3.1]	85.02 (6.49) [7.6]
3	14.70 (0.30) [2.2]	42.70 (1.12) [2.6]	79.17 (10.25) [13]
Interobserver COV	1.8	2.8	9.3
Subject 4			
1	3.80 (0.10) [2.2]	6.30 (0.40) [6.4]	9.19 (1.27) [13.8]
2	3.70 (0.20) [4.1]	6.05 (0.63) [10.5]	8.26 (1.21) [14.6]
3	3.80 (0.20) [5.9]	6.39 (0.35) [5.4]	7.03 (0.96) [13.6]
Interobserver COV	4.1	7.4	14
Subject 5			
1	5.00 (0.10) [3]	6.14 (0.35) [5.7]	9.71 (0.96) [9.9]
2	4.60 (0.30) [5.8]	5.40 (0.49) [9.2]	6.94 (1.03) [14.8]
3	4.50 (0.30) [6.1]	5.54 (0.45) [8.1]	5.96 (0.82) [13.7]
Interobserver COV	4.9	7.6	12.4
Subject 6			
1	20.50 (0.10) [0.3]	32.74 (0.61) [1.9]	37.42 (2.43) [6.5]
2	19.90 (1.00) [5.2]	30.66 (2.63) [8.6]	45.21 (4.37) [9.7]
3	19.60 (0.50) [2.7]	30.11 (1.27) [4.2]	37.91 (4.61) [12.2]
Interobserver COV	2.7	4.8	9.5
Subject 7			
1	8.50 (0.10) [1]	11.96 (0.35) [2.9]	40.40 (10.82) [26.8]
2	8.00 (0.30) [3.9]	10.60 (0.77) [7.3]	38.93 (8.76) [22.5]
3	7.60 (0.10) [0.7]	9.81 (0.24) [2.5]	39.60 (1.30) [3.3]
Interobserver COV	1.9	4.2	17.6

1D, one-dimensional; 2D, two-dimensional; 3D, three-dimensional; COV, coefficient of variance; SD, standard deviation.
Intra- and inter-observer COV is expressed in %.

are provided in Table 2 for three observers. A one-way ANOVA indicated that there was no significant difference between observer and ground truth measurements for all three spherical lung tumor phantoms and all measurements (1D/2D/3D). For all three irregularly shaped tumor phantoms, 1D and 2D measurements were significantly different from ground truth. For 3D measurements, however, only one of the three observers reported significantly different measurements from ground truth. Similar results were obtained for all other slice thickness reconstructions. The relationship between ground truth and CT-derived measurements for all tumor phantoms is shown in Figure 3a–c and the relationship between measurement accuracy and slice thickness is summarized in Figure 3d for irregularly shaped phantoms. As shown in Figure 3a–c, there was a strong and significant relationship between ground truth and 1D ($r^2 = 0.97$, $r = 0.98$, $P < .001$), 2D ($r^2 = 0.99$, $r = 0.99$, $P < .001$), and 3D ($r^2 = 0.99$, $r = 0.99$, $P < .001$) measurements. As shown in Figure 3d, mean slope was 0.94 for 3D measurements compared to 1D (mean slope = 0.77) and 2D measurements (slope = 0.515), respectively. Interobserver COV is also provided in Table 2 and intraclass correlation coefficients for spherical and irregularly shaped phantoms are provided in Table 3.

Patient Lung Tumor Measurements

Repeated 1D, 2D, and 3D measurements for 29 tumors in seven patients were performed five times by three observers to generate intraobserver and interobserver reproducibility estimates. CT images of six representative patient lung tumors with 1D, 2D, and 3D measurements are shown in Figure 4. Mean, standard deviation, and intra- and interobserver

TABLE 5. Mean Tumor Burden ± Standard Deviation for 1D, 2D, and Volumetric Measurements

Subject No.	No. of Tumors	Baseline Mean Tumor Burden (±Standard Deviation)	Follow-up Mean Tumor Burden (±Standard Deviation)	Fractional Change (%)	Response Classification
1D (cm)					
1	2	6.84 ± 0.06	6.52 ± 0.04	−4.68	SD
2	5	14.8 ± 0.03	13.66 ± 0.04	−7.7	SD
3	2	3.86 ± 0.06	4.50 ± 0.05	16.58	SD
4	3	4.52 ± 0.04	5.34 ± 0.04	18.14	SD
5	11	20.34 ± 0.02	19.98 ± 0.05	−1.77	SD
2D (cm^2)					
1	2	20.33 ± 0.46	19.16 ± 0.41	−5.76	SD
2	5	43.32 ± 0.15	36.68 ± 0.23	−15.33	SD
3	2	6.56 ± 0.16	8.17 ± 0.19	24.56	SD
4	3	5.53 ± 0.06	7.01 ± 0.08	26.76	PD
5	11	31.88 ± 0.05	26.18 ± 0.33	−17.88	SD
3D (cm^3)					
1	2	38.26 ± 0.80	39.99 ± 1.11	4.52	SD
2	5	84.98 ± 1.20	77.91 ± 0.73	−8.32	SD
3	2	7.67 ± 0.87	8.72 ± 0.40	13.69	SD
4	3	6.30 ± 0.51	8.50 ± 0.29	34.92	SD
5	11	40.4 ± 0.23	40.79 ± 0.22	0.97	SD

1D, one-dimensional; 2D, two-dimensional; 3D, three-dimensional; PD, progressive disease; SD, stable disease.

Performed by a single observer at baseline and follow-up scan along with fractional change (%) and corresponding response classifications for each subject.

COV for all subject lung tumor measurements are provided for three observers in Table 4. ICC for repeated measurements are provided in Table 3.

Five subjects with 23 tumors were evaluated at a second time point, and three observers evaluated tumor sizes in 1D, 2D, and 3D at both time points. Mean tumor burden, the sum of all tumor measurements in each subject, is reported in Table 5 at both time points for the five subjects. The fractional change is reported as a percent change, which corresponds to the difference in size between baseline and follow-up divided by the size at baseline expressed as a percent (13). Positive values of change represent tumor growth, and negative values represent tumor shrinkage. These were used to stratify tumor response by classifying the tumors into a response category as progressive disease, partial response, stable disease, or complete response. For 1D measurements, tumor response was categorized using the new RECIST guidelines (5) and for 2D measurements, tumor response was categorized using the established WHO criteria for adult patients with cancer (4). For volumetric 3D measurement of tumor response, we used a volume increase greater than 40% for progressive disease and a volume reduction of at least 65% for partial response. A change in size less than the above fractional changes would classify the response as stable. These thresholds were used as they corresponded to existing response categories for 2D measures of response, assuming the tumor changed uniformly (13).

All five response classifications determined by direct 3D measurements agreed with the five RECIST classifications, whereas four 3D classifications agreed with the WHO classifications. Two tumors in patient 3 were also evaluated on nine occasions over 2 years. Changes in tumor dimensions were used to generate response classifications by calculating the fractional change (%) between scans. CT images of both tumors at each time point are shown in Figure 5. Tumor 1 is shown using the typical lung viewing window parameters, whereas tumor 2 is shown with both lung and bone window parameters, because of difficulties in defining tumor boundaries using the lung window alone. Plots of the multidimensional tumor changes are provided in Figure 6.

DISCUSSION

The successful development and translation of volumetric CT image quantification methods, whether manual, semiautomated, or fully automated requires an understanding of measurement precision and accuracy and an understanding of the relationship between the objective responses obtained using the different measurements. To better understand imaging measurement precision and reproducibility and to provide guidance for the use of 3D measurements of lung tumors from clinical CT, we prospectively evaluated lung tumor phantoms and retrospectively evaluated lung tumors in patients using 1D, 2D, and 3D measurements. Previously published studies have also recently evaluated 1D, 2D, and 3D phantom and tumor measurements as summarized in Table 6 (1,9,12,14,16,20–22,24). Unfortunately, and despite the excellent foundation this previous work provides, none of

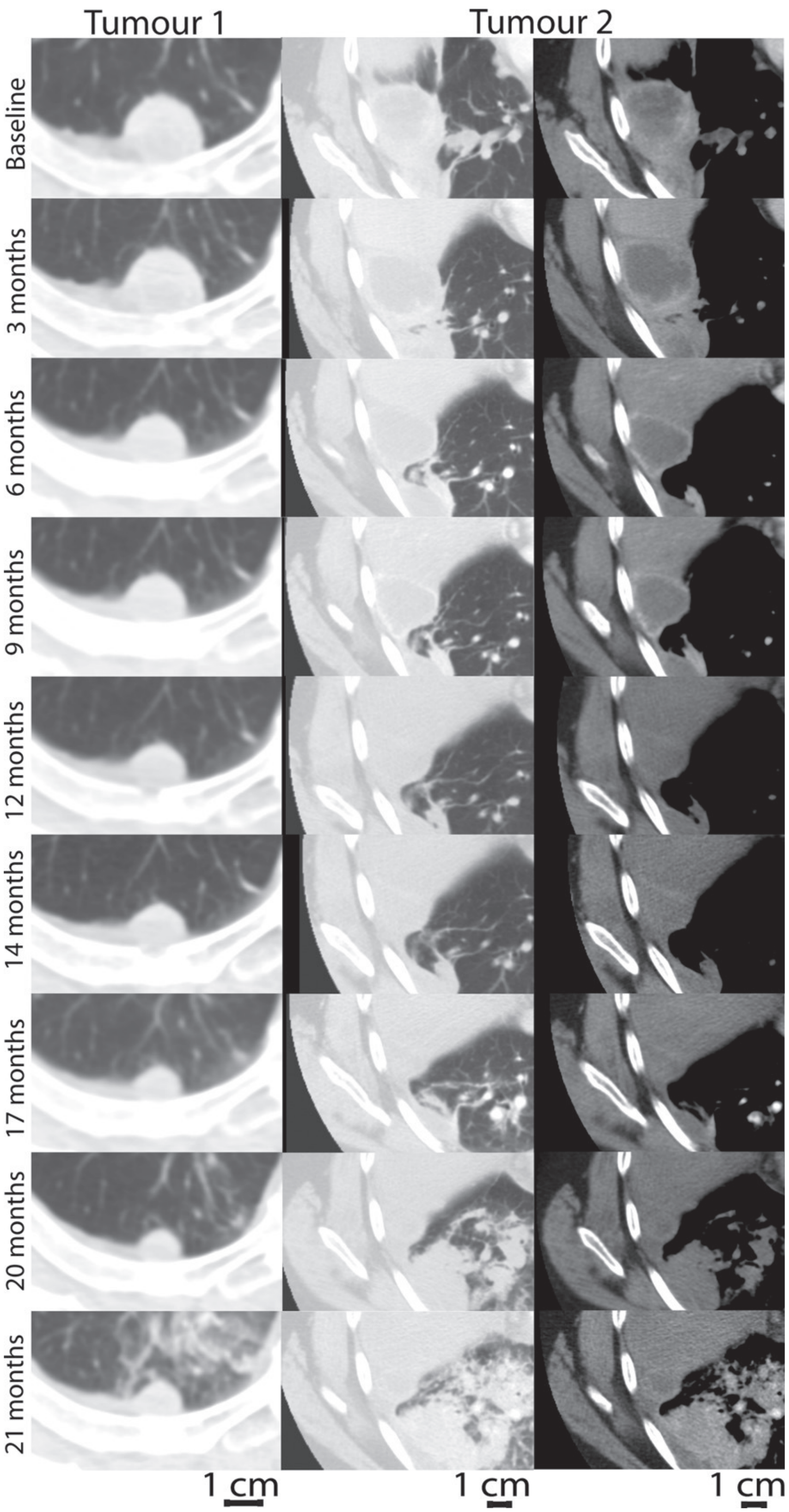

Figure 5. Computed tomography images of two metastatic lung tumors (*left panel*: tumor 1, lung window; tumor 2, middle, lung window, and right panel, chest window) for subject at nine time points over 2 years.

these studies evaluated a single tool by interrogating measurement accuracy and precision in phantoms, repeated measures reproducibility and correlations in patients and potential differences in patient response during multiple time-point imaging evaluations. Because of this, we were motivated to specifically compare the accuracy and reproducibility of

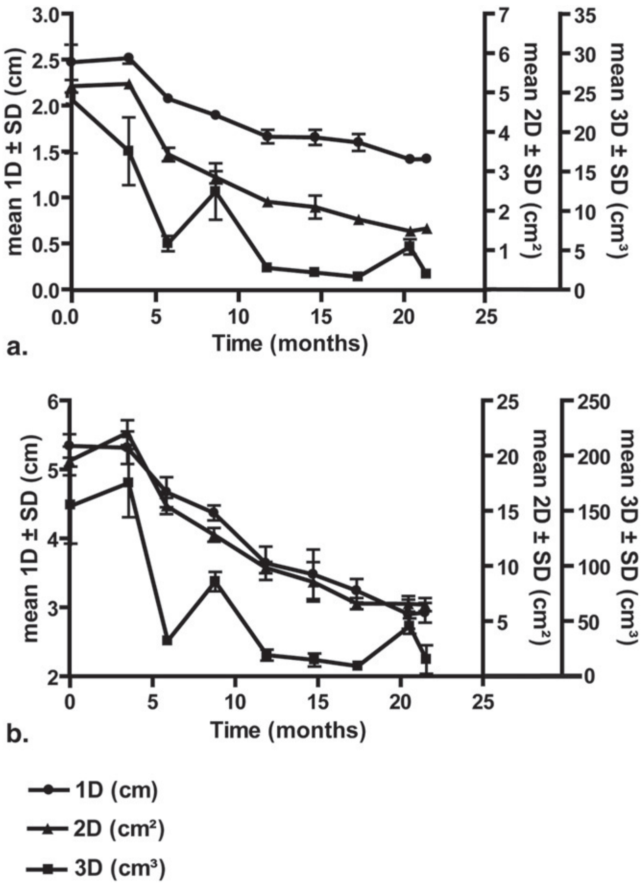

Figure 6. Longitudinal changes in **(a)** tumor 1 and **(b)** tumor 2 one-dimensional, two-dimensional, and three-dimensional measurements.

multidimensional CT-derived tumor measurements in regular and irregular phantoms and in clinical CT of patients with lung tumors. Therefore the novelty of this work stems from the integrated evaluation of precision and accuracy estimates of tumor phantoms under research conditions and patient data acquired in the clinical setting without parameter optimization for segmentation. We also recognized the potential for volumetric measurements to aid in the development of new therapies that when administered to patients might result in changes in tumor volume but not conventional 1D and 2D measurements. Accordingly, here we provide the results of a phantom and patient tumor study that compares pulmonary tumor measurements from CT and report multiple observer 1D, 2D, and 3D: 1) measurement accuracy and interobserver and intraobserver reproducibility of spherical and irregular tumor phantoms, 2) patient tumor intra- and interobserver reproducibility, 3) comparison of patient response criteria based on two imaging sessions, and 4) evaluation of two lung tumors in a single patient scanned on nine occasions over a 2-year period.

First, we evaluated spherical and irregular phantoms accuracy and observed that for regular spherical tumor phantoms; all measurements were not significantly different from ground truth for all observers. However, and as might be expected, for the irregularly shaped tumor phantoms, ANOVA detected significant differences for all observers for 1D and 2D measurements, but correlations were strong and significant. On the other hand, for two of three observers, volumetric measurements were not significantly different from ground truth. The inaccuracy observed for a single observer may have been due to the chosen rotational axis, because important features of the tumor may not have been captured between each of the 10 18° rotations. Measurement accuracy of spherical and irregularly shaped phantoms was not influenced by slice thickness as evidenced by the relatively constant slope (ratio of CT-derived measurement to ground truth) as a function of slice thickness. Figure 3d clearly indicates that 3D measurements of irregular phantoms were highly accurate with a slope near 1, although at the largest slice thickness there appears to have been an overestimate of the CT measurement compared to ground truth for 3D measurements only. This might be expected given the dimensions of the tumors compared to the 5-mm slice thickness reconstruction images evaluated. These results also suggest that for optimal 3D tumor imaging and segmentation in the clinic and clinical trials, slice thicknesses less than 5 mm should be used.

Intra- and interobserver reproducibility was also evaluated using COV, linear regression, and ICC for spherical and irregularly shaped tumor phantoms. We observed that all measurements were highly reproducible (ICC >0.900) for each observer and interobserver COV ranged from 0.0% to 29.9%. These findings were in good agreement with previous findings of Prionas et al (21), Ravenel et al (12), and Winer-Muram et al (25).

Three observers also evaluated 29 pulmonary metastases in seven different subjects and the same observers evaluated repeated scanning measurements for five of the original seven subjects (with 23 tumors) who returned for follow-up imaging. Previous studies have also evaluated the reproducibility of 1D, 2D, and 3D measurements and observed high interobserver and intraobserver reproducibility (26). In this study, all three measurements showed high intra- and interobserver reproducibility with ICC(A) and ICC(C) values exceeding 0.900 and intra- and interobserver COV ranging from 0.0% to 26.8% and 1.9% to 17.6%, respectively. For longitudinal imaging, RECIST and volumetric measurement response classifications were in complete agreement, but one of five response classifications obtained from WHO criteria was not in agreement with volumetric measurements. In this case, patient 5 was classified as having progressive disease by WHO, whereas volumetric analysis generated a classification of stable disease. This discrepancy in response classification can have major effects on a patient's treatment plan, making it clear how imperative it is to have an accurate and sensitive method of quantifying tumor growth.

Finally, we evaluated multidimensional tumor measurements for a single patient with two pulmonary metastases over nine examinations in 2 years. Because irregular patterns of growth tend to increase over time (8), evaluating tumor response over nine time points is key to truly determining how 1D, 2D, and 3D measurements influence treatment

TABLE 6. Previous Studies Related to the Quantification of Lung Tumor Growth or Response

	1D	2D	3D	Slice Thicknesses (mm)	Phantom Spherical	Phantom Irregular	Patient 1 Time Point	Patient Multiple Time Points
Prionas et al, 2010 (21)	ND	ND	Yes	0.625 1.25 2.50 5.0	Yes	ND	ND	ND
Sohns et al, 2010 (20)	Yes	Yes	Yes	0.625	ND	ND	ND	baseline + 1 follow-up
Ravenel et al, 2008 (12)	ND	ND	Yes	0.625 1.25	Yes	ND	ND	ND
Schwartz et al, 2006 (1)	Yes	Yes	ND	ND	ND	ND	ND	Baseline + avg. 3.1 follow-ups
Petrou et al, 2006 (24)	ND	ND	Yes	1.25 2.50 5.0	ND	ND	Yes	ND
Zhao et al, 2006 (14)	Yes	Yes	Yes	1.25	ND	ND	ND	Baseline + 1 follow-up
Revel et al, 2004 (9)	ND	Yes	ND	1.25 2.50	ND	ND	Yes	ND
Tran et al, 2004 (16)	Yes	Yes	Yes	3	ND	ND	ND	Baseline + 2 follow-ups
Erasmus et al, 2003 (22)	Yes	Yes	ND	7	ND	ND	ND	Baseline + 1 follow-up

response evaluation. In this examination of response classifications, there was significant discordance between 3D measurement response and those generated using 1D and 2D measurements. For example, in this case, where WHO and RECIST criteria is classified response as stable disease, volumetric measurements more frequently classified the disease as progressive or partial response. This inconsistency in response classifications was also previously observed by Tran and colleagues (16). On the other hand, there was no notable difference in tumor response classification between 1D and 2D measures of tumor response, which agrees with the findings of Sohaib et al (13).

We must acknowledge a number of specific study limitations that warrant discussion. First we must acknowledge that although phantoms and patient data were evaluated, there was a limited sample size for phantom (6) and the multiple time-point patient study (nine time points, two tumors) that certainly limits generalizable conclusions beyond repeated measures precision and accuracy estimates. We recognize that for irregular tumor phantoms, the ground truth longest and perpendicular axes were orientation-specific and the underestimation of 1D and 2D measurements may be related to the positioning of tumors within the chest phantom. The longest axis displayed on the CT image may not have been the same longest axis measured on the tumor and this can also be the case with patient imaging as well. This further demonstrates the reliance of 1D and 2D measurement dependence on the exact location where the observer chooses to measure these axes. We must also consider for all measurements that there certainly is the potential for observer variability because of the window level (WL) and window width (WW) settings when making such measurements. In other words, it is well known that observer manual segmentation of tumors is often dependent on WL and WW settings. In practice, the WL/WW may be adjusted to optimize 3D measurements rather than using established lung/bone window settings. Automation of such measurements will clearly help in this regard. Automation of such measurements will clearly help in this regard and this is the critical next step required to accelerate translation to mainstream radiology workflows. We also acknowledge that manual 3D segmentations is very time consuming, which is a limitation that has been previously acknowledged (11) as an obstacle for translation to clinical workflows. One solution to this limitation may be achieved with the development of automated segmentation tools and this study provides important groundwork for the development of such semiautomated and automated 3D measurement tools.

Before volumetric tumor quantification can replace current 1D and 2D methods, the relationship of these measurements' accuracy and precision should be determined. For regularly shaped lung tumors in patients and phantoms and as well irregularly shaped phantoms, volume measurements were highly reproducible and accurate. Comparisons between response classifications obtained from 1D, 2D, and 3D measurements suggests that volumetric measurements may provide a different window on clinical response, which argues for improved automated volumetric measurement approaches.

ACKNOWLEDGMENTS

The authors thank S. Halko, S. McKay, and A. Wheatley for their ongoing support.

REFERENCES

1. Schwartz LH, Colville JA, Ginsberg MS, et al. Measuring tumor response and shape change on CT: esophageal cancer as a paradigm. Ann Oncol 2006; 17:1018–1023.
2. Dempsey MF, Condon BR, Hadley DM. Measurement of tumor "size" in recurrent malignant glioma: 1D, 2D, or 3D? AJNR Am J Neuroradiol 2005; 26:770–776.
3. World Health Organization: WHO Handbook for reporting results of cancer treatment. WHO offset publication no. 48. Geneva, Switzerland: World Health Organization, 1979.
4. Miller AB, Hoogstraten B, Staquet M, et al. Reporting results of cancer treatment. Cancer 1981; 47:207–214.
5. Therasse P, Arbuck SG, Eisenhauer EA, et al. New guidelines to evaluate the response to treatment in solid tumors. European Organization for Research and Treatment of Cancer, National Cancer Institute of the United States, National Cancer Institute of Canada. J Natl Cancer Inst 2000; 92: 205–216.
6. Belton AL, Saini S, Liebermann K, et al. Tumor size measurement in an oncology clinical trial: comparison between off-site and on-site measurements. Clin Radiol 2003; 58:311–314.

7. Lavin PT, Flowerdew G. Studies in variation associated with the measurement of solid tumors. Cancer 1980; 46:1286–1290.
8. Mozley PD, Schwartz LH, Bendtsen C, et al. Change in lung tumor volume as a biomarker of treatment response: a critical review of the evidence. Ann Oncol 2010; 21:1751–1755.
9. Revel MP, Bissery A, Bienvenu M, et al. Are two-dimensional CT measurements of small noncalcified pulmonary nodules reliable? Radiology 2004; 231:453–458.
10. Thiesse P, Ollivier L, Di Stefano-Louineau D, et al. Response rate accuracy in oncology trials: reasons for interobserver variability. Groupe Francais d'Immunotherapie of the Federation Nationale des Centres de Lutte Contre le Cancer. J Clin Oncol 1997; 15:3507–3514.
11. Mantatzis M, Kakolyris S, Amarantidis K, et al. Treatment response classification of liver metastatic disease evaluated on imaging. Are RECIST unidimensional measurements accurate? Eur Radiol 2009; 19: 1809–1816.
12. Ravenel JG, Leue WM, Nietert PJ, et al. Pulmonary nodule volume: effects of reconstruction parameters on automated measurements—a phantom study. Radiology 2008; 247:400–408.
13. Sohaib SA, Turner B, Hanson JA, et al. CT assessment of tumour response to treatment: comparison of linear, cross-sectional and volumetric measures of tumour size. Br J Radiol 2000; 73:1178–1184.
14. Zhao B, Schwartz LH, Moskowitz CS, et al. Lung cancer: computerized quantification of tumor response—initial results. Radiology 2006; 241: 892–898.
15. Shah GD, Kesari S, Xu R, et al. Comparison of linear and volumetric criteria in assessing tumor response in adult high-grade gliomas. Neuro Oncol 2006; 8:38–46.
16. Tran LN, Brown MS, Goldin JG, et al. Comparison of treatment response classifications between unidimensional, bidimensional, and volumetric measurements of metastatic lung lesions on chest computed tomography. Acad Radiol 2004; 11:1355–1360.
17. Buckler AJ, Mulshine JL, Gottlieb R, et al. The use of volumetric CT as an imaging biomarker in lung cancer. Acad Radiol 2010; 17:100–106.
18. Yankelevitz DF, Reeves AP, Kostis WJ, et al. Small pulmonary nodules: volumetrically determined growth rates based on CT evaluation. Radiology 2000; 217:251–256.
19. Goodman LR, Gulsun M, Washington L, et al. Inherent variability of CT lung nodule measurements in vivo using semiautomated volumetric measurements. AJR Am J Roentgenol 2006; 186:989–994.
20. Sohns C, Mangelsdorf J, Sossalla S, et al. Measurement of response of pulmonal tumors in 64-slice MDCT. Acta Radiol 2010; 51:512–521.
21. Prionas ND, Ray S, Boone JM. Volume assessment accuracy in computed tomography: a phantom study. J Appl Clin Med Phys 2010; 11:3037.
22. Erasmus JJ, Gladish GW, Broemeling L, et al. Interobserver and intraobserver variability in measurement of non-small-cell carcinoma lung lesions: implications for assessment of tumor response. J Clin Oncol 2003; 21: 2574–2582.
23. Landry A, Spence JD, Fenster A. Quantification of carotid plaque volume measurements using 3D ultrasound imaging. Ultrasound Med Biol 2005; 31:751–762.
24. Petrou M, Quint LE, Nan B, et al. Pulmonary nodule volumetric measurement variability as a function of CT slice thickness and nodule morphology. AJR Am J Roentgenol 2007; 188:306–312.
25. Winer-Muram HT, Jennings SG, Meyer CA, et al. Effect of varying CT section width on volumetric measurement of lung tumors and application of compensatory equations. Radiology 2003; 229:184–194.
26. Hopper KD, Kasales CJ, Van Slyke MA, et al. Analysis of interobserver and intraobserver variability in CT tumor measurements. AJR Am J Roentgenol 1996; 167:851–854.

Appendix – B: Three-dimensional lung tumor segmentation from x-ray computed tomography using sparse field active models

The work presented in this chapter has been previously published in *Medical Physics* as indicated below, and is reproduced here with permission (Appendix D).

Joseph Awad, Amir M. Owrangi, Lauren Villemaire, Elaine O'Riordan, Grace Parraga and Aaron Fenster. "Three-dimensional lung tumor segmentation from x-ray computed tomography using sparse field active models" Med Phys. 2012 Feb;39(2):851-65.

Three-dimensional lung tumor segmentation from x-ray computed tomography using sparse field active models

Joseph Awad
Imaging Research Laboratories, Robarts Research Institute, London, Ontario N6A 5K8, Canada

Amir Owrangi
Imaging Research Laboratories, Robarts Research Institute, London, Ontario N6A 5K8, Canada and Graduate Program in Biomedical Engineering, The University of Western Ontario, London, Ontario N6A 5B9, Canada

Lauren Villemaire
Imaging Research Laboratories, Robarts Research Institute, London, Ontario N6A 5K8, Canada and Department of Medical Biophysics, The University of Western Ontario, London, Ontario N6A 5C1, Canada

Elaine O'Riordan
Department of Medical Imaging, The University of Western Ontario, London, Ontario N6A 5B8, Canada

Grace Parraga and Aaron Fenster
Imaging Research Laboratories, Robarts Research Institute, London, Ontario N6A 5K8, Canada; Graduate Program in Biomedical Engineering, The University of Western Ontario, Ontario N6A 5B9, London, Canada; Department of Medical Biophysics, The University of Western Ontario, London, Ontario N6A 5C1, Canada; and Department of Medical Imaging, The University of Western Ontario, London, Ontario N6A 5B8, Canada

(Received 31 July 2011; revised 5 December 2011; accepted for publication 21 December 2011; published 24 January 2012)

Purpose: Manual segmentation of lung tumors is observer dependent and time-consuming but an important component of radiology and radiation oncology workflow. The objective of this study was to generate an automated lung tumor measurement tool for segmentation of pulmonary metastatic tumors from x-ray computed tomography (CT) images to improve reproducibility and decrease the time required to segment tumor boundaries.

Methods: The authors developed an automated lung tumor segmentation algorithm for volumetric image analysis of chest CT images using shape constrained Otsu multithresholding (SCOMT) and sparse field active surface (SFAS) algorithms. The observer was required to select the tumor center and the SCOMT algorithm subsequently created an initial surface that was deformed using level set SFAS to minimize the total energy consisting of mean separation, edge, partial volume, rolling, distribution, background, shape, volume, smoothness, and curvature energies.

Results: The proposed segmentation algorithm was compared to manual segmentation whereby 21 tumors were evaluated using one-dimensional (1D) response evaluation criteria in solid tumors (RECIST), two-dimensional (2D) World Health Organization (WHO), and 3D volume measurements. Linear regression goodness-of-fit measures ($r^2 = 0.63$, $p < 0.0001$; $r^2 = 0.87$, $p < 0.0001$; and $r^2 = 0.96$, $p < 0.0001$), and Pearson correlation coefficients ($r = 0.79$, $p < 0.0001$; $r = 0.93$, $p < 0.0001$; and $r = 0.98$, $p < 0.0001$) for 1D, 2D, and 3D measurements, respectively, showed significant correlations between manual and algorithm results. Intra-observer intraclass correlation coefficients (ICC) demonstrated high reproducibility for algorithm (0.989–0.995, 0.996–0.997, and 0.999–0.999) and manual measurements (0.975–0.993, 0.985–0.993, and 0.980–0.992) for 1D, 2D, and 3D measurements, respectively. The intra-observer coefficient of variation (CV%) was low for algorithm (3.09%–4.67%, 4.85%–5.84%, and 5.65%–5.88%) and manual observers (4.20%–6.61%, 8.14%–9.57%, and 14.57%–21.61%) for 1D, 2D, and 3D measurements, respectively.

Conclusions: The authors developed an automated segmentation algorithm requiring only that the operator select the tumor to measure pulmonary metastatic tumors in 1D, 2D, and 3D. Algorithm and manual measurements were significantly correlated. Since the algorithm segmentation involves selection of a single seed point, it resulted in reduced intra-observer variability and decreased time, for making the measurements. © *2012 American Association of Physicists in Medicine*. [DOI: 10.1118/1.3676687]

Key words: Lung tumors, 3D segmentation, sparse field active surface, level set, CT images

I. INTRODUCTION

Metastatic cancer results in approximately 90% of all cancer deaths.[1,2] Advances in the treatment of metastatic disease require new biomarkers and tools that adequately reflect the changing size and shape of malignant tumors over time. The most widely-accepted method of evaluating tumor response *in vivo* is the response evaluation criteria in solid tumors (RECIST), a unidimensional (1D) measurement of the longest axis of solid tumors.[3] This 1D measurement cannot fully capture the changes of three-dimensional (3D) structures such as lung tumors. Two-dimensional (2D) measurements such as proposed by the World Health Organization (WHO) is generated by multiplying the longest axis (RECIST) by longest perpendicular bisector.[4] Three-dimensional measurements of tumor size change may overcome some of these limitations by taking into account both in-plane and out-of-plane measurements; however, observer time and precision have certainly limited the translation of volumetric measurements in radiology and radiation oncology.

Many algorithms have been proposed to segment lung tumors.[5–14] Since the mean x-ray attenuation of tumors is generally higher than that of the lung, thresholding methods[5–9] have been widely used. Goo *et al.*[5] used chest phantom to test the effects of threshold value (−300, −400, −500, and −600 HU) and section thickness (0.75, 1.0, 2.0, 3.0, and 5.0 mm) on the volume absolute percentage error APE of four spherical synthetic lung nodules with diameters (3.2, 4.8, 6.4, and 12.7 mm). Using MANOVA, they found statistically significant effects for threshold ($P = 0.02$), section thickness ($P < 0.01$), and interaction of threshold and section thickness ($P = 0.04$). Using regression analysis, they found that APE progressively increases with decreasing synthetic nodule size ($R^2 = 0.99$, $P < 0.01$). Morphological operators[6–9] have been utilized with thresholding techniques to prevent segmentation of the lung lesions' adjacent anatomic structures since thresholding techniques are not sufficient to accurately segment vascularized and juxtapleural nodules.[7] Golosio *et al.*[6] developed a multithresholding technique with morphological operators for nodule detection in lung CT. They also utilized artificial neural networks (ANNs) classifier to detect lung nodule using volume, roundness, maximum density, mass, and principal moments of inertia features as function of six threshold values (from −500 to 0 HU with step of 100 HU). They used a training set of 109 low-dose MSCT scans to design and optimize their algorithm. They tested their algorithm using 23 low-dose MSCT scans (Pisa Italung-CT center) and 83 scans (Lung Image Database Consortium LIDC). The authors acknowledged that the algorithm produced high false positive FP. The best results achieved with minimum FP with a reasonable sensitive for tumors greater than or equal to 3 mm are: (1) Italung-CT data set: From 45 tumors, 32 tumors were detected by the algorithm with 92 false positive. (2) LIDC data set: From 38 tumors, 30 tumors were detected by algorithm with 332 false positive. Kostis *et al.*[7] also used a thresholding and morphology-based segmentation algorithm to develop a model for volumetric growth characterization based on longitudinal CT studies. They performed a sensitivity analysis to study the effect of the threshold value and the structuring kernel diameter using scans of 50 acrylic spherical nodules of two diameters (3.96 and 3.20 mm) phantoms. They, first, found the standard threshold value which produced the least variance from the actual volume of the spheres. They observed that the variation of the threshold value around the standard value varies the nodule volume of 0.2 and 0.5%/HU for the 3.96 and 3.20 mm spheres, respectively. They also observed that identifying the appropriate kernel size is important since using small kernel will not remove the vessels connected to nodules and large kernel will affect the measured nodules volumes. Since lung tumors can vary in size considerably, it is difficult to find a fixed size structure kernel that is suitable to segment nodules with different sizes.[7] Consequently, the morphological operators may fail to prevent leakage into adjacent anatomic structures. Tran *et al.*[8] used a semiautomated nodule segmentation by threshold halfway between the a user supplied seed point and the image backgoround. Then, using region growing the algorithm segment all connected voxels to the seed point which has an attenuation greater than the threshold. Then, using morphologic operations, the algorithm tries to separate nodules from adjacent anatomy. To overcome the possible morphologic operator failure, the user manually draw a wall contour to stop region growing from leaking into adjacent anatomy. They evaluated their algorithm with 32 lesions from 15 patients. Each of the patients had a baseline and two follow-up scans leading to 30 response classifications. They found that 1D, 2D, and 3D measuremnts were in agreement in 21, 1D and 3D measurements were in agreement in 29, and 2D and 3D measurements were in agreement in 23 of 30 classifications. The level of agreement was evaluated using Kappa statistics K for 1D compared to 3D [$K = 0.739 \pm 0.345$ (visits 1, 2) and 0.273 ± 0.323 (visits 2, 3)], for 2D compared with 3D, ($K = 0.655 \pm 0.325$ (visits 1, 2) and 0.200 ± 0.208 (visits 2, 3). Moltz *et al.*[9] presented a lung nodules segmentation algorithm that combines a threshold-based approach with model-based morphological processing. Since mophological operators are not sufficient to separate lung nodules from adjacent anatomic structures, they incorporated manual interactive correction to contorol the erosion. Their algorithm was evaluated on 101 lung nodules from 28 patient. In 88% were classified visually as acceptable or better. Kuhnigk *et al.*[10] utilized region growing, morphological processing and manual interaction to segment pulmonary lesions. The authors evaluated their algorithm with 105 lesions from 16 CT scans of 8 patients (two scans per patient with few minutes in between). The radiologist classified visually 96 of the 105 nodules to be successful. The authors developed manual interaction to interactively correct the results. Furthermore, Kakar *et al.*[11] utilized Gabor filters texture features and fuzzy C Means for 2D segmentation of lesion and lungs from CT images. The authors evaluated the algorithm with 42 images. They achieved 89.04% accuracy for lesion segmentation. The authors acknowledged that the main drawback of this technique is that it takes substantial amount of processing time even on modern computers for the segmentation (approximately 2h). Way *et al.*[12] have also used texture and morphological features along with active contours to segment pulmonary nodules. Their algorithm requires a volume of interest (VOI) containing lung nodule manually selected by experienced radiologists. They evaluated their algorithm with 23 nodules from LIDC. The mean overlap between the segmented volume and the gold standard volume is ranging from 0.62 to 0.95 depending on the thresholding value. However, generating texture feature, feature selection, and classification require substantial long processing time. Okada *et al.* have elegantly proposed segmenting pulmonary nodules by fitting ellipsoidal Gaussian intensity model.[13] However, the assumption of an ellipsoid shape does not hold for many tumors as they often have irregular or difficult-to-define geometries. They evaluated their algorithm with large data set consists of 39 patients with 1310 nodules. Eighty-one percent of the segmentation results of these nodules were labeled as successful segmentation using visual inspection, while 76% of the nodules were accepted as correct estimates. A dynamic programming model has also been utilized by Wang *et al.*[14] to segment lung nodules in axial, coronal, and sagittal directions by fusing the segmentation results to obtain the final segmentation. The authors have evaluated their algorithm with two data sets consist of 23 nodules and 64 nodules from Lung Imaging Database Consortium. The mean overlap, true-positive fraction, and false-positive fraction were 66%, 75%, and 15% for first dataset and 58%, 71%, and 22% for the second data set.

We previously developed a 2D semi-automated algorithm that can accurately segment well-circumscribed lung tumors as well as vascularized and juxtapleural tumors.[15] Here, we describe the development and evaluation of a 3D automated algorithm requiring only that the user select the tumor to be segmented by placing a point in the approximate center of the lesion. The algorithm is used to segment lung tumors from chest x-ray computed tomography (CT) 3D images using shape constrained Otsu multithresholding (SCOMT) and sparse field active surface (SFAS) technique that utilizes ten geometric-based and intensity-based energies to segment lung tumors.

II. METHODS

II.A. Algorithm overview

The proposed segmentation algorithm consists of two main parts as shown in Fig. 1: SCOMT and SFAS.

II.A.1. Initial surface

The initial surface was generated using SCMOT technique, which is summarized as follows:

1. The user selects the tumor to be segmented by single click on the approximate center of the tumor; this is to the seed point.
2. Using Otsu's thresholding technique,[16] an initial threshold value (T) is computed.
3. The CT image is then segmented using this threshold value T.
4. The connected region containing the seed point (VOI) is then segmented and its centroid is subsequently computed.
5. Finally, the shape index measure (SI) is computed by dividing the radius (r_s) of the sphere that has the same volume (V_{VOI}) as the VOI to the maximum radius ($r_{\max}$) of VOI.

$$\mathrm{SI} = \frac{r_s}{r_{\max}} = \frac{\sqrt[3]{3V_{\mathrm{VOI}}/4\pi}}{r_{\max}}. \qquad (1)$$

6. If shape index is less than shape index threshold value ($\mathrm{SI}_{\mathrm{Th}}$) given in Table I, a new Otsu threshold value (T) is calculated from VOI region only. Then, the procedure is repeated starting at step 4
7. If $\mathrm{SI} > \mathrm{SI}_{\mathrm{Th}}$, an initial surface for the lung tumor is constructed.

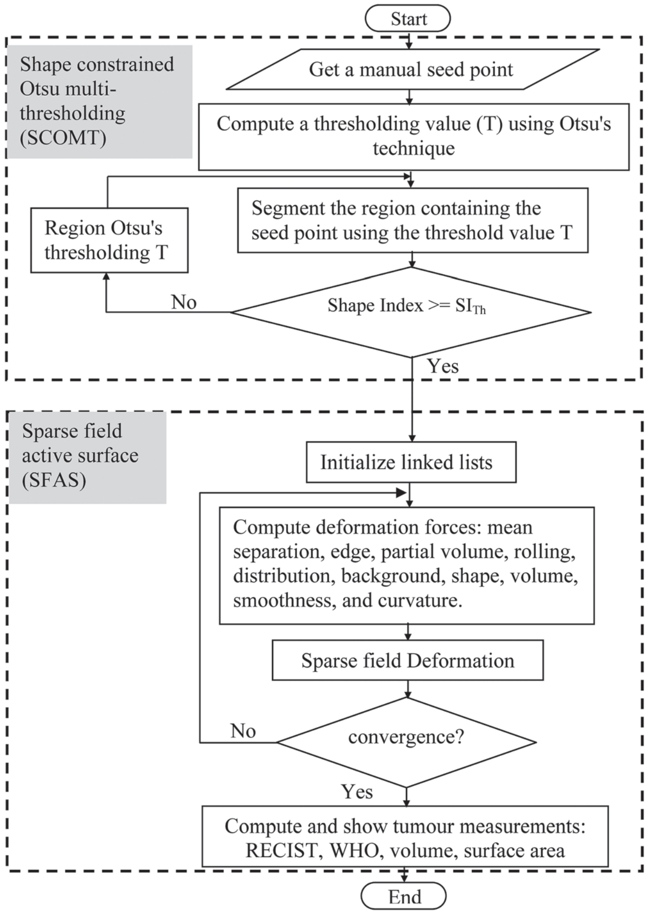

FIG. 1. The block diagram of the proposed algorithm showing the two main parts: the SCOMT and the SFAS.

II.A.2. Surface deformation

The SFAS technique is based on sparse field active model. The active model is an evolving surface constrained by energy objective function, which evolves until it reaches the minimum of the objective function. Let I be a 3D image defined on a domain Ω, which is a bounded open subset of $\Re^3$, and let x, y represent independent spatial variables; each of them denotes a single point in Ω. Any surface S in Ω can be implicitly represented as the zero level set of Lipschitz function ϕ, by $S = \{x|\phi(x) = 0\}$. The interior of the surface S is represented by the regularized Heaviside function, where the regularization parameter $\varepsilon \to 0$.[17]

$$H(\phi(x)) = \begin{cases} 1, & \phi(x) < -\varepsilon \\ 0, & \phi(x) > \varepsilon \\ \frac{1}{2}\left[1 + \frac{\phi(x)}{\varepsilon} + \frac{1}{\pi}\sin\left(\frac{\pi\phi(x)}{\varepsilon}\right)\right], & \text{Otherwise} \end{cases} \qquad (2)$$

Hence, the exterior of S is represented by $(1 - H(\phi(x)))$. The derivative of $H(\phi(x))$ is the Dirac delta function $\delta(\phi(x))$, which represents the volume around the surface S:[17]

TABLE I. Parameters used in the segmentation algorithm.

Description	Parameter	Value
Shape index thresholding	$\mathrm{SI}_{\mathrm{Th}}$	0.4
Mean separation energy (E_M) weight	α_M	1.0
Edge information energy (E_E) weight	α_E	0.85
Partial volume energy (E_P) weight	α_P	0.8
Rolling energy (E_R) weight	α_R	0.3
Distribution energy (E_D) weight	α_D	0.5
Background energy (E_B) weight	α_B	0.7
Shape energy (E_H) weight	α_H	0.07
Smoothness energy (E_S) weight	α_S	0.4
Curvature energy (E_C) weight	α_C	0.4
volume energy (E_V) weight	α_V	0.7
Mean separation radius	r_M	3 mm
Edge information radius	r_E	3 mm
Partial volume radius	r_P	3 mm
Rolling radius	r_R	3 mm
Distribution radius	r_D	3 mm
Background radius	r_B	3 mm
Smoothness radius	r_S	3 mm
Weak edge parameter	λ_E	0.5
Shape convex spikes penalty	a	2.0
Shape concave spikes penalty	b	0.25
Convex curvature penalty	γ_v	1.0
Concave curvature penalty	γ_c	1.0
Volume parameter	λ_v	1.0
Implementation constant	ζ	0.001

$$\delta(\phi(x)) = \begin{cases} 1, & \phi(x) = 0 \\ 0, & |\phi(x)| > \varepsilon \\ \dfrac{1}{2\varepsilon}\left[1 + \cos\left(\dfrac{\pi\phi(x)}{\varepsilon}\right)\right], & \text{Otherwise} \end{cases}. \tag{3}$$

The objective function used to control the surface deformation is as follows:

$$E_T = \alpha_M E_M + \alpha_E E_E + \alpha_P E_P + \alpha_R E_R + \alpha_D E_D + \alpha_B E_B + \alpha_H E_H + \alpha_S E_S + \alpha_C E_C + \alpha_V E_V. \tag{4}$$

The weighting parameters α_M, α_E, α_P, α_R, α_D, α_B, α_H, α_S, α_C, and α_V used to produce the results presented in this paper are given in Table I. Ten energies were implemented to control the contour deformation: localized mean separation (E_M),[18] edge information (E_E), partial volume (E_P), rolling energy (E_R), distribution energy (E_D), background energy (E_B), shape energy (E_H), smoothness (E_S), curvature (E_C),[19] and volume energy (E_V). The localized mean separation energy deforms the surface to maximize the separation between the mean Hounsfield values inside and outside the surface S.[18] The edge information energy deforms the surface to the higher gradient. The partial volume energy ensures that the whole tumor is segmented, especially with CT images with a large voxel size as in our case (5 mm). Since the lung tumors have higher Hounsfield values compared to the background, the rolling energy pushes the surface to the bottom of the Hounsfield curve at tumors boundaries. The distribution energy includes the nearby voxel if the probability of being part of the tumor is high. The background energy drives the surface to fill the hole that occurred in the lung segmentation due to the tumor. The shape energy protects the geometry of the solid tumor by limiting the expansion of surface parts that have high radii from the center of the tumor compared to the median radius of the tumor. It also encourages expansion of surface parts that have small radii compared to the tumor median radius. The smoothness energy smoothes the surface by locally penalizing the convexity and concavity of the surface. The curvature energy preserves the continuity of the surface. The volume energy has an effect only for very small tumors. It prevents the surface from vanishing since most of the volume of small tumor is partial volume, especially with large voxel-sized CT images. Each of the corresponding speed functions of these energies was normalized to $[-1, 1]$ range before computing the total speed function. For fast convergence, the sign of the total speed function was only used to deform the contour as suggested by Shi *et al.*[20] A convergence criterion was implemented to stop the surface deformation when it converged or the normalized segmented region change becomes very small

$$\frac{\int_\Omega H(\O^{n+1}(x))\mathrm{d}x + \int_\Omega H(\O^{n}(x))\mathrm{d}x - 2\int_\Omega H(\O^{n+1}(x))H(\O^{n}(x))\mathrm{d}x}{\int_\Omega H(\O^{n+1}(x))\mathrm{d}x} < \zeta, \tag{5}$$

where $H(\O^n(x))$ and $H(\O^{n+1}(x))$ are the Heaviside functions at iterations n and $n+1$. The stopping constant ζ equals to 0.001 as shown in Table I. The level set technique introduced by Osher and Sethian[21] is a powerful approach since the active contours can be expanded, contracted, and even split or merged. However, the conventional level set formulation is not computationally efficient since the iterative solution is carried out for the entire domain of the image I. There are some modifications to the conventional formulation to reduce the time complexity. Since the interest is on the interface, narrow band level set proposed by Adalsteinsson and Sethian[22] restricts the computations to a thin band of pixels surrounding the interface. No computation is required for the points outside the narrow band—their level set values are simply set to constant values. Adalsteinsson and Sethian used a narrow band with a width of 12 pixels, which significantly reduced the deformation time. Sparse field level set introduced by Whitaker[23] reduced the narrow band to a set of linked list to track the interface and pixels around it, which eliminate the time complexity.

In this paper, we utilized five linked lists to track five ranges of the level set function: $L_0 \rightarrow [-0.5, 0.5]$, $L_{-1} \rightarrow [-1.5, -0.5)$, $L_1 \rightarrow (0.5, 1.5]$, $L_{-2} \rightarrow [-2.5, -1.5)$, and $L_2 \rightarrow (1.5, 2.5]$. The sparse field deformation process deforms the initial surface produced by SCOMT and is summarized as follows:

1. Evolution: Compute the evolution equation that minimizes the objective energy function [Eq. (4)] along zero level set L_0. Then, modify the existing level set value ϕ along L_0.
2. Re-initialization: modify the level set values of voxels immediately surrounding L_0 to maintain a city-block distance from the nearest L_0.
3. Updating: Move points from and to linked lists to maintain the level set range of each linked list.
4. Convergence: If the stopping criterion is not met, go back to step 1.
5. Segmentation: Use the final zero level L_0 to segment the lung tumor from the image.

The evolution equation, that minimizes the objective energy function given in Eq. (4) with respect to Lipschitz function ϕ, can be obtained by solving Euler-Lagrange equation for ϕ as follows:[17]

$$\begin{aligned}\frac{\partial\phi(x)}{\partial t} &= \alpha_M F_M(x) + \alpha_E F_E(x) + \alpha_P F_P(x) + \alpha_R F_R(x)\\ &\quad + \alpha_D F_D(x) + \alpha_B F_B(x) + \alpha_H F_H(x)\\ &\quad + \alpha_S F_S(x) + \alpha_C F_C(x) + \alpha_V F_V(x). \end{aligned} \tag{6}$$

The mean separation speed function F_M is given by[17]

$$\begin{aligned}F_M(x) &= \delta(\phi(x)) \int_\Omega \beta_M(x,y)\delta(\phi(y))\\ &\quad \times \left(\frac{(I(y)-u_x)^2}{A_{ux}} - \frac{(I(y)-v_x)^2}{A_{vx}}\right)dy,\end{aligned} \tag{7}$$

where $\beta_M(x,y)$ represents a mean separation spherical binary mask centered at x with a radius r_M given in Table I

$$\beta_M(x,y) = \begin{cases} 1, & \|x-y\| < r_M \\ 0, & \text{otherwise.} \end{cases}, \tag{8}$$

where u_x and v_x are the mean Hounsfield values of interior and exterior regions of the localized mask β_M, respectively, given by[17]

$$u_x = \frac{\int_\Omega \beta_M(x,y)\cdot H(\phi(y))\cdot I(y)dy}{\int_\Omega \beta_M(x,y)\cdot H(\phi(y))dy}, \tag{9}$$

$$v_x = \frac{\int_\Omega \beta_M(x,y)\cdot(1-H(\phi(y)))\cdot I(y)dy}{\int_\Omega \beta_M(x,y)\cdot(1-H(\phi(y)))dy}, \tag{10}$$

where A_{ux} and A_{vx} are the interior and exterior areas of the localized mask β_M, respectively, given by[17]

$$A_{ux} = \int_\Omega \beta_M(x,y)\cdot H(\phi(y))dy, \tag{11}$$

$$A_{vx} = \int_\Omega \beta_M(x,y)\cdot(1-H(\phi(y)))dy. \tag{12}$$

The edge information speed function drives the surface to the high image gradient, which represents an edge. The proposed edge information speed function F_E can be written as

$$F_E(x) = \delta(\phi(x))(|G_{ux}| - \lambda_E|G_{vx}|), \tag{13}$$

where λ_E is a positive parameter $(0 \le \lambda_E \le 1)$, given in Table I, that prevents the surface from segmenting the adjacent anatomic structures with the lung tumor by decreasing the weight of the outside gradient compared to the inside gradient to compensate for weak edges. G_{ux} and G_{vx} are the interior and exterior mean magnitude of the image gradient, respectively, for a localized mask β_E.

$$\beta_E(x,y) = \begin{cases} 1, & \|x-y\| < r_E \\ 0, & \text{otherwise.} \end{cases}, \tag{14}$$

The $\beta_E(x,y)$ is an edge spherical binary mask centered at x, with a radius r_E defined in Table I, to prevent distant edges of other objects to affect the deformation. G_{ux} and G_{vx} are defined as

$$G_{ux} = \frac{\int_\Omega \beta_E(x,y)\cdot H(\phi(y))\cdot|\nabla I(y)|dy}{\int_\Omega \beta_E(x,y)\cdot H(\phi(y))dy}, \tag{15}$$

$$G_{vx} = \frac{\int_\Omega \beta_E(x,y)\cdot(1-H(\phi(y)))\cdot|\nabla I(y)|dy}{\int_\Omega \beta_E(x,y)\cdot(1-H(\phi(y)))dy}. \tag{16}$$

To overcome the partial volume problem due to the large voxel size in z direction (5 mm), a partial volume speed function F_P is used. F_P uses the information that lung tumors have higher Hounsfield values compared to the background. This speed function encourages the contour to segment the entire tumor and at the same time to prevent the contour from leaking to other high Hounsfield value structures near the tumor. F_P is given by

$$F_P(x) = \delta(\phi(x))\beta_P(x,y)\left(\frac{v_{xPp1} - u_{xPz}}{u_{xPz}}\right), \tag{17}$$

where $\beta_P(x,y)$ represents a partial volume spherical binary mask centered at x with a radius r_P given in Table I

$$\beta_P(x,y) = \begin{cases} 1, & \|x-y\| < r_P \\ 0, & \text{otherwise.} \end{cases} \tag{18}$$

v_{xPp1} and u_{xPz} are the mean Hounsfield values of Level-one and Level-zero regions of the localized mask β_P, respectively, defined as

$$v_{xPp1} = \frac{\int_\Omega \beta_P(x,y)\cdot H_{p1}(\phi(y))\cdot I(y)dy}{\int_\Omega \beta_P(x,y)\cdot H_{p1}(\phi(y))dy}, \tag{19}$$

$$u_{xPz} = \frac{\int_\Omega \beta_P(x,y)\cdot H_z(\phi(y))\cdot I(y)dy}{\int_\Omega \beta_P(x,y)\cdot H_z(\phi(y))dy}, \tag{20}$$

where, H_{p1} and H_z are positive-one and zero Level set Heaviside functions, respectively, as given by:

$$H_{p1}(\phi(y)) = \begin{cases} 1, & 0.5 < \phi(y) \le 1.5 \\ 0, & \text{Otherwise} \end{cases}, \tag{21}$$

$$H_z(\phi(y)) = \begin{cases} 1, & -0.5 \le \phi(y) \le 0.5 \\ 0, & \text{Otherwise} \end{cases}. \tag{22}$$

The proposed rolling speed function F_R is given by

$$F_R(x) = \delta(\phi(x))\beta_R(x,y),(1-\chi_R(x))(v_{xRp1} - u_{xRn1}), \tag{23}$$

where $\beta_R(x,y)$ represents a rolling spherical binary mask centered at x with a radius r_R given in Table I

$$\beta_R(x,y) = \begin{cases} 1, & \|x-y\| < r_R \\ 0, & \text{otherwise.} \end{cases}, \tag{24}$$

and $\chi_R(x)$ is a local minimum or maximum mask

$$\chi_R(x) = \begin{cases} 1, & \left(u_{xRz}\left(v_{xRp1} + u_{xRn1} - u_{xRz}\right) - v_{xRp1}u_{xRn1}\right) < 0 \\ 0, & \text{otherwise} \end{cases}. \tag{25}$$

v_{xRp1}, u_{xRz}, and v_{xRn1} are the mean Hounsfield values of Level-one, Level-zero, and negative-one level regions of the localized mask β_P, respectively, defined as

$$v_{xRp1} = \frac{\int_\Omega \beta_R(x,y) \cdot H_{p1}(\phi(y)) \cdot I(y)dy}{\int_\Omega \beta_R(x,y) \cdot H_{p1}(\phi(y))dy}, \tag{26}$$

$$u_{xRz} = \frac{\int_\Omega \beta_R(x,y) \cdot H_z(\phi(y)) \cdot I(y)dy}{\int_\Omega \beta_R(x,y) \cdot H_z(\phi(y))dy}, \tag{27}$$

$$v_{xRn1} = \frac{\int_\Omega \beta_R(x,y) \cdot H_{n1}(\phi(y)) \cdot I(y)dy}{\int_\Omega \beta_R(x,y) \cdot H_{n1}(\phi(y))dy}, \tag{28}$$

where, H_{p1}, H_z, and H_{n1} are positive-one, zero, negative-one Level set Heaviside functions, respectively. H_{p1} and H_z are defined in Eqs. (21) and (22), respectively. H_{n1} is defined by

$$H_{n1}(\phi(y)) = \begin{cases} 1, & -1.5 \le \phi(y) < -0.5 \\ 0, & \text{Otherwise} \end{cases}. \tag{29}$$

The proposed distribution speed function F_D encourages the addition of the nearby voxel (positive-one level set) to the segmented volume if the probability [$\Pr(v_{xDp1})$] of its Hounsfield value (v_{xDp1}) belongs to the segmented volume is high compared to the maximum probability ($\Pr_{x\max}$) inside the segmented volume. F_D is given by

$$F_D(x) = -\delta(\phi(x))\beta_D(x,y)\lambda_D(v_{xDp1}, \mu_x, \sigma_x)\frac{\Pr(v_{xDp1})}{\Pr_{x,\max}}, \tag{30}$$

where $\beta_D(x,y)$ represents a distribution spherical binary mask centered at x with a radius r_D given in Table I

$$\beta_D(x,y) = \begin{cases} 1, & \|x-y\| < r_D \\ 0, & \text{otherwise.} \end{cases} \tag{31}$$

v_{xDp1} is the mean Hounsfield value of Level-one regions of the localized mask β_D, defined as

$$v_{xDp1} = \frac{\int_\Omega \beta_D(x,y) \cdot H_{p1}(\phi(y)) \cdot I(y)dy}{\int_\Omega \beta_D(x,y) \cdot H_{p1}(\phi(y))dy}, \tag{32}$$

where, H_{p1} is positive-one Level set Heaviside function defined in Eq. (21). $\lambda_D(v_{xDp1}, \mu_x, \sigma_x)$ is a confidence interval parameter ($0 < \lambda_D \le 1$) as shown in Fig. 2(A).

$$\lambda_D\left(v_{xDp1}, \mu_i, \sigma_i\right) = e^{-\frac{\left|v_{xDp1} - \mu_i\right|}{\sigma_i}}. \tag{33}$$

λ_D has a maximum value (=1), when the mean Hounsfield value of the voxels near the surface, positive-one Level set (v_{xDp1}), within the distribution spherical mask is equal to the mean Hounsfield value inside the surface defined by

$$\mu_i = \frac{\int_\Omega H(\phi(y)) \cdot I(y)dy}{\int_\Omega H(\phi(y))dy}. \tag{34}$$

λ_D is decreased exponentially when v_{xDp1} is multiple standard deviations (σ_i) away from the mean. σ_i is the standard deviation of the Hounsfield values inside the surface, and it is defined by

$$\sigma_i = \left[\frac{\int_\Omega H(\phi(y)) \cdot (I(y) - \mu_i)^2 dy}{\int_\Omega H(\phi(y))dy}\right]^{0.5}. \tag{35}$$

Since the Hounsfield values of lung tissue are low compared to the tumor and adjacent anatomic structures, the segmentation can be accomplished using an Otsu thresholding approach. The tumors that are difficult to segment for observers and automated algorithm methods are those that are connected to adjacent anatomic structures. These tumors create holes/concavities in the segmented lung surface S_L as shown in Fig. 2(B). These holes/concavities can be closed by applying a convex hull filter, which squeezes a convex surface until it touches the lung surface. By subtracting the lung surface from the resulted convex surface S_{LC}, we can obtain an estimate for lung tumor surface S_T. This estimated tumor surface S_T may be also used to construct the tumor initial surface instead of or with the SCOMT technique; however, for the results shown in this paper S_T was used only in the background speed function and all initial tumor surfaces were constructed by the SCOMT technique. The proposed background speed function F_B encourages the surface to get closer to the estimated tumor surface S_T.

$$F_B(x) = \delta(\phi(x)) \times \left[-\text{sgn}(\phi(X_B(x)))\beta_B(x)\frac{1}{\xi + \|x - X_B(x)\|}\right]. \tag{36}$$

The negative sign function expands the deformable surface if the nearest estimated tumor surface S_T is outside the segmented surface $\phi(X_B(x)) > 0$ and shrinks the deformable surface when the nearest S_T surface is inside the segmented surface $\phi(X_B(x)) < 0$. ξ is a scalar parameter, given in Table I, to avoid dividing by zero when the segmented surface is on the estimated surface. $\beta_B(x,y)$ is the background spherical binary mask centered at x with a radius r_B given in Table I.

$$\beta_B(x) = \begin{cases} 1, & 0 < \|x - X_B(x)\| < r_B \\ 0, & \text{otherwise.} \end{cases}, \tag{37}$$

The nearest estimated surface is defined by

$$X_B(x) = \arg\min_{y \in S_T} \|x - y\|, \tag{38}$$

The proposed shape speed function F_H is given by

$$F_H(x) = \delta(\phi(x))\lambda_H(r_x, R_m), \tag{39}$$

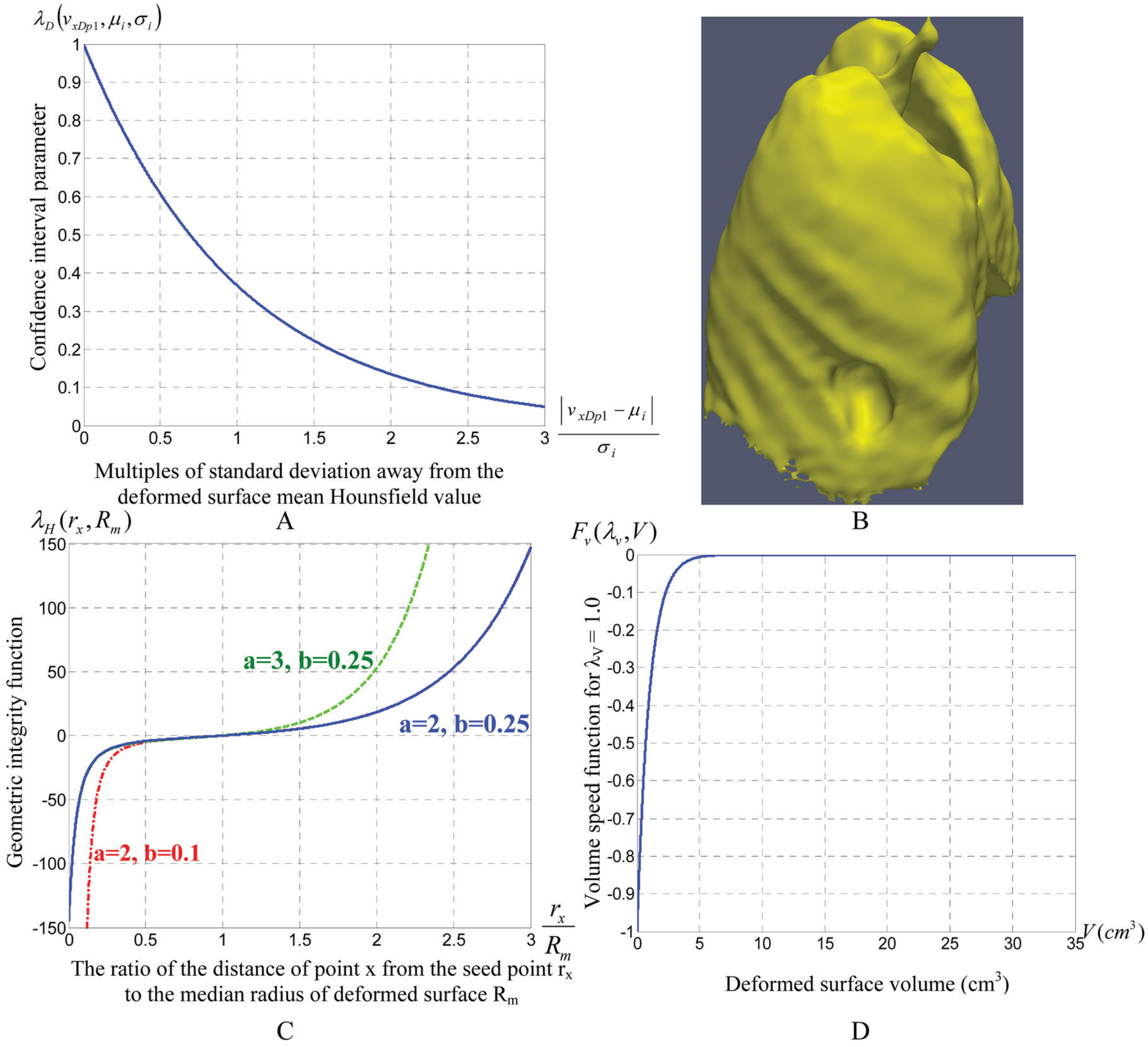

FIG. 2. (A) Confidence interval parameter (λ_D), (B) lung Segmentation with a tumor appears as a surface concavity, (C) geometric integrity function, and (D) volume speed function for $\lambda_v = 1.0$.

where $\lambda_H(r_x, R_m)$ is the proposed geometric integrity function shown in Fig. 2(C), and it is defined by

$$\lambda_H(r_x,R_m) = e^{a\left(\frac{r_x}{R_m}-1.0\right)+1.0} - e^{\frac{b+1.0}{\left(\frac{r_x}{R_m}+b\right)}} \tag{40}$$

where r_x is the distance of point x from the seed point. This explains why the seed point should be approximately in the center of the tumor. R_m is the median radius of the deformed surface. There are two parameters controlling λ_H: a and b defined in Table I. Increasing a increases the penalty for surface parts with large radii compared to the median radius and encourages these parts to shrink. Decreasing b increases the penalty for surface parts with a very small radius compared to the median radius and encourages these parts to expand.

The proposed smoothness speed function F_S smoothes the surface by reducing the convexity and concavity inside the localized spherical mask β_S with a radius r_s given in Table I. F_S can be written as follows:

$$F_S(x) = \delta(\phi(x))(\gamma_v A_{Svx} - \gamma_c A_{Sux}), \tag{41}$$

where A_{Sux} and A_{Svx} are interior and exterior volumes, respectively, inside the localized mask β_S

$$\beta_S(x,y) = \begin{cases} 1, & \|x-y\| < r_S \\ 0, & \text{otherwise.} \end{cases}, \tag{42}$$

and they are defined as

$$A_{Sux} = \int_\Omega \beta_S(x,y)\cdot H(\phi(y))dy, \tag{43}$$

$$A_{Svx} = \int_\Omega \beta_S(x,y)\cdot(1-H(\phi(y)))dy, \tag{44}$$

γ_v and γ_c are positive parameters (≤ 1), given in Table I, that control convexity and concavity. Decreasing γ_v encourages convexity, whereas decreasing γ_c encourages concavity. If $\gamma_v = \gamma_c$, this speed function does not favour convexity or concavity and smoothes the surface. In this study, we used $\gamma_v = \gamma_c = 1$.

The curvature speed function F_C is given by[19]

$$F_C(x) = \delta(\phi(x))div\left(\frac{\nabla\phi(x)}{|\nabla\phi(x)|}\right). \qquad (45)$$

Since most of the volume of a small tumor is partial volume, especially, with large voxel-sized CT images, we proposed a volume speed function F_v as shown in Fig. 2(D) to prevent the deformable surface of small tumors from vanishing into a point. F_v is defined as

$$F_v = -e^{-\lambda_v V}, \qquad (46)$$

where V is the tumor volume in cm^3 and λ_v is a parameter, defined in Table I, controlling how big is the volume that is affected by the volume speed function.

II.B. Image acquisition

The study protocol was approved by the University of Western Ontario Research Ethics Board, and written informed consent was not required from the study subjects because image data were de-identified, anonymized, and retrospectively collected. Images from five subjects with a total of 21 metastatic tumors with primary renal carcinomas were imaged. There were 10 smooth and 11 lobulated tumors. Of these, 5 were intraparenchymal and 16 were juxtapleural tumors. The tumors ranged in size from 0.9 to 47.1 cm^3 with a mean and a standard deviation of 7.4 ± 11.3 cm^3 were evaluated. The minimum to maximum radius ratio from tumors centroids for the 21 tumors ranged from 0.3 to 0.8 with a mean and a standard deviation of 0.6 ± 0.1. All subjects scanning was performed using a helical General Electric (GE) LightSpeed Series CT scanner (VCT or Ultra; GE HealthCare, Waukesha, WI) (Exposure time = 600 ms, width = 512 voxels, height = 512 voxels, number of frames = 58–136 frames, and the voxel size is $0.73 \times 0.73 \times 5$ mm).

II.C. Manual segmentation

Four trained observers participated in this study; two observers (OBS1: graduate student, OBS2: a board-certified, fellowship trained radiologist with 10 years' experience) performed five repeated manual measurements of 21 tumors using 1D, 2D, and 3D measurements[24] and two different observers (OBS3: undergraduate student, OBS4: graduate student) performed algorithm segmentation of the same 21 tumors, five times each. Observers were blinded to subject identity and clinical status and each repetition round was randomized to minimize observer memory bias. CT images were displayed on LCD screens, which was adequate to display the image at full resolution, using conventional parameters for lung (window width: 1600 HU, window centre: −550).[25,26] Each observer was able to magnify and manipulate window setting to optimize the display of each tumor. Manipulating the displayed image may affect the selection of the initial seed point for the algorithm observers and the segmentation for the manual observers; however, it was important to allow each observer to optimize his/her display for each tumor to mimic normal work environment.

Manual analysis was performed by segmenting tumor boundaries after creating an axis of rotation in the center of the tumor, and rotating the tumor by an angle of 18° generating 10 2D segmentations. Image analysis for 1D and 2D measurements was performed using electronic calipers in an open-source picture archiving and communication system (PACS), ClearCanvas (ClearCanvas, Inc., Toronto, Canada). Volumetric analysis was performed using a customized visualization and segmentation software developed in-house, 3D Quantify (Robarts Research Institute, London, ON), as previously described.[27] Lung tumor volumes were calculated from the manual segmentation of tumor boundaries using VTK (Visualization Toolkit; Kitware, Inc, Clifton Park, NY).

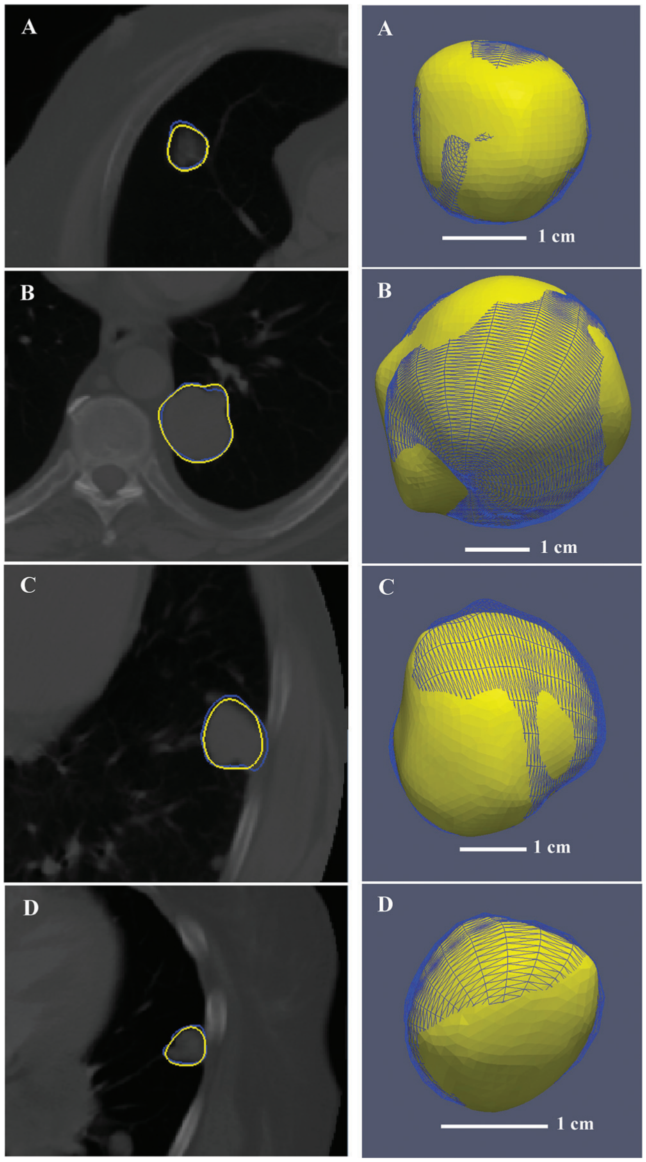

FIG. 3. 1D (RECIST), 2D (WHO), and 3D (Volume) measurements [Manual (M): blue (dark color) mesh, Algorithm (A): yellow (light color) surface] (A) T1: (M: 3.0 cm, 8.1 cm^2, 9.0 cm^3; A: 2.9 cm, 7.7 cm^2, 9.0 cm^3) (B) T2: (M: 4.2 cm, 16.5 cm^2, 28.2 cm^3; A: 4.2 cm, 16.7 cm^2, 30.0 cm^3) (C) T7: (M: 3.3 cm, 9.6 cm^2, 10.8 cm^3; A: 3.2 cm, 8.6 cm^2, 9.4 cm^3) (D) T15: (M:2.1 cm, 3.7 cm^2, 2.9 cm^3; A:2.0 cm, 3.5 cm^2, 2.7 cm^3).

II.D. Evaluation

A two-way repeated measures ANOVA was used to compare the means of manual 1D, 2D, and 3D measurements, the means of algorithm measurements, and the means of manual and algorithm segmentation measurements. To assess precision, the reproducibility was evaluated using the intraclass correlation coefficient (ICC), using both the single measure absolute agreement [ICC(A)] and consistency [ICC(C)] ICC coefficients for each of the four observers. The intraclass measures the reliability by computing the proportion of variance between observations.[28] ICC with values less than 0.2 indicates poor correlation, 0.21–0.40 fair, 0.41–0.60 moderate, 0.61–0.80 good, and 0.81–1.00 very good correlation.[28] The intra-observer coefficient of variation (CV%), which is the standard deviation divided by the mean, was also used to assess reproducibility. The coefficients of variation are computed to evaluate the variability (relative to the mean) among five measurement repetitions of each of the four observers. To estimate the degree of agreement between manual and algorithm measurements, Bland-Altman plots[29] were used to show the mean differences between manual and algorithm 1D, 2D, and 3D measurements plotted against the manual and algorithm mean measurements. Linear regression goodness-of-fit measures and Pearson correlation coefficients were generated to assess agreement between the measurements of manual observers, algorithm observers, and between manual and algorithm measurements for 1D, 2D, and 3D measurements. All statistical analyses were performed using IBM SPSS Statistics version 19 (IBM Corporation, 2010) and results were considered significant when the probability of making a Type I error was less than 5% ($p < 0.05$).

III. RESULTS

Figure 3 shows axial CT images, as well as the manual and algorithm segmented boundaries, and corresponding 1D, 2D, and 3D measurements for representative tumors T1, T2, T7, and T15. T1 is a well-circumscribed tumor; however, the other three tumors (T2, T7, and T15) are vascularized and juxtapleural nodules. The surfaces for manual segmentation are shown in a dark mesh and for the algorithm segmentation in a light surface.

Mean 1D, 2D, and volume measurements plus their standard deviations for manual and algorithm segmentation of all 21 tumors are provided in Table II. For the data set used in this research, Table II shows that the highest standard deviations for manual measurements are 1.1 cm (T15), 2.1 cm^2 (T15), and 15.1 cm^3 (T3), whereas the highest standard deviations for the algorithm measurements are 0.3 cm (T4), 0.6 cm^2 (T4), and 0.8 cm^3 (T2) for 1D, 2D, and 3D measurements, respectively. For our data set, Table II shows that the algorithm has a lower standard deviation compared to manual for most of 1D and 2D measurements and all of 3D measurements suggesting less variability in the algorithm measurements.

Table III shows the results (p-values, average values, and standard deviations) of a two-way repeated measures ANOVA for all measurements of the 21 tumors, indicating a statistically significant differences between the observers for manual volume measurements ($p = 0.023$) but no difference

TABLE II. Manual and Algorithm RECIST (1D), WHO (2D), and volume mean measurements ± standard deviations (5 repeats, both observers) for 21 lung tumors.

		RECIST (1D) (cm)		WHO (2D) (cm^2)		Volume (3D) (cm^3)	
Subjects	Tumors	Manual	Algorithm	Manual	Algorithm	Manual	Algorithm
Subject-1	1	2.6 ± 0.1	2.8 ± 0.1	6.6 ± 0.6	7.6 ± 0.3	9.5 ± 1.4	8.6 ± 0.7
	2	4.0 ± 0.1	4.3 ± 0.0	13.5 ± 0.6	17.2 ± 0.5	31.6 ± 3.7	30.9 ± 0.8
Subject-2	3	3.8 ± 0.3	5.7 ± 0.1	12.3 ± 1.8	20.5 ± 0.4	47.1 ± 15.1	33.2 ± 0.7
	4	2.0 ± 0.2	2.4 ± 0.3	3.6 ± 0.4	4.7 ± 0.6	6.4 ± 1.4	4.5 ± 0.6
	5	1.3 ± 0.1	1.8 ± 0.1	1.6 ± 0.2	2.5 ± 0.1	2.7 ± 1.0	1.8 ± 0.1
	6	2.9 ± 0.3	3.1 ± 0.0	6.6 ± 0.8	8.4 ± 0.2	10.8 ± 2.1	9.2 ± 0.2
Subject-3	7	1.5 ± 0.2	2.3 ± 0.0	1.8 ± 0.2	4.4 ± 0.1	2.7 ± 0.9	3.7 ± 0.1
	8	2.2 ± 0.1	3.1 ± 0.1	4.4 ± 0.3	7.3 ± 0.4	5.8 ± 1.9	5.4 ± 0.3
Subject-4	9	1.5 ± 0.1	1.6 ± 0.1	1.9 ± 0.2	2.2 ± 0.3	1.9 ± 0.5	1.1 ± 0.1
	10	1.4 ± 0.1	1.5 ± 0.0	1.2 ± 0.1	2.1 ± 0.1	1.5 ± 0.5	1.2 ± 0.1
	11	1.8 ± 0.2	2.3 ± 0.1	2.6 ± 0.3	4.1 ± 0.2	4.3 ± 0.8	2.8 ± 0.1
Subject-5	12	2.7 ± 0.1	2.9 ± 0.1	6.8 ± 0.4	6.9 ± 0.4	9.8 ± 3.0	6.1 ± 0.2
	13	2.3 ± 0.7	1.7 ± 0.1	3.1 ± 0.8	2.2 ± 0.1	3.5 ± 2.3	1.2 ± 0.1
	14	1.8 ± 0.1	1.6 ± 0.0	2.5 ± 0.3	2.3 ± 0.1	2.2 ± 1.0	1.5 ± 0.1
	15	3.4 ± 1.1	1.9 ± 0.0	6.5 ± 2.1	3.3 ± 0.1	4.9 ± 2.4	2.5 ± 0.2
	16	1.6 ± 0.6	1.4 ± 0.1	2.6 ± 1.7	1.4 ± 0.1	0.9 ± 0.5	0.6 ± 0.1
	17	1.5 ± 0.6	2.4 ± 0.1	1.7 ± 1.1	2.6 ± 0.1	1.0 ± 0.4	1.5 ± 0.1
	18	1.6 ± 0.2	1.6 ± 0.1	1.8 ± 0.4	2.1 ± 0.2	1.5 ± 0.4	1.2 ± 0.1
	19	1.4 ± 0.3	1.7 ± 0.1	1.8 ± 0.8	2.3 ± 0.2	1.0 ± 0.3	1.2 ± 0.3
	20	1.3 ± 0.2	1.7 ± 0.1	1.6 ± 0.5	2.4 ± 0.1	2.8 ± 0.4	1.5 ± 0.1
	21	1.7 ± 0.2	1.7 ± 0.1	1.9 ± 0.2	2.7 ± 0.3	2.7 ± 1.0	1.4 ± 0.2

Table III. Results of a two-way repeated measures ANOVA showing the comparison between the measurements of manual observers, algorithm observers, and between manual and algorithm measurements.

p-value (AV1 ± SD1, AV2 ± SD2)	RECIST (1D) (cm)	WHO (2D) (cm^2)	Volume (3D) (cm^3)
Manual observers	0.380 (2.03 ± 0.09, 2.17 ± 0.14)	0.642 (4.04 ± 0.33, 4.20 ± 0.40)	0.023 (5.8 ± 1.25, 8.95 ± 1.30)
Algorithm observers	0.807 (2.35 ± 0.07, 2.36 ± 0.11)	0.510 (5.19 ± 0.25, 5.22 ± 0.31)	0.997 (5.77 ± 0.33, 5.77 ± 0.34)
Manual and algorithm	0.084 (2.1 ± 0.38, 2.36 ± 0.10)	0.033 (4.12 ± 0.86, 5.21 ± 0.29)	0.023 (7.38 ± 3.64, 5.77 ± 0.34)

between observers for 1D, 2D, and 3D measurements performed using the proposed algorithm ($p > 0.05$). In addition, Table III shows that there was no statistically significant difference between manual and algorithm methods for RECIST measurements ($p = 0.084$), although there was a statistical significant difference between the manual and algorithm for the 2D ($p = 0.033$) and 3D ($p = 0.023$) measurements.

Intra-observer correlation coefficients for the four observers are provided in Table IV for 1D, 2D, and 3D manual (0.975–0.993, 0.985–0.993, and 0.980–0.992) and algorithm measurements (0.989–0.995, 0.996–0.997, and 0.999–0.999). The intra-observer coefficient of variation (CV%) was also used to compare the manual and the proposed algorithm as shown in Table V. The plots of the CV% for manual and algorithm observers for RECIST, WHO, and volume measurements are shown in Fig. 4. In general, the plots show that the CV%s are smaller for larger mean values of the measurements.

Bland-Altman plots[29] were also utilized to evaluate the agreement between the manual and the algorithm for RECIST, WHO, and volume as show in Fig. 5. These plots indicate that the mean bias for the RECIST, WHO, and volume measurements are 0.26 cm, 1.09 cm^2, and -1.61 cm^3, respectively.

Figure 6 shows linear regression between the measurements of the two manual observers ($r^2 = 0.48$, $p = 0.0005$; $r^2 = 0.84$, $p < 0.0001$; and $r^2 = 0.93$, $p < 0.0001$), between the measurements of the two algorithm observers ($r^2 = 0.99$, $p < 0.0001$; $r^2 = 1.00$, $p < 0.0001$; and $r^2 = 1.00$, $p < 0.0001$), and between the mean measurements of manual and algorithm observers ($r^2 = 0.63$, $p < 0.0001$; $r^2 = 0.87$, $p < 0.0001$; and $r^2 = 0.96$, $p < 0.0001$) for the RECIST, WHO, and volume measurements, respectively. In addition, the 95% confidence intervals are also plotted (as dashed lines) to indicate that some outliers were present in our manual measurements as indicated by the consistency of the algorithm measurements shown in Fig. 6(B).

Table VI summarizes the Pearson correlation coefficients between the measurements of manual observers ($r = 0.69$, $p = 0.0005$; $r = 0.92$, $p < 0.0001$; and $r = 0.97$, $p < 0.0001$), algorithm observers ($r = 1.00$, $p < 0.0001$; $r = 1.00$, $p < 0.0001$; and $r = 1.00$, $p < 0.0001$), and between the mean of manual and algorithm observers ($r = 0.79$, $p < 0.0001$; $r = 0.93$, $p < 0.0001$; and $r = 0.98$, $p < 0.0001$) for the RECIST, WHO, and volume measurements, respectively. In addition, Table VI also summarizes the slopes and y-intercepts of the correlation lines. The p-values answer the following question: if there is no correlation between X and Y population, what is the chance that random samples would produce the observed correlation coefficients. Since, the p-values are small, we can reject the hypothesis that the observed correlation coefficients were a coincidence.

Table IV. Intra-observer correlation coefficients for manual (observers 1 and 2) and algorithm (observers 3 and 4).

	RECIST (1D)		WHO (2D)		Volume (3D)	
	ICC(A)	ICC (C)	ICC(A)	ICC (C)	ICC(A)	ICC (C)
Manual observer 1	0.991	0.993	0.993	0.993	0.980	0.985
Manual observer 2	0.975	0.980	0.985	0.988	0.991	0.992
Algorithm observer 3	0.995	0.995	0.997	0.997	0.999	0.999
Algorithm observer 4	0.989	0.990	0.996	0.996	0.999	0.999

The average time required for manual RECIST, WHO, and volume measurements (which included tumor segmentation) was 7 min. Whereas, the average time for use of the proposed algorithm to segment and generate the RECIST, WHO, and volume measurements required a total 36 s ranging from 21 to 105 s, including selecting the approximate centre of the tumor (initialization) (15 s), segmentation and generating the measurements (21 s). A shorter segmentation time is required for small tumor and when the initial surface, produced by SCMOT technique, is close to the boundary of the tumor.

IV. DISCUSSION

Our objective was to develop and validate an automated 3D algorithmic assessment tool that could accurately and reproducibly segment and measure pulmonary nodules from CT images. To validate the proposed tool, each tumor was segmented and measured using RECIST, WHO, and volume manually 5 times each by two observers and using the developed segmentation tool by two other observers, five times each. The results from these measurements were compared to assess the variability of each technique and the correlation of the manual to algorithm techniques. Several important observations were made in this study. We showed that: (1) there is no statistically significant difference between manual and algorithm segmentation for RECIST measurement, (2)

Table V. Intra-observer coefficient of variation (CV%) for manual (observers 1 and 2) and algorithm (observers 3 and 4).

	RECIST (1D)	WHO (2D)	Volume (3D)
Manual observer 1	4.20	8.14	21.61
Manual observer 2	6.61	9.57	14.57
Algorithm observer 3	3.09	4.85	5.65
Algorithm observer 4	4.67	5.84	5.88

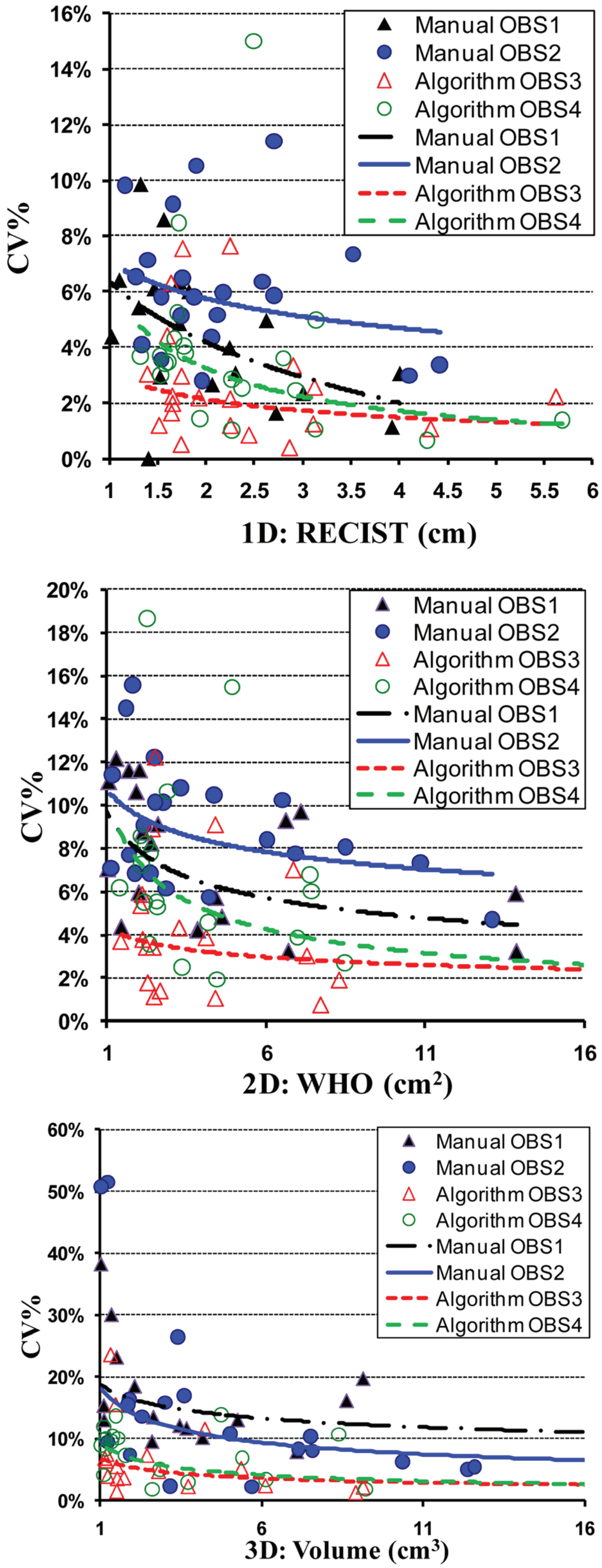

FIG. 4. Intra-observer coefficient of variation of RECIST (1D), WHO (2D), and volume (3D) measurements for the four observers (manual: OBS1, OBS2; algorithm: OBS3, OBS4) and their trend lines.

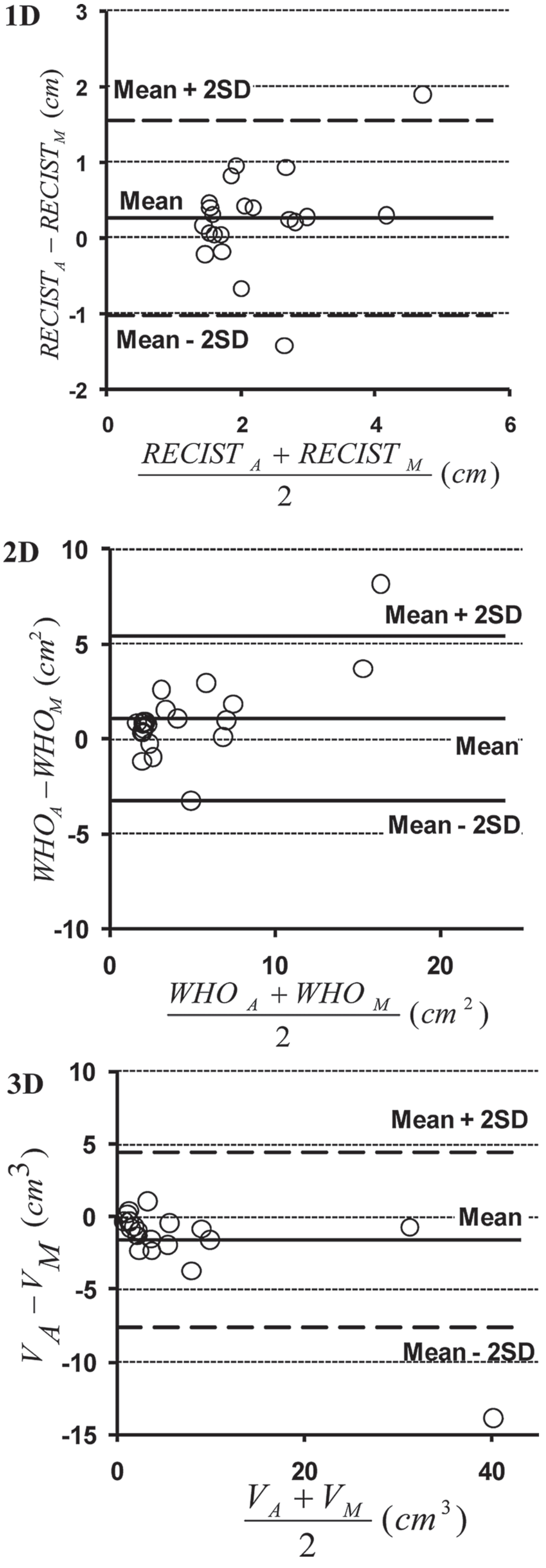

FIG. 5. Bland-Altman plots of RECIST (1D), WHO (2D), and volume (3D) measurements. The plots graph the differences between the manual and algorithm measurements with respect to their means.

the algorithm segmentation/measuring tool has high reproducibility, (3) the intra-observer coefficient of variation for 1D, 2D, and 3D measurements produced by the observers using the algorithm was low ($< 6\%$), (4) there is high correlation between manual and algorithm measurements (RECIST, WHO, and volume) with volume being the most highly correlated, (5) Bland-Altman plots showed a strong agreement between manual and algorithm measurements, and (6) the

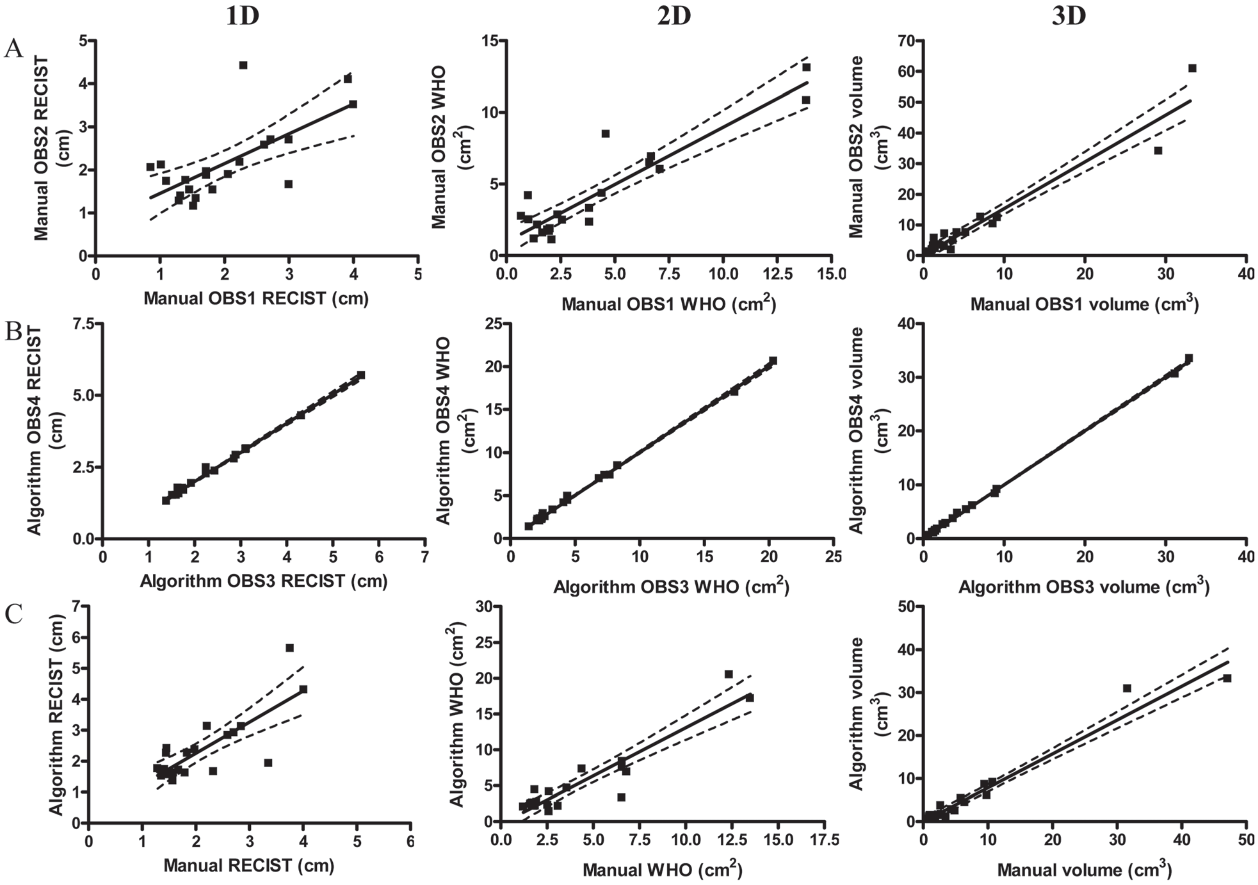

FIG. 6. Linear regression between the measurements of (A) manual observers, (B) algorithm observers, and (C) manual and algorithm observers.

proposed algorithm saves more than 91% of the time required to obtain the three measurements manually.

Two-way repeated measures ANOVA summarized in Table III failed to show a statistically significant difference between manual and algorithm segmentation for RECIST measurement ($p = 0.084$), indicating that the RECIST measurement produced by the algorithm and manual methods are similar. However, there is a statistically significant difference for the WHO ($p = 0.033$) and volume ($p = 0.023$) measurements. We also carried out two-way repeated measures ANOVA between observers for the manual and algorithm methods. We found a statistically significant difference between the manual observers for volume calculations, whereas there is no statistically significant difference between the observers for the algorithm method for RECIST, WHO, or volume measurements. This result indicates that the algorithm method is less observer dependent than the manual method for making these measurements. The significant difference between manual and algorithm WHO measurements (third row of Table III) may be due the following two reasons. First, variation in the manual and algorithm segmented tumor boundaries will result in different longest tumor axis location and angle, which will also result in a different measurement of the longest perpendicular bisector required for the WHO measurement. Second, the manual RECIST and WHO measurements were carried out from only one of the ten manually selected 2D slices (18° apart), whereas the algorithm used the a 3D tumor boundary mesh to select the RECIST and bisector axes. Thus, the manual approach will underestimate the WHO measurements. In addition, Table III also shows that manual observer 2

TABLE VI. Pearson correlation coefficient (r), Linear regression goodness-of-fit measure (r^2), slope, y-intercept, and p-value for the comparison between the measurements of manual observers, algorithm observers, and between manual and algorithm measurements.

		Manual observers	Algorithm observers	Algorithm versus Manual
RECIST	p	0.0005	<0.0001	<0.0001
	r	0.69	1.00	0.79
	r^2	0.48	0.99	0.63
	slope	0.69	1.01	1.01
	y-intercept (cm)	0.76	−0.02	0.24
WHO	p	<0.0001	<0.0001	<0.0001
	r	0.92	1.00	0.93
	r^2	0.84	1.00	0.87
	slope	0.80	1.00	1.34
	y-intercept (cm^2)	0.96	0.03	−0.32
volume	p	<0.0001	<0.0001	<0.0001
	r	0.97	1.00	0.98
	r^2	0.93	1.00	0.96
	Slope	1.52	1.00	0.79
	y-intercept (cm^3)	0.11	−0.01	−0.04

overestimated the volume (8.95 ± 1.30 cm^3) compared to manual observer 1 (5.8 ± 1.25 cm^3), especially, for tumor 3 as demonstrated with high standard deviation (15.1 cm^3) in Table II. That is why there was a statistically significant difference in volume measurement between the two manual observers. The *p*-value of repeated measure ANOVA between manual observer 1 and algorithm observer 3 in volume measurements was 0.821 indicating there is no statistically significant difference between these two observers in volume measurements. Using repeated measure ANOVA, we also found no statistically significant difference ($p = 0.788$) between manual observer 1 and algorithm observer 4 in volume measurements. Since manual observer 2 overestimated the volume measurements, the manual mean value of the volume measurement was overestimated leading to a statistically significant difference between manual and algorithm in volume measurements.

The ICC were computed for RECIST, WHO, and volume measurements as shown in Table IV to study the reproducibility of the algorithm and manual measurements. Table IV shows that the intra-observer correlation coefficients over the five segmentation/measurement rounds for all four observers are over 0.97, which indicates that every observer (manual or algorithm) produced almost the same measurements for all tumors over the five rounds.

The CV% of the algorithm and manual observers are similar for the RECIST measurements; however, the algorithm CV% is lower than that of the manual for both WHO and volume measurements for our data set as shown in Table V. The graphical representation of the CV% for all tumors and measurements shown in Fig. 4 indicate that these values are lower with increasing tumor size and that the algorithm-based measurements are lower than those of the manual measurements.

The Pearson correlation coefficients between manual and algorithm were found to be high ($r = 0.79$, $p < 0.0001$), ($r = 0.93$, $p < 0.0001$), and ($r = 0.98$, $p < 0.0001$), for RECIST (1D), WHO (2D), and volume (3D) measurements, respectively, with volume being the most highly correlated as summarized in Table VI. Moreover, we found a that the linear regression goodness-of-fit measure (r^2) between the algorithm observers was close to 1.0 and the slope of the regression line is close to 1.0 indicating that the results of the algorithm-based measurements are not user dependent (Table VI and Fig. 6). However, r^2 and the slope for the manual RECIST and WHO measurements are not close to 1.0 indicating that they are user dependent. The manual volume measurements had a r^2 close to 1.0 but a slope of 1.52 indicating that the two users consistently different.

Table VI and Fig. 6 show that the slopes and y-intercepts of the linear regression plots are (1.01, 0.24 cm), (1.34, -0.32 cm^2), and (0.79, -0.04 cm^3) for RECIST, WHO, and volume, respectively, indicating that the algorithm slightly over-estimated the RECIST and the WHO measurements, and slightly under-estimated the volume measurements compared to manual measurements, for the reasons discussed above. Furthermore, Bland-Altman plots shown in Fig. 5 show a strong agreement between manual and algorithm measurements of RECIST, WHO, and volume.

Moreover, the proposed algorithm required less than 9% of the time required to manually obtained the three measurements. The average time required to segment and obtained the three measurements by the algorithm was 36 s (21–105 s) compared to 7 min manually. The average time required by the algorithm operator to place a point in the approximate center of the tumor was 15 s, whereas the average time required by the algorithm to segmentation and measure the tumor was 21 s ranging from 6 to 90 s. Large tumors required more time by the algorithm compared to small tumors since the number of vertices deformed by the algorithm were higher for the large tumors compared to small ones. When the initial surface obtained by the SCOMT technique, shown in Fig. 1, is close to the tumor boundary, the deformation using SFAS technique, shown in Fig. 1, requires a short time to produce the final result. The algorithm processing time can be dramatically reduced by optimizing the code using parallel processing and GPU. Since the deformation part of the algorithm using SFAS computes the local speed functions given in Eq. (6) for each vertex of the mesh, it consumes most of the processing time required by the algorithm. To reduce the deformation time considerably, the code should be improved to use the fact that some of the mesh vertices converge faster than others. Therefore, the local speed functions should not be computed for converged vertices, which can save considerable time.

Although this study reports that the proposed tool is faster and less observer dependent than manual segmentation while accurately segmenting and measuring lung tumor, we acknowledge a number of specific limitations of our approach. The data set used to evaluate the algorithm consists of 21 tumors (5 intraparenchymal and 16 juxtapleural tumors). Although our results were tested statistically and demonstrated statistical significance, the algorithm would benefit for validation with a larger data set. This large data set should also be publicly available to enable comparing our algorithm with other techniques using the same data set. Currently, it is very hard to compare our results to the existing techniques since every technique is using different datasets with different ground truth (visual inspection in some cases) and different measures as discussed in the Sec. I. Therefore, in our future work we will evaluate our algorithm with LIDC database.[30,31] LIDC database provides not only the CT images, but also the ground truth of lung tumor segmentation, allowing investigators to compare results without having to implement and optimize other investigators' algorithms.

The algorithm was evaluated in metastatic lung tumors. Primary lung carcinomas were not evaluated. The algorithm may require a modification to correctly segment nonsolid tumors since it was designed assuming a solid lung tumor with a shape index SI equals or more than SI_{Th} (0.4). This SI_{Th} value was determined experimentally as low as possible to allow constructing initial surfaces for various tumor shapes and at the same time to remove the other tissues attached to the tumor such as blood vessels. The selected SI_{Th} performed well with our dataset since the SI average and standard deviation for the 21 tumors are 0.81 ± 0.08.

However, if the tumor does not satisfy this assumption, the SCOMT technique may not be able to find an initial surface. There are three solutions to this problem. The first solution is to request the observer to place one or more anchor points on the boundary of the tumor. The anchor point(s) can be used to construct an initial surface and also in an anchor speed function to drive the deformed surface to the nearest anchor point. The second solution is to construct the initial surface S_T by subtracting the lung surface S_L from the lung convex surface S_{LC} as described in the background speed function. The third solution is to construct a small sphere surface centered at the initial center point. The drawback of the last solution is that the surface deformation will take longer time to reach the tumor boundary if the initial surface is far away from it.

Although the selected fixed values (Table I) used for the weighting parameters of the energy function [Eq. (4)] produced accurate results, we cannot grantee that the same values can work with any tumor. In our future work, we will explore the following approaches for the weighting parameters. The first approach is to find the optimum values of these parameters for a large data set to avoid over fitting issue. Another approach is to allow the weighting parameters to be changed dynamically from one tumor to another based on the tumor Hounsfield distribution, geometric and location properties. Thus, the weighting parameters could be changed dynamically from one iteration to the next for the same tumor based on the properties of the current deformed surface. Additionally, scalar weighting parameters can be replaced by vector ones. Hence, each speed function can have a different weighting value for every vertex during any iteration depending on a confidence probability C_P. The maximum C_P can reach a value of one if we are totally confident about the current speed function value in case of an anchor speed function. The C_P may not only depend on the properties of the speed function itself, but also may depend on the current speed function value compared to other speed functions at the same vertex. In other words, higher C_P can be assigned to the current speed function if it is pushing the surface in the same direction as the majority of the other speed functions at the same vertex.

Although, the observers were instructed to initiate the algorithm by selecting a single seed point approximately in the center of the tumor, our experiments showed that the resulting segmented surface is not sensitive to the selection of the seed point as demonstrated by the algorithm observers high reproducibility (ICC = 0.989–0.995, 0.996–0.997, and 0.999–0.999), high correlation ($r = 1.00$, $p < 0.0001$; $r = 1.00$, $p < 0.0001$; and $r = 1.00$, $p < 0.0001$), and high goodness-of-fit ($r^2 = 0.99$, $p < 0.0001$; $r^2 = 1.00$, $p < 0.0001$; and $r^2 = 1.00$, $p < 0.0001$) for 1D, 2D, and 3D measurements, respectively, as shown in Fig. 6(B). There are three reasons that the algorithm is not sensitive to the selection of the seed point. First, the initial surface constructed by SCMOT does not depend on the location of the seed point as long as it is on the tumor since the shape index measure (SI) is measured from the centroid of the segmented region (VOI) and not from the seed point as described in Sec. II A 1. Second, the only speed function depends on the location of the seed point is the shape speed function F_H which has the minimum weighting parameter ($\alpha_H = 0.07$). Third, the geometric integrity function [Eq. (40)] of this speed function is designed to mainly affect outlier vertices to prevent segmenting blood vessel attached to tumors.

In conclusion, our findings suggest that the proposed algorithm for segmenting lung tumors from CT images is at least as accurate as manual segmentation/measurement and is less observer dependency than manual method. Thus, the reduced variability of our algorithm segmentation tool compared to manual-based measurements suggests that it can be used to produce accurate lung tumor measurements and that it is more sensitive to small changes in lung tumor dimensions and volume. This makes our tool suitable for translation into use in clinical trials and monitoring tumor response to therapy.

ACKNOWLEDGMENTS

This study was supported by the Ontario Institute for Cancer Research—Imaging Pipeline Platform. Fenster holds a Canada Research Chair in Biomedical Engineering and acknowledges the support of the Canada Research Chair Program. Parraga holds a Canadian Institutes of Health Research New Investigator Award and acknowledges support for from this agency.

[1] I. J. Fidler, "The organ microenviroment and cancer metastasis," Differentiation **70**, 498–505 (2002).

[2] I. J. Fidler, "Critical determinants of metastasis," Cancer Biol. **12**, 89–96 (2002).

[3] P. Therasse, S. G. Arbuck, E. A. Eisenhauer, J. Wanders, R. S. Kaplan, L. Rubinstein, J Verweij, M. V. Glabbeke, A. T. V. Oosterom, M. C. Christian, and S. G. Gwyther, "New guidelines to evaluate the response to treatment in solid tumors," J. Natl. Cancer Inst. **92**, 205–216 (2000).

[4] World Health Organization, *WHO Handbook for Reporting Results of Cancer Treatment* (World Health Organization Offset Publication No. 48, WHO, Geneva, 1979).

[5] J. M. Goo, T. Tongdee, R. Tongdee, K. Yeo, C. F. Hildebolt, and K. T. Bae, "Volumetric measurement of synthetic lung nodules with multi-detector row CT: Effect of various image reconstruction parameters and segmentation thresholds on measurement accuracy," Radiology **235**, 850–856 (2005).

[6] B. Golosio, G. L. Masala, A. Piccioli, P. Oliva, M. Carpinelli, R. Cataldo, P. Cerello, F. D. Carlo, and G. Gargano, "A novel multithreshold method for nodule detection in lung CT," Med. Phys. **36**, 3607–3618 (2009).

[7] W. J. Kostis, A. P. Reeves, D. F. Yankelevitz, and C. I. Henschke, "Three-dimensional segmentation and growth-rate estimation of small pulmonary nodules in helical CT images," IEEE Trans. Med. Imaging **22**, 1259–1274 (2003).

[8] L. N. Tran, M. S. Brown, J. G. Goldin, X. Yan, R. C. Pais, M. F. McNitt-Gray, D. Gjertson, S. R. Rogers, and D. R. Aberle, "Comparison of treatment response classifications between unidimensional, bidimensional, and volumetric measurements of metastatic lung lesions on chest computed tomography," Acad. Radiol. **11**, 1355–1360 (2004).

[9] J. H. Moltz, L. Bornemann, J. M. Kuhnigk, V. Dicken, E. Peitgen, S. Meier, H. Bolte, M. Fabel, H. C. Bauknecht, M. Hittinger, A. Kiessling, M. Pusken, and H. O. Peitgen, "Advanced segmentation techniques for lung nodules, liver metastases, and enlarged lymph nodes in ct scans," IEEE J. Sel. Top. Signal Process. **3**, 122–134 (2009).

[10] J. M. Kuhnigk, V. Dicken, L. Bornemann, A. Bakai, D. Wormanns, S. Krass, and H. O. Peitgen, "Morphological segmentation and partial

volume analysis for volumetry of solid pulmonary lesions in thoracic CT scans," IEEE Trans. Med. Imaging **25**, 417–434 (2006).

[11] M. Kakar and D. R. Olsen, "Automatic segmentation and recognition of lungs and lesion from CT scans of thorax," Comput. Med. Imaging Graph. **33**, 72–82 (2009).

[12] T. W. Way, L. M. Hadjiiski, B. Sahiner, H. P. Chan, P. N. Cascade, E. A. Kazerooni, N. Bogot, and C. Zhou, "Computer-aided diagnosis of pulmonary nodules on CT scans: Segmentation and classification using 3D active contours," Med. Phys. **33**, 2323–2337 (2006).

[13] K. Okada, D. Comaniciu, and A. Krishnan, "Robust anisotropic Gaussian fitting for volumetric characterization of Pulmonary nodules in multislice CT," IEEE Trans. Med. Imaging **24**, 409–423 (2005).

[14] Q. Wang, E. Song, R. Jin, P.Han, X. Wang, Y. Zhou, and J. Zeng, "Segmentation of lung nodules in computed tomography images using dynamic programming and multidirection fusion techniques," Acad. Radiol. **16**, 678–688 (2009).

[15] J. Awad, L. Wilson, G. Parraga, and A. Fenster, "Lung tumours segmentation on CT using sparse field active model," SPIE **7963**, 79632Y1–79632Y10 (2011).

[16] N. Otsu, "A threshold selection method from gray-level histograms," IEEE Trans. Syst. Man Cybern. **9**, 62–66 (1979).

[17] S. Lankton and A. Tannenbaum, "Localizing region-based active contours," IEEE Trans. Image Process. **17**, 2029–2039 (2008).

[18] J. A. Yezzi, A. Tsai, and A. Willsky, "A fully global approach to image segmentation via coupled curve evolution equations," J. Visual. Commun. Image Represent **13**, 195–216 (2002).

[19] T. Chan and L. Vese, "Active contour without edges," IEEE Trans. Image Process. **10**, 266–277 (2001).

[20] Y. Shi and W. C. Karl, "A real-time algorithm for the approximation of level-set-based curve evolution," IEEE Trans. Image Process. **17**, 645–656 (2008).

[21] S. Osher and J. A. Sethian, "Fronts propagating with curvature-dependent speed: Algorithms based on Hamilton-Jacobi formulations," J. Comput. Phys. **79**, 12–49 (1988).

[22] D. Adalsteinsson and J. A. Sethian, "A fast level set method for propagating interfaces," J. Comput. Phys. **118**, 269–277 (1995).

[23] R. A. Whitaker, "level-set approach to 3D reconstruction from range data," Int. J. Comput. Vis. **29**, 203–231 (1998).

[24] L. Villemaire *et al.*, "Pulmonary tumor measurements from x-ray computed tomography in one, two, and three dimensions," Acad. Radiol. **18**, 1391–1402 (2011).

[25] J. J. Erasmus, G. W. Gladish, L. Broemeling, B. S. Sabloff, M. T. Truong, R. S. Herbst, and R. F. Munden, "Interobserver and intraobserver variability in measurement of non-small-cell carcinoma lung lesions: Implications for assessment of tumor response," J. Clin. Oncol. **21**, 2574–2582 (2003).

[26] K. D. Hopper, C. J. Kasales, M. A. V. Slyke, T. A. Schwartz, T. R. Ten-Have, and J. A. Jozefiak, "Analysis of interobserver and intraobserver variability in CT tumor measurements," AJR, Am. J. Roentgenol. **167**, 851–854 (1996).

[27] A. Landry, J. D. Spence, and A. Fenster, "Quantification of carotid plaque volume measurements using 3D ultrasound imaging," Ultrasound Med. Biol. **31**, 751–762 (2005).

[28] K. McGraw and S. Wong, "Forming inferences about some intraclass correlation coefficients," Psychol. Methods **1**, 30–46 (1996).

[29] D. G. Altman and J. M. Bland, "Measurement in medicine: The analysis of method comparison studies," Statistician **32**, 307–317 (1983).

[30] S. G. Armato III *et al.*, "Lung image database consortium: Developing a resource for the medical imaging research community," Radiology **232**, 739–748 (2004).

[31] M. F. McNitt-Gray *et al.*, "The Lung Image Database Consortium (LIDC) data collection process for nodule detection and annotation," Acad. Radiol. **14**, 1464–1474 (2007).

Appendix – C: Chest MRI in Children: Why Bother?

The work presented in this chapter has been previously published in the journal of *Respirology* as indicated below, and is reproduced here with permission (Appendix C).

Amir M. Owrangi and Grace Parraga.“Chest MRI in Children: Why Bother?” Respirology. 2012 Jan;17(1):3-4.

Official Journal of the Asian Pacific Society of Respirology
Respirology

EDITORIAL

Chest MRI in children: Why bother?

Key words: high resolution CT, image quality, MRI, pediatric imaging, visual assessment.

In this issue of *Respirology*, Montella and colleagues[1] ask this question: How does high-field chest MRI compare with CT of children with non-cystic fibrosis (CF) lung disease? In an important extension of the first description of this study[2] where they compared MRI and CT with pulmonary function measurements, the authors evaluated how widely-used chest CT and almost never-utilized lung MRI compare for diagnostic imaging of chronic lung disease. Here they show that high-field (3Tesla as compared with the 1.5Tesla clinical standard) thoracic MRI has high reliability and good-to-excellent agreement with CT, definitively answering the important question at hand; their results support more widespread and routine use of MRI in longitudinal monitoring of chronic lung disease, especially in children as well as further optimization and improvement of lung MRI methods. Importantly, non-CF lung disease accounts for the majority of paediatric pulmonary abnormalities[3] and the increasing prevalence and economic burden[4] related to chronic respiratory disease should motivate the research and development of novel MRI methods for serial and longitudinal imaging.[5]

X-ray-based high resolution CT (HRCT) still provides the tool of choice for chest imaging of adults and children with respiratory disease mainly because of its short acquisition times, high spatial resolution and rich information content based on the differential attenuation of x-rays in the lung tissue and airspaces. Although HRCT provides a way to display and qualitatively/quantitatively interpret lung abnormalities, all x-ray based methods including HRCT deliver a small but potentially significant radiation dose to the patient. This limits repeated or longitudinal imaging, a particular problem for children with chronic respiratory disorders. To directly address this limitation, one approach has involved the development of low-dose HRCT techniques[6] and these have become a routine part of screening for, and examination of, lung disease,[7] although the radiation risks are not eliminated. Another approach involves the development of thoracic MRI—mainly overlooked as a clinical application, although its diagnostic potential was recognized nearly two decades ago.[8]

Conventional proton MRI (^{1}H MRI) is readily available in most clinical care centres and radiology departments, however, until now, a number of fundamental challenges have limited its use as a clinical tool for lung imaging. MRI provides exquisite soft tissue contrast of the brain, abdomen and musculoskeletal system by virtue of its detection of water-bound protons in slightly different chemical environments. Proton MRI therefore is understandably dependent on the proton density of the tissues involved but the lung has relatively low tissue density (and high gas density) and is mainly devoid of water. Therefore the lung has very low proton density—and this is one reason why thoracic MRI, even when optimized for the lung, results in an image that resembles a black hole,[9,10] apparently devoid of tissue and morphological information. Compounding this, the lung consists of millions of air-tissue interfaces (on the micrometre scale) designed to aid in gas exchange and because of this, the different magnetic environments in the air and tissue result in so-called magnetic 'susceptibility artefacts'. High-field lung MRI susceptibility artefacts result in transverse relaxation times ($T2^*$) that are shortened ($T2^* = 740\ \mu s$ at 3T), and the practical implication for imaging is that signal decay is accelerated and pulse sequences must be optimized for faster echo times (on the order of 10–100 µs). Taken together, low proton density and susceptibility artefacts mean that lung MRI must incorporate both short echo time/acquisition and long acquisition times for signal averaging and improved signal-to-noise ratios.

Recently there has been a renewed interest in the clinical potential of thoracic proton MRI stimulated by cardiac MRI developments[11] as well as novel pulmonary functional MRI using noble gas contrast agents[12] and Fourier-decomposition proton MRI.[13,14] Pertinent to the current evaluation is the development of the use of ultra-short echo times for lung structure imaging pioneered by Mayo and Muller[8] with recent applications to CF[15] and non-CF lung diseases.[16]

Here, Montella *et al*[1] utilize a straightforward MRI protocol, available on most hospital scanners without the need for additional programming, enabling a practical comparison between two clinically available methods; this is a definite strength of their approach and speaks to the relevance of their results. Although future work will likely incorporate optimized pulse sequences and methods with decreased echo times (e.g. echo time here was 92 ms and with UTE, echo time of 12 µs is possible), the current results are very promising and urge us to continue to develop and test improved lung structural and functional MRI for routine clinical use.

Up until recently, the imaging modality of choice for clinical diagnosis and monitoring of respiratory disease has unquestionably been x-ray-based HRCT. Although good agreement between MRI and CT was observed and reported here, it is clear that lung

Respirology (2012) **17**, 3–4
doi: 10.1111/j.1440-1843.2011.02079.x

imaging using MRI currently cannot surpass HRCT in terms of speed, image contrast and content as well as spatial resolution. In fact, because of the inherent limitations based on the physics of MRI itself, pulmonary MRI may never replace HRCT for lung disease diagnoses. However, in recognition of the fact that the lung is the most radiosensitive organ in the chest[17,18] and longitudinal monitoring will increase the risk of cumulative radiation doses,[19] especially in children, MRI, even without optimization, should be considered. As shown here, the information derived is certainly complementary to HRCT and in some longitudinal applications in chronic disease, is superior to CT because of its relatively low risk and high information content. Certainly, the current study highlights the practical diagnostic information available now using thoracic MRI acquired on conventional clinical scanners.

Yes, we think chest MRI is definitely worth the bother, now, and in the future.

Amir M. Owrangi[1,2] MSc and Grace Parraga[1–4] PhD
[1]*Imaging Research Laboratories, Robarts Research Institute,* [2]*Graduate Program in Biomedical Engineering,* [3]*Department of Medical Imaging, and* [4]*Department of Medical Biophysics, The University of Western Ontario, London, Ontario, Canada*

REFERENCES

1 Montella S, Maglione M, Bruzzese D *et al.* Is chest magnetic resonance imaging reliable in non-cystic fibrosis paediatric lung disease evaluation? *Respirology* 2012; **17**: 87–91.
2 Montella S, Santamaria F ,Salvatore M *et al.* Assessment of chest high-field magnetic resonance imaging in children and young adults with noncystic fibrosis chronic lung disease: comparison to high-resolution computed tomography and correlation with pulmonary function. *Invest. Radiol.* 2009; **44**: 532–8.
3 Grosse SD, Boyle CA, Botkin JR *et al.* Newborn screening for cystic fibrosis: evaluation of benefits and risks and recommendations for state newborn screening programs. *MMWR Recomm. Rep.* 2004; **53**: 1–36.
4 Zar HJ, Mulholland K. Global burden of pediatric respiratory illness and the implications for management and prevention. *Pediatr. Pulmonol.* 2003; **36**: 457–61.
5 Puderbach M, Eichinger M, Gahr J *et al.* Proton MRI appearance of cystic fibrosis: comparison to CT. *Eur. Radiol.* 2007; **17**: 716–24.
6 Naidich DP, Marshall CH, Gribbin C *et al.* Low-dose CT of the lungs: preliminary observations. *Radiology* 1990; **175**: 729–31.
7 Kaneko M, Eguchi K, Ohmatsu H *et al.* Peripheral lung cancer: screening and detection with low-dose spiral CT versus radiography. *Radiology* 1996; **201**: 798–802.
8 Mayo JR, MacKay A, Muller NL. MR imaging of the lungs: value of short TE spin-echo pulse sequences. *AJR Am. J. Roentgenol.* 1992; **159**: 951–6.
9 Kauczor HU, Ley S. Thoracic magnetic resonance imaging 1985 to 2010. *J. Thorac. Imaging* 2010; **25**: 34–8.
10 Kirby M, Owrangi A, Wong J *et al.* Pulmonary magnetic resonance imaging of obstructive airways disease. *Minerva Pnemol.* 2011; **50**: 17–19.
11 Finn JP, Nael K, Deshpande V *et al.* Cardiac MR imaging: state of the technology. *Radiology* 2006; **241**: 338–54.
12 Fain S, Schiebler ML, McCormack DG *et al.* Imaging of lung function using hyperpolarized helium-3 magnetic resonance imaging: Review of current and emerging translational methods and applications. *J. Magn. Reson. Imaging* 2010; **32**: 1398–408.
13 Bauman G, Puderbach M, Deimling M *et al.* Non-contrast-enhanced perfusion and ventilation assessment of the human lung by means of fourier decomposition in proton MRI. *Magn. Reson. Med.* 2009; **62**: 656–64.
14 Bauman G, Lutzen U, Ullrich M *et al.* Pulmonary functional imaging: qualitative comparison of Fourier decomposition MR imaging with SPECT/CT in porcine lung. *Radiology* 2011; **260**: 551–9.
15 Failo R, Wielopolski PA, Tiddens HA *et al.* Lung morphology assessment using MRI: a robust ultra-short TR/TE 2D steady state free precession sequence used in cystic fibrosis patients. *Magn. Reson. Med.* 2009; **61**: 299–306.
16 Takahashi M, Togao O, Obara M *et al.* Ultra-short echo time (UTE) MR imaging of the lung: comparison between normal and emphysematous lungs in mutant mice. *J. Magn. Reson. Imaging* 2010; **32**: 326–33.
17 Angel E, Yaghmai N, Jude CM *et al.* Dose to radiosensitive organs during routine chest CT: effects of tube current modulation. *AJR Am. J. Roentgenol.* 2009; **193**: 1340–45.
18 Mayo JR, Aldrich J, Muller NL. Radiation exposure at chest CT: a statement of the Fleischner Society. *Radiology* 2003; **228**: 15–21.
19 Brenner DJ, Hall EJ. Computed tomography—an increasing source of radiation exposure. *N. Engl. J. Med.* 2007; **357**: 2277–84.

Appendix – D: Permissions for Reproduction of Scientific Articles

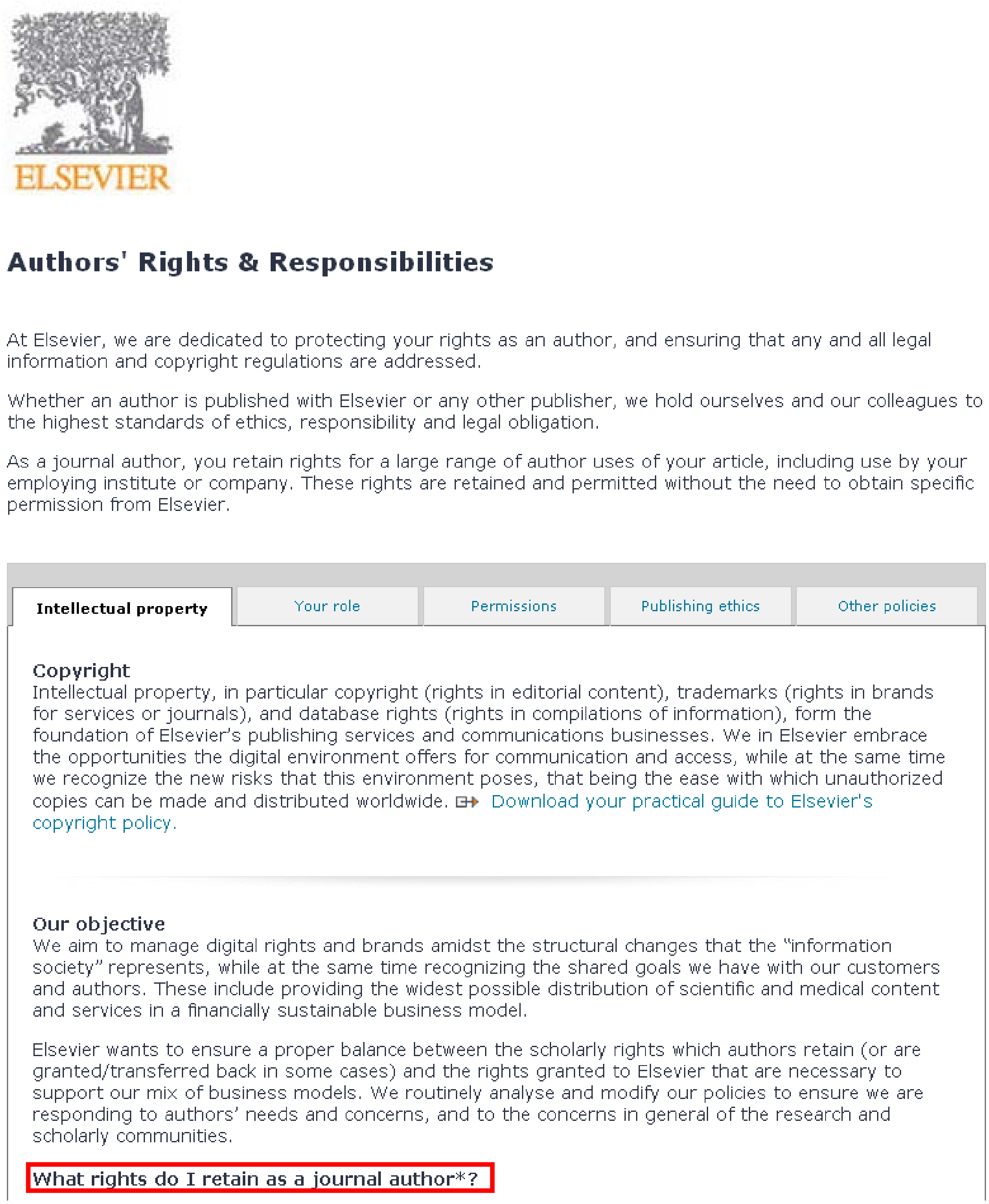

Authors' Rights & Responsibilities

At Elsevier, we are dedicated to protecting your rights as an author, and ensuring that any and all legal information and copyright regulations are addressed.

Whether an author is published with Elsevier or any other publisher, we hold ourselves and our colleagues to the highest standards of ethics, responsibility and legal obligation.

As a journal author, you retain rights for a large range of author uses of your article, including use by your employing institute or company. These rights are retained and permitted without the need to obtain specific permission from Elsevier.

Copyright

Intellectual property, in particular copyright (rights in editorial content), trademarks (rights in brands for services or journals), and database rights (rights in compilations of information), form the foundation of Elsevier's publishing services and communications businesses. We in Elsevier embrace the opportunities the digital environment offers for communication and access, while at the same time we recognize the new risks that this environment poses, that being the ease with which unauthorized copies can be made and distributed worldwide. Download your practical guide to Elsevier's copyright policy.

Our objective

We aim to manage digital rights and brands amidst the structural changes that the "information society" represents, while at the same time recognizing the shared goals we have with our customers and authors. These include providing the widest possible distribution of scientific and medical content and services in a financially sustainable business model.

Elsevier wants to ensure a proper balance between the scholarly rights which authors retain (or are granted/transferred back in some cases) and the rights granted to Elsevier that are necessary to support our mix of business models. We routinely analyse and modify our policies to ensure we are responding to authors' needs and concerns, and to the concerns in general of the research and scholarly communities.

What rights do I retain as a journal author*?

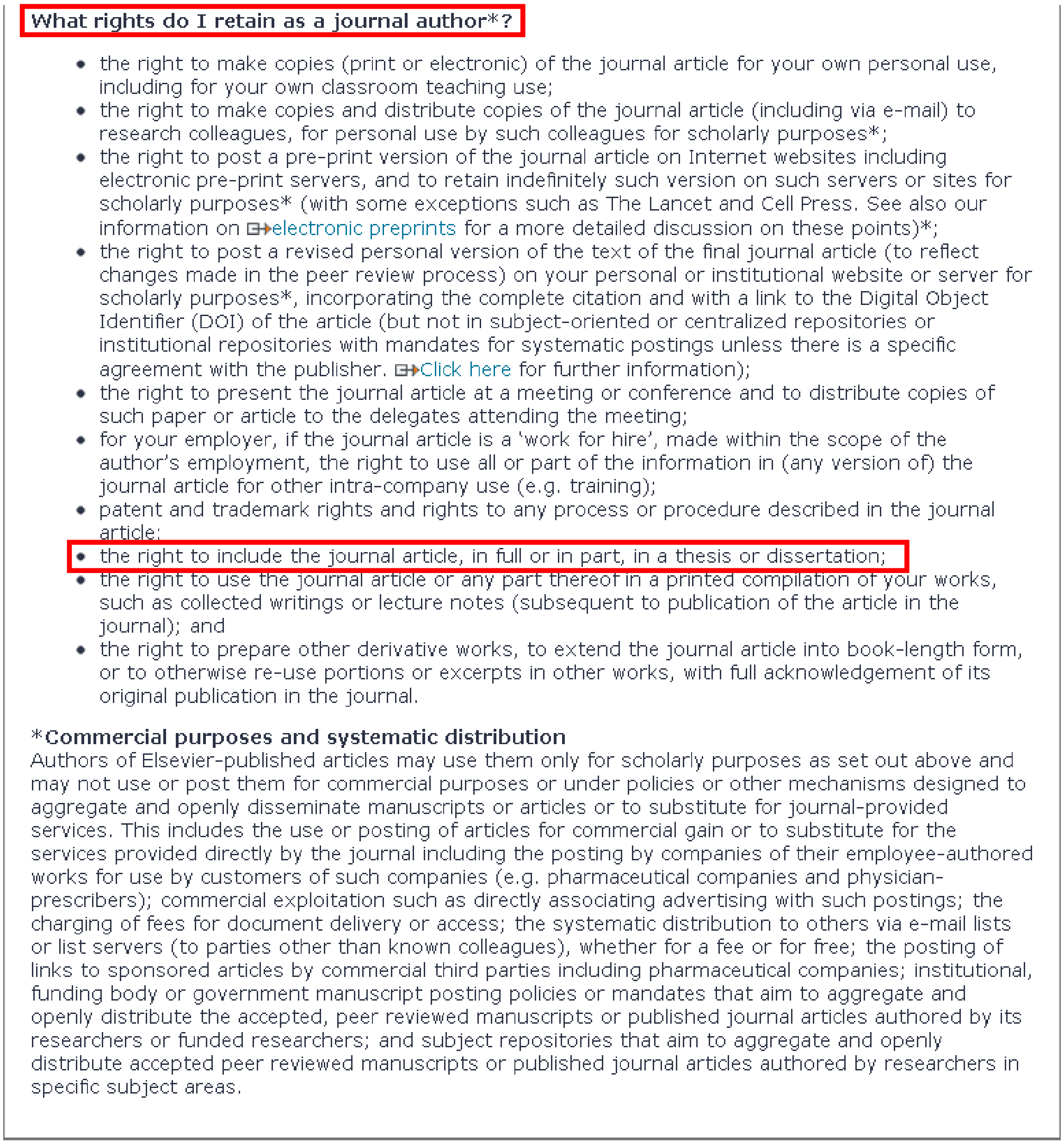

What rights do I retain as a journal author*?

- the right to make copies (print or electronic) of the journal article for your own personal use, including for your own classroom teaching use;
- the right to make copies and distribute copies of the journal article (including via e-mail) to research colleagues, for personal use by such colleagues for scholarly purposes*;
- the right to post a pre-print version of the journal article on Internet websites including electronic pre-print servers, and to retain indefinitely such version on such servers or sites for scholarly purposes* (with some exceptions such as The Lancet and Cell Press. See also our information on electronic preprints for a more detailed discussion on these points)*;
- the right to post a revised personal version of the text of the final journal article (to reflect changes made in the peer review process) on your personal or institutional website or server for scholarly purposes*, incorporating the complete citation and with a link to the Digital Object Identifier (DOI) of the article (but not in subject-oriented or centralized repositories or institutional repositories with mandates for systematic postings unless there is a specific agreement with the publisher. Click here for further information);
- the right to present the journal article at a meeting or conference and to distribute copies of such paper or article to the delegates attending the meeting;
- for your employer, if the journal article is a 'work for hire', made within the scope of the author's employment, the right to use all or part of the information in (any version of) the journal article for other intra-company use (e.g. training);
- patent and trademark rights and rights to any process or procedure described in the journal article;
- the right to include the journal article, in full or in part, in a thesis or dissertation;
- the right to use the journal article or any part thereof in a printed compilation of your works, such as collected writings or lecture notes (subsequent to publication of the article in the journal); and
- the right to prepare other derivative works, to extend the journal article into book-length form, or to otherwise re-use portions or excerpts in other works, with full acknowledgement of its original publication in the journal.

***Commercial purposes and systematic distribution**
Authors of Elsevier-published articles may use them only for scholarly purposes as set out above and may not use or post them for commercial purposes or under policies or other mechanisms designed to aggregate and openly disseminate manuscripts or articles or to substitute for journal-provided services. This includes the use or posting of articles for commercial gain or to substitute for the services provided directly by the journal including the posting by companies of their employee-authored works for use by customers of such companies (e.g. pharmaceutical companies and physician-prescribers); commercial exploitation such as directly associating advertising with such postings; the charging of fees for document delivery or access; the systematic distribution to others via e-mail lists or list servers (to parties other than known colleagues), whether for a fee or for free; the posting of links to sponsored articles by commercial third parties including pharmaceutical companies; institutional, funding body or government manuscript posting policies or mandates that aim to aggregate and openly distribute the accepted, peer reviewed manuscripts or published journal articles authored by its researchers or funded researchers; and subject repositories that aim to aggregate and openly distribute accepted peer reviewed manuscripts or published journal articles authored by researchers in specific subject areas.

JOHN WILEY AND SONS LICENSE
TERMS AND CONDITIONS

Sep 19, 2012

This is a License Agreement between Amir Owrangi ("You") and John Wiley and Sons ("John Wiley and Sons") provided by Copyright Clearance Center ("CCC"). The license consists of your order details, the terms and conditions provided by John Wiley and Sons, and the payment terms and conditions.

All payments must be made in full to CCC. For payment instructions, please see information listed at the bottom of this form.

License Number	2992730686209
License date	Sep 19, 2012
Licensed content publisher	John Wiley and Sons
Licensed content publication	Respirology
Licensed content title	Chest MRI in children: Why bother?
Licensed content author	Amir M. Owrangi,Grace Parraga
Licensed content date	Dec 21, 2011
Start page	3
End page	4
Type of use	Dissertation/Thesis
Requestor type	Author of this Wiley article
Format	Print and electronic
Portion	Full article
Will you be translating?	No
Order reference number	
Total	0.00 USD
Terms and Conditions	

TERMS AND CONDITIONS

This copyrighted material is owned by or exclusively licensed to John Wiley & Sons, Inc, or one of its group companies (each a "Wiley Company") or a society for whom a Wiley Company has exclusive publishing rights in relation to a particular journal (collectively WILEY"). By clicking "accept" in connection with completing this licensing transaction, you agree that the following terms and conditions apply to this transaction (along with the billing and payment terms and conditions established by the Copyright Clearance Center Inc., ("CCC's Billing and Payment terms and conditions"), at the time that you opened your Rightslink account (these are available at any time at http://myaccount.copyright.com)

Terms and Conditions

1. The materials you have requested permission to reproduce (the "Materials") are protected by copyright.

2. You are hereby granted a personal, non-exclusive, non-sublicensable, non-transferable,

Appendix – E: Health Science Research Ethics Board Approval Notices

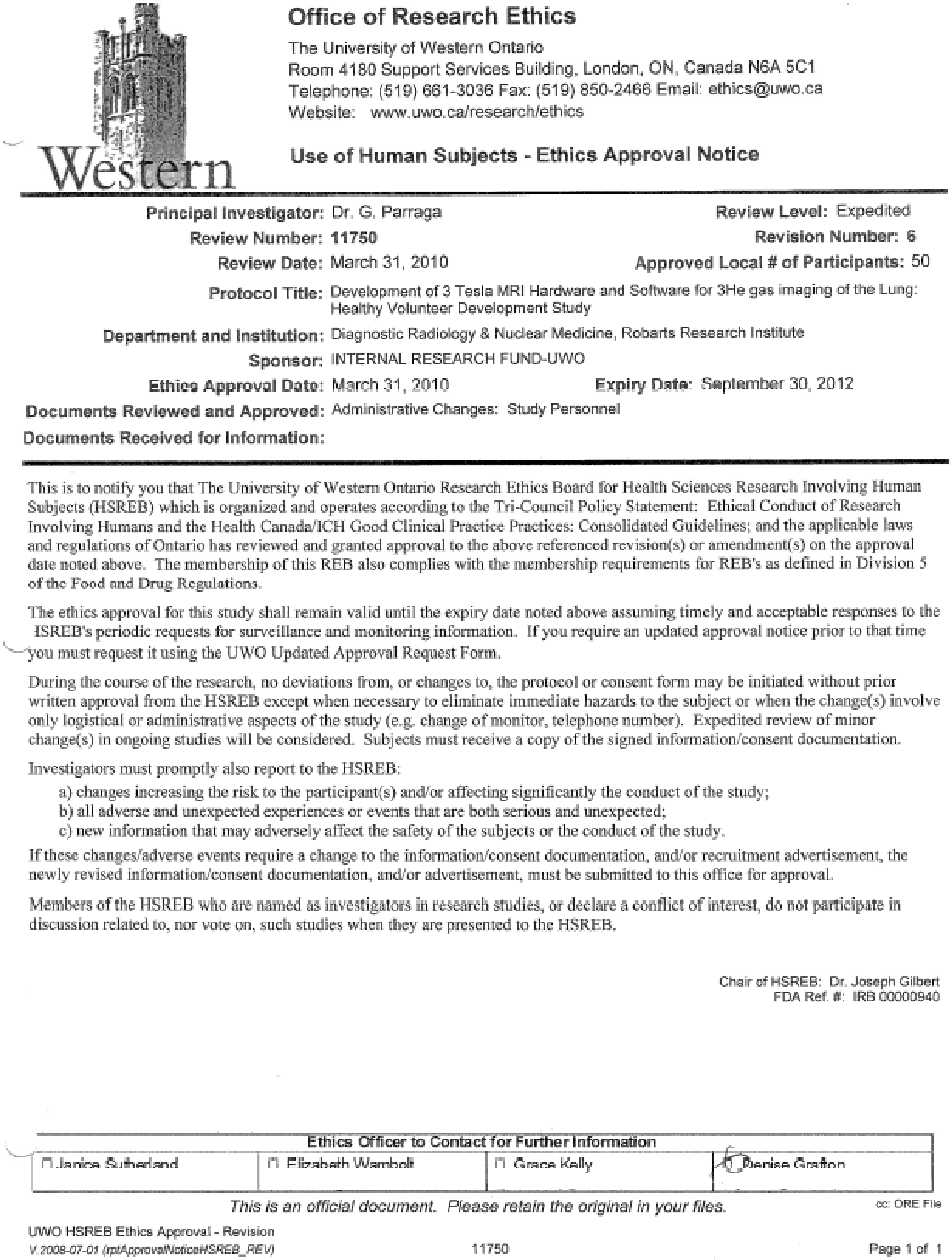

Western

Office of Research Ethics

The University of Western Ontario
Room 4180 Support Services Building, London, ON, Canada N6A 5C1
Telephone: (519) 661-3036 Fax: (519) 850-2466 Email: ethics@uwo.ca
Website: www.uwo.ca/research/ethics

Use of Human Subjects - Ethics Approval Notice

Principal Investigator: Dr. G. Parraga
Review Level: Expedited
Review Number: 11750
Revision Number: 6
Review Date: March 31, 2010
Approved Local # of Participants: 50
Protocol Title: Development of 3 Tesla MRI Hardware and Software for 3He gas imaging of the Lung: Healthy Volunteer Development Study
Department and Institution: Diagnostic Radiology & Nuclear Medicine, Roberts Research Institute
Sponsor: INTERNAL RESEARCH FUND-UWO
Ethics Approval Date: March 31, 2010
Expiry Date: September 30, 2012
Documents Reviewed and Approved: Administrative Changes: Study Personnel
Documents Received for Information:

This is to notify you that The University of Western Ontario Research Ethics Board for Health Sciences Research Involving Human Subjects (HSREB) which is organized and operates according to the Tri-Council Policy Statement: Ethical Conduct of Research Involving Humans and the Health Canada/ICH Good Clinical Practice Practices: Consolidated Guidelines; and the applicable laws and regulations of Ontario has reviewed and granted approval to the above referenced revision(s) or amendment(s) on the approval date noted above. The membership of this REB also complies with the membership requirements for REB's as defined in Division 5 of the Food and Drug Regulations.

The ethics approval for this study shall remain valid until the expiry date noted above assuming timely and acceptable responses to the HSREB's periodic requests for surveillance and monitoring information. If you require an updated approval notice prior to that time you must request it using the UWO Updated Approval Request Form.

During the course of the research, no deviations from, or changes to, the protocol or consent form may be initiated without prior written approval from the HSREB except when necessary to eliminate immediate hazards to the subject or when the change(s) involve only logistical or administrative aspects of the study (e.g. change of monitor, telephone number). Expedited review of minor change(s) in ongoing studies will be considered. Subjects must receive a copy of the signed information/consent documentation.

Investigators must promptly also report to the HSREB:

a) changes increasing the risk to the participant(s) and/or affecting significantly the conduct of the study;
b) all adverse and unexpected experiences or events that are both serious and unexpected;
c) new information that may adversely affect the safety of the subjects or the conduct of the study.

If these changes/adverse events require a change to the information/consent documentation, and/or recruitment advertisement, the newly revised information/consent documentation, and/or advertisement, must be submitted to this office for approval.

Members of the HSREB who are named as investigators in research studies, or declare a conflict of interest, do not participate in discussion related to, nor vote on, such studies when they are presented to the HSREB.

Chair of HSREB: Dr. Joseph Gilbert
FDA Ref. #: IRB 00000940

Ethics Officer to Contact for Further Information			
☐ Janice Sutherland	☐ Elizabeth Wambolt	☐ Grace Kelly	☑ Denise Grafton

This is an official document. Please retain the original in your files.

cc: ORE File

UWO HSREB Ethics Approval - Revision
V.2008-07-01 (rptApprovalNoticeHSREB_REV)

11750

Page 1 of 1

Office of Research Ethics

The University of Western Ontario
Room 4180 Support Services Building, London, ON, Canada N6A 5C1
Telephone: (519) 661-3036 Fax: (519) 850-2466 Email: ethics@uwo.ca
Website: www.uwo.ca/research/ethics

Use of Human Subjects - Ethics Approval Notice

Principal Investigator: Dr. G. Parraga
Review Number: 15930 **Review Level:** Full Board
Review Date: February 10, 2009
Protocol Title: Longitudinal Study of Helium-3 Magnetic Resonance Imaging of COPD
Department and Institution: Diagnostic Radiology & Nuclear Medicine, Robarts Research Institute
Sponsor: INTERNAL RESEARCH FUND-UWO
Ethics Approval Date: May 25, 2009 **Expiry Date:** November 30, 2013
Documents Reviewed and Approved: UWO Protocol, Letter of information & consent form for Patients dated March 26/09 & Letter of information & consent form for Healthy Volunteers dated March 26/09
Documents Received for Information: Protocol, January 27, 2009; IB, ed 6, 09 Sep. 05

This is to notify you that The University of Western Ontario Research Ethics Board for Health Sciences Research Involving Human Subjects (HSREB) which is organized and operates according to the Tri-Council Policy Statement: Ethical Conduct of Research Involving Humans and the Health Canada/ICH Good Clinical Practice Practices: Consolidated Guidelines; and the applicable laws and regulations of Ontario has reviewed and granted approval to the above referenced study on the approval date noted above. The membership of this REB also complies with the membership requirements for REB's as defined in Division 5 of the Food and Drug Regulations.

The ethics approval for this study shall remain valid until the expiry date noted above assuming timely and acceptable responses to the HSREB's periodic requests for surveillance and monitoring information. If you require an updated approval notice prior to that time you must request it using the UWO Updated Approval Request Form.

During the course of the research, no deviations from, or changes to, the protocol or consent form may be initiated without prior written approval from the HSREB except when necessary to eliminate immediate hazards to the subject or when the change(s) involve only logistical or administrative aspects of the study (e.g. change of monitor, telephone number). Expedited review of minor change(s) in ongoing studies will be considered. Subjects must receive a copy of the signed information/consent documentation.

Investigators must promptly also report to the HSREB:

a) changes increasing the risk to the participant(s) and/or affecting significantly the conduct of the study;
b) all adverse and unexpected experiences or events that are both serious and unexpected;
c) new information that may adversely affect the safety of the subjects or the conduct of the study.

If these changes/adverse events require a change to the information/consent documentation, and/or recruitment advertisement, the newly revised information/consent documentation, and/or advertisement, must be submitted to this office for approval.

Members of the HSREB who are named as investigators in research studies, or declare a conflict of interest, do not participate in discussion related to, nor vote on, such studies when they are presented to the HSREB.

Chair of HSREB: Dr. Joseph Gilbert

Ethics Officer to Contact for Further Information			
☑ Janice Sutherland	☐ Elizabeth Wambolt	☐ Grace Kelly	☐ Denise Grafton

This is an official document. Please retain the original in your files.

cc: ORE File
LHRI

Appendix – F: Curriculum Vitae

Curriculum Vitae

Curriculum Vitae

Amir Owrangi MSc

PhD Candidate
Imaging Research Laboratories
Robarts Research Institute
The University of Western Ontario

EDUCATION

2009-	PhD Candidate (Biomedical Engineering) **The University of Western Ontario, London Canada** Quantitative Evaluation of Pulmonary Emphysema Using Magnetic Resonance Imaging and x-ray Computed Tomography **Supervisor: Dr. Grace Parraga**
2005-2007	MSc (Radiation-Medicine Engineering) 2007 **Shiraz University, Shiraz, Iran** Monte Carlo Simulation of the Medical Linear Accelerator Photon Beam Using MCNP4C and EGSnrc **Supervisor: Dr. Amin Mosleh-Shirazi**
1999-2004	BSc Physics 2004 **Shiraz University, Shiraz, Iran** Dose Measurements using Thermoluminescence in Interventional Radiology **Supervisor: Simin Mehdizadeh, MSc**

PUBLICATIONS

Peer Reviewed Manuscripts

Published and In Press

1. **A. Owrangi**, R. Etemad-Rezai, D.G. McCormack, I. Cunningham and G. Parraga, Computed tomography density histogram analysis to evaluate pulmonary emphysema in ex-smokers. *Acad Radiol*, Nov 2012 (In Press)

2. **A. Owrangi**, J.X. Wang, A. Wheatley, D.G. McCormack, G. Parraga, Quantitative analysis of ^{1}H magnetic resonance imaging signal intensity in chronic obstructive pulmonary disease and comparison to ^{3}He MRI. *Eur J Radiol*. 2012 May 7, [Epub ahead of print]

3. J.C. Chow, **A. Owrangi**. Surface dose reduction from bone interface in kilovoltage X-ray radiation therapy: a Monte Carlo study of photon spectra. *J Appl Clin Med Phys*. 2012 Sep; 13(5):215-222.

4. M. Kirby, S. Svenningsen, **A. Owrangi**, A. Wheatley, A. Farag, A. Ouriadov, G.E. Santyr, R. Etemad-Rezai, H.O. Coxson, D.G. McCormack and G. Parraga, Hyperpolarized Helium-3 and Xenon-129 Magnetic Resonance Imaging in Never-smokers and Ex-smokers with Chronic Obstructive Pulmonary Disease. *Radiology* 2012 Sep 5. [Epub ahead of print]

5. **A. Owrangi**, G. Parraga, Chest MRI in children: why bother? *Respirology.* 2012 Jan;17(1):3-4

6. J. Awad, **A. Owrangi**, L. Villemaire, E. O'Riordan, Grace Parraga, A. Fenster, Three-dimensional Lung Tumour Segmentation from x-ray Computed Tomography using Sparse Field Active Models. *Med Phys.* 2012; 39(2):851.

7. L. Villemaire, **A. Owrangi**, L. Wilson, E. O'Riordan, R. Etemad-Rezai, H. Keller, B. Driscoll, G. Bauman, A. Fenster, Grace Parraga, Pulmonary Tumour Measurements from X-Ray Computed Tomography in One- Two- and Three-dimensions. *Acad Radiol*. 2011 Nov; 18(11):1391-402.

8. J.C. Chow, **A. Owrangi**. Dependences of mucosal dose on photon beams in head-and-neck intensity-modulated radiation therapy: A Monte Carlo study. *Med Dosim*. 2012 Summer; 37(2):195-200.

9. M. Kirby, **A. Owrangi**, J.X. Wang, S. Costella, S. Choy, D.G. McCormack and G. Parraga. Pulmonary Magnetic Resonance Imaging of Obstructive Airways Disease. *Minerva Pnemologica* 2011; 50(1): 17-29

10. J.C. Chow, **A. Owrangi**. Monte Carlo study on mucosal dose in oral and nasal cavity using photon beams with small field. *J. Radiother. Pract.* 2011; 10(4): 261-271

11. D. Letourneau, M. Sharpe, **A. Owrangi**, D. Jaffray, Automated beam model optimization. *Med Phys*. 2010 May; 37(5):2110-20.

12. C. Coolens, S. Breen, T. Purdie, **A. Owrangi**, J. Publicover, S. Bartolac, D. Jaffray, Implementation and characterization of a 320-slice volumetric CT scanner for simulation in radiation oncology. *Med Phys*. 2009 Nov; 36(11):5120-7.

13. J.C. Chow, **A. Owrangi**. Solid Water as phantom material for dosimetry of electron backscatter using low-energy electron beams: A Monte Carlo evaluation. *Med Phys.* 2009 May; 36(5):1587-94

14. J.C. Chow, **A. Owrangi**. Depth dependence of electron backscatter: an energy spectral and dosimetry study using Monte Carlo simulation. *Med Phys.* 2009 Feb; 36(2):594-601.

15. S. Mehdizadeh, **A. Owrangi**, S. Derakhshan, Cardiologist's Hand Dose Measurements in Interventional Radiology. *Asian J. Exp. Sci.* 2007, 21(2): 407-409

16. S. Mehdizadeh, **A. Owrangi**, S. Derakhshan. Patient Dose Measurements in Interventional Radiology. *Asian J. Exp. Sci. 2007 21(1): 105-108*

Submitted

1. **A. Owrangi**, B. Entwistle, A. Lu, J. Chiu, N. Hussain, R. Etemad-Rezai and G. Parraga, Semi-automated scoring of pulmonary emphysema from x-ray CT: Trainee reproducibility and accuracy. Submitted to *AJR Am J Roentgenol,* Oct 2012

2. M. Kirby, S. Svenningsen, N. Kanhere, **A. Owrangi**, A. Wheatley, H.O. Coxson, G.E. Santyr, N. Paterson, D.G. McCormack and G. Parraga. Pulmonary Ventilation Visualized using Hyperpolarized Helium-3 and Xenon-129 Magnetic Resonance Imaging: Differences in COPD and Relationship to Emphysema. Submitted to *J Appl Physiol,* Oct 2012

3. M. Kirby, **A. Owrangi**, S. Svenningsen, A. Wheatley, H.O. Coxson, N. Paterson, D.G. McCormack and G. Parraga. Hyperpolarized ^{3}He MRI, symptoms and exercise capacity in ex-smokers without airflow obstruction. Submitted to *Chest,* Sep 2012

ABSTRACTS AND PRESENTATIONS

A Oral Presentations

1. **A. Owrangi**, J.X. Wang , A. Wheatley, D.G. McCormack, I.A. Cunningham, G. Parraga, Development of Novel ^{1}H Magnetic Resonance Imaging Methods to Map Lung Structure and Function, Joint American Association of Physicists in Medicine (AAPM)/ Canadian Organization of Medical Physicists (COMP) Annual Meeting, Vancouver, BC, Canada. July 2011

2. J. Awad, L. Villemaire, **A. Owrangi**, G. Parraga, A. Fenster, 3D Automatic Segmentation of Lung Tumours Using Sparse Field Active Surface on CT Image, Ontario Institute for Cancer Research (OICR) Annual meeting, Toronto, ON, Canada. 2011

3. **A**. **Owrangi**, JX. Wang, E. O'Riordan, D.G. McCormack, G. Parraga, The relationship of ultra short time ^{1}H magnetic resonance imaging and pulmonary function in chronic obstructive pulmonary disease, Biomedical Engineering Society (BMES) Annual meeting, Austin, TX, USA. 2010

4. **A**. **Owrangi**, H. Ahmed, S. Choy, A. Wheatley, R. Etemad-Rezai, D.G. McCormack, G. Parraga, Development of hyperpolarized Helium-3 Magnetic resonance imaging of pulmonary ventilation, American Thoracic Society (ATS), New Orleans, LA, USA. 2010

5. **A**. **Owrangi**, J. Jezioranski, I. Yeung, H. Keller, Brachytherapy dosimetry simulation of Eye Physics Slotted Plaque: a Monte Carlo study. American Brachytherapy Society (ATS) Annual Meeting, Toronto, ON, Canada. 2009

6. S. Mehdizadeh, **A. Owrangi**, S. Derakhshan, Thermoluminescence dosimetry of patients in interventional radiology**,** The 1st International Human, Life and Radiation Conference Rafsanjan, Iran. 2006
7. S. Mehdizadeh, **A. Owrangi**, S. Derakhshan, Thermoluminescence dosimetry of cardiologist's hands in interventional radiology**,** The 1st International Human, Life and Radiation Conference Rafsanjan, Iran. 2006

B Poster Presentations

1. **A. Owrangi**, L. Villemaire, A. Wheatley, R. Etemad-Rezai, D.G. McCormack, I. Cunningham and G. Parraga, Quantification of Emphysema using x-ray Computed Tomography Histogram Analysis, London Health Research Day (LHRD) Annual Meeting, London, ON, Canada. 2012

2. B. Entwistle, A. Lu, J. Chiu, N. Hussain, **A. Owrangi**, L. Villemaire, D. G. McCormack, G. Parraga and R. Etemad-Rezai, Development of a New Tool for Training Purposes and Subjective Quantification of Pulmonary Emphysema, London Imaging Day (LID) Annual Meeting, London, ON, Canada. 2012

3. **A. Owrangi**, L. Villemaire, A. Wheatley, R. Etemad-Rezai, D.G. McCormack, I. Cunningham and G. Parraga, Quantitative Evaluation of Emphysema in Subjects with Carotid Atherosclerosis, Imaging Network Ontario (ImNO) Annual Meeting, Toronto, ON, Canada. 2011

4. J.C. Chow, **A. Owrangi**, G. Grigorov , A. Wheatley, D.G. McCormack, I.A. Cunningham, G. Parraga, Surface Dose Reduction From Bone Interface in Superficial X-Ray Radiation Therapy: A Monte Carlo Study, Joint American Association of Physicists in Medicine (AAPM)/ Canadian Organization of Medical Physicists (COMP) Annual Meeting, Vancouver, BC, Canada. July 2011

5. **A. Owrangi**, JX. Wang, E. O'Riordan, DG. McCormack, and G. Parraga. The relationship between whole lung ^{1}H density of magnetic resonance imaging and hyperpolarized ^{3}He apparent diffusion coefficient in emphysema, London Imaging Discovery Day, Schulich School of Medicine, The University of Western Ontario June 2011

6. **A. Owrangi**, J.X. Wang, A. Wheatley, D.G. McCormack, G. Parraga, Quantitative analysis of ^{1}H magnetic resonance imaging signal intensity in chronic obstructive pulmonary disease and comparison to ^{3}He MRI, Canadian Student Conference on Biomedical Computing and Engineering (CSCBCE), London, ON, Canada. May 2011

7. **A. Owrangi**, J.X. Wang, A. Wheatley, D.G. McCormack, G. Parraga, The relationship between whole lung ^{1}H density of magnetic resonance imaging and computed tomography densitometry in emphysema, American Thoracic Society (ATS), Denver, CO, USA. May 2011

8. J. Awad, L. Villemaire, **A. Owrangi**, G. Parraga, A. Fenster, 3D Automatic Segmentation of Lung Tumours Using Sparse Field Active Surface on CT Images, Imaging Network Ontario (ImNO) Annual meeting, Toronto, ON, Canada. 2011

9. J. Chow, **A. Owrangi**, G. Grigorov, Dependence of mucosal dose on small photon beams: A Monte Carlo study, Canadian Organization of Medical Physicists (COMP) Annual Meeting, Ottawa, ON, Canada. July 2010

10. **A. Owrangi**, JX. Wang, E. O'Riordan, DG. McCormack, and G. Parraga. The Relationship of Ultra Short Echo Time ^{1}H Magnetic Resonance Imaging and Pulmonary Function in Chronic Obstructive Pulmonary Disease, London Imaging Discovery Day, Schulich School of Medicine, The University of Western Ontario June 2010

11. A. Wheatley, H. Ahmed, S. Choy, **A**. **Owrangi**, R. Etemad-Rezai, D.G. McCormack, G. Parraga, A rapid quality Assurance Technique for Multi-Centre, Multi-Reader Clinical Trials of Hyperpolarized Helium-3 Magnetic Resonance Imaging, American Thoracic Society (ATS), New Orleans, LA, USA. May 2010

12. **A**. **Owrangi**, H. Ahmed, S. Choy, A. Wheatley, R. Etemad-Rezai, D.G. McCormack, G. Parraga, Development of hyperpolarized Helium-3 Magnetic resonance imaging of pulmonary ventilation, Lawson Research Day, Lawson Health Research Institute, The University of Western Ontario, March 2010

13. **A. Owrangi**, H. Keller, D. Jaffray, C. Coolens. Effect of Motion on High Contrast Vessel-Like Objects for Volumetric DCE. The American Association of Physicists in Medicine (AAPM) Annual Meeting, Anaheim, CA, USA. July 2009

14. **A. Owrangi**, M. Masudiefar, R. Jaberi, F. Ghahramani, R. Clarkson, J. Chow. Monte Carlo dose calculation of critical organs in MDR Cs-137 afterloading intracavitary brachytherapy. Canadian Organization of Medical Physicists (COMP) Annual Meeting, Victoria, BC, Canada. July 2009

15. **A. Owrangi**, M. Masudifar, H. Nedaie, Z. Anjomani, A. Mosleh-Shirazi, External electron beam comparison of Monte Carlo codes (BEAMnrc, MCNP4C) in homogeneous phantom and interfaces. The American Association of Physicists in Medicine (AAPM) Annual Meeting, Houston, TX, USA. July 2008

16. J. Chow, **A. Owrangi**. Depth dependence of electron backscatter for electron radiotherapy: A Monte Carlo study. COMP 2008, Québec, QC, Canada. July 2008

17. **A. Owrangi**, M. Masudifar, R. Faghihi, A. Mosleh-Shirazi. Comparison of the MCNP4C and BEAMnrc Monte Carlo codes when simulating different electron energies of a Neptun 10pc linear accelerator. International Conference on Medical Physics (ICMP) Dubai, UAE. April 2008

18. M. Masudifar, **A. Owrangi**, R. Faghihi, A. Mosleh-Shirazi. Comparison of the MCNP4C and BEAMnrc Monte Carlo codes when simulating different electron

energies of a Neptun 10pc linear accelerator. International Conference on Medical Physics (ICMP) Dubai, UAE. April 2008

HONOURS AND AWARDS

2009-	**Western Graduate Research Scholarship** Awarded to graduate students who enrolled with an average of 80% or above. Institutional - **$7178 per year**
2011-2012	**Queen Elizabeth II Graduate Scholarship in Science and Technology (QEIIGSST)** **$15000 per year (Provincial)**
2011	**JR Cameron and JR Cunningham Young Investigator competition** **Finalist (AAPM/COMP Joint Annual Meeting)**
2011	**Canadian Thoracic Society (CTS)** First Annual Poster Competition **-Finalist**
2007	**The Highest Ranked Graduate in the Radiation-Medicine Engineering program (MSc)** Shiraz University, Shiraz, Iran Institutional
2006	**Best Presentation Award -1st International Human, Life and Radiation Conference (HLR 2006)** Rafsanjan University of Medical Science, Rafsanjan, Iran - International

WORK EXPERIENCE

2008-2009: **Princess Margaret Hospital.**

- A Novel auto thresholding method for PET images. (Research Analyst for Dr. Harald Keller)
- Monte Carlo simulation of low energy brachytherapy sources in eye plaques. (Summer Student for Dr. Ivan Yeung)
- Volumetric dynamic contrast enhanced study of lung tumours and vessels (Design and test a phantom for contrast imaging calibration that worked with a Modus ***QUASAR***^{TM} programmable respiratory motion phantom). (Research Analyst for Dr. Harald Keller)
- Monte Carlo simulation and characterization of electron beams in external beam radiotherapy. (Research Analyst for Dr. James Chow)
- Linear accelerators morning QA and IMRT QA. (Part time Physics Associate)

RELEVANT COURSE WORK

Radiological Physics, Radiation Biology, Physics of Radiation Therapy, Dosimetry and Radiation Detection, Medical Imaging, Imaging Principles, NMR Physics, MRI Physics, Human Anatomy, Human Physiology, Scientific Communications, Advanced Research & Knowledge Translation, Research Ethics and Biostatistics, Vascular Imaging, Digital Image Processing, Inferencing from Data Analysis

TRAINEE and RESEARCH SUPERVISION

Undergraduate 4th year thesis 2010-2011
Student Name: Lauren Villemaire
Thesis title: Pulmonary Tumour Measurements from X-Ray Computed Tomography in One- Two- and Three-dimensions

> L. Villemaire, **A. Owrangi**, L. Wilson, E. O'Riordan, R. Etemad-Rezai, H. Keller, B. Driscoll, G. Bauman, A. Fenster, Grace Parraga, Pulmonary Tumour Measurements from X-Ray Computed Tomography in One- Two- and Three-dimensions. *Acad Radiol*. 2011 Nov; 18(11):1391-402.

POST-GRADUATE EDUCATION DEVELOPMENT

Teaching Assistantship, Graduate Program in Biomedical Engineering

- Scientific Communications
- Advanced Research & Knowledge Translation

TECHNICAL SKILLS

1. **MATLAB** (Matrix Laboratory)
2. **MCNP** (Monte Carlo N-Particle)
3. **EGSnrc** (Electron Gamma Shower from National Research Council Canada)

PROFESSIONAL MEMEBERSHIPS

1. Canadian Organization of Physicists in Medicine ***Student Member*** (since January 2010)
2. American Association of Physicists in Medicine. ***Student Member*** (since October 2011)
3. Canadian Thoracic Society. ***Student Member*** (since September 2010)
4. American Thoracic Society. ***Student Member*** (since September 2010)

COCURRICULAR AND VOLUNTEER ACTIVITIES

2009-	Member, Network of Imaging Students (NOISe) Robarts Research Institute
2011	Intramurals Soccer, The University of Western Ontario

REFERENCES:

1. Dr. Grace Parraga,
   Scientist, Imaging Research Laboratories, Robarts Research Institute and
   Associate Professor, Medical Biophysics and Biomedical Engineering, The
   University of Western Ontario, London, Ontario, Canada

2. Dr. Aaron Fenster,
   Director and Scientist, Imaging Research Laboratories, Robarts Research
   Institute and Professor, Medical Biophysics and Biomedical Engineering, The
   University of Western Ontario, London, Ontario, Canada

3. Dr. Harald Keller,
   Medical Physicist, Department of Radiation Physics, Princess Margaret Hospital
   and Assistant Professor, Department of Radiation Oncology, University of
   Toronto, Toronto, Ontario, Canada